



HAL
open science

Beating the standard quantum limit for the gravitational wave detector Advanced Virgo

Angélique Lartaux-Vollard

► **To cite this version:**

Angélique Lartaux-Vollard. Beating the standard quantum limit for the gravitational wave detector Advanced Virgo. Astrophysics [astro-ph]. Université Paris-Saclay, 2020. English. NNT : 2020UP-ASP046 . tel-03038300

HAL Id: tel-03038300

<https://theses.hal.science/tel-03038300>

Submitted on 3 Dec 2020

HAL is a multi-disciplinary open access archive for the deposit and dissemination of scientific research documents, whether they are published or not. The documents may come from teaching and research institutions in France or abroad, or from public or private research centers.

L'archive ouverte pluridisciplinaire **HAL**, est destinée au dépôt et à la diffusion de documents scientifiques de niveau recherche, publiés ou non, émanant des établissements d'enseignement et de recherche français ou étrangers, des laboratoires publics ou privés.

Beating the Standard Quantum Limit for the gravitational wave detector Advanced Virgo

Thèse de doctorat de l'Université Paris-Saclay

École doctorale n° 576, particules hadrons énergie et noyau :
instrumentation, image, cosmos et simulation (Pheniics)
Spécialité de doctorat: Astroparticules et Cosmologie
Unité de recherche: Université Paris-Saclay, CNRS, IJCLab, 91405, Orsay,
France.
Référent: Faculté des sciences d'Orsay

Thèse présentée et soutenue à Orsay, le 12 novembre 2020, par

Angélique LARTAUX-VOLLARD

Composition du jury:

Jacques ROBERT Professeur, Université Paris-Saclay, LPGP	Président
Sébastien TANZILLI Directeur de recherche, CNRS, INPHYNI	Rapporteur & Examineur
Jean-Pierre ZENDRI Directeur de recherche, INFN, Padova	Rapporteur & Examineur
Sophie HENROT-VERSILLÉ Directrice de recherche, CNRS, IJCLab	Examinatrice
Giovanni LOSURDO Directeur de recherche, INFN, Pisa	Examineur
Fabien Cavalier Directeur de recherche, CNRS, IJCLab	Directeur
Nicolas Leroy Chargé de recherche HDR, CNRS, IJCLab	Co-Directeur

Remerciements

Me voici arrivée à la fin d'une longue aventure et il est temps désormais de remercier ceux qui l'ont rendue possible. Tout d'abord, je remercie Achille Stocchi de m'avoir accueillie au sein de son laboratoire (d'abord le Laboratoire de l'Accélérateur Linéaire puis le Laboratoire de Physique des 2 Infinis Irène Joliot Curie après fusion).

Je remercie Sébastien Tanzilli et Jean-Pierre Zendri d'avoir accepté d'être rapporteurs de ma thèse et d'avoir pris le temps nécessaire pour examiner mon travail. Je remercie Sophie Henrot-Versillé, Giovanni Losurdo et Jacques Robert d'avoir accepté d'examiner ma thèse. Merci également à Jacques Robert d'avoir accepté de présider mon jury.

Cette thèse n'aurait pas été la même sans Fabien et Nicolas. Merci Nicolas de m'avoir proposé et si bien vendu ce sujet alors même que l'idée de travailler dans le domaine des ondes gravitationnelles m'avait à peine effleurée. Merci Fabien d'avoir partagé ton bureau avec moi pendant toutes ces années, modulo une année où tu as opté pour un bureau bien plus grand mais avec bien plus de charges administratives. Merci à tous les deux pour votre gentillesse, votre compréhension, vos encouragements et votre partage aussi bien scientifique qu'humain. Merci pour les fous rires, le temps que vous m'avez consacré malgré vos nombreuses responsabilités, la confiance que vous m'avez accordée pour mener à bien ce projet. En bref, merci pour ce que chacun de vous m'a apporté.

Le groupe ondes gravitationnelles s'est beaucoup transformé au cours de ma thèse. Il y a ceux qui sont partis ailleurs pour de nouvelles aventures : Dominique, Julia, Marie-Anne, Valentin, Imène. Il y a également ceux qui sont arrivés en cours de route pour une thèse : David, Jean-Grégoire, Shaymaa, Pierre-Alexandre et la dernière Marion. Je vous souhaite à tous bon courage, en particulier pour ceux qui sont dans la dernière ligne droite (pour les autres ça viendra vite!). Les post-docs qui sont par essence de passage plus ou moins long : Sarah, David et des remerciements particuliers à Pierre pour m'avoir supportée pendant 4 ans (il faudra te trouver un nouveau post-it). Et puis Tito, le nouveau membre permanent du groupe à qui je souhaite de s'épanouir dans ce beau groupe, entouré des piliers qui étaient là à mon arrivée et seront encore là après mon départ : Patrice, Nicolas et Florent. Merci à tous pour les moments passés avec vous.

Je n'oublie pas non plus les compères de l'ESPCI dans CALVA. Merci Ivan de m'avoir enseigné les rudiments des alignements optiques. Merci Vincent pour les discussions optiques et ton aide pour comprendre les phénomènes observés.

Je tiens à remercier les membres d'Exsqueeze des différents laboratoires ayant participé, de près ou de loin, à la partie haute fréquence d'Exsqueeze. In particular a very huge thank you to Sheon without whom none of this would have been possible. Thank you to have taken your personal time to help me to go to the end of this thesis. I hope like you that we will measure squeezing soon. Merci à Michael, Samuel et Pierre-François au LKB pour votre aide en particulier sur la RedPitaya. Merci Jérôme et Benoît pour votre travail sur les coatings à l'IP2I. Merci à Alain, Nicolas, Romain, Michal et Emmanuel au LAPP sur toute la partie électronique, des photodiodes à VPM. Je remercie également Eleonora pour nos échanges instructifs sur les simulations des pertes du squeezing.

Les services techniques du laboratoire ont été d'une grande aide pour la réalisation de ma thèse. J'aimerais tous les remercier et en particulier Patrick Cornebise, François Wicek, Denis Douillet, Christian Bourgeois, Christopher Magueur, Rodolphe Marie, Alice Thiebault, Julien Bonis, Bruno Mercier, Frédéric Letellier, Éric Guerard, Remy Dorkel, Marc Fernandez, Jeremy Favre, Charles Mendy et probablement d'autres que j'oublie et je m'en excuse.

Merci à Grégory Perrin pour sa gestion de la visio-conférence de ma soutenance de thèse.

Merci aux équipes LaserIX et TomX/Eli travaillant sur d'autres expériences optiques pour les discussions et emprunts de matériels plus ou moins grands sur une plus ou moins longue durée! En particulier merci à Olivier G., Sophie, Moana, Julien, Elsa, Olivier N., Bruno, Kevin D., Fabian, Aurélien, Kevin C., Pierre, Cheikh, Loic et Titouan.

Merci à l'équipe enseignante dans laquelle j'ai pu découvrir les joies de l'enseignement et tout particulièrement Jérôme, Séverine et Pierre ainsi que Bertrand et Hans.

J'ai une pensée pour les stagiaires que j'ai encadrés, de tous niveaux et de toute durée. Cadmos, Yugang, Timothé, Thimothée, Kevin, Cyril, Alexandre, Adrien, Emeline et Yanis, je vous souhaite à tous de réussir dans la voie que vous vous choisissez.

Je voudrais également remercier toutes les autres personnes avec qui j'ai interagi au cours de ma thèse, les visages croisés sans toujours y associer de noms, les bonjours échangés aux bâtiments 200, 208 et au magasin, Marie-Hélène, Yasmine, Sergey, Sylvie, Didier, Annick, Eric, Alain, Marc, Roland, Gérard, Thierry, Tommy, Sylvain et tant d'autres. Merci Dominique pour tout ton travail de reprographie et les belles photos de la vie du labo que tu nous fais. Merci Catherine pour toutes ces discussions dans ton bureau et les chocolats chauds gentiments offerts.

Enfin, des remerciements plus personnels à ma mère et ma belle-famille m'ayant toujours encouragée pour arriver au bout de cette thèse. Et une pensée émue pour nos êtres chers.

Merci aux 4 piliers croisés sur ma route ces dix dernières années. Vous m'avez beaucoup apporté et je n'en serais peut-être pas là aujourd'hui si je ne vous avais pas rencontrés.

Pour finir par le meilleur, merci infiniment Alexandre d'être toujours là à mes côtés dans toutes les épreuves. Merci d'avoir signé ton engagement auprès de moi me permettant aujourd'hui de porter ton nom.

Contents

Résumé	1
Introduction	9
1 Gravitational waves	11
1.1 Gravitational waves in general relativity	11
1.2 Effect of gravitational waves	12
1.3 Gravitational waves generation	14
1.4 Astronomical sources	16
1.4.1 Transient sources	17
1.4.2 Continuous signals	22
1.5 Motivations	22
1.5.1 Astrophysics	23
1.5.2 Tests of general relativity	23
1.5.3 Cosmology	23
2 Gravitational wave detectors	25
2.1 Overview of gravitational wave detectors	25
2.1.1 Weber bars	25
2.1.2 Pulsar timing	26
2.1.3 Space interferometers	27
2.1.4 Atom interferometers	27
2.2 Ground based interferometric detectors	28
2.2.1 History	28
2.2.2 Simple Michelson interferometer	28
2.3 Noise sources	32
2.3.1 Sensitivity	32
2.3.2 Seismic noise	32
2.3.3 Quantum noise	34
2.3.4 Other sources of noise	37
2.4 First sensitivity improvements	39
2.4.1 Fabry-Perot arm cavity	39
2.4.2 Power recycling	44
2.4.3 Signal recycling	45
2.5 Further improvements	46
2.5.1 Motivations	46
2.5.2 Noises reduction possibilities	47
3 Squeezing	49
3.1 Basics of quantum optics	49
3.1.1 Quantization of the electromagnetic field	49
3.1.2 Heisenberg uncertainty relation	50
3.2 States of light	50

3.2.1	Classical phasor diagram	51
3.2.2	The vacuum state	51
3.2.3	Coherent states	52
3.2.4	Squeezed states	53
3.3	Quantum noise in gravitational wave detectors	55
3.4	Frequency dependent squeezing	58
3.4.1	Two-photon formalism	58
3.4.2	Filter cavity	59
3.5	Experimental squeezed states of light	61
3.5.1	Generation of squeezed states	61
3.5.2	Detection of squeezed states	65
3.6	Squeezing degradation budget	67
3.6.1	Injection and readout losses	68
3.6.2	Filter cavity losses	68
3.6.3	Mode matching losses	69
3.6.4	Phase noise	69
3.6.5	Linear noise transfer and noise budget	70
3.7	State of the art	73
3.7.1	Squeezing production	73
3.7.2	Squeezing in gravitational wave detectors	73
3.7.3	Frequency dependent squeezing	74
4	Design of a Frequency Dependent Squeezing Experiment: Exsqueeze	77
4.1	Exsqueeze experiment overview	78
4.1.1	Simplified conceptual design	78
4.1.2	Introduction of the full conceptual design	79
4.1.3	Pound-Drever-Hall Locking technique	83
4.2	Second Harmonic Generators	84
4.2.1	Non linear medium	84
4.2.2	Temperature control	85
4.2.3	Cavity	86
4.3	Optical Parametric Oscillator	87
4.3.1	Non linear medium	87
4.3.2	The doubly resonant bow-tie cavity	88
4.4	Control of the squeezing production	92
4.4.1	Power fluctuation reduction using a Mach-Zehnder	92
4.4.2	Modified Coherent Locking scheme	94
4.4.3	Phase Locking Loop	96
4.4.4	Seed beam	97
4.5	Filter cavity	99
4.5.1	Mirrors radius of curvature	99
4.5.2	Mirrors coating specifications	100
4.5.3	Control of the filter cavity	101
4.6	Summary	103
4.6.1	Filter Cavity Control beam	103
4.6.2	Filter Cavity Verification beam	104
4.6.3	Local Oscillator beam	104
4.6.4	Modified Coherent Locking beam	105
4.6.5	Phase Locking beam	106
4.6.6	Pump beam	106
4.6.7	Seed beam	107
4.6.8	Squeezed beam	108
4.6.9	Parameters summary	108

5	Integration of the Exsqueezer experiment on the CALVA facility	109
5.1	Acquisition electronics	109
5.2	In-air beams preparation bench	111
5.2.1	Main laser green beam production	111
5.2.2	Main laser fibers injections	118
5.2.3	Auxiliary laser green beam production	120
5.2.4	Auxiliary laser fiber injection	125
5.3	In-vacuum bench	127
5.3.1	Preparation of the in-vacuum bench integration	127
5.3.2	Laser phase locking	130
5.3.3	Filter cavity	132
5.4	Conclusion	134
6	Preparation of the squeezing measurement	135
6.1	Alignment of the Optical Parametric Oscillator cavity	135
6.2	Characterization of the Optical Parametric Oscillator	138
6.2.1	Intra-cavity losses	139
6.2.2	Nonlinear effects	141
6.2.3	Parametric gain	144
6.3	Homodyne detection efficiency	148
6.3.1	Beam splitter characterization	149
6.4	Conclusion	153
	Conclusion and outlooks	155
	Bibliographie	156

Résumé

Les ondes gravitationnelles ont été prédites par Albert Einstein en 1916 comme une conséquence de sa théorie de la relativité générale. Ce sont des oscillations de la courbure de l'espace-temps, produites par des masses accélérées, se propageant à la vitesse de la lumière dans le vide. Les sources les plus intenses d'ondes gravitationnelles sont les coalescences de systèmes binaires d'objets compacts (tels les trous noirs et étoiles à neutrons), les explosions de supernovae et d'autres mécanismes décrits au Chapitre 1.

La première détection directe d'une onde gravitationnelle a été faite le 14 septembre 2015 par les détecteurs interférométriques américains Advanced LIGO et a été suivie par de nombreuses autres détections au cours de 3 phases d'observations, dont une partie en commun avec le détecteur interférométrique européen Advanced Virgo.

Le principe de base de la détection interférométrique d'ondes gravitationnelles est celui de l'interféromètre de Michelson avec des bras de longueurs kilométriques, détaillé au Chapitre 2. Un changement relatif de la longueur des bras de l'interféromètre causé par le passage d'une onde gravitationnelle entraîne un changement de la condition d'interférence sur le détecteur et donc un changement de la puissance lumineuse mesurée. La sensibilité des détecteurs est augmentée par l'ajout d'une cavité Fabry-Perot dans chacun des bras du Michelson, ainsi que des miroirs de recyclages créant des cavités couplées.

Les principaux bruits limitants la sensibilité des détecteurs interférométriques d'ondes gravitationnelles sont également présentés au Chapitre 2. Le bruit de pression de radiation et le bruit de grenaille sont deux facettes du bruit quantique limitant la sensibilité qui nous intéresse dans le cadre de cette thèse.

Limite quantique standard

Le bruit de pression de radiation provient de l'impact des photons sur les miroirs de l'interféromètre causant leur déplacement. Ce déplacement est proportionnel à la puissance optique incidente sur le miroir et entraîne un changement relatif de la longueur des bras de l'interféromètre, de même qu'une onde gravitationnelle. Les miroirs des détecteurs étant suspendus, le bruit de pression de radiation limite la sensibilité des détecteurs de façon inversement proportionnelle au carré de la fréquence des fluctuations comme le montre la courbe verte de la Figure 1.

Le bruit de grenaille provient des fluctuations de la puissance mesurée sur la photodiode de détection dues à la nature discrète des photons. Sur un intervalle de mesure caractérisé par un nombre moyen de photons \bar{N} , la probabilité de mesurer N photons est décrite par une distribution de Poisson qui peut être approximée par une distribution gaussienne pour $\bar{N} \gg 1$. Le bruit de grenaille est indépendant de la fréquence pour un Michelson simple¹ comme représenté en bleu sur la Figure 1.

Pour un détecteur interférométrique d'ondes gravitationnelles avec une puissance P_{in} stockée dans ses bras, l'impact du bruit de pression de radiation sur la sensibilité des détecteurs est proportionnel à $\sqrt{P_{in}}$ tandis que celui du bruit de grenaille est inversement proportionnel

¹Pour les détecteurs interférométriques d'ondes gravitationnelles, les cavités Fabry-Perot dans les bras du Michelson agissent comme des filtres passe-bas sur la sensibilité du détecteur.

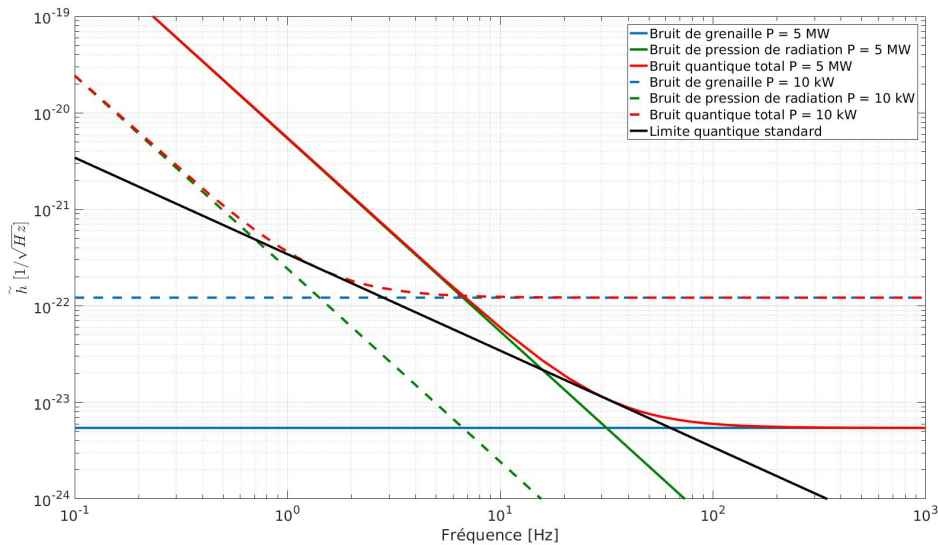


FIGURE 1 – Simulation du bruit de grenaille (en bleu), du bruit de pression de radiation (en vert) et de leur somme : le bruit quantique (en rouge) pour deux puissances optiques stockées dans les bras des interféromètres. La limite quantique standard est tracée en noir.

à $\sqrt{P_{in}}$. Ainsi en faisant varier la puissance P_{in} , on peut diminuer l'un des deux bruits quantiques, mais au prix d'augmenter l'autre. Ceci conduit à une limitation de la sensibilité des détecteurs due aux bruits quantiques : la limite quantique standard représentée en noir sur la Figure 1.

Le bruit quantique est l'un des bruits limitant pour les détecteurs interférométriques d'ondes gravitationnelles. L'objet de cette thèse est de tester expérimentalement une technique d'optique quantique permettant de dépasser la limite quantique standard. Cette technique utilise des états comprimés de la lumière que l'on nomme plus souvent *squeezing*.

Squeezing

La notion de squeezing est introduite et détaillée au Chapitre 3 dans un formalisme basé sur les opérateurs création et annihilation en physique quantique. Ce formalisme donne une représentation graphique du squeezing en utilisant la relation d'incertitude de Heisenberg pour visualiser l'incertitude sur la phase et sur l'amplitude d'un état lumineux dans un diagramme de phase. Un état cohérent de la lumière, tel celui généré par un laser, y est représenté par un disque dont la surface minimale est donnée par la relation d'incertitude de Heisenberg comme on peut le voir sur la Figure 2a.

La relation d'incertitude de Heisenberg ne donne une limite minimale que sur la surface qu'un état occupe dans un diagramme de phase. Il est donc possible qu'un état ait une incertitude sur son amplitude plus faible qu'un état cohérent, au prix d'une plus grande incertitude sur sa phase : il s'agit du squeezing en amplitude représenté sur la Figure 2b. Inversement un état peut également avoir une incertitude sur sa phase plus faible qu'un état cohérent, au prix d'une plus grande incertitude sur son amplitude : il s'agit du squeezing en amplitude représenté sur la Figure 2c.

Pour un détecteur interférométrique d'ondes gravitationnelles, le bruit quantique provient de fluctuations du vide entrant dans l'interféromètre par le port de détection. Ces fluctuations sont amplifiées par la puissance laser présente dans l'interféromètre avant de revenir sur la photodiode de détection.

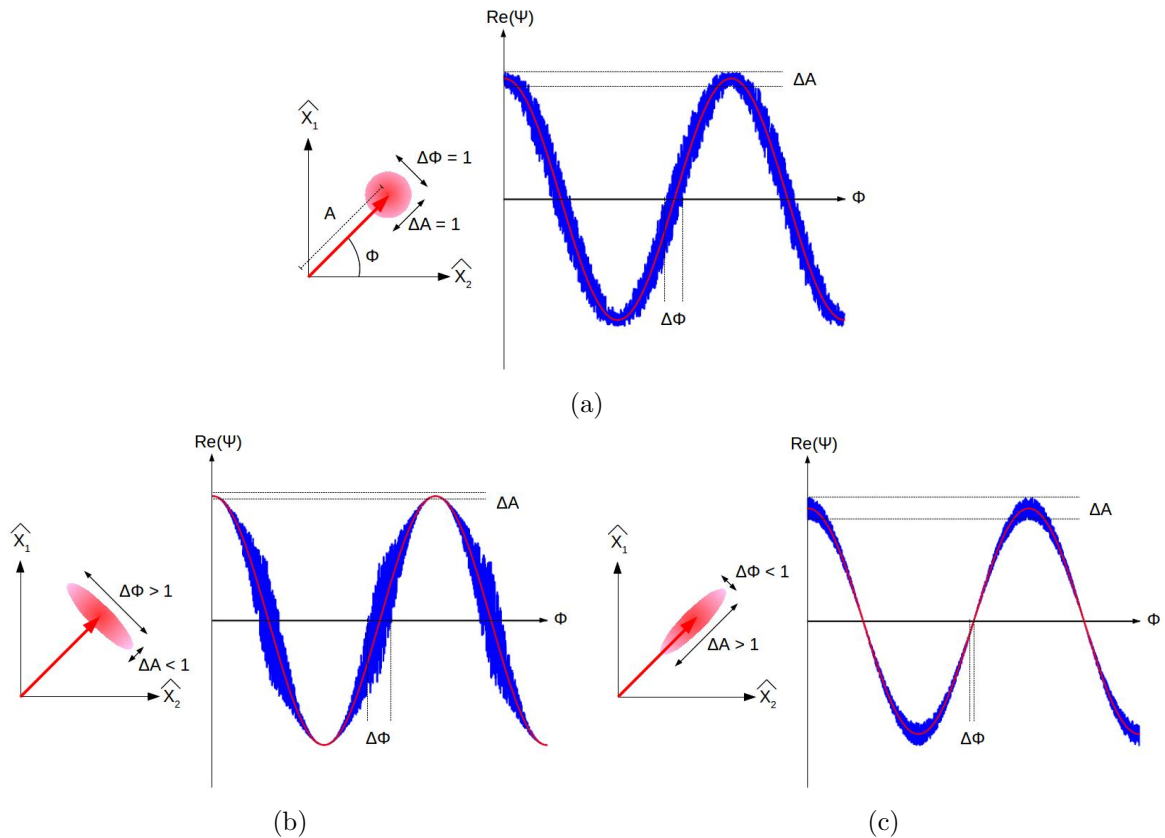


FIGURE 2 – Représentations de trois états de la lumière : (a) cohérent, (b) squeezing en amplitude, (c) squeezing en phase. Pour chaque état sont représentés : (à gauche) un diagramme de phase quantique dans les quadratures d’amplitude et de phase, (à droite) la partie réelle du champ électrique montrant le résultat typique d’une mesure.

Si on applique du squeezing en amplitude aux fluctuations du vide entrant dans l’interféromètre, on peut améliorer la sensibilité des détecteurs à basse fréquence, au prix d’une détérioration à haute fréquence et inversement si on leur applique du squeezing en phase, on peut améliorer la sensibilité des détecteurs à haute fréquence au prix d’une détérioration à basse fréquence comme le montre la Figure 3.

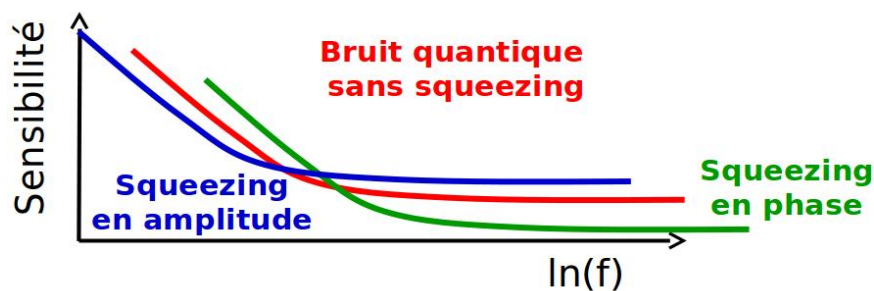


FIGURE 3 – Graphique présentant la limitation de la sensibilité des détecteurs interférométriques d’ondes gravitationnelles due au bruit quantique sans squeezing (en rouge), avec du squeezing en amplitude (en bleu) et avec du squeezing en phase (en vert).

Squeezing dépendant de la fréquence

Une solution pour améliorer la sensibilité des détecteurs interférométriques d’ondes gravitationnelles dans toute leur gamme de fréquence est d’utiliser du squeezing dépendant de la fréquence.

La description du squeezing dépendant de la fréquence utilise un autre formalisme dit à “deux-photons” qui est détaillé au Chapitre 3. Le point de départ est un état de squeezing indépendant de la fréquence qui est envoyé dans une cavité Fabry-Perot dite de filtrage.

Dans le formalisme à “deux-photons”, la génération du squeezing se fait par la transformation, par interaction non linéaire dans un cristal, d’un photon 2ω en 2 photons $\omega \pm \Omega$ intriqués avec $\Omega \ll \omega$. C’est l’intrication entre les 2 photons générés simultanément qui est à l’origine des propriétés de squeezing.

La réflectivité de la cavité de filtrage dépend de la fréquence. Ainsi les 2 photons intriqués sont réfléchis par la cavité avec une phase cumulée différente qui se traduit par un opérateur de rotation dépendant de la fréquence. En revenant à la représentation du diagramme de phase, cela correspond à une rotation d’un angle $\alpha_p(f)$ de l’ellipse de squeezing par rapport au squeezing indépendant de la fréquence injecté dans la cavité.

L’angle $\alpha_p(f)$ est représenté en Figure 4 pour une cavité de longueur $L = 50$ m et de finesse $\mathcal{F} = 3000$ à la longueur d’onde du squeezing. C’est ce type de cavité qui sera utilisé pour l’expérience Exsqueeze, l’objet de cette thèse. Ces paramètres permettent d’obtenir un passage de squeezing en amplitude à un squeezing en phase à une fréquence de ~ 700 Hz. Pour les détecteurs interférométriques d’ondes gravitationnelles, l’objectif sera d’obtenir un changement de type de squeezing à 50 – 70 Hz, ce qui nécessite soit d’allonger la cavité de filtrage, soit d’augmenter sa finesse.

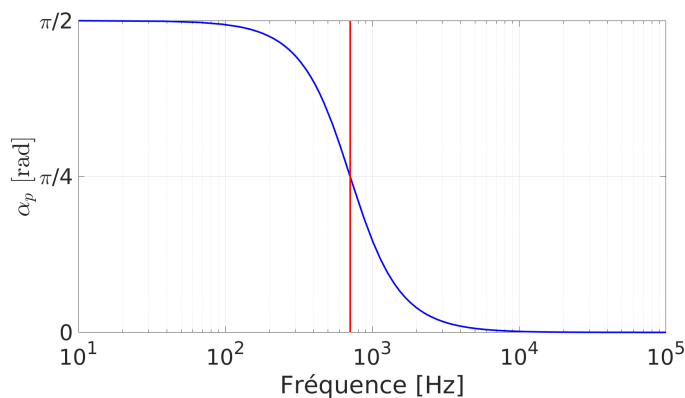


FIGURE 4 – Angle $\alpha_p(f)$ de l’ellipse de squeezing pour une cavité de filtrage de longueur $L = 50$ m et de finesse $\mathcal{F} = 3000$ à la longueur d’onde du squeezing permettant d’obtenir un changement de type de squeezing à la fréquence $f_t = 707$ Hz indiquée par la droite en rouge.

Les pertes représentent un facteur important à prendre en compte pour concevoir une expérience de squeezing car toutes les pertes vont dégrader le niveau de squeezing mesuré. Les sources de pertes sont nombreuses et apparaissent à différents endroits le long de la propagation du squeezing entre sa génération et sa détection. Elles sont décrites au Chapitre 3 ainsi que leur impact sur le squeezing mesuré.

On peut classer les pertes en 2 catégories : celles indépendantes de la fréquence et celles dépendantes de la fréquence. Il y a 4 sources de pertes indépendantes de la fréquence :

- *pertes d’injection* : pertes optiques sur la trajectoire du squeezing,
- *pertes d’acquisition* : pertes au niveau de la détection provenant principalement de l’efficacité quantique des photodiodes avec lesquelles la mesure de squeezing est faite,

- *bruit de phase indépendant de la fréquence* : fluctuations de l'orientation de l'ellipse de squeezing injecté dans la cavité de filtrage,
- *adaptation à l'oscillateur local* : adaptation du faisceau de squeezing mesuré au faisceau de l'oscillateur local utilisé pour la mesure détaillée au Chapitre 3.

Les pertes dépendantes de la fréquence sont liées à l'effet de la cavité de filtrage et se décomposent en 3 sources :

- *pertes de la cavité de filtrage* : pertes optiques dues à de l'absorption ou de la diffusion dans la cavité de filtrage,
- *adaptation à la cavité de filtrage* : pertes dues à la différence entre le mode du faisceau de squeezing et le mode propre de la cavité de filtrage,
- *bruit de phase dépendant de la fréquence* : fluctuations de la longueur de la cavité de filtrage.

La simulation de ces sources de pertes et leur impact sur le niveau de squeezing correspondant à la réduction du bruit quantique par rapport à un état cohérent sont représentés en Figure 5 pour des niveaux de pertes attendus pour Exsqueez et détaillés au Chapitre 3.

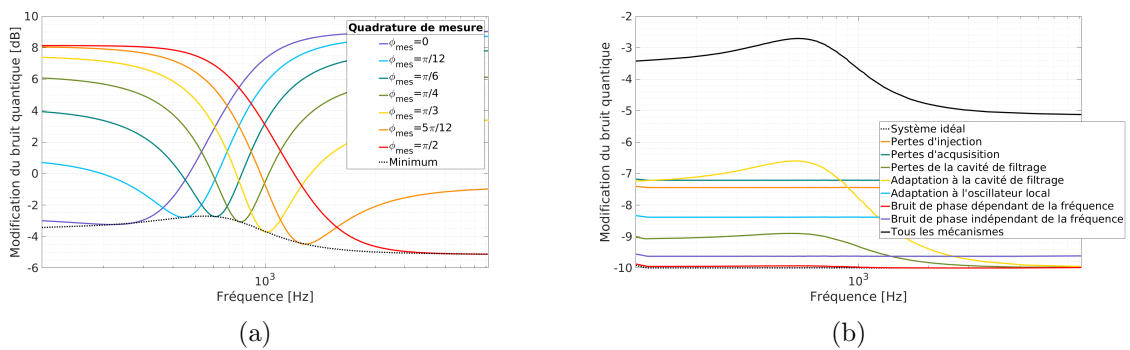


FIGURE 5 – Simulation du squeezing dépendant de la fréquence mesuré : (a) pour différentes quadratures de mesure ϕ en tenant compte de toutes les pertes, (b) différentes sources de pertes en choisissant à chaque fréquence la quadrature de mesure ϕ optimale. La simulation prend pour point de départ 10 dB de squeezing et des valeurs de pertes réalistes détaillées au Chapitre 3. La ligne noire en pointillés en (a) correspond à celle en trait plein en (b).

Exsqueez

Le projet Exsqueez est une collaboration entre 4 laboratoires : LKB¹, LAL/IJCLab², LMA/IP2I³ et LAPP⁴. La partie basse fréquence de ce projet consiste à tester le squeezing dépendant de la fréquence avec un changement de type de squeezing à une fréquence inférieure au kHz et une source de squeezing sous vide. Elle utilise l'infrastructure existante au LAL/IJCLab avec une cavité Fabry-Perot de 50 m sur la plateforme CALVA dont une salle est visible sur la Figure 6. La conception et le début de l'installation expérimentale de la partie basse fréquence de ce projet est l'objet de cette thèse.

¹Laboratoire Kastler Brossel (LKB) à Paris.

²Laboratoire de l'Accélérateur Linéaire (LAL) avant fusion le 1^{er} janvier 2020 au sein du Laboratoire de Physique des 2 Infinis Irène Joliot-Curie (IJCLab) à Orsay.

³Laboratoire des Matériaux Avancés (LMA), plateforme nationale de recherche au sein de l'Institut de Physique des 2 Infinis (IP2I) à Lyon depuis le 1^{er} janvier 2019.

⁴Laboratoire d'Annecy de Physique des Particules (LAPP) à Annecy.



FIGURE 6 – Première salle blanche de CALVA montrant la cuve rouge, appelée Ferrarix, utilisée pour le banc sous-vide d'Exsqueeze, et la cuve grise dans laquelle se trouve le premier miroir de la cavité de filtrage de 50 m.

La conception théorique d'Exsqueeze est détaillée au Chapitre 4. Un schéma de principe simplifié est présenté en Figure 7. Le principal système pour générer du squeezing est l'Oscillateur Paramétrique Optique (OPO) dont le cristal non linéaire convertit 1 photon vert en une paire de photons corrélé infrarouge, portant le squeezing. La cavité entourant le milieu non linéaire permet à la fois d'augmenter le nombre d'interactions non linéaires et donc l'efficacité de la production de squeezing, mais également de filtrer les fréquences des photons du squeezing autour de la fréquence infrarouge utilisée pour la détection.

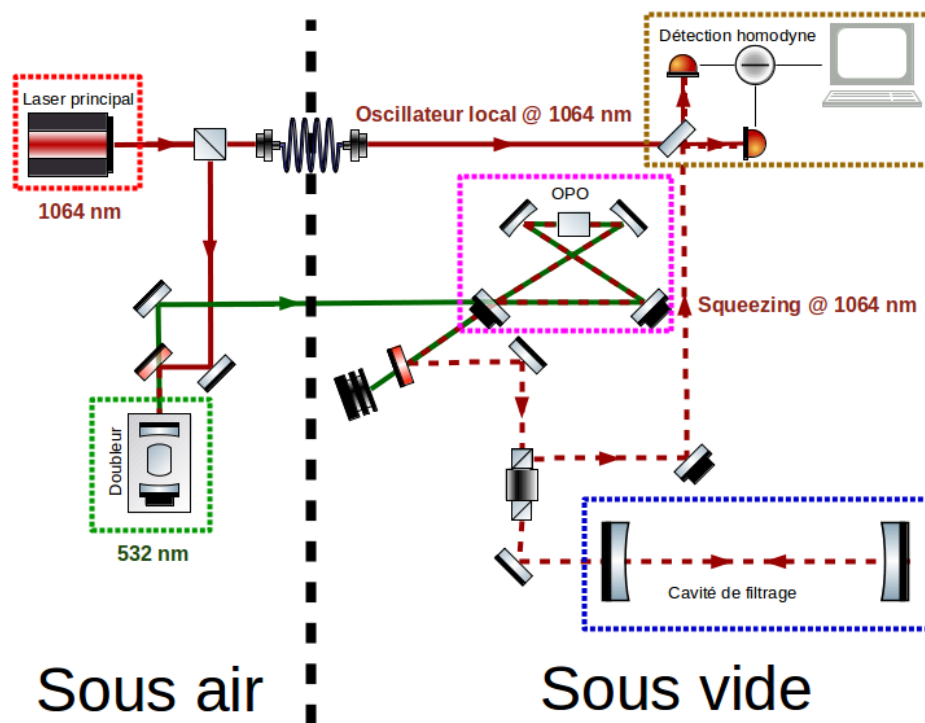


FIGURE 7 – Schéma de principe simplifié d'Exsqueeze montrant uniquement les systèmes principaux de la production et mesure de squeezing dépendant de la fréquence. En rouge le laser principal, en vert le doubleur, en rose l'Oscillateur Paramétrique Optique (OPO) source du squeezing, en bleu la cavité de filtrage et en marron la détection homodyne permettant la mesure du squeezing.

Le faisceau de squeezing est ensuite injecté dans la cavité de filtrage et sa réflexion est envoyée sur le dispositif de mesure utilisant un système de détection homodyne. Cette mesure se fait en combinant le squeezing à un oscillateur local à la même longueur d'onde. Pour s'assurer que le squeezing et l'oscillateur local ont la même longueur d'onde, le faisceau vert permettant de générer le squeezing dans l'OPO est lui-même généré à partir d'un laser infrarouge doublé en fréquence. C'est ce même laser infrarouge qui fournit l'oscillateur local.

L'installation et la caractérisation des sous-systèmes annexes au squeezing sont présentées au Chapitre 5 tandis que la caractérisation de l'OPO générant le squeezing et la détection homodyne permettant sa mesure sont présentées au Chapitre 6. En particulier, le gain paramétrique¹ de l'OPO a été mesuré en fonction de la puissance du faisceau pompe vert de l'OPO en Figure 8 dans le régime d'amplification du signal ainsi que dans celui de désamplification.

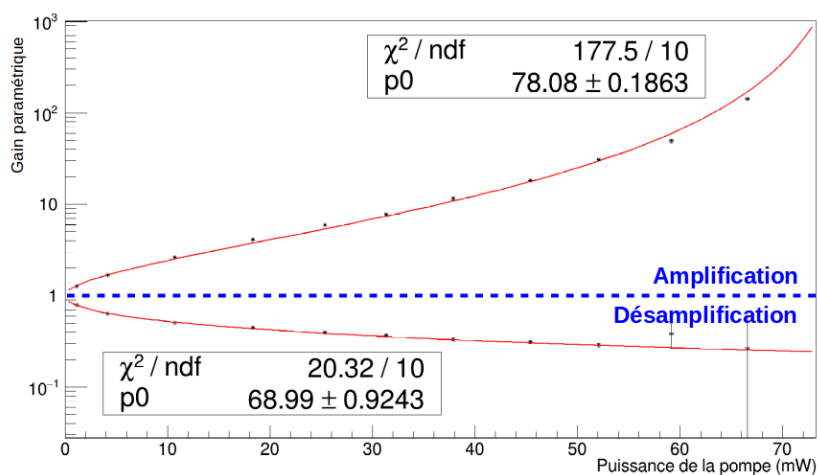


FIGURE 8 – Mesure du seuil de puissance du pump sur l'OPO. p_0 est la valeur extrapolée du seuil à partir des mesures en régime d'amplification et de désamplification.

Introduction

Gravitational waves are ripples in the spacetime curvature that have been predicted by Albert Einstein in 1916 as a consequence of his general theory of relativity. Their first direct observation in 2015 by the interferometric detectors Advanced LIGO was followed by many others in three observational runs that the Advanced Virgo detector joined in August 2017.

The basic properties of gravitational waves and their astronomical sources will be presented in Chapter 1, along with a summary of the detections made until now. Then, in Chapter 2, I will give an overview of gravitational wave detectors before detailing the ground based interferometric detectors principles and noise sources, in particular the quantum noise.

I will then focus on a solution to increase the detectors sensitivity by reducing the quantum noise using squeezed states of light that will be described in Chapter 3. I will first describe frequency independent squeezing and before moving on to the way to obtain frequency dependent squeezing improving the detectors sensitivity in their whole bandwidth.

In Chapter 3 I will also present the squeezing degradation budget, detailing the losses that can reduce the squeezing level and their impact on the quantum noise reduction. The conclusion of this chapter will give a brief state of the art of squeezing production, frequency independent squeezing already used in gravitational waves detectors and frequency dependent squeezing test experiments.

Chapter 4 will focus on the design of the frequency dependent test experiment done at LAL/IJCLab¹ in the framework of the ExsqueeZ project in collaboration with LKB², LMA/IP2I³ and LAPP⁴. The integration of the ExsqueeZ experiment on the CALVA facility at IJCLab will be presented in Chapter 5.

Finally, the characterization of the main optical system generating the squeezing will be presented in Chapter 6 along with the characterization of the measurement system to prepare the first frequency independent squeezing measurement that will be done on the CALVA facility.

¹Laboratoire de l'Accélérateur Linéaire (LAL) before merger on the 1st of January 2020 within the Laboratoire de Physique des 2 Infinis Irène Joliot-Curie (IJCLab) in Orsay.

²Laboratoire Kastler Brossel (LKB) in Paris.

³Laboratoire des Matériaux Avancés (LMA) national research platform within the Institut de Physique des 2 Infinis (IP2I) in Lyon since the 1st of January 2019.

⁴Laboratoire d'Annecy the Physique des Particules (LAPP) in Annecy.

Chapter 1

Gravitational waves

In the seventeenth century, Newton imagined space as a rigid and absolute frame where time passes uniformly and where gravitation is an instantaneous force. In this context, the gravitational field generated by a mass propagates instantaneously.

In the nineteenth century, the theory of electromagnetism based on Maxwell's equations spotlighted the speed of light as the speed of electromagnetic waves. The experiment done by Michelson and Morley in 1887 [1] proved that the speed of light is constant in all directions and independent of the velocity of the source. These experiments were then explained by Einstein's special theory of relativity with result that no information can travel faster than the light in vacuum which speed is now recognized as a fundamental constant.

In this perspective, the instantaneous propagation of the gravitational field is an example of the limitation of Newton's theory. By the way, this was not the only one and for instance there was a deviation in the observed perihelion precession of Mercury with respect to the one predicted by Newton's laws.

The Einstein's general theory of relativity solved these problems considering space and time as combined in a unique dynamical framework where the effect of matter is to deform spacetime. John Archibald Wheeler summarized the basis of general relativity by [2]:

“Spacetime tells matter how to move; matter tells spacetime how to curve.”

Consequently, the gravitational field (or equivalently the curvature of space time) does not change instantaneously when a mass is in movement but the information of the motion of the mass propagates as a wave at the speed of light just like electromagnetic waves. In other words, gravitational waves are ripples in the curvature of spacetime caused by accelerating masses and propagating at the speed of light.

In this chapter I will briefly introduce how gravitational waves are described in general relativity and what the effect of their passage is. Then, I will give some orders of magnitude related to gravitational waves generation and present their main sources and the first detections. Finally I will explain part of the science obtained from the study of gravitational waves.

1.1 Gravitational waves in general relativity

In general relativity, the relationship between the curvature of spacetime and the mass-energy distribution is given by the Einstein equation [3–5]:

$$G^{\mu\nu} = \frac{8\pi G}{c^4} T^{\mu\nu}, \quad (1.1)$$

where $G^{\mu\nu}$ is the Einstein curvature tensor describing the curvature of spacetime, $T^{\mu\nu}$ is the stress-energy tensor describing mass-energy distribution, c is the speed of light and G is Newton's gravitational constant. As the coupling coefficient $8\pi G/c^4$ is very small, on the

order of 10^{-43} , spacetime is extremely rigid and difficult to deform, leading to small amplitude gravitational waves as we will see in Section 1.3.

In the special theory of relativity, one can describe the spacetime interval ds between two points that are infinitesimally close to each other by the expression:

$$ds^2 = \eta_{\mu\nu} dx^\mu dx^\nu, \quad (1.2)$$

where the Greek indices range from 0 to 3 and represent the t , x , y and z coordinates respectively and where there is an implicit summation over the repeated indices. $\eta_{\mu\nu}$ is the Minkowski metric corresponding to a flat spacetime, that we can write in Cartesian coordinates:

$$\eta_{\mu\nu} = \begin{pmatrix} -1 & 0 & 0 & 0 \\ 0 & 1 & 0 & 0 \\ 0 & 0 & 1 & 0 \\ 0 & 0 & 0 & 1 \end{pmatrix}. \quad (1.3)$$

In general relativity, spacetime is no longer necessarily flat and we can write a similar expression to Equation (1.2) encoding the information about the curvature of spacetime in a new metric $g_{\mu\nu}$:

$$ds^2 = g_{\mu\nu} dx^\mu dx^\nu. \quad (1.4)$$

When we are far from a gravitational wave source, we can consider that the metric is close to the flat spacetime with only small perturbations and we can use the weak field limit:

$$g_{\mu\nu} = \eta_{\mu\nu} + h_{\mu\nu}, \quad (1.5)$$

where $h_{\mu\nu}$ represents a small metric perturbation away from Minkowski spacetime so that $|h_{\mu\nu}| \ll 1$.

In the weak field approximation, considering that there is no stress-energy source term in the Einstein Equation (1.1), i.e. $T^{\mu\nu} = 0$, one can make a gauge choice to obtain an explicit statement of the metric perturbations $h_{\mu\nu}$. The Transverse-Traceless (TT) gauge is an especially good choice in which coordinates are defined by the world lines of free falling test masses. Under the above assumptions, the Einstein equation becomes a system of wave equations [6]:

$$\left(\nabla^2 - \frac{1}{c^2} \frac{\partial^2}{\partial t^2} \right) h_{\mu\nu} = 0. \quad (1.6)$$

This equation indicates that gravitational waves are plane waves propagating at the speed of light c . If we consider the case of a wave propagating along the z -axis, the statement that the wave field $h_{\mu\nu}^{TT}$ is transverse and traceless can be expressed by:

$$h_{\mu\nu}^{TT} = \begin{pmatrix} 0 & 0 & 0 & 0 \\ 0 & h_+ & h_\times & 0 \\ 0 & h_\times & -h_+ & 0 \\ 0 & 0 & 0 & 0 \end{pmatrix} e^{-i\omega(t-z/c)}, \quad (1.7)$$

where h_+ and h_\times represent the dimensionless scalar amplitude of the two polarizations of a gravitational wave propagating along the z -axis and ω is the angular frequency of the gravitational wave.

1.2 Effect of gravitational waves

We can interpret the two polarizations by saying that the h_+ polarization alternatively lengthens distances along the x -axis and simultaneously shrinks them along the y -axis and then, half a period later, shrinks distances along the x -axis and simultaneously lengthens them along

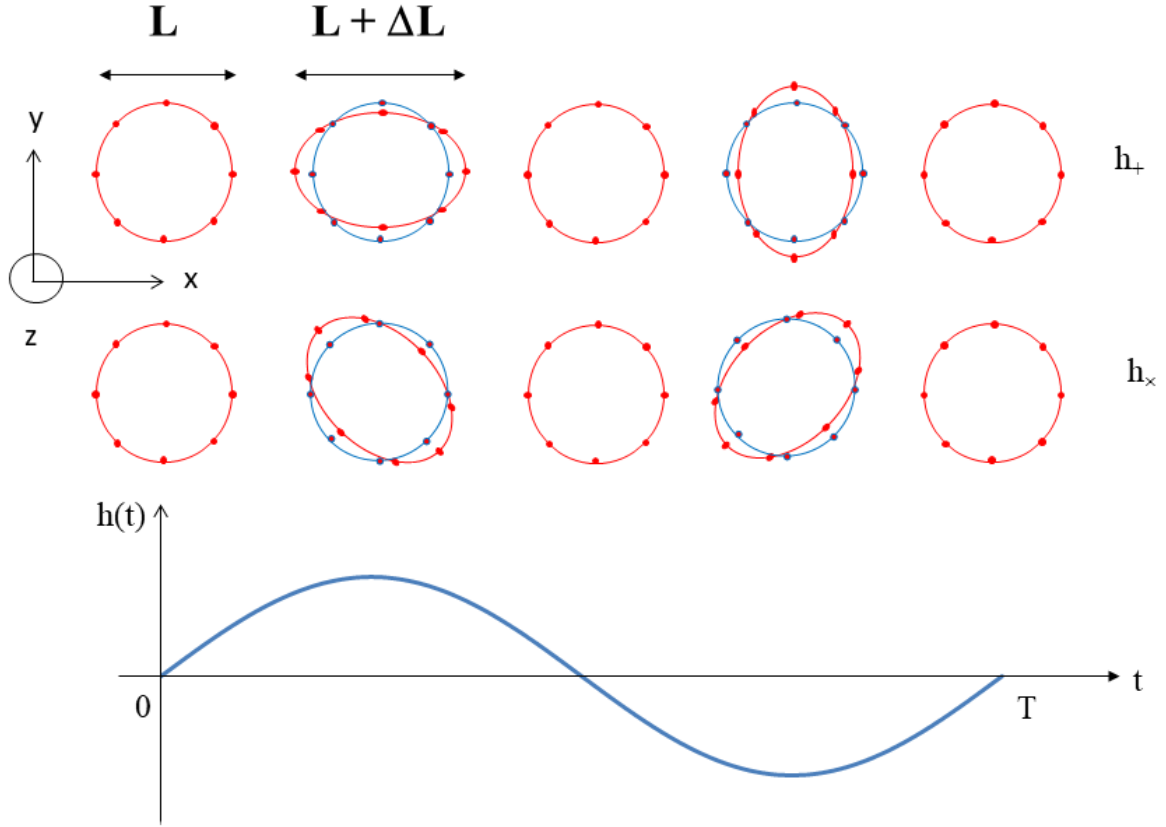


Figure 1.1 – Effect of the h_+ and h_\times polarizations of a gravitational wave propagating along the z -axis on a ring of free test masses according to the evolution with time of the amplitude of the gravitational wave h .

the y -axis. The effect is differential and depends on the amplitude of the gravitational wave. According to Equation (1.7), the h_\times polarization has the same effect but with its principal axes rotated by 45° as shown in Figure 1.1.

Now to determine the effect of the passage of a gravitational wave on matter, let's consider:

- two test masses on the x -axis
- a gravitational wave h_+ polarized and propagating along z
- the amplitude of the gravitational wave h is constant during light propagation between the two test masses

According to special relativity, light travels at a constant speed c in any inertial frame of reference. This is still true in general relativity. A ray of light connects two points in spacetime by an interval $ds^2 = 0$. Consequently, according to Equation (1.4), we can write:

$$ds^2 = 0 = -c^2 dt^2 + (1 + h_+) dx^2, \quad (1.8)$$

then leading to:

$$dt = \frac{1}{c} \sqrt{1 + h_+} dx, \quad (1.9)$$

and we can approximate it using $|h_+| \ll 1$ by:

$$dt \simeq \frac{1}{c} \left(1 + \frac{h_+}{2}\right) dx. \quad (1.10)$$

If we integrate over time, the light travel time t between the two test masses is:

$$t = \frac{L}{c} + \frac{h_+ L}{2c} = t_0 + \delta t = \frac{L + \delta L}{c}, \quad (1.11)$$

where L and $t_0 = L/c$ are the distance and the travel time between the two test masses in absence of gravitational wave. According to Equation (1.11), the passage of a gravitational wave of amplitude h_+ induces a variation δt of the travel time t of the light between the two test masses. This can be interpreted as a variation of length δL between the two test masses:

$$\frac{\delta L}{L} = \frac{h_+}{2}. \quad (1.12)$$

Note that it can equivalently be interpreted as a variation of the speed of light or of the vacuum optical index between the two test masses.

It can be understood from Figure 1.1 that the detected amplitude of a gravitational wave depends on the angle under which it is observed. Especially from a 45° angle of incidence with respect to the polarization axis, it is impossible to detect the gravitational wave.

Einstein predicted the existence of gravitational waves in 1916 but never convinced himself of their real existence. Until his death in 1955, he was never sure whether those waves were a coordinate effect only with no physical reality. The controversy lasted until the Chapel Hill Conference in 1957 where Felix Pirani showed that gravitational waves must have physical reality because one could invent an experiment that could detect them using a spring for instance [7]. This conference led Weber to propose a gravitational wave detector [8].

1.3 Gravitational waves generation

Now that we understand how gravitational waves affect spacetime, we may wonder how gravitational waves can be generated and what is the order of magnitude of their amplitude.

First we can make an analogy between gravitational waves and electromagnetic waves. Electromagnetic waves are generated by accelerating charges and especially by time-varying dipole moments at least and not by monopole because of charge conservation.

For gravity, there is no monopole term either, because of energy conservation, but there is no dipole term because of momentum conservation. This indicates that gravitational waves are generated at least by time varying quadrupole moments.

The gravitational wave amplitude h at a distance r from the source is proportional to the second time derivative of the Transverse-Traceless projection of the quadrupole moment I_{ij}^{TT} evaluated at the retarded time $(t - r/c)$ [5]:

$$h_{ij}^{TT} = \frac{2G}{c^4 r} \ddot{I}_{ij}^{TT} \left(t - \frac{r}{c} \right). \quad (1.13)$$

Equation (1.13) is the Einstein quadrupole formula, where the Latin indices range from 1 to 3 and represent the x , y and z coordinates respectively.

One can also define the gravitational luminosity L_{GW} of a source of quadrupole radiation integrating the gravitational wave flux over all solid angles as [5]:

$$L_{GW} = \frac{G}{5c^5} \left\langle \ddot{I}_{ij}^{TT} \ddot{I}_{TT}^{ij} \right\rangle, \quad (1.14)$$

where the angle brackets represent a time average over several periods of the wave.

Orders of magnitude

If we consider a system of mass m , typical length l and of mass distribution asymmetry factor ϵ , its moment of inertia I can be approximated by:

$$I \sim \epsilon m l^2. \quad (1.15)$$

Consequently we have:

$$\dot{I} \sim \varepsilon m v_{NS}^2, \quad (1.16)$$

$$\ddot{I} \sim \frac{\dot{I}}{T}, \quad (1.17)$$

where $T = l/v_{NS}$ and $v_{NS} = \omega l$ are the characteristic time and velocity of the non-spherically symmetric motion of the source, with ω the angular frequency of the source. Then, according to Equations (1.13) and (1.14), the gravitational wave amplitude emitted by this system, observed at a distance r from the source, is:

$$h \sim \varepsilon \frac{G m l^2 \omega^2}{c^4 r}, \quad (1.18)$$

and the luminosity of this sources is:

$$L_{GW} \sim \varepsilon^2 \frac{G m^2 v_{NS}^6}{c^5 l^2}. \quad (1.19)$$

It is easier to interpret this equation by enlightening the velocity of the source v_{NS} with respect to the speed of light c and introducing the Schwarzschild radius $R_S = 2Gm/c^2$, which is the radius that should have a black hole of the source's mass, given that black holes are the most compact objects in the Universe:

$$L_{GW} \sim \frac{c^5}{G} \varepsilon^2 \left(\frac{R_S}{l} \right)^2 \left(\frac{v_{NS}}{c} \right)^6. \quad (1.20)$$

Equation (1.20) provides information about the main characteristics of a powerful gravitational wave source:

- asymmetric, with a mass distribution asymmetry factor ε close to 1,
- compact, with a characteristic length l on the order of the Schwarzschild radius R_S ,
- relativistic, with a velocity v_{NS} close to the speed of light c .

Example 1: the spinning bar

It seems that generating gravitational waves on Earth would be very inefficient, but let's check that with some simple calculation. The easiest way to generate a gravitational quadrupole moment is to use a spinning bar.

Let's assume we can construct an ideal $m = 2000$ kg and $l = 2$ m long bar and spin it at an angular frequency of $\omega = 2\pi \times 1$ kHz. We can consider this bar as strongly asymmetric, i.e. $\varepsilon \sim 1$.

According to Equation (1.20) this spinning bar has a gravitational wave luminosity of:

$$L_{GW} \sim 10^{-22} \text{ W}, \quad (1.21)$$

and according to Equation (1.18) the amplitude of the gravitational waves generated will be:

$$h \sim 10^{-33} \times \left(\frac{1 \text{ m}}{r} \right), \quad (1.22)$$

where r is the distance of the observer from the source. This is really a weak signal, too weak to be detected as we will see in Chapter 2.

Example 2: binary black hole

Now, let's examine what seems to be one of the most promising source of gravitational waves: compact binary systems. Consider a realistic system composed of 2 black holes of masses $m = 30 M_{\odot}$, where M_{\odot} is the mass of the Sun, separated by a distance l of 5 Schwarzschild radii R_S , spinning around each other at a speed v_{NS} of 0.3 times the speed of light c and at a distance $r = 400$ Mpc from the Earth. This system is also considered as strongly asymmetric, ie $\varepsilon \sim 1$.

According to Equation (1.20) this system has a gravitational wave luminosity of:

$$L_{GW} \sim 10^{48} \text{ W.} \quad (1.23)$$

This is really huge compared to that of the spinning bar of Equation (1.21). Moreover, according to Equation (1.18) the amplitude of the gravitational waves detected on Earth will be:

$$h \sim 10^{-21}, \quad (1.24)$$

which, as we will see, is detectable with the current ground based gravitational wave detectors.

These 2 examples illustrate the fact that we cannot generate measurable gravitational waves on Earth. Consequently we rely on astronomical sources which comes with other drawbacks. The main one is that we do not control the sources. The second one is the rate of observable astronomical events which can be small and difficult to evaluate.

1.4 Astronomical sources

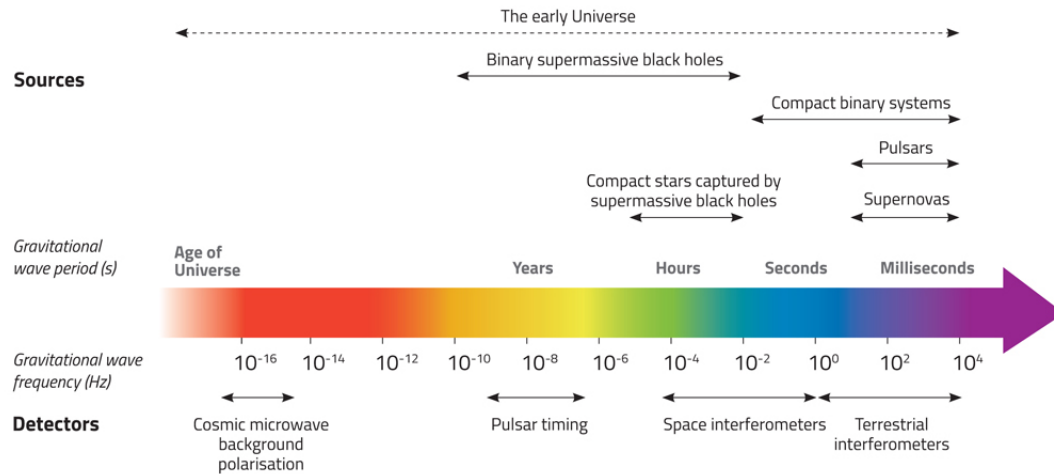


Figure 1.2 – The gravitational wave spectrum [9]. It represents the gravitational waves sources according to their frequency of emission in parallel with the frequency range of sensitivity of different types of detectors.

There are many astronomical sources of gravitational waves, but not all of them are detectable with ground based interferometric gravitational wave detectors described in Chapter 2. In fact, we can, at a first stage, classify the gravitational wave sources by the frequency band in which they produce gravitational waves as can be seen in Figure 1.2.

I will only present the main astronomical gravitational waves sources we can detect using terrestrial interferometers, radiating in the high frequency band: from 1 Hz to 10 kHz.

We can divide such sources into two main classes. Transient sources are short duration signals. The duration of the signal (at least in the frequency bandwidth of interest) is way shorter than the observational time. On the contrary, continuous signals have a duration much larger than the observational time.

1.4.1 Transient sources

Let's start with the transient sources. Two good examples of transient sources are compact binary coalescences and core collapse supernovae.

Compact binary coalescence

When two massive objects orbit around each other, they form a binary system which emits gravitational waves leading to momentum and energy loss. The binary system progressively tightens until the two objects merge. The frequency of the emitted gravitational waves is twice the orbital frequency and the amplitude of the signal depends on the mass of the two objects according to Equation (1.18). At first order, with terrestrial interferometers, we can only detect the end of the inspiral phase and the coalescence of binaries composed of two black holes (BBH) up to $400 M_{\odot}$, two neutron stars (BNS) or a neutron star and a black hole (NSBH).

In fact the first indirect proof of the existence of gravitational waves came from the observation of the Hulse-Taylor binary system composed of two neutron stars orbiting around each other, one of them being a pulsar emitting a periodic radio pulse. The orbital decay of this system is observed since 1974 using the pulsar periodicity and corresponds exactly to the Einstein prediction of the energy loss from gravitational wave emission [10].

Binary inspirals have a well-known theoretical waveform called a chirp: the frequency and the amplitude increase with time with a characteristic evolution depending on the "chirp mass", a combination of the mass m_1 and m_2 of the two objects of the system:

$$\mathcal{M} = \frac{(m_1 m_2)^{3/5}}{(m_1 + m_2)^{1/5}}. \quad (1.25)$$

Moreover, we consider these sources as transient sources because they enter the bandwidth of ground based interferometric detectors (from few Hz to few kHz) close to their merger, leading, for current gravitational wave detectors, to the detection of the last milliseconds to 30 minutes of the coalescence.

Detections

The first direct detection of gravitational waves, GW150914, was observed on the 14th of September 2015 by the Advanced LIGO Hanford and Livingston gravitational wave detectors during their first observing run (O1).

The gravitational wave was emitted by the coalescence of two black holes of initial masses about $36 M_{\odot}$ and $29 M_{\odot}$ which formed a black hole of about $62 M_{\odot}$. An energy of about $3.0 M_{\odot} c^2$ was radiated in gravitational waves. This coalescence took place at a luminosity distance of about 410 Mpc from the Earth [11].

One can see in Figure 1.3 that the reconstructed gravitational wave signal is well-modeled by general relativity prediction and that the strain peak (corresponding to the maximum amplitude of the gravitational wave), is on the order of 10^{-21} , which is the order of magnitude calculated using Equation (1.24). This is extremely weak and this is the reason why it is so important to increase the detector's sensitivity.

The source localization in the sky for this detection is shown on the left of Figure 1.4. The localization is determined using the time delay between two detectors and the amplitude of the signal. With only two detectors, the detection region is roughly an annulus in the sky with a width given by time detection uncertainty. Using three detectors we can reduce this

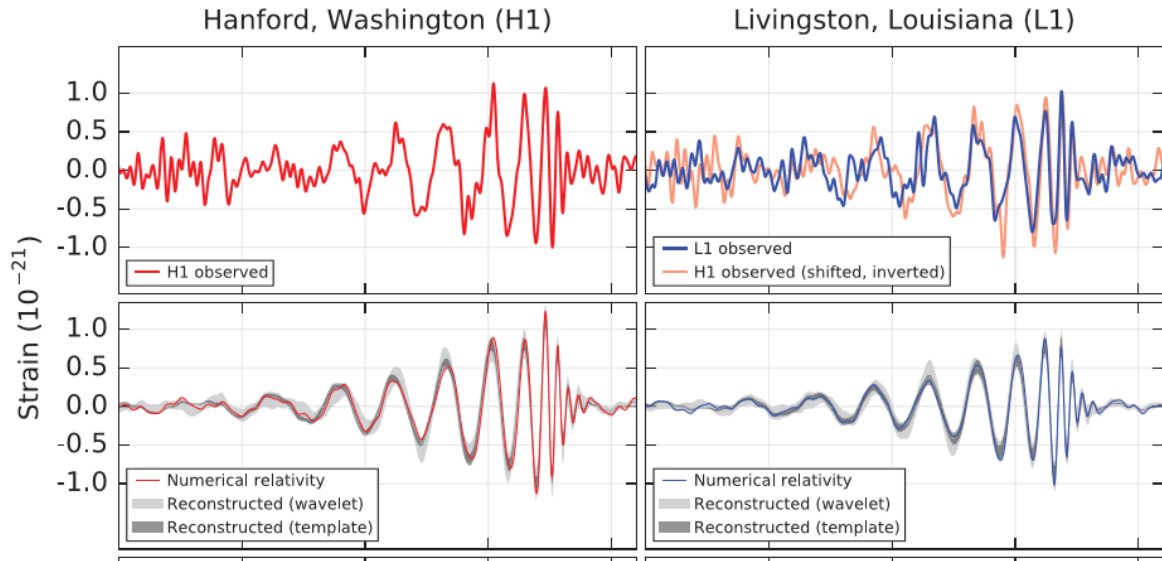


Figure 1.3 – *Upper row*: Band limited filtered Advanced LIGO data (Hanford on the left and Livingston superposed with Hanford on the right) on the 14th of September 2015. *Lower row*: Reconstructed signal waveforms compared to the general relativity prediction as given by numerical relativity simulations [11].

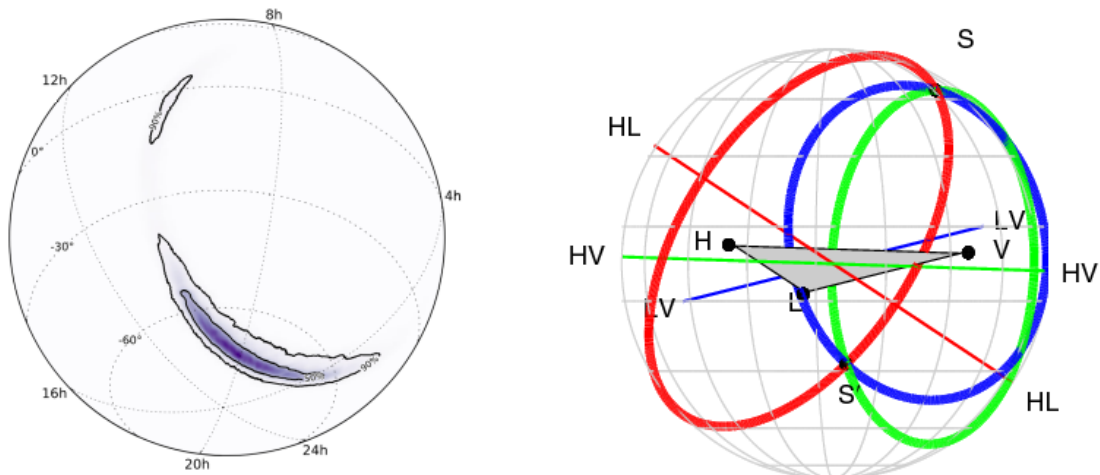


Figure 1.4 – *Left*: Skymap location of GW150914 given in terms of right ascension α measured in hours and the declination δ measured in degrees. The dark blue corresponds to the 50% credible region and the light blue corresponds to the 90% credible region [12]. *Right*: Triangulation principle using three detectors : H LIGO Hanford, L LIGO Livingston and V Virgo.

region to two points as shown on the right of Figure 1.4 and in practice to only one because of the beam pattern of the detectors which are antenna sensitive to almost the whole sky but not all [13].

There were only two detectors for the first detected event and its localization corresponds to a two-dimensional credible region with 50% probability of 150 deg^2 and a two-dimensional credible region with 90% probability of 610 deg^2 , representing about $2800 S_{\odot}$ [12], where S_{\odot} is the apparent surface of the full moon, or 1.5 % of the full sky sphere. This is a really huge zone to look for hypothetical electromagnetic counterpart.

Three other events were observed then before the second event I want to discuss, GW170814

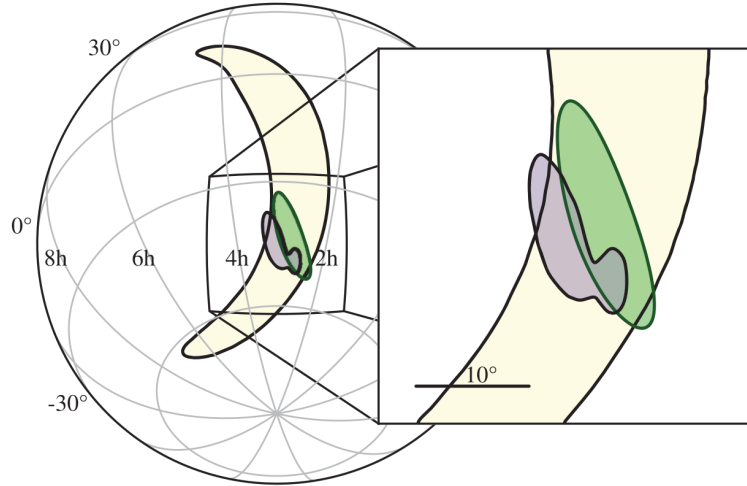


Figure 1.5 – Skymap location of GW170814 90% credible regions given in terms of right ascension α measured in hours and the declination δ measured in degrees. The yellow zone corresponds to the rapid localization using data from the two Advanced LIGO detectors, the green one is the same but with the inclusion of data from Advanced Virgo. The purple region is the refined localization using the 3 detectors [14].

that was obtained in coincidence with 3 detectors: the two Advanced LIGO detectors and the Advanced Virgo detector. The gravitational waves were emitted by the coalescence of two black holes of initial masses about $31 M_{\odot}$ and $25 M_{\odot}$. This coalescence took place at a luminosity distance of about 540 Mpc from the Earth [14].

In fact, without the third detector, the sky localization of the source of GW170814 with only the two Advanced LIGO detectors would have had a two-dimensional credible region with 90% probability of 1160 deg^2 , representing about $5300 S_{\odot}$.

Using Advanced Virgo data shrinks this credible region to a surface of 100 deg^2 with a first rapid localization and only 60 deg^2 for the refined localization, representing about $275 S_{\odot}$ as shown in Figure 1.5 [14]. This surface is manageable to cover using large field of view telescopes on Earth.

The last event I want to describe is the GW170817 detected on the 17th of August 2017. The signal was detected in the two Advanced LIGO detectors. According to its amplitude and to Advanced Virgo sensitivity, it should have been detected in the Advanced Virgo detector if it had not been in a blind zone of the Virgo antenna pattern. Consequently, the fact that it was not seen gave information on the position in the sky of the source.

What is exceptional with this event is that the gravitational waves were emitted by the coalescence of two neutron stars with a total system mass of about $2.74 M_{\odot}$. This coalescence took place at a luminosity distance of about 40 Mpc from the Earth [15].

Moreover, this event was coincident with a short Gamma Ray Burst detected 1.7 s after by the Fermi and INTEGRAL telescopes, GRB170817A. The combined 90% credible region localization from the two Advanced LIGO detectors and the Advanced Virgo one was of 28 deg^2 representing only $130 S_{\odot}$ and in complete agreement with the localization obtained from GBM-Fermi and INTEGRAL as shown in Figure 1.6.

There were about few dozens of galaxies in the 90% credible volume [18] which allows a rapid optical localization of the apparent host galaxy, NGC4993, an elliptical galaxy in the constellation Hydra, about 11 hours after the coalescence, by the Swope telescope with the detection of a kilonova and independently confirmed by 5 other telescopes [17].

There were 3 observing runs during which many detections were made leading to the publication of a gravitational wave transient catalog for the runs O1 and O2 [19] and two other catalogs in preparation for the two parts O3a and O3b of the O3 run. A summary of the observing runs is given in Table 1.1.

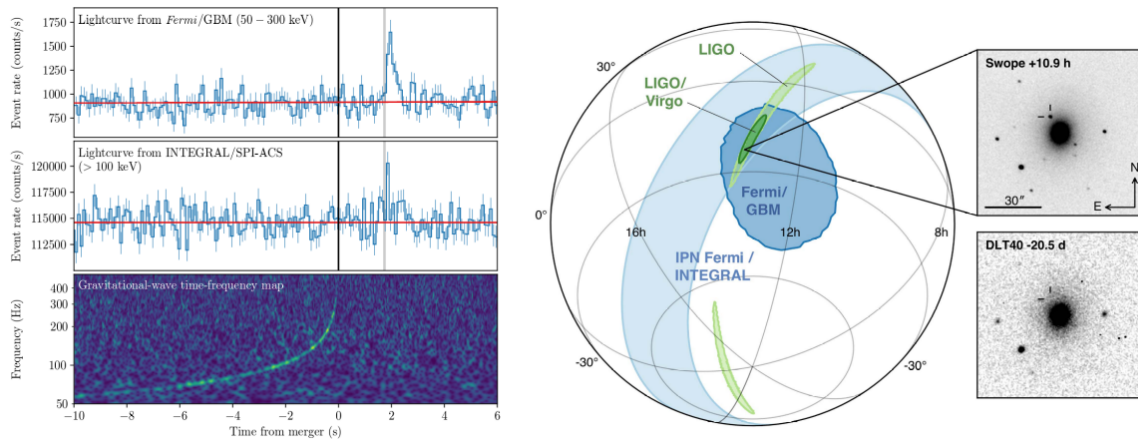


Figure 1.6 – *Left column*: Top: Summed lightcurve from the GBM instrument of the Fermi telescope between 50 and 300 keV around the GRB 170817 A event. Middle: Summed lightcurve from the INTEGRAL telescope above 100 keV around the GRB 170817 A event. Bottom: The time-frequency map of GW170817 obtained by coherently combining data from the two Advanced LIGO detectors [16]. *Right column*: Skymap location of GW170817 90% credible regions given in terms of right ascension α measured in hours and the declination δ measured in degrees. The light green zone corresponds to rapid localization using data from the two Advanced LIGO detectors, the dark green one is the same but with the inclusion of informations from Advanced Virgo. The light blue region corresponds to the localization using a triangulation from the time delay between Fermi and INTEGRAL and the dark blue is the localization from the GBM instrument of the Fermi telescope. The inset shows the location of the apparent host galaxy NGC4993 in the Swope optical discovery image at 10.9 hr after the merger (top right) and the DLT40 pre-discovery image from 20.5 days prior to merger (bottom right). The reticle marks the position of the transient in both images [17].

Run	Date	Active detectors	Results
O1	2015/09/12 to 2016/01/19	H,L	3 BBH detections
O2	2016/11/30 to 2017/07/31 2017/08/01 to 2017/08/25	H,L H,L,V	3 BBH detections 4 BBH and 1 BNS detections
O3a	2019/04/01 to 2019/09/30	H,L,V	21 BBH candidates 4 BNS candidates 4 NSBH candidates 4 other candidates
O3b	2019/11/01 to 2020/03/27	H,L,V	16 BBH candidates 2 BNS candidates 1 NSBH candidate 4 other candidates

Table 1.1 – Summary of the three observing runs made by the Advanced LIGO Hanford (H), Advanced LIGO Livingston (L) and Advanced Virgo (V) detectors [19, 20].

Rates

Using the 11 detections of the 2 first observing runs, one can better evaluate the rate of BBH and BNS merger in the Universe with respect to the first estimations [21].

The rate density of BBH and BNS mergers are respectively estimated to be 9.7-101 $\text{Gpc}^{-3}\text{yr}^{-1}$ and 110-3840 $\text{Gpc}^{-3}\text{yr}^{-1}$ [19]. Moreover, the maximum detection range at design of the Advanced detectors (LIGO, Virgo and KAGRA) for BBH merger is about 1500 Mpc and the one for BNS merger is about 200 Mpc [22]. Consequently we can expect 100-1000 BBH mergers and 2-100 BNS mergers per year at design sensitivities.

The last possible compact binary coalescence detectable by ground based interferometric detectors is formed from one neutron star and one black hole (NSBH). It has not been detected during the first two observing runs and the rate density of NSBH merger is estimated to be below 610 $\text{Gpc}^{-3}\text{yr}^{-1}$ [19].

5 NSBH candidates were observed during the third observing run. The first one, GW190814 was further analyzed and the conclusion suggested that it unlikely came from an NSBH event but more a BBH event. Nevertheless the uncertainty on the masses were too high and close to the neutron star/black hole border to draw a definitive conclusion [23]. The 4 other candidates of the third observing run still have to be further analyzed.

Core collapse supernovae

Supernovae are known and observed by astronomers from a very long time, but at a low rate. The first observation of a supernovae took place in 1006, 48 years before the one in the Crab constellation leading to the Crab Nebula and pulsar. Two other well-known historical supernovae are the ones of Tycho Brahe and Johannes Kepler in 1572 and 1604. All these supernovae happened in the Milky Way and Kepler's one was the most recent one to be seen in our galaxy.

Some other supernovae have been observed in the neighborhood of our galaxy. The most recent was observed in 1987 in the Large Magellanic Cloud with optical telescopes and neutrino detectors [24].

Astronomers divide supernovae into many categories. The type Ia Supernovae are produced by white dwarfs in binary systems accreting mass from their companion leading to a collapse when the mass of the white dwarf goes beyond its stability limit. As this is not a compact system, we do not expect substantial gravitational waves emission from this type of supernovae.

The types Ib, Ic and II supernovae are produced from the core collapse of massive stars ($M \gtrsim 8 M_{\odot}$) when nuclear burning fails to support them leading to a neutron star or black hole remnant. In this case we expect asymmetries in the core collapse leading to gravitational waves emission.

For long, core collapse supernovae have been considered as a primary source of gravitational wave bursts [25]. The modelling of stellar core collapse is extremely challenging because of the complexity of the physical processes to take into account: general relativistic hydrodynamics, magnetic fields, rotation, neutrino transport and nuclear physics [26].

Consequently, the gravitational wave waveform produced by the stellar core collapse is only known through numerical simulations. Many waveforms have been simulated [27] leading to a few common features:

- the efficiency of the gravitational wave emission depends on the angular momentum of the progenitor star,
- the frequency stands in the range between 100 Hz to few kHz,
- the duration of the event is short, but up to few seconds.

Moreover the typical gravitational wave amplitude at 10 kpc is expected to be in the 10^{-23} to few 10^{-22} range [26] constraining our detection capabilities to the Milky Way and Small and Large Magellanic Clouds where we only expect a few events per century [28].

Consequently core collapse supernovae will be hard to detect because of their low rate and unknown waveform but this would be a great discovery for multimessenger astronomy and to understand the supernovae explosion mechanism.

1.4.2 Continuous signals

Continuous signal are of two types. The first one corresponds to sources emitting gravitational waves continuously with a nearly constant frequency over a period of time that is long compared to the observational time. The best example of such sources are rapidly rotating neutron stars. The second type of continuous signals is stochastic background.

Neutron stars

Rotating neutron stars are the principal sources of continuous gravitational waves in the ground based detectors frequency band. They emit gravitational waves if they are non-axisymmetric or if the axis of symmetry of the star is not the same as the rotational axis [29], at a frequency f equal to twice the rotational frequency. Considering a typical pulsar, a particular type of neutron stars emitting a periodic radio pulse the wave amplitude can be approximated by [30]:

$$h \sim 3 \times 10^{-31} \left(\frac{f}{1 \text{ kHz}} \right)^2 \left(\frac{10 \text{ kpc}}{r} \right). \quad (1.26)$$

In the case of observed pulsars the rotational frequency can be precisely measured. Consequently we can reconstruct the gravitational wave signal emitted by the known pulsars, corresponding to a gravitational wave amplitude of the order of 10^{-26} [31].

This gravitational waves emission contributes to slow down the rotation of the neutron star in addition to the electromagnetic energy loss. Using the LIGO and Virgo data it is possible to put a constrain on the amount of gravitational waves emission contributing to the spin-down of some pulsars. In particular, for the Crab and Vela pulsars, gravitational waves emission contributes to respectively less than 1% and 10% of their respective spin-down [32].

Stochastic background

Part of the stochastic gravitational background can be defined as a superposition of random sources arising from an extremely large number of unresolved, independent and uncorrelated events that happened shortly after the Big Bang or more recently in the past several billion years [33]. Consequently it appears as noise in a single gravitational wave detector and we have to combine data from several detectors with uncorrelated noises to distinguish the signal from the noise.

The sources of stochastic background are of different types from cosmological sources such as cosmic strings [34] to the superposition of compact binary mergers [35] too weak to be resolved. Other sources of stochastic background can be found in theories predicting some phase transitions in the early Universe. Using the first Advanced LIGO observing run [36] and the BNS merger detection GW170817 [37], upper limits have been put on the stochastic gravitational background since it has not been detected yet.

1.5 Motivations

The detection of gravitational waves is not only important because it confirms the prediction of their existence. It is a complete new way to study our Universe using a new messenger in addition to the photon.

1.5.1 Astrophysics

The first detection of gravitational waves, GW150914, had many astrophysical implications [38]. In fact it was the first evidence of BBH systems and moreover the masses of the progenitors ($> 25 M_{\odot}$) were surprising because such massive stellar black hole had never been observed in the known X-ray binaries which were until then the only evidence of the existence of stellar black holes.

We can explain these high masses if the progenitors were formed in a low metallicity environment, e.g. half the metallicity of the Sun, so that the massive stars which gave birth to the black holes did not suffer high winds. Consequently this give information on the medium where the progenitor stars formed.

Moreover, using the detections of gravitational waves from BBH and in particular the spin information, we can constrain the astrophysical formation models of such BBH systems [39].

Otherwise, the detection of a BNS merger, GW170817, allows us to constrain the models of neutron star equation of state [16]. Furthermore, the simultaneous detection of a short GRB leads to the conclusion that BNS can be the progenitors of such short GRB.

Finally, we observed a kilonova, due to radioactive decay of rapid neutron capture process (r-process), in coincidence with a BNS merger observed through gravitational waves, giving the evidence that nucleosynthesis of heavy elements like gold takes place in such BNS mergers [17].

1.5.2 Tests of general relativity

In addition to astrophysical implications, the detection of gravitational waves allows to test the general theory of relativity in the strong field regime. It was for instance shown that the predicted compact binary coalescence waveform was in complete agreement with the detected ones. Moreover, waveform models with parameters beyond general relativity were used to put bounds on several high order post-Newtonian coefficients [40].

Only with the first detection, GW150914, the Compton wavelength of the graviton was constrained to a 90% confidence level to be higher than 10^{13} km corresponding to a hypothetic mass of the graviton $m_g \leq 1.2 \times 10^{-22}$ eV/ c^2 . Then using the coincidence detection between the BNS merger GW170817 and the GRB, we can constrain the difference between the speed of gravity and the speed of light to be between -3×10^{-15} and 7×10^{-16} [16], which is consistent with 0 invalidating many models beyond general relativity.

Moreover, using GW170817 and its electromagnetic counterpart, bounds have been put on the violation of Lorentz invariance and a new test of the equivalence principle has been performed [16].

Finally, the three detectors observation of the BBH merger GW170814 allowed the first test of the gravitational waves polarizations from the antenna response of the LIGO-Virgo network [14] testing polarizations predicted by theory beyond general relativity.

So far, there was no evidence of deviations from the Einstein theory of relativity, but gravitational waves are the best probes to test this theory and put constrains on other gravitational theories.

1.5.3 Cosmology

Gravitational waves detections have also an impact on cosmology. In fact the study of the stochastic background of cosmological origin is the best way to probe the early Universe, before recombination and the Cosmological Microwave Background. For instance, we may see amplification of vacuum fluctuations, phase transitions in the early Universe or cosmic strings [41].

Furthermore, the detection of BNS in coincidence with an electromagnetic counterpart is a new independent way to measure the Hubble constant H_0 as the luminosity distance d_L of the gravitational wave source is well reconstructed and depends mostly on the inclination

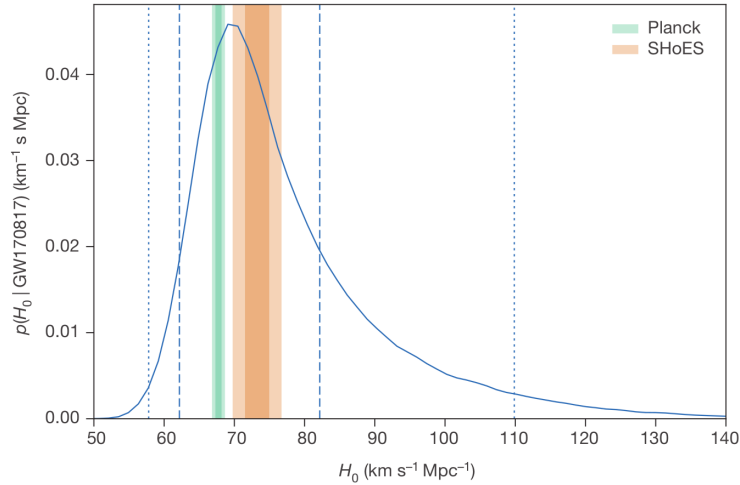


Figure 1.7 – GW170817 measurement of the Hubble constant H_0 compared with two other measurements: the CMB measurement from Planck in green and the type Ia supernova measurements from SHoES in orange [42]

angle of the source [42] which could be better reconstructed with more detectors. As we can see in Figure 1.7, there are tensions in the cosmological community about the value of H_0 and the value determined using GW170817 stands just in the middle of two other measurements, but with far more larger uncertainty with only one event.

It is also possible to constrain the Hubble constant even without electromagnetic observation to an accuracy of few percents using an analysis based on wide-field galaxy surveys for the location, and consequently redshift, of the source. It would need few tens of observations from a network of advanced gravitational wave detectors [43].

Chapter 2

Gravitational wave detectors

Gravitational wave detectors based on an optical interferometer have first been proposed soon after the Chapel Hill Conference in 1957 where Pirani convinced the community that gravitational waves have a physical reality [7]. In fact the first proposals were published at the beginning of the 1960's [44] in parallel with Weber first proposal of a bar detector [8].

In this chapter I will give a short introduction about gravitational wave detectors. Then I will focus on the operation of a ground based interferometric detector and its main noise sources. Finally I will present the impact of several sensitivity improvements on the possibilities of detection.

2.1 Overview of gravitational wave detectors

2.1.1 Weber bars

The first gravitational wave detectors were constructed in the 1960's by Joseph Weber as shown in Figure 2.1. They were large cylindrical test masses in which gravitational waves could induce quadrupole vibrations exciting the longitudinal vibrational mode of the bar. This receiver can be modeled as a pair of point masses linked by a mechanical spring. The stiffer the spring the better the coupling to gravitational waves is. In such a mechanically coupled detector, the effect of a wave is to create an acoustic signal which is then transduced and amplified in order to convert it into an electromagnetic signal which can be analyzed [8].

By construction, Weber bars are able to detect gravitational wave at frequencies on the order of the kHz, corresponding to the resonance frequency of the bar, with a tiny bandwidth, on the order of 100 Hz. The main sources which can be seen at these frequencies are core collapse supernovae.

In 1969, Weber claimed an evidence for discovery of gravitational radiation using this kind of detector [45]. Nevertheless, the energy detected seemed too high to be true. Moreover, many research groups built their own bar detectors but found no evidence of gravitational radiation.

A new generation of resonant mass detectors has been developed, cooled to reduce thermal noise and to enable the use of low noise superconducting transducers. From 1997 to 2000 a network of five cryogenically cooled resonant bar detectors, the International Gravitational Event Collaboration (IGEC), searched for transient events but their observations were consistent with no detection, setting upper limit on the rate of gravitational wave transients [46].

In 2006, new instruments were designed using a spherical antenna. This provides an isotropic sky coverage and the determination of the source position and wave polarization. Nevertheless there sensitivity would be at a first stage on the order of the sensitivity of initial LIGO and Virgo but only in the bandwidth $900 \text{ Hz} < f < 1100 \text{ Hz}$ [47].



Figure 2.1 – Joseph Weber with an aluminum bar instrumented with piezoelectric crystals to read out the vibrations.

2.1.2 Pulsar timing

Pulsars have been discovered in 1967 in the data of a radio telescope as a regular strain of pulse radiation. Many factors determine the intensity, shape and arrival times of the pulses. Among them are the pulsar’s magnetosphere, the pulse propagation through the interstellar medium and the radio telescope.

During its travel from the pulsar to the observatory, light can be delayed by gravitational waves. As a result, information related to gravitational waves passing between the Earth and the pulsar are encoded into the pulse arrival times.

The pulsar timing method is based on the comparison of the observed pulses times-of-arrival of several pulsars with a prediction from a model of the pulsars and the propagation of the pulses through the interstellar medium. Gravitational wave signals are not included in a pulsar timing model and, hence, any such wave will induce deviations between the predicted and observed times-of-arrival. The expected signal induced by gravitational waves is small with typical deviations < 100 ns.

The International Pulsar Timing Array project (IPTA) [48] combines observations of millisecond pulsars from several observatories aiming to detect gravitational waves in the ultra-low frequency, i.e. of the order of few nHz. The possible sources at these frequencies are binary supermassive black holes. No detection have been reported yet, but the arrival of many new telescopes in the coming years will increase the number of known pulsars and the precision of pulsar timing. The integration of few years of data will be necessary to get detection with a significant signal to noise ratio.

2.1.3 Space interferometers

Binary supermassive black holes emit gravitational waves up to mHz frequencies. It is possible to detect them using an interferometer with million of kilometers arms which requires to go in space. The Laser Interferometer Space Antenna (LISA) mission is planned jointly by NASA and ESA to be launched in 2030's [49].

The LISA data analysis will have to manage with a background of lighter binary inspirals in our galaxy. Moreover, LISA could detect BBH, BNS and NSBH in their inspiral phase several years before their merger in the LIGO/Virgo frequency bandwidth [50]. This would enable coordinated observations between ground based detectors and electromagnetic telescopes.

As illustrated in Figure 2.2, LISA will consist of an equilateral triangle constellation of three spacecrafts in heliocentric orbits at 1 astronomical unit from the Sun and 20° behind the Earth. The distance between two spacecrafts will be 2.5×10^9 m and each spacecraft will contain two test masses. Laser interferometry is used to monitor the distance changes between the test masses and the optical bench inside each spacecraft. [51].

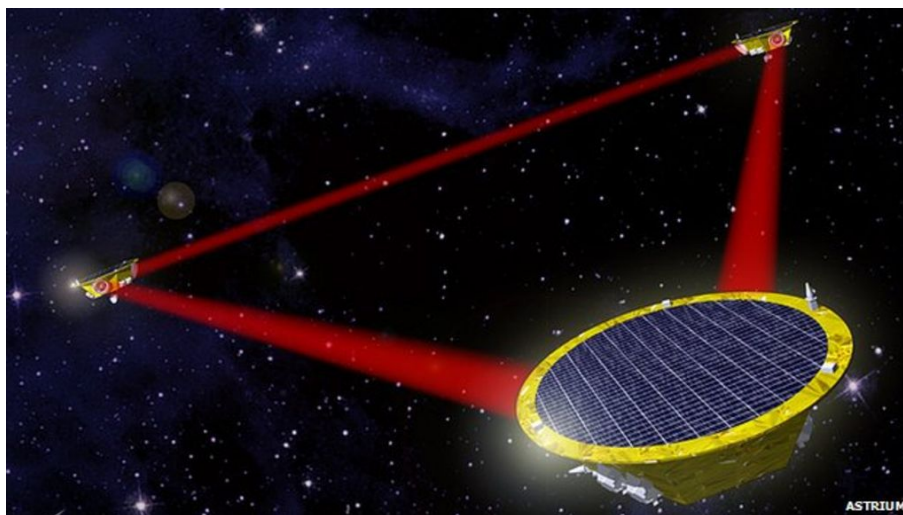


Figure 2.2 – Artist's impression of the LISA mission composed of three spacecraft.

The LISA Pathfinder spacecraft successfully tested several technologies which will be used on LISA. It demonstrates that two test masses can be put in free fall with a relative accelerating noise performance close to the one requested for LISA [52].

2.1.4 Atom interferometers

A new technique has been proposed in the past decade to detect gravitational waves in the bandwidth between space interferometers and ground based interferometers, i.e. from 0.3 Hz to 3 Hz. This technique is based on a correlated array of atom interferometers [53].

Atom interferometers replace mirrors by ballistic atoms as inertial test masses [54]. Laser light finely tuned is used as beamsplitter and mirror for atoms and interferences between two paths of the quantum probability function of the atom are used to probe the gravitational field.

For some conservative models, strain sensitivities below $1 \times 10^{-19}/\sqrt{\text{Hz}}$ could be reached between 0.3 and 3 Hz with a peak sensitivity of $3 \times 10^{-23}/\sqrt{\text{Hz}}$ at 2 Hz.

A summary picture of the different types of detectors is presented in Figure 2.3 with their frequency range and real or foreseen sensitivities. We can see that they are complementary from each others. The sensitivity of a detector will be defined in Section 2.3 and ground based interferometric detectors will be described in the next sections.

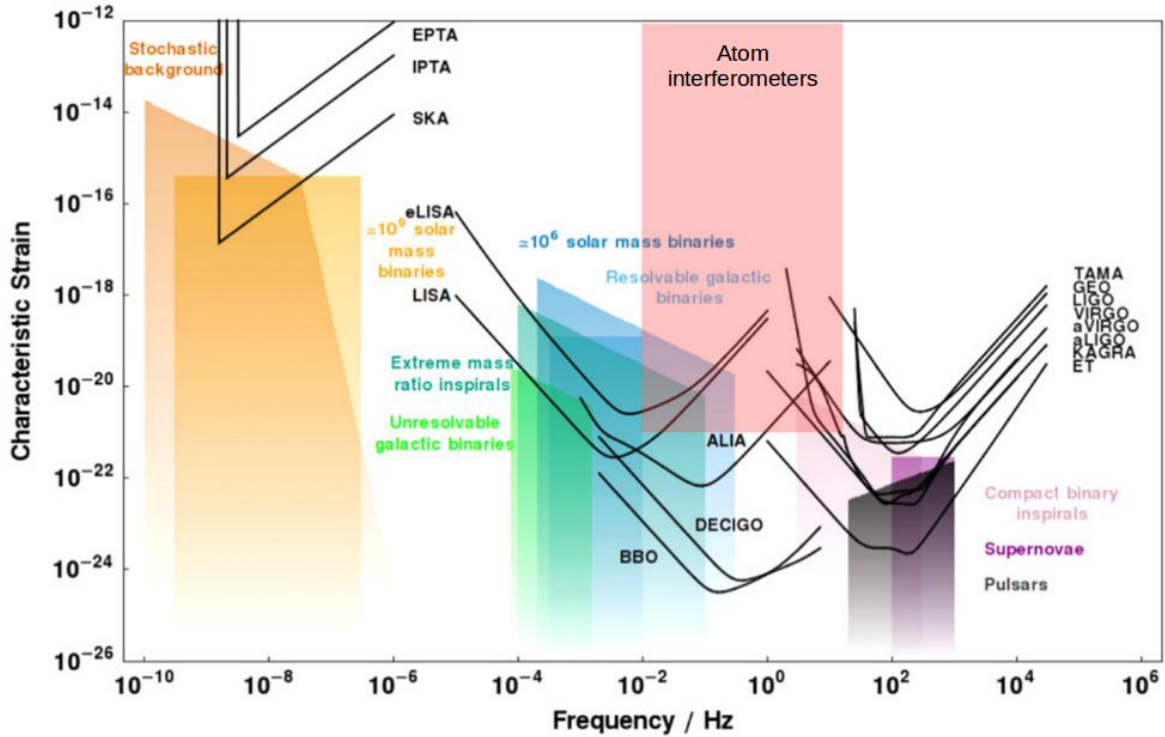


Figure 2.3 – Sensitivity curves of different types of gravitational wave detector projects and some sources according to the frequency. Pulsar timing: EPTA, IPTA, SKA; space-based interferometers: eLISA, LISA, ALIA, DECIGO, BBO; ground based interferometers: TAMA, GEO, LIGO, Virgo, aLIGO, aVirgo, KAGRA, ET [55].

2.2 Ground based interferometric detectors

2.2.1 History

First studies were undertaken in the 1970's on kilometer-scale interferometers and estimation of their noise sources. In the mid-1980's the first discussion about LIGO and Virgo detectors started, leading to proposal submissions by the end of this decade and approval in the beginning of 1990's [56, 57]. They are respectively at the origin a US collaboration and a France-Italy collaboration. Other European countries then joined the Virgo collaboration.

In the mid-1990's, the construction of the three sites (LIGO in Hanford, LIGO in Livingston and Virgo in Cascina near Pisa) started, ending at the end of 1990's/beginning of 2000's. Data were taken independently by the two collaborations in the 2000's and the first joint observations with enhanced initial LIGO and Virgo detectors happened in 2007 before installation and commissioning of advanced LIGO and advanced Virgo detectors leading to the detections described in Chapter 1.

These detectors are sensitive in the audio frequency, from few Hz to few kHz. The description of this kind of detectors will be the object of the rest of this chapter.

2.2.2 Simple Michelson interferometer

A simple Michelson interferometer is composed of a light source, often a laser, a beam splitter and two mirrors as shown in Figure 2.4. At the beam splitter, light is separated in two beams: one beam is reflected towards the mirror M_Y , the other beam is transmitted towards the mirror M_X . They constitute the two arms of the interferometer. Each light beam is then reflected on a mirror back to the beam splitter where they are recombined: one beam towards the laser source and the other beam towards a detection photodiode.

The amplitude of the light sent to the detection photodiode depends on the phase differ-

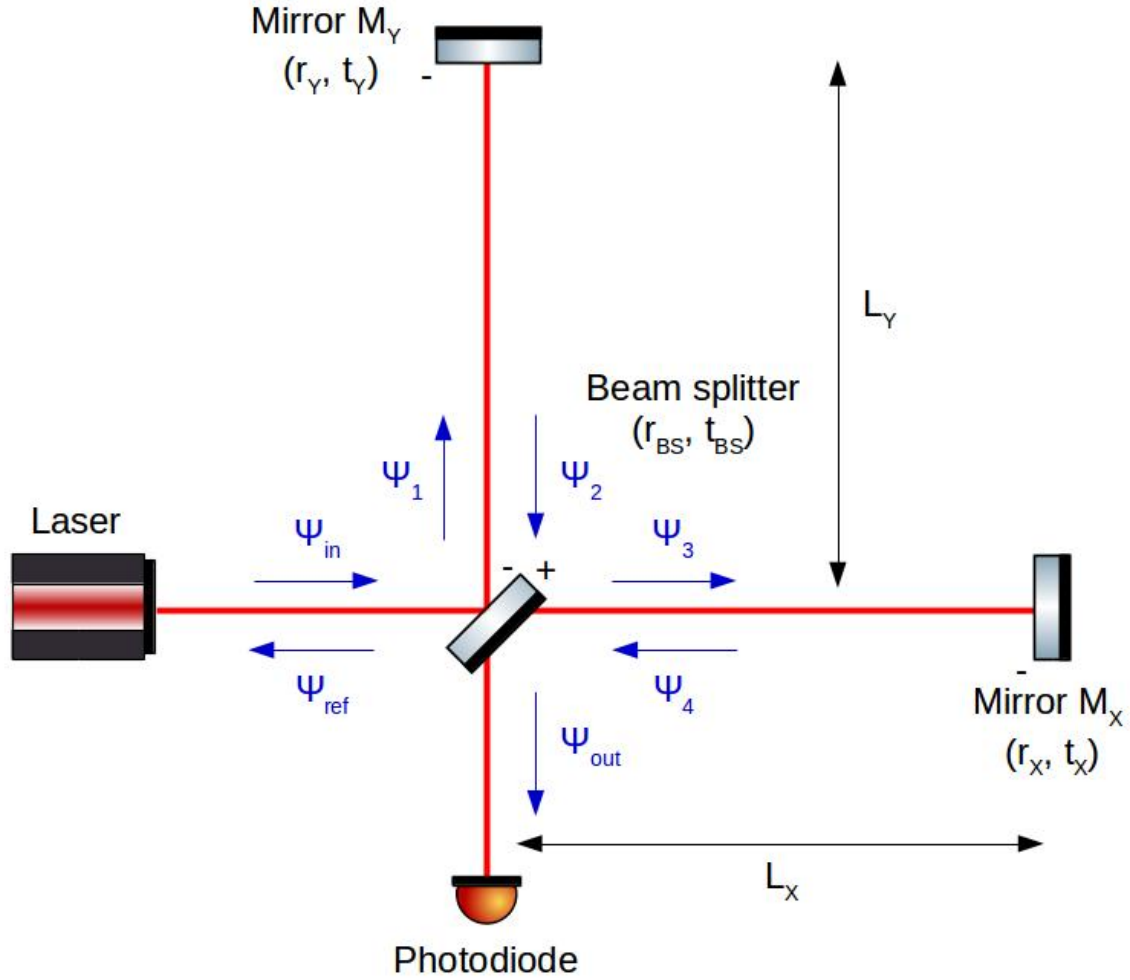


Figure 2.4 – Scheme of a simple Michelson interferometer. r_X , r_Y and t_X , t_Y are the amplitude reflectivities and transmissivities of the end mirrors M_X and M_Y

ence between the two arms, in other words on the differential length of the two arms and, as explained in Chapter 1, gravitational waves have a differential effect on lengths. That is why such kind of interferometers can be used to detect gravitational waves. I will give more details on the simple Michelson interferometer.

First let's introduce some definitions and conventions. The laser beam at a position $\vec{r} = x\hat{u}_x + y\hat{u}_y + z\hat{u}_z$ and a time t can be described by its electromagnetic field :

$$\psi(\vec{r}, t) = \psi_0 e^{-i(\vec{k}_0 \cdot \vec{r} - \omega_0 t)} \quad (2.1)$$

where \vec{k}_0 is the wave vector with $|\vec{k}_0| = \omega_0/c$, ω_0 is the angular frequency and ψ_0 is the initial field. According to Equation (2.1), when light propagates over a distance L , it undergoes a phase shift $k_0 L$.

An optical system, such as a mirror or a lens, can be characterized by its amplitude reflectivity r , its amplitude transmissivity t and losses \mathcal{L} such that $r^2 + t^2 + \mathcal{L} = 1$.

When light is reflected on a medium with a higher refractive index, it undergoes a local phase shift of π . Consequently the electromagnetic field ψ is multiplied by $e^{-i\pi} = -1$. The

convention used for the reflection and transmission coefficient on a surface is then:

$$\begin{pmatrix} t & t \\ -r & r \end{pmatrix}.$$

Using these rules and the scheme of Figure 2.4, we can write the electromagnetic field at several points in the interferometer with respect to the incoming field ψ_{in} on the beam splitter:

$$\psi_1 = -r_{BS}\psi_{in}, \quad (2.2)$$

$$\psi_2 = r_Y r_{BS} \psi_{in} e^{-2ik_0 L_Y}, \quad (2.3)$$

$$\psi_3 = t_{BS} \psi_{in}, \quad (2.4)$$

$$\psi_4 = -t_{BS} r_X \psi_{in} e^{-2ik_0 L_X}, \quad (2.5)$$

$$\psi_{ref} = -r_{BS} \psi_2 + t_{BS} \psi_4, \quad (2.6)$$

$$\psi_{out} = t_{BS} \psi_2 + r_{BS} \psi_4. \quad (2.7)$$

The two important beams are the one reflected towards the laser source defining the *symmetric port* and the one transmitted towards the detection photodiode defining the *anti-symmetric port* of the interferometer. We can write their fields ψ_{ref} and ψ_{out} with respect to the incoming field ψ_{in} :

$$\psi_{ref} = - \left(t_{BS}^2 r_X e^{-2ik_0 L_X} + r_{BS}^2 r_Y e^{-2ik_0 L_Y} \right) \psi_{in}, \quad (2.8)$$

$$\psi_{out} = r_{BS} t_{BS} \left(r_Y e^{-2ik_0 L_Y} - r_X e^{-2ik_0 L_X} \right) \psi_{in}. \quad (2.9)$$

Finally, considering a perfect beam splitter, with $r_{BS} = t_{BS} = 1/\sqrt{2}$, corresponding to 50% of the incoming power in each arm, we get:

$$\psi_{ref} = -\frac{\psi_{in}}{2} \left(r_X e^{-2ik_0 L_X} + r_Y e^{-2ik_0 L_Y} \right), \quad (2.10)$$

$$\psi_{out} = \frac{\psi_{in}}{2} \left(r_Y e^{-2ik_0 L_Y} - r_X e^{-2ik_0 L_X} \right). \quad (2.11)$$

For simplicity, and to simplify calculations in the next sections, we can interpret the Michelson interferometer as a mirror with complex amplitude reflectivity and transmissivity r_{MI} and t_{MI} defined as:

$$r_{MI} = \frac{\psi_{ref}}{\psi_{in}}, \quad (2.12)$$

$$t_{MI} = \frac{\psi_{out}}{\psi_{in}}. \quad (2.13)$$

With the detection photodiode, we measure the power in the anti-symmetric port:

$$P_{out} = |\psi_{out}|^2 = \frac{P_{in}}{4} \left(r_X^2 + r_Y^2 \right) (1 - C \cos(\Delta\phi_0)), \quad (2.14)$$

with $P_{in} = |\psi_{in}|^2$ the input power, $\Delta\phi_0 = 2k_0 \Delta L_0 = 2k_0(L_Y - L_X)$ the phase difference in the light paths in the two arms at their nominal lengths L_X and L_Y and $C = 2r_X r_Y / (r_X^2 + r_Y^2)$ the contrast factor.

If we consider the end mirrors M_X and M_Y as perfectly reflective, i.e. $r_X \sim r_Y \sim 1$, we can approximate Equation (2.14):

$$P_{out} = \frac{P_{in}}{2} (1 - \cos(\Delta\phi_0)). \quad (2.15)$$

We saw in Chapter 1 the effect of the passage of a gravitational wave on a circle of free test masses represented in Figure 1.1 and its mathematical expression in Equation (1.11). The variation δt of the travel time t along the two arms of length L due to a gravitational wave of amplitude h leads to a variation of the phase difference $\Delta\phi = \Delta\phi_0 + \delta\phi_{GW}$ with:

$$\delta\phi_{GW} = 2k_0 h L \ll 1. \quad (2.16)$$

We can use a Taylor expansion to express the power detected on the photodiode in the presence of a gravitational wave:

$$P_{out} \simeq \frac{P_{in}}{2} (1 - \cos(\Delta\phi_0) + \delta\phi_{GW} \sin(\Delta\phi_0)). \quad (2.17)$$

Consequently, the power variation induced on the photodiode by the passage of a gravitational wave is:

$$\delta P_{out}^{GW} = \frac{P_{in}}{2} \delta\phi_{GW} \sin(\Delta\phi_0). \quad (2.18)$$

Until now we considered only stationary gravitational wave. Introducing a time dependence, we can write $h(t) = h_0 e^{i\omega t}$. Consequently the phase difference due to a gravitational wave can be written as:

$$\delta\phi_{GW} = 2 \int_{t-\frac{2L}{c}}^t \omega_0 h_0 e^{i\omega t} dt, \quad (2.19)$$

where ω_0 is the angular frequency of the laser light source of the interferometer. By integration we find:

$$\delta\phi_{GW} = \frac{4L\omega_0}{c} \frac{\sin(\frac{L\omega}{c})}{\frac{L\omega}{c}} h_0 e^{-ikL} e^{i\omega t}. \quad (2.20)$$

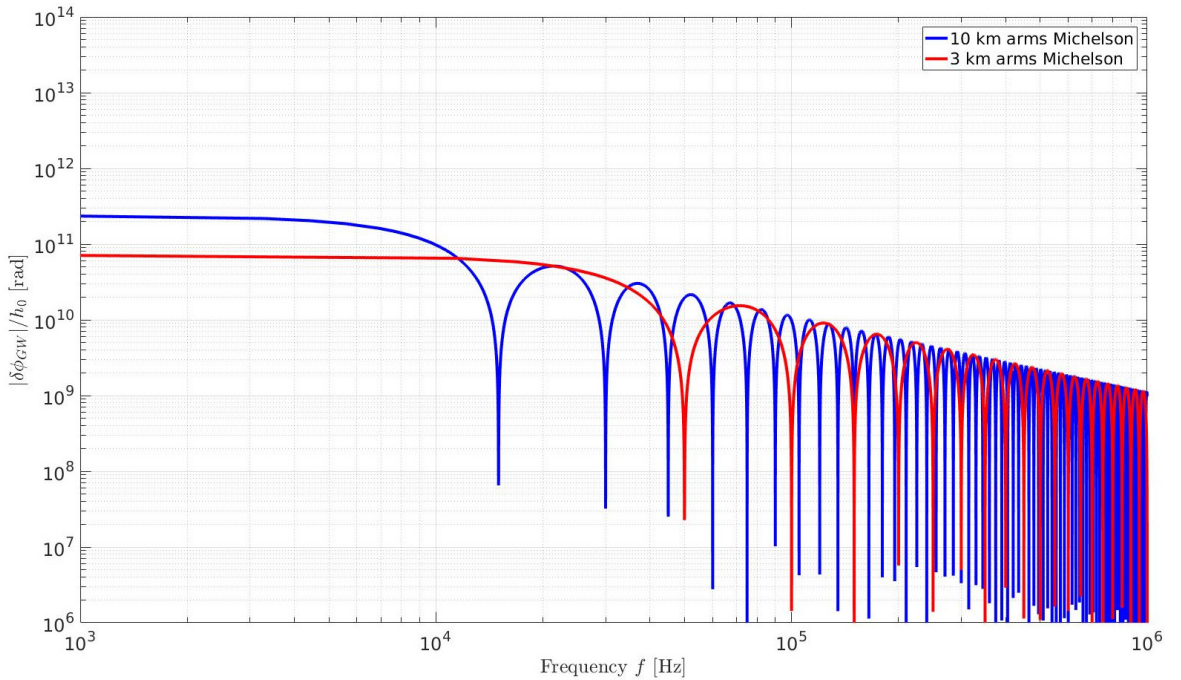


Figure 2.5 – Frequency response of a simple Michelson interferometer with arm length of 3 km (red line), 10 km (blue line).

Equation (2.20) is plotted in Figure 2.5 for a laser wavelength $\lambda_0 = 1064$ nm and arm lengths L of 3 km and 10 km for comparison. The frequency f is the frequency of gravitational waves such as $\omega = 2\pi f$. We can note some features:

- When $f \ll c/2L$ the amplitude of the effect is constant for a fixed arm length and increase with the arm length.
- When f is an integer multiple of $c/2L$ the interferometer is not sensitive to the gravitational wave signal.
- When f is above $c/2L$ the envelope of the amplitude decays as $1/f$.
- The longer are the arms, the more sensitive is the instrument.

2.3 Noise sources

Gravitational wave detectors are limited by many kinds of noise sources. It is important to understand them in order to limit their impact on the detector and mitigate the signal from the noise. To do so I will define the sensitivity of a detector and then the impact of the main noise sources on the detector sensitivity.

2.3.1 Sensitivity

The sensitivity of a detector is defined by the minimal amplitude h of a gravitational wave that the instrument is able to detect. The sensitivity is defined over a certain frequency range as an *amplitude spectral density* $\tilde{h}(f)$ expressed in $1/\sqrt{\text{Hz}}$.

To define the amplitude spectral density we can start with a general deterministic function of time $s(t)$ and define its *auto-correlation function*:

$$s \star s(\tau) = \lim_{T \rightarrow +\infty} \frac{1}{2T} \int_{-T}^T s(t)s(t+\tau) dt. \quad (2.21)$$

The width of the function in Equation (2.21) conveyed the temporal coherence of the function $s(t)$, i.e. it is related to the speed at which the function changes over time. According to the Wiener-Khintchine theorem, the *power spectral density* is the Fourier transform of the auto-correlation function:

$$S(f) = \frac{1}{\sqrt{2\pi}} \int_{-\infty}^{+\infty} s \star s(\tau) e^{-i2\pi f\tau} d\tau. \quad (2.22)$$

Finally the amplitude spectral density is simply:

$$\tilde{S}(f) = \sqrt{S(f)}. \quad (2.23)$$

The designed sensitivity of the Advanced Virgo detector is represented in black in Figure 2.6. Only the main noise sources have been reported in this plot. They will be described in the next sections.

2.3.2 Seismic noise

The seismic noise is not a dominant noise in the bandwidth of interest of Advanced Virgo but I want to first describe it because this defined an important feature of ground based interferometric detectors. Seismic noise is due to ground motion. Below 1 Hz it has mainly natural factors such as earthquakes, wind or ocean waves. Above 1 Hz, it is mainly produced by human activity. The characteristic scale of the spectrum of the displacement noise due to the seismic noise is:

$$\tilde{x}(f) \sim 10^{-9} \text{ m}/\sqrt{\text{Hz}} \begin{cases} 1 & 1 \text{ Hz} < f \leq 10 \text{ Hz} \\ \left(\frac{10\text{Hz}}{f}\right)^2 & f > 10 \text{ Hz} \end{cases} \quad (2.24)$$

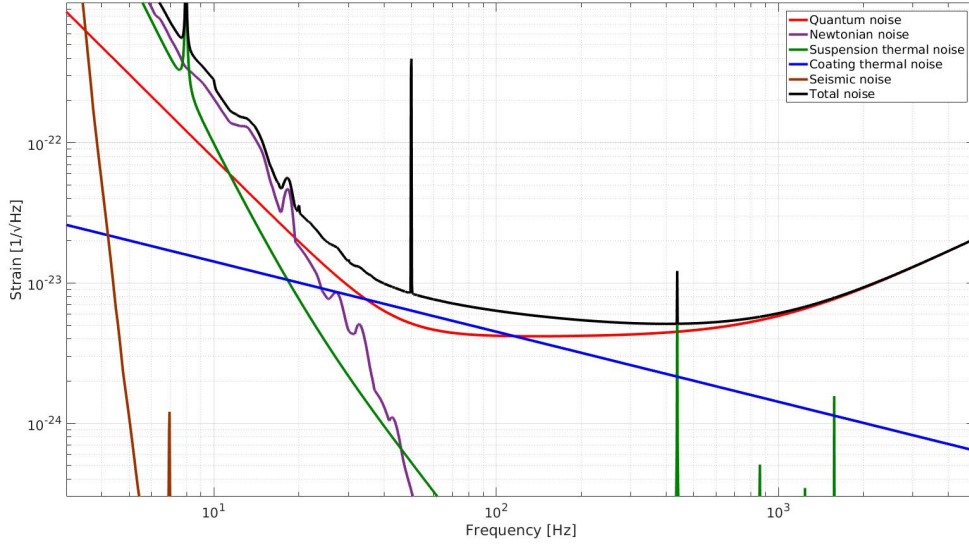


Figure 2.6 – Simulation of the sensitivity curve of the Advanced Virgo detector at design.

The equivalent strain noise $\tilde{h}_{seis}(f)$ is obtained by taking into account the round trip travel of the photon in the interferometer arms:

$$\tilde{h}_{seis}(f) \sim 2 \frac{\tilde{x}(f)}{L}. \quad (2.25)$$

Consequently, for a km-scale interferometer at $f = 10$ Hz we get:

$$\tilde{h}_{seis}(f) \sim 10^{-12}/\sqrt{\text{Hz}}. \quad (2.26)$$

This noise is 9 orders of magnitude higher than what we want to detect. Consequently it must be attenuated. To do so we use a pendulum chain with an inverted pendulum represented in Figure 2.7.

The attenuation principle can be approximated by a simple damper with a transfer function:

$$\tilde{H}(\omega) = \frac{\omega_r^2}{\omega_r^2 - \omega^2}, \quad (2.27)$$

where $f_r = \omega_r/2\pi$ is the damper fundamental frequency. For $\omega \gg \omega_r$ the module of the transfer function can be approximated by:

$$|\tilde{H}(\omega)| \simeq \left(\frac{\omega_r}{\omega}\right)^2. \quad (2.28)$$

Consequently a chain of N dampers has a transfer function:

$$|\tilde{H}(\omega)| \simeq \left(\frac{\omega_r}{\omega}\right)^{2N}. \quad (2.29)$$

For Advanced Virgo 5 pendula are used with a fundamental frequency $f_r \sim 0.6$ Hz and an inverted pendulum with a fundamental frequency $f_r \sim 40 - 80$ mHz. The strain noise due to seismic noise at 10 Hz is now [59]:

$$\tilde{h}_{seis}(f) \sim 10^{-29}/\sqrt{\text{Hz}}. \quad (2.30)$$

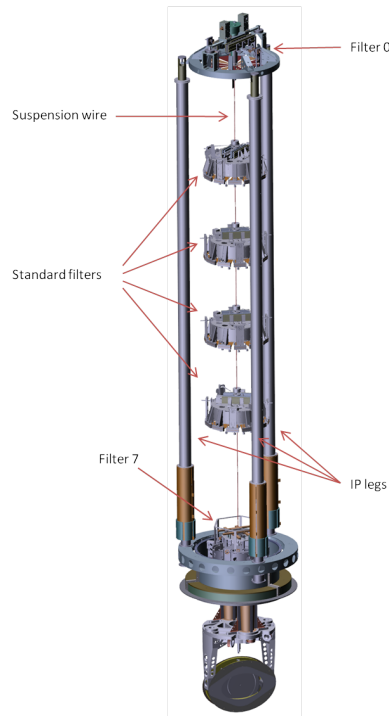


Figure 2.7 – Scheme of an Advanced Virgo superattenuator [58]. Each cavity mirror and the beam splitter are placed at the bottom of a superattenuator.

2.3.3 Quantum noise

Quantum noise plays an important role over the whole bandwidth. It is even a limiting noise at high frequency. Quantum noise is the sum of two noises inherent to the quantum nature of light: *shot noise* and *radiation pressure fluctuation noise*, that I will describe here. The aim of this thesis is to reduce this quantum noise. The way we plan to reduce it will be described in Chapter 3.

Shot noise

As I described in Section 2.2.2, the observable effect of the passage of a gravitational wave is a variation of power detected on the photodiode of the antisymmetric port of the interferometer. Thus the detection sensitivity is limited by the smallest power change we can detect.

Rewriting Equation (2.17) we find:

$$P_{out} \simeq P_{in} \left(\underbrace{\sin^2 \left(\frac{\Delta\phi_0}{2} \right)}_{\text{Source of noise}} + \underbrace{\delta\phi_{GW} \sin \left(\frac{\Delta\phi_0}{2} \right) \cos \left(\frac{\Delta\phi_0}{2} \right)}_{\text{Signal}} \right), \quad (2.31)$$

with $\Delta\phi_0$ the phase difference between the two arms of the interferometer at their nominal lengths. Consequently we can write the powers associated with the signal and the source of noise P_{signal} and P_{noise} :

$$P_{signal} = P_{in} \delta\phi_{GW} \sin \left(\frac{\Delta\phi_0}{2} \right) \cos \left(\frac{\Delta\phi_0}{2} \right), \quad (2.32)$$

$$P_{noise} = P_{in} \sin^2 \left(\frac{\Delta\phi_0}{2} \right). \quad (2.33)$$

The detected signal power P_{in} of Equation (2.32) reaches its maximum when $\Delta\phi_0 = \pi/2$ corresponding to a mid-fringe. But we will see that this is not optimal for the detection

because the noise is also important at mid-fringe. What we want to maximize is not the detected signal power but the signal to noise ratio defined as the ratio between signal power and the detected power fluctuation of the noise δP_{noise} .

The detected power fluctuation is due to the fact that the arrival of photons on the photodiode are discrete independent events described by a *Poisson distribution*. In a counting interval characterized by a mean number \bar{N} , the probability to count N events is:

$$P(N) = \frac{\bar{N}^N e^{-\bar{N}}}{N!}. \quad (2.34)$$

If $\bar{N} \gg 1$, the Poisson distribution can be approximated by a Gaussian distribution with a standard deviation $\sigma_{\bar{N}} = \sqrt{\bar{N}}$.

Note \bar{n} the rate of arrival of photons on the photodiode in Hz. The average number of photons incident on the photodiode during a time τ is then:

$$\bar{N} = \bar{n}\tau. \quad (2.35)$$

Now we can evaluate the average power detected P_{noise} by a photodiode impinged by a laser light at frequency $f_0 = \omega_0/2\pi$. Each photon carries a energy $\hbar\omega_0$. Consequently we have:

$$P_{noise} = \bar{n}\hbar\omega_0 = \bar{N} \frac{\hbar\omega_0}{\tau}. \quad (2.36)$$

Thus the detected power fluctuation due to Poisson statistics is:

$$\delta P_{noise} = \sigma_{\bar{N}} \frac{\hbar\omega_0}{\tau}. \quad (2.37)$$

Equalizing Equations (2.33) and (2.36) we find:

$$\bar{N} \frac{\hbar\omega_0}{\tau} = P_{in} \sin^2 \left(\frac{\Delta\phi_0}{2} \right). \quad (2.38)$$

Consequently:

$$\bar{N} = \frac{P_{in}\tau}{\hbar\omega_0} \sin^2 \left(\frac{\Delta\phi_0}{2} \right). \quad (2.39)$$

And then:

$$\sigma_{\bar{N}} = \sqrt{\bar{N}} = \sqrt{\frac{P_{in}\tau}{\hbar\omega_0}} \sin \left(\frac{\Delta\phi_0}{2} \right). \quad (2.40)$$

Finally injecting Equation (2.40) in Equation (2.37) we get the expression of the detected power fluctuation:

$$\delta P_{noise} = \sqrt{\frac{P_{in}\hbar\omega_0}{\tau}} \sin \left(\frac{\Delta\phi_0}{2} \right). \quad (2.41)$$

Then the signal to noise ratio is:

$$\text{SNR} = \frac{P_{signal}}{\delta P_{noise}} = \sqrt{\frac{P_{in}\tau}{\hbar\omega_0}} \cos \left(\frac{\Delta\phi_0}{2} \right) \delta\phi_{GW}. \quad (2.42)$$

It is maximum when $\Delta\phi_0 = 0$ corresponding to a dark fringe on the detection photodiode of the antisymmetric port. On this dark fringe, the signal to noise ratio is now:

$$\text{SNR} = \sqrt{\frac{P_{in}\tau}{\hbar\omega_0}} \delta\phi_{GW} \quad (2.43)$$

Remembering that the sensitivity of the detector is the minimal amplitude h of a gravitational wave that the instrument is able to detect, we can determine the amplitude spectral density $\tilde{h}(f)$ supposing that the minimal SNR detectable is $\text{SNR} = 1$. Thus:

$$\delta\phi_{GW,min} = \sqrt{\frac{\hbar\omega_0}{P_{in}\tau}}, \quad (2.44)$$

leading to:

$$\tilde{\delta\phi}_{GW}(f) = \sqrt{\frac{\hbar\omega_0}{P_{in}}}. \quad (2.45)$$

And according to Equation (2.16):

$$\tilde{\delta\phi}_{GW}(f) = \frac{4\pi\tilde{h}(f)L}{\lambda_0}. \quad (2.46)$$

Finally we get the shot noise limited sensitivity of the detector $\tilde{h}_{SN}(f)$ at dark fringe with respect to the laser wavelength λ_0 , the length L of the arms of the interferometer and the input power P_{in} :

$$\tilde{h}_{SN}(f) = \frac{\lambda_0}{4\pi L} \sqrt{\frac{\hbar\omega_0}{P_{in}}}. \quad (2.47)$$

According to Equation (2.47), the shot noise limit is independent on the frequency and inversely proportional to $\sqrt{P_{in}}$.

Radiation pressure fluctuation noise

The impact of the photons on a mirror of the interferometer induces a mirror displacement due to the *radiation pressure force* as shown in Figure 2.8.

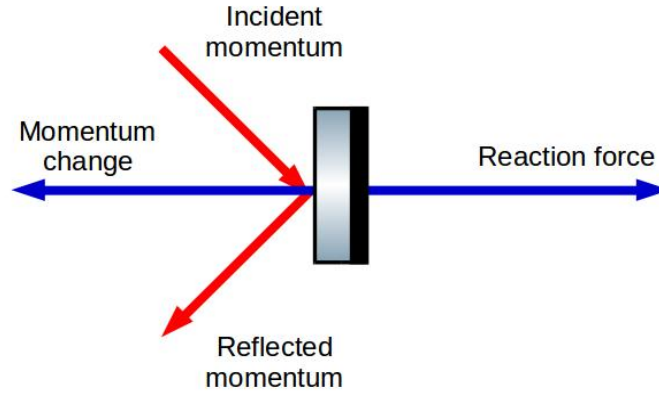


Figure 2.8 – Scheme of the radiation pressure force on a mirror.

The radiation pressure force F_{RP} is proportional to the input power P_{in} as:

$$F_{RP} = \frac{2P_{in}}{c}. \quad (2.48)$$

Using the same approach as for shot noise we can write the fluctuation of radiation pressure force on the mirror:

$$\delta F_{RP} = \frac{\delta P_{in}}{c} = \frac{\sqrt{\bar{N}\hbar\omega_0}}{\tau c} = \frac{1}{c} \sqrt{\frac{P_{in}\hbar\omega_0}{\tau}}, \quad (2.49)$$

leading to an amplitude spectral density $\tilde{\delta F}_{RP}(f)$:

$$\tilde{\delta F}_{RP}(f) = \frac{\sqrt{P_{in}\hbar\omega_0}}{c}. \quad (2.50)$$

From the pendulum equation, the mirror of mass m moves with a spectrum:

$$\tilde{x}(f) = \frac{1}{m\omega^2}\tilde{\delta F}_{RP}(f) = \frac{1}{mf^2}\sqrt{\frac{P_{in}\hbar}{8\pi^3\lambda_0c}}. \quad (2.51)$$

Moreover, as the power fluctuations in the two arms are anti-correlated [60], the effect on the output of the interferometer is doubled and as for Equation (2.25) we have:

$$\tilde{h}_{RP}(f) = 2\frac{\tilde{x}(f)}{L} = \frac{1}{mf^2L}\sqrt{\frac{P_{in}\hbar}{2\pi^3\lambda_0c}}. \quad (2.52)$$

According to Equation (2.52), the radiation pressure fluctuation noise limit depends on the frequency as $1/f^2$ and is proportional to $\sqrt{P_{in}}$.

Standard quantum limit

Now we can define the total quantum noise represented in red (dashed and continuous lines) in Figure 2.9 for two different input power. It is the sum of the shot noise and the radiation pressure fluctuation noise:

$$\tilde{h}_{QN}(f) = \tilde{h}_{SN}(f) + \tilde{h}_{RP}(f). \quad (2.53)$$

We can see from Equations (2.47) and (2.52) that if we increase the laser power, we reduce the shot noise while increasing the radiation pressure fluctuation noise. In the same way, if we reduce the laser power, we reduce the radiation pressure fluctuation noise while increasing the shot noise as illustrated in Figure 2.9.

This leads to the standard quantum limit which can be approximated using the limiting power P_{opt} such that $\tilde{h}_{SN}(f) = \tilde{h}_{RP}(f)$. We find:

$$P_{opt} = \frac{\lambda_0}{2}\pi cmf^2, \quad (2.54)$$

$$\tilde{h}_{SQL}(f) \sim \tilde{h}_{SN}(f, P_{opt}) = \tilde{h}_{RP}(f, P_{opt}). \quad (2.55)$$

Thus:

$$\tilde{h}_{SQL}(f) \sim \frac{1}{\pi Lf}\sqrt{\frac{\hbar}{2m}}. \quad (2.56)$$

The standard quantum limit is inversely proportional to the frequency. It is represented in black in Figure 2.9. This is this standard quantum limit we are interested to beat in a way I will describe in Chapter 3.

2.3.4 Other sources of noise

The two other dominant sources of noise represented in Figure 2.6 I want to describe are the *thermal noise* and the *gravity gradient noise*, also called *Newtonian noise*. There are other noise sources [61] but I won't describe them because they don't limit our design sensitivity.

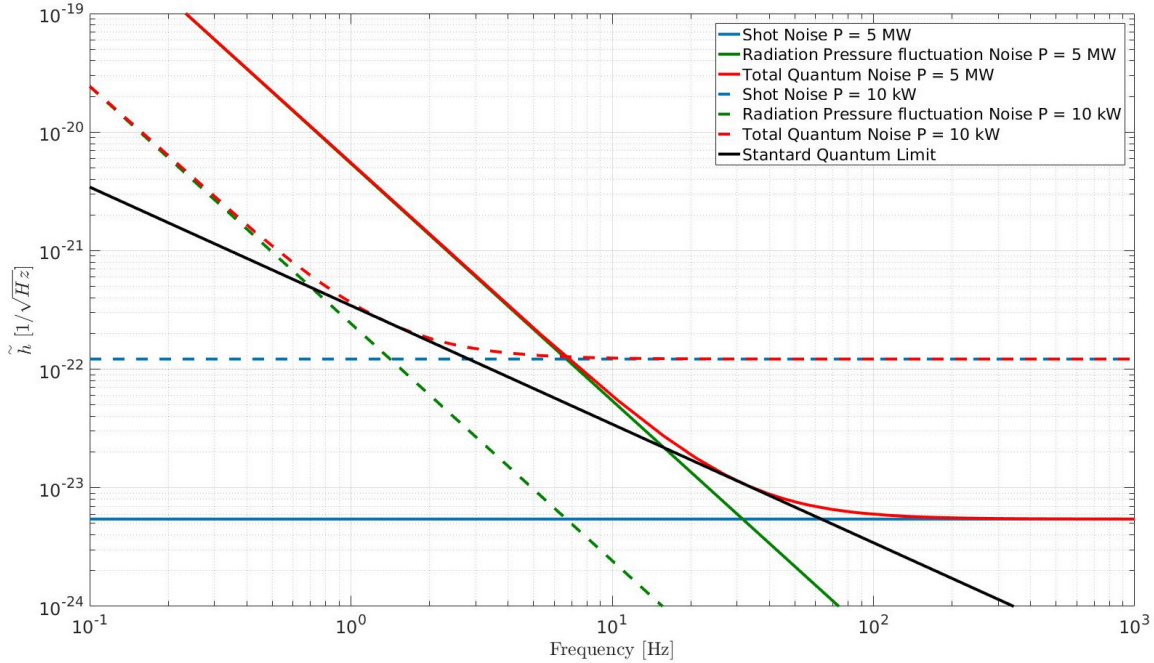


Figure 2.9 – Plot of the shot noise (blue), radiation pressure fluctuation noise (green) and their sum: quantum noise (red) for two beam powers (10 kW and 5 MW). The standard quantum limit is plotted in black.

Thermal noise

The dominant thermal noises are the one from the coating of the mirrors and the suspensions. They are due to random excitation of vibration modes proportional to the temperature of the system.

The thermal noise due to coating vibration modes limits the sensitivity between 50 and 200 Hz.

The pendulum thermal noise has a resonance frequency at 0.6 Hz due to the suspension described in Section 2.3.2. It is a main noise below 10 Hz but it is minimized using silica suspension wire fused on the mirrors with a high quality factor.

The violin modes are vibration modes of the suspension wires. They have some resonant frequencies around 450 Hz and its multiple integers.

The spectrum of the mirror movements due to thermal noise can be written [31]:

$$\tilde{x}(f) = \sqrt{\frac{4k_B T \omega_r^2}{Q m \omega} \frac{1}{(\omega_r^2 - \omega^2)^2 + \frac{\omega_r^4}{Q^2}}} \text{ m}/\sqrt{\text{Hz}}, \quad (2.57)$$

where Q is the *quality factor* of the suspension, m the mirror mass, T the temperature, ω_r is linked to the resonance frequency of the suspension and ω to the frequency of the gravitational wave. Under this form we can understand the possible improvement concerning thermal noise that will be describe in Section 2.5.2.

Gravity gradient noise

The gravity gradient noise or Newtonian noise is due to local change in the gravitational field induced by a variation of the mass distribution. It is produced by seismic waves in the ground and density fluctuations in the atmosphere.

This noise is very difficult to mitigate, because it is hardly measured and modeled. Moreover, as shown in Figure 2.6, it is a limiting noise from few Hz to 20 Hz. Nevertheless some solution to reduce its impact will be presented in Section 2.5.2.

2.4 First sensitivity improvements

To have a better sensitivity, gravitational wave detectors are not simple Michelson interferometers. In Section 2.3, I derived the expressions of some main noise sources through Equations (2.25), (2.47) and (2.52). They are all inversely proportional to the arm length. However it would be difficult and too expensive to build on Earth a 100-km arm length detector. In addition, as shown in Figure 2.9, the laser power in the arms needed to reach Advanced Virgo sensitivity are much higher than what we can achieve with a simple laser source.

Fabry-Perot cavities are a way to solve these issues by increasing the optical path length as well as the laser power in the arms. I will describe their effect in this section. Moreover, the sensitivity can also be optimized using other solutions: *power recycling* and *signal recycling*.

2.4.1 Fabry-Perot arm cavity

Description of the Fabry-Perot cavity

A Fabry-Perot cavity is composed of two mirrors M_1 and M_2 with respectively an amplitude reflectivity and transmissivity r_1, t_1 and r_2, t_2 separated by a distance L as represented in Figure 2.10. Light of wave vector k_0 is sent through the entrance mirror. A simplified view is to say that a part of the light is reflected and a part of it is transmitted towards the cavity making several round trips inside the cavity before being reflected back towards the entrance mirror M_1 or transmitted by the end mirror M_2 .

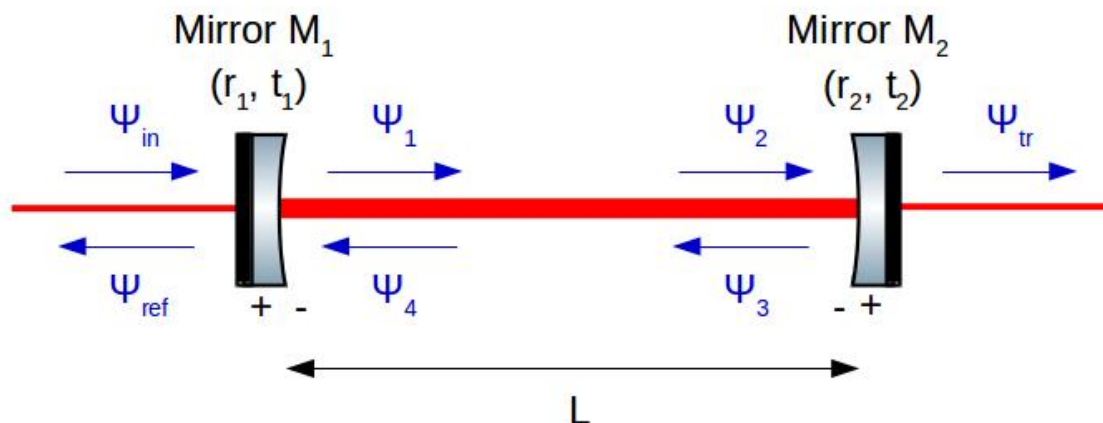


Figure 2.10 – Scheme of a Fabry-Perot cavity.

As for the Michelson interferometer, we can write the electromagnetic field at several points in the Fabry-Perot cavity with respect to the input field ψ_{in} at the entrance mirror M_1 :

$$\psi_1 = t_1\psi_{in} - r_1\psi_4, \quad (2.58)$$

$$\psi_2 = \psi_1 e^{-ik_0 L}, \quad (2.59)$$

$$\psi_3 = -r_2\psi_2, \quad (2.60)$$

$$\psi_4 = \psi_3 e^{-ik_0 L}, \quad (2.61)$$

$$\psi_{tr} = t_2\psi_2, \quad (2.62)$$

$$\psi_{ref} = r_1\psi_{in} + t_1\psi_4, \quad (2.63)$$

$$\psi_{cav} = \psi_1. \quad (2.64)$$

Using these equations we can write the complex amplitude transmissivity t_{FP} , reflectivity r_{FP} and the gain g_{FP} of the cavity:

$$t_{FP} = \frac{\psi_{tr}}{\psi_{in}} = \frac{t_1 t_2 e^{-ik_0 L}}{1 - r_1 r_2 e^{-2ik_0 L}}, \quad (2.65)$$

$$r_{FP} = \frac{\psi_{ref}}{\psi_{in}} = \frac{r_1 - r_2 (r_1^2 + t_1^2) e^{-2ik_0 L}}{1 - r_1 r_2 e^{-2ik_0 L}}, \quad (2.66)$$

$$g_{FP} = \left| \frac{\psi_{cav}}{\psi_{in}} \right| = \left| \frac{t_1}{1 - r_1 r_2 e^{-2ik_0 L}} \right|. \quad (2.67)$$

To obtain the power P_i , which is the measurable quantity, from the electromagnetic field ψ_i we have:

$$P_i = \psi_i \cdot \psi_i^* = |\psi_i|^2. \quad (2.68)$$

Consequently, from Equation (2.65), the transmitted power P_{tr} is:

$$P_{tr} = P_{in} \frac{t_1^2 t_2^2}{1 + r_1^2 r_2^2 - 2r_1 r_2 \cos(2k_0 L)}. \quad (2.69)$$

According to Equation (2.69), the power transmitted by the Fabry-Perot cavity is maximum when the phase shift $\phi = 2k_0 L$ fulfill the **resonance condition**:

$$\phi = 2\pi n, \quad n \in \mathbb{N} \quad (2.70)$$

Using Equations (2.66) and (2.67), we can see that at resonance, the circulating power is maximum and the reflected power is minimum. The separation between two consecutive resonances is called a **free spectral range**. It can be expressed as a length with respect to the laser wavelength λ_0 :

$$\Delta L_{FSR} = \frac{\lambda_0}{2}, \quad (2.71)$$

or as a frequency with respect to the cavity length L :

$$\Delta \nu_{FSR} = \frac{c}{2L}. \quad (2.72)$$

The full width at half maximum of the transmitted power is the linewidth $\delta\nu$ of the cavity. From Equation (2.69), we have:

$$\delta\nu = \frac{\Delta \nu_{FSR}}{\pi} \arccos \left(-\frac{1 + r_1^2 r_2^2 - 4r_1 r_2}{2r_1 r_2} \right). \quad (2.73)$$

For gravitational wave detectors, we use cavities with high reflectivities, i.e. $r_1 r_2 \sim 1$. Consequently we can approximate the full width at half maximum by:

$$\delta\nu \simeq \Delta \nu_{FSR} \frac{1 - r_1 r_2}{\pi \sqrt{r_1 r_2}}. \quad (2.74)$$

The **finesse** of a cavity is defined by the ratio between the free spectral range and the linewidth of the cavity:

$$\mathcal{F} \simeq \frac{\pi \sqrt{r_1 r_2}}{1 - r_1 r_2}. \quad (2.75)$$

We often characterize a cavity by its finesse. The finesse and the linewidth depend on the reflectivities of the mirrors of the cavity. As r_1 and r_2 become higher, the finesse increases and the linewidth decreases.

The **storage time** τ of the cavity is the mean time a photon stays trapped in the cavity before it escapes through one of the mirrors. It is related to the linewidth of the cavity by:

$$\tau = \frac{1}{\pi \delta\nu}. \quad (2.76)$$

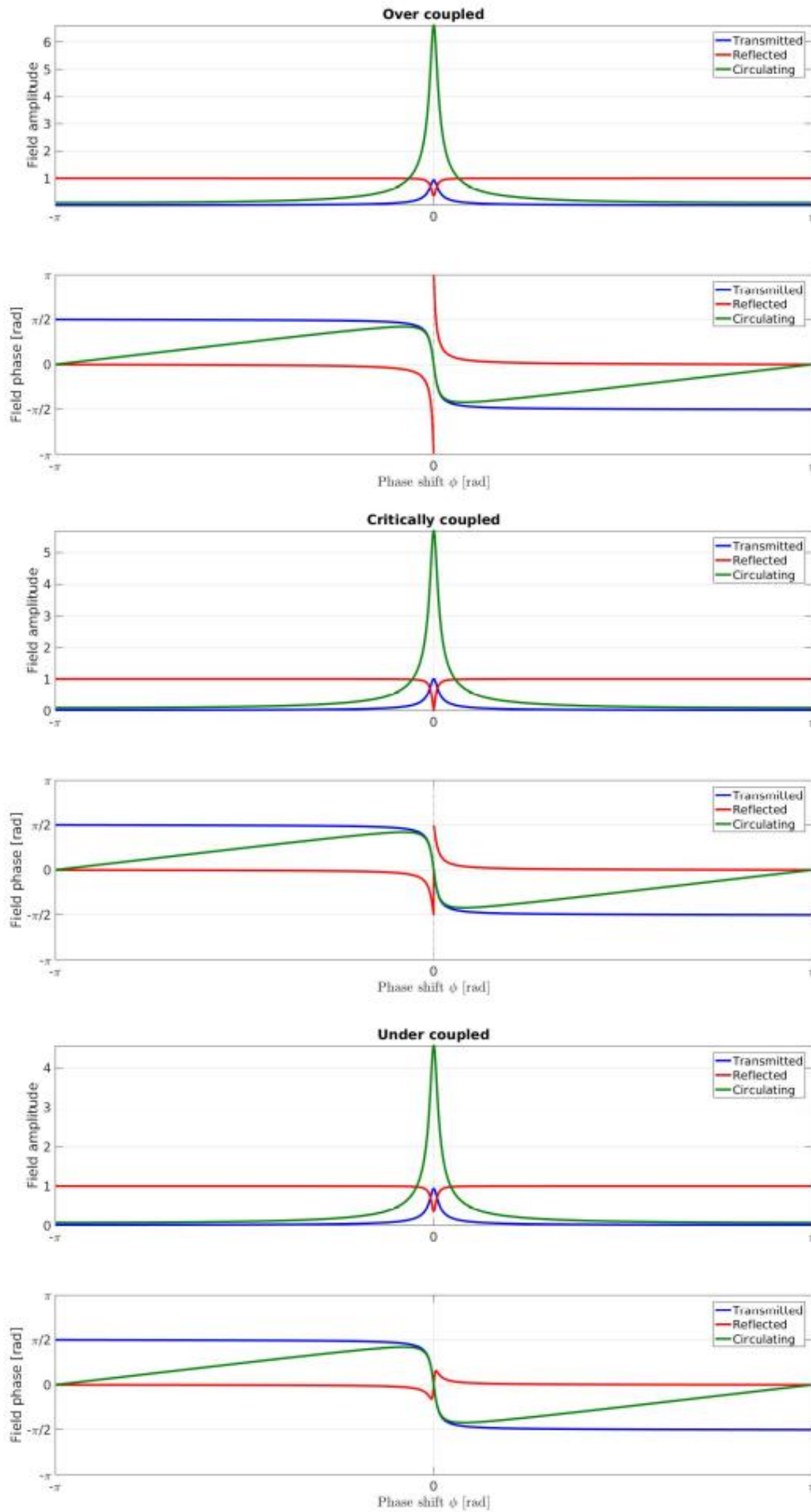


Figure 2.11 – Transmitted, reflected and circulating (ψ_1) fields amplitude and phase as a function of the phase shift $\phi = 2k_0L$ from resonance. The three types of cavities are represented, in all cases with a finesse $\mathcal{F} = 100$ (for representative purpose). No losses are considered. From top to bottom: over coupled, critically coupled, under coupled cavity type.

Then the travel length L_{eq} of a photon inside a cavity is:

$$L_{eq} = \tau c = \frac{2L\mathcal{F}}{\pi}. \quad (2.77)$$

Consequently when the finesse increases, the travel length of the photons increases by the same amount. That is why we use high finesse cavities for gravitational wave detectors. For instance, Advanced Virgo uses Fabry-Perot cavities in its arms with a finesse $\mathcal{F} \simeq 450$ leading to equivalent arm length $L_{eq} \simeq 860$ km instead of $L = 3$ km.

The same finesse can be obtained with several couples of reflectivities r_1 and r_2 . From Equation (2.66), we can distinguish three types of cavities, introducing \mathcal{L}_1 the losses of mirror M_1 such as $r_1^2 + t_1^2 + \mathcal{L}_1 = 1$. They are represented in Figure 2.11.

- *Over coupled cavity:* $r_1 - r_2(1 - \mathcal{L}_1) < 0$, the part of the reflected beam leaking out of the cavity dominates the promptly reflected one. The phase of the reflected field changes significantly across the resonance.
- *Critically coupled cavity:* $r_1 - r_2(1 - \mathcal{L}_1) = 0$, the circulating field, i.e. the power gain, is maximal at resonance but there is no reflected beam and the incident beam is fully transmitted.
- *Under coupled cavity:* $r_1 - r_2(1 - \mathcal{L}_1) > 0$, the promptly reflected beam dominates the the reflected one leaking out of the cavity.

For gravitational wave detection we measure a phase shift. We can see in Figure 2.11 that the phase shift is enhanced around resonance for an over coupled cavity. Consequently gravitational wave detectors use over coupled cavities.

Phase shift of the reflected field

According to Equation (2.66), the reflected field for a Fabry-Perot cavity of length L is:

$$\psi_{ref}(L) = \psi_{in} \frac{r_1 - r_2(t_1^2 + r_1^2)e^{-2ik_0L}}{1 - r_1r_2e^{-2ik_0L}}. \quad (2.78)$$

At resonance we have $L = L_{res}$ and $e^{-2ik_0L} = 1$ and the Taylor expansion of the reflected field for a small variation of length δL around the resonance L_{res} is:

$$\psi_{ref}(L_{res} + \delta L) \simeq \psi_{ref}(L_{res}) + \delta L \psi'_{ref}(L_{res}). \quad (2.79)$$

After some computation and introducing the finesse in the expression, we obtain:

$$\psi_{ref}(L_{res} + \delta L) \simeq \frac{\mathcal{F}}{\pi} \frac{r_1 - r_2(t_1^2 + r_1^2)}{\sqrt{r_1r_2}} \left[1 - 2ik_0\delta L \frac{\mathcal{F}}{\pi} \frac{(1 - r_1^2)\sqrt{r_1r_2}}{r_1^2r_2(r_1 - r_2(t_1^2 + r_1^2))} \right]. \quad (2.80)$$

The phase shift $\delta\phi$ of the reflected field can now be approximated by:

$$\delta\phi \simeq 2k_0\delta L \frac{\mathcal{F}}{\pi} \frac{(1 - r_1^2)\sqrt{r_1r_2}}{r_1^2r_2(r_1 - r_2(t_1^2 + r_1^2))}. \quad (2.81)$$

If we neglect the losses, i.e. $r_1^2 + t_1^2 = 1$ and consider an over coupled cavity with $r_2 \sim 1$, we get:

$$\delta\phi \simeq 2k_0\delta L \frac{\mathcal{F}}{\pi} \frac{(1 + r_1)\sqrt{r_1}}{r_1^2}. \quad (2.82)$$

And finally if we consider that $r_1 \sim 1$ which is consistent with high finesse cavities used in gravitational wave detectors, we finally obtain a simple expression for the phase shift of the reflected field:

$$\delta\phi \simeq 2k_0\delta L \frac{2\mathcal{F}}{\pi}. \quad (2.83)$$

Consequently a Fabry-Perot cavity around resonance amplifies the phase shift with respect to a single mirror by a factor $2\mathcal{F}/\pi$.

Frequency response

Until now we did not consider the time dependence of the gravitational wave amplitude. We can model the effect of the passage of a gravitational wave as a sinusoidal motion of the end mirror. If the change of length is faster than the storage time, its effect is attenuated by the cavity. The cavity acts as a low-pass filter and consequently, taking into account this frequency behavior we can rewrite the phase shift of the reflected field from the Fabry-Perot cavity:

$$\delta\phi \simeq 2k_0\delta L \frac{2\mathcal{F}}{\pi} \frac{1}{\sqrt{1 + \left(\frac{f}{f_c}\right)^2}}, \quad (2.84)$$

where $f_c = \frac{c}{4\mathcal{F}L}$ is the cut-off frequency of the cavity. This is the frequency over which the frequency response of the cavity starts to be attenuated.

The frequency response of the Michelson interferometer with Fabry-Perot arm cavities is shown in Figure 2.12 for an Advanced Virgo like detector with 3 km arm length and a finesse $\mathcal{F} = 450$ compared with 3km-arms and 850km-arms simple Michelson interferometers.

The sensitivity of the detector is multiplied by a factor:

$$\frac{\pi}{2\mathcal{F}} \sqrt{1 + \left(\frac{f}{f_c}\right)^2}. \quad (2.85)$$

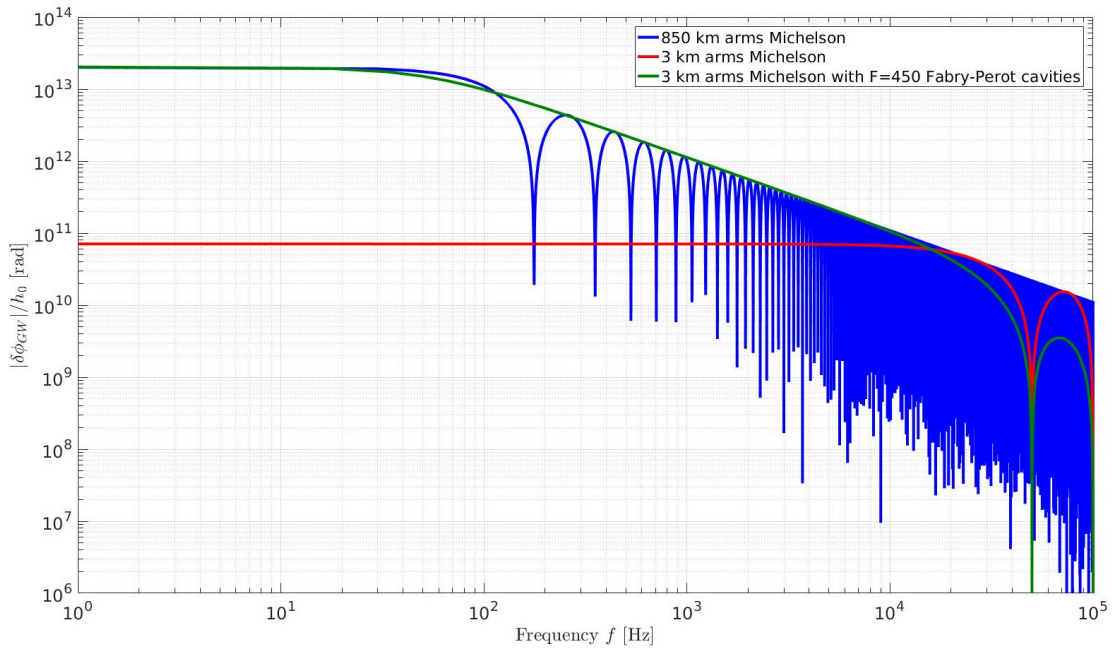


Figure 2.12 – Frequency response of a simple Michelson interferometer with arm length of 3 km (red line), 850 km (blue line) and a Michelson interferometer with Fabry-Perot arm cavities of length 3 km with a finesse 450 (green line).

The general scheme of a gravitational wave detector with Fabry-Perot arm cavities is shown in Figure 2.13.

Equivalent Michelson interferometer

We can model the Michelson interferometer with Fabry-Perot arm cavities as an equivalent simple Michelson interferometer with mirror reflectivities and transmissivities given from the the Fabry-Perot cavities reflectivities and transmissivities $r_{FP,X}$, $r_{FP,Y}$, $t_{FP,X}$ and $t_{FP,Y}$ instead of the single mirrors one r_X , r_Y , t_X and t_Y .

As in Section 2.2.2, we can define the amplitude reflectivity and transmissivity of the Fabry-Perot arm cavity Michelson interferometer r_{FRMI} and t_{FPMI} from Equations (2.12) and (2.13), using the amplitude reflectivities and transmissivities of the equivalent Michelson interferometer end mirrors.

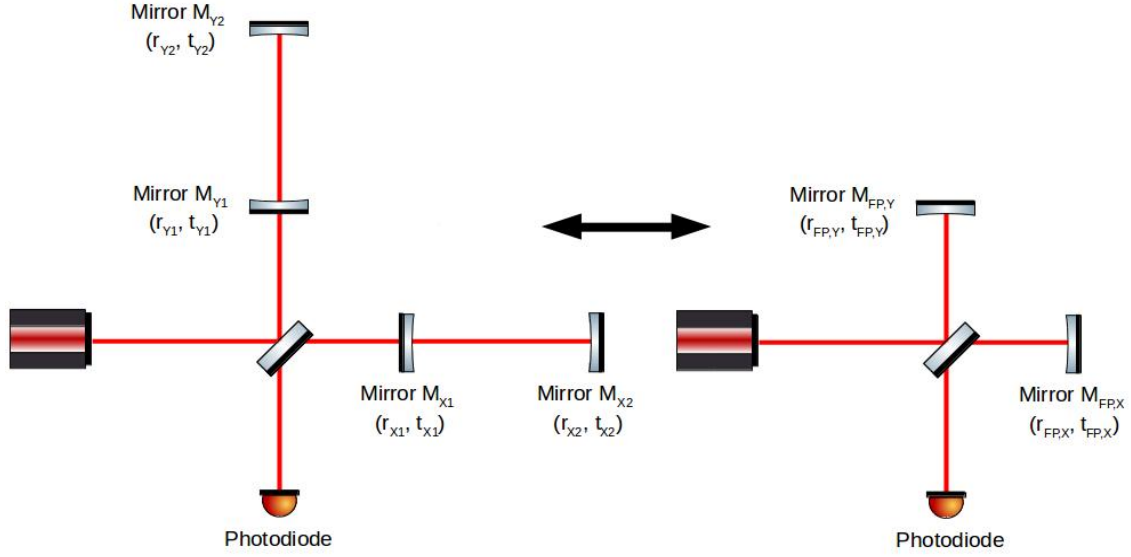


Figure 2.13 – Scheme of a Michelson interferometer with Fabry-Perot arm cavities and the equivalent Michelson interferometer.

2.4.2 Power recycling

There are technical limitations to increase the power from the laser source. The simplest way to improve the beam power inside the interferometer is to use another mirror to *recycle* the power reflected by the Michelson interferometer.

Indeed, at dark fringe all the power is reflected by the Michelson towards the laser source. Consequently we can add a mirror between the laser source and the beam splitter to recover the power coming back as shown in Figure 2.14.

We can write the fields transmitted and reflected by the power recycling mirror ψ_{MICH} and $\psi_{ref,PR}$:

$$\psi_{MICH} = t_{PR}\psi_{in} - r_{PR}\psi_{ref}, \quad (2.86)$$

$$\psi_{ref,PR} = r_{PR}\psi_{in} + t_{PR}\psi_{ref}, \quad (2.87)$$

with $\psi_{ref} = r_{FPMI}\psi_{MICH}$ for a Michelson interferometer with Fabry-Perot cavity arms. Replacing ψ_{ref} in Equation (2.86) we obtain the optical gain of the power recycling cavity:

$$G_{PR} = \left| \frac{\psi_{MICH}}{\psi_{in}} \right|^2 = \left| \frac{t_{PR}}{1 + r_{PR}r_{FPMI}} \right|^2. \quad (2.88)$$

Then the sensitivity of the interferometer is multiplied by a factor:

$$\frac{1}{\sqrt{G_{PR}}} \quad (2.89)$$

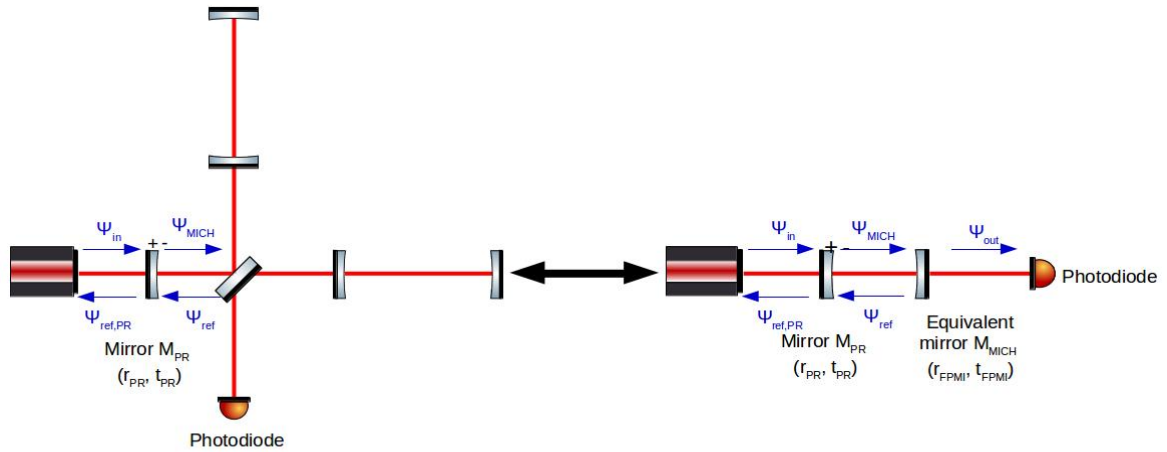


Figure 2.14 – Scheme of a power recycled Fabry-Perot arm cavities Michelson interferometer and equivalent Fabry-Perot cavity.

2.4.3 Signal recycling

Finally another way to increase the sensitivity is to add an extra mirror in the antisymmetric port between the photodiode and the beam splitter as shown in Figure 2.15, for recycling the signal light.

With this configuration, it is possible to tune the shape of the detector sensitivity by changing the length of the signal recycling cavity. The phase difference due to a gravitational wave is plotted in Figure 2.16 for several tuning of the signal recycling cavity, formed by the signal recycling mirror and the input mirrors of the Fabry-Perot cavities. Tuning the cavity corresponds to changing the transmissivity of the input mirrors of the Fabry-Perot cavities.

At 0° tuning, the cavity is at resonance. The reflectivity of the equivalent input mirror of the Fabry-Perot cavity is the lowest possible, reducing the finesse of the cavity. As a result the bandwidth of the detector is increased. At high frequencies, the sensitivity is increased and at low frequencies, even if it seems to decrease sensitivity, in fact, other noises presented in Section 2.3 dominate. Consequently this is a possible choice for gravitational wave detectors.

At 180° tuning, the cavity is anti-resonant. The reflectivity of the equivalent input mirror is the highest possible, increasing the finesse of the cavity. The bandwidth is reduced and the sensitivity is improved at low frequency. This is not an interesting choice for gravitational wave detectors.

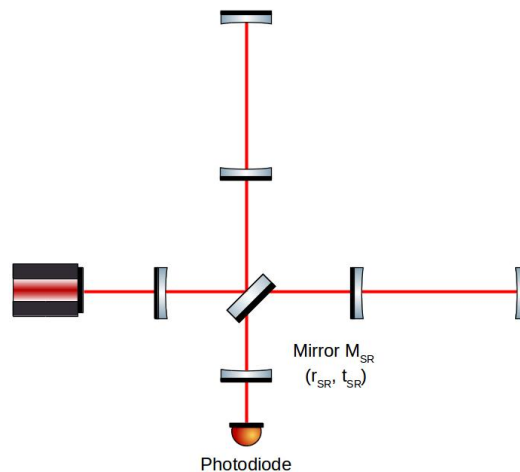


Figure 2.15 – Scheme of a dual recycled Fabry-Perot arm cavities Michelson interferometer.

Finally, for intermediate tuning, the cavity is *detuned* and there is a peak at a frequency depending on the tuning. This is useful if we want to optimize the detection around a given frequency. For instance, for BNS merger, we may want to increase the sensitivity around 100 Hz with a 60° tuning.

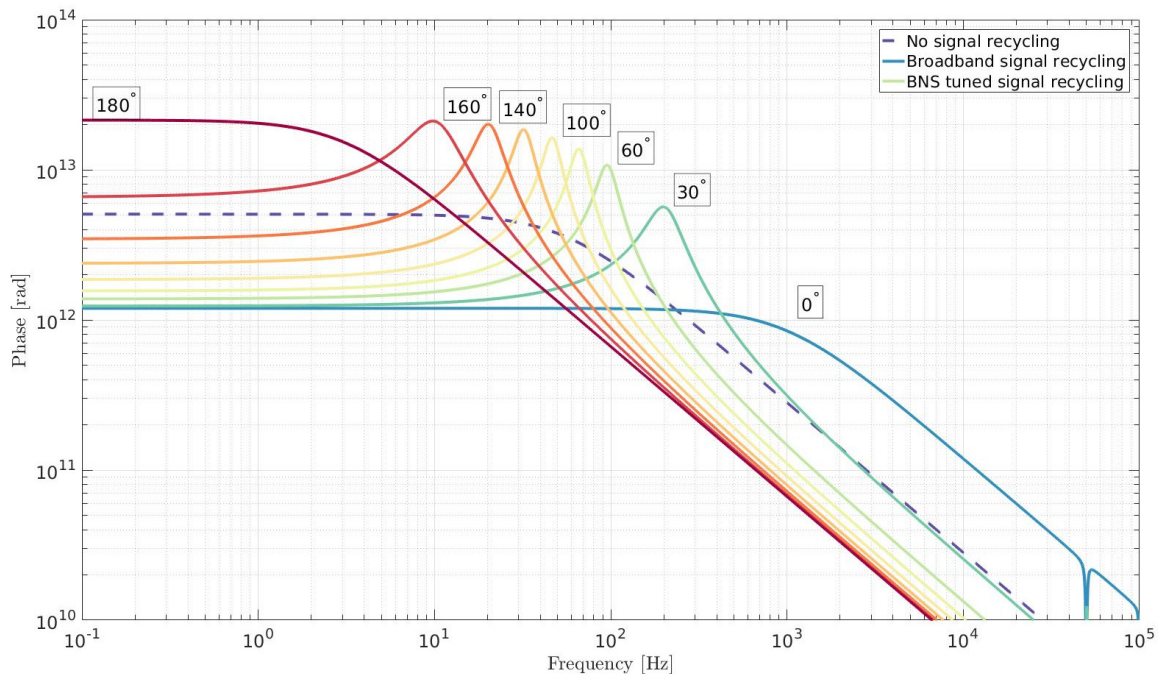


Figure 2.16 – Phase response of the detector for different tuning of the signal recycling cavity.

2.5 Further improvements

2.5.1 Motivations

Before improving the sensitivity of the instrument, we may wonder if it's worth doing it. To do so we have to understand what is the information that we can learn at each frequency to focus on specific technical improvements on the frequency bandwidth of interest.

For instance, if we consider BNS, as shown in Figure 2.17, most of the information is below 100 Hz, around 10 Hz, except tidal parameters which are far above 100 Hz. Consequently we won't get the same information with respect to the frequencies we choose to improve.

The effect of the improvements at various frequencies can be summarized as [63]:

- At low frequency (below 10 Hz), improvements can increase the signal length in the detector enabling earlier warning, useful for multi-messenger astronomy. We could probe the early Universe with high redshifts black holes and detect more massive black holes.
- In the middle band, between 10 Hz and 200 Hz, sensitivity improvements lead to higher signal to noise ratio, increasing the number of detectable BBH, BNS and NSBH, and more accurate parameter estimations.
- At higher frequency (above 200 Hz), there is information about binary mergers and ringdowns, neutron star tidal deformation constraining the neutron star equation of state. Finally supernovae core collapses are also expected at high frequency.

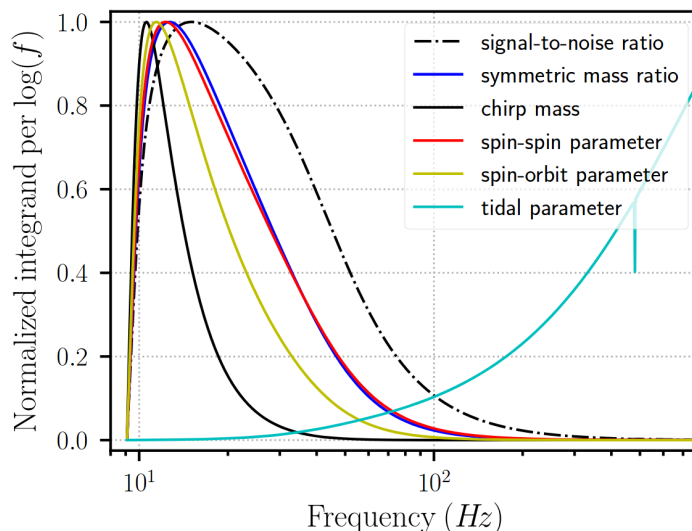


Figure 2.17 – Illustration of the frequencies at which information about intrinsic binary neutron star parameters are predominantly [62].

2.5.2 Noises reduction possibilities

Several solutions have been proposed to reduce some of the noise sources, and I won't describe them all. I will only give a brief overview of some solutions to reduce the mirror thermal noise, Newtonian noise and quantum noise. The technique we will use to reduce quantum noise will be presented in more details in Chapter 3.

Mirror thermal noise

The dominant mirror thermal noise is due to coating Brownian noise. To reduce it, we can use larger beam size on larger mirrors [64], or change coating materials [65]. Another solution studied for the 3rd generation of gravitational wave detectors is to use cryogenic mirrors with a temperature between 10 and 20 K [66]. This technique will be used on KAGRA detector in Japan [67].

Newtonian noise

Newtonian noise is due to change in the gravitational force acting on the mirror because of seismic noise. It is not possible to isolate the mirror from gravity. Consequently this noise will be very hard to reduce. An idea is to use an array of seismometers to monitor ground motion and infer from it the gravitational force change on the mirror [68].

Another idea is just trying to reduce gravitational field fluctuation selecting a quieter site and eventually going underground to reduce seismic noise and Newtonian noise [69].

Quantum noise

A promising idea to reduce quantum noise is to use squeezed light [70] and especially frequency dependent squeezing [71] that will be described in Chapter 3.

Other independent solutions are studied to reduce quantum noise. For instance theoretical studies have been carried out to try to use Einstein-Podolsky-Rosen (EPR) entanglement [72]. One advantage of this solution, is that it does not require to change the interferometers configurations, only the readout detection scheme using quantum correlations between two beams injected through the antisymmetric port.

Another solution is to completely change the way of measuring the effect of the passage of a gravitational wave using a speedmeter [73]. Several designs have been proposed but this would need to build a new km-scale infrastructure.

Chapter 3

Squeezing

As explained in the previous chapter, quantum noise is one of the main limiting noises of ground based interferometric gravitational wave detectors. The solution to reduce quantum noise I will focus on the use of *squeezed light*. It was first proposed by Caves in 1981 [74] and many proof-of-principle experiments were implemented to test its impact on gravitational wave detectors.

In this chapter I will give the basis of quantum optics necessary to understand the quantum nature of light and its application to reduce quantum noise in gravitational wave detectors. Then I will explain squeezed states of light in two equivalent formalisms to apprehend how it can be used in gravitational wave detectors and the challenge of frequency dependent squeezing. I will also present how squeezed states of light can be generated and how the losses impact the level of squeezing. Finally, I will give already existing experimental results of frequency independent and dependent squeezing.

3.1 Basics of quantum optics

3.1.1 Quantization of the electromagnetic field

The first step to study quantum features of light is to quantized the electromagnetic field starting from source-free Maxwell's equations. At a position \vec{r} and time t , the quantized electric field is [75]:

$$\vec{E}(\vec{r}, t) = i \sum_k \sqrt{\frac{\hbar\omega_k}{2\varepsilon_0}} \left[\hat{a}_k \vec{u}_k(\vec{r}) e^{-i\omega_k t} - \hat{a}_k^\dagger \vec{u}_k^*(\vec{r}) e^{i\omega_k t} \right], \quad (3.1)$$

where ω_k is the angular frequency of the mode k , ε_0 is the permittivity of free space, $\vec{u}_k(\vec{r})$ is the vector mode function, and \hat{a}_k and \hat{a}_k^\dagger are respectively the dimensionless boson annihilation and creation operators satisfying the boson commutation relations:

$$[\hat{a}_k, \hat{a}_{k'}] = 0, \quad (3.2)$$

$$[\hat{a}_k^\dagger, \hat{a}_{k'}^\dagger] = 0, \quad (3.3)$$

$$[\hat{a}_k, \hat{a}_{k'}^\dagger] = \delta_{kk'}, \quad (3.4)$$

where the commutator of two quantum mechanical operators \hat{A} and \hat{B} is defined by [76]:

$$[\hat{A}, \hat{B}] = \hat{A}\hat{B} - \hat{B}\hat{A}. \quad (3.5)$$

Experimentally, we can only measure observable operators. Nevertheless, according to Equation (3.4), $\hat{a}_k \neq \hat{a}_k^\dagger$. Thus the boson creation and annihilation operators are non-hermitian and are consequently not observables. It is possible to construct hermitian, i.e.

observable, operators from the creation and annihilation operators:

$$\hat{X}_1 = \hat{a} + \hat{a}^\dagger, \quad (3.6)$$

$$\hat{X}_2 = i(\hat{a}^\dagger - \hat{a}). \quad (3.7)$$

\hat{X}_1 and \hat{X}_2 are respectively known as the *amplitude quadrature* and *phase quadrature* operators. It is possible to describe an arbitrary quadrature operator \hat{X}_θ from a linear combination of \hat{X}_1 and \hat{X}_2 :

$$\hat{X}_\theta = \hat{X}_1 \cos \theta + \hat{X}_2 \sin \theta. \quad (3.8)$$

It is interesting to note that the amplitude and phase quadrature operators \hat{X}_1 and \hat{X}_2 are respectively proportional to the position and momentum operators \hat{q} and \hat{p} :

$$\hat{q} = \frac{\hat{a} + \hat{a}^\dagger}{\sqrt{2}}, \quad (3.9)$$

$$\hat{p} = i \frac{\hat{a}^\dagger - \hat{a}}{\sqrt{2}}. \quad (3.10)$$

3.1.2 Heisenberg uncertainty relation

Considering two observables \hat{O}_i and \hat{O}_j with standard deviation $\Delta\hat{O}$ defined as the root mean square of the variance:

$$\Delta\hat{O} = \sqrt{\langle\hat{O}^2\rangle - \langle\hat{O}\rangle^2}, \quad (3.11)$$

the *Heisenberg uncertainty relation* states that [76]:

$$\Delta\hat{O}_i\Delta\hat{O}_j \geq \frac{1}{2} |[\hat{O}_i, \hat{O}_j]|. \quad (3.12)$$

If the commutator of two observables is non zero, they are said to be *non-commuting observables*. The consequence of the Heisenberg uncertainty relation on two non-commuting observables is that their properties interfere with each other and it is not possible to measure their respective values simultaneously with complete accuracy. A measurement of one of the observable can change the result obtained in a subsequent measurement of the other one.

Considering the amplitude and phase quadratures, from Equations (3.4), (3.6) and (3.7), we can determined their commutator:

$$[\hat{X}_1, \hat{X}_2] = 2i, \quad (3.13)$$

which is non zero, meaning they are non-commuting observables. The Heisenberg uncertainty relation for the amplitude and phase quadrature is then:

$$\Delta\hat{X}_1\Delta\hat{X}_2 \geq 1. \quad (3.14)$$

The main consequence of Equation (3.14) is that amplitude and phase quadratures are defined with some dispersion, and this property lies at the very heart of quantum noise.

3.2 States of light

The uncertainty relation of Equation (3.14) gives rise to the fact that several states of light exist with different relations between phase and amplitude quadratures uncertainties. I will describe here some *minimum uncertainty states*, such as $\Delta\hat{X}_1\Delta\hat{X}_2 = 1$: the coherent state, the vacuum state and the squeezed state. I will give their main features and pictorial representations using *phasor diagrams*, that I will introduce through their classical forms.

3.2.1 Classical phasor diagram

Let's consider the classical electric field at a specific point in space of Equation (2.1):

$$\psi = \psi_0 e^{i\phi}, \quad (3.15)$$

where ψ_0 is the amplitude of the electric field and ϕ is a phase factor. It can be represented in the complex plane as an arrow of length ψ_0 and angle ϕ with respect to the real axis. It is also possible to rewrite ψ with respect to \hat{X}_1 and \hat{X}_2 [76]:

$$\psi \propto \cos(\phi)\hat{X}_1 + \sin(\phi)\hat{X}_2. \quad (3.16)$$

Using Equation (3.16), we can represent the electric field in the amplitude and phase quadratures plane as an arrow of length A proportional to ψ_0 and at an angle ϕ with respect to the amplitude quadrature axis \hat{X}_1 , as shown in Figure 3.1. This is called a classical phasor diagram.

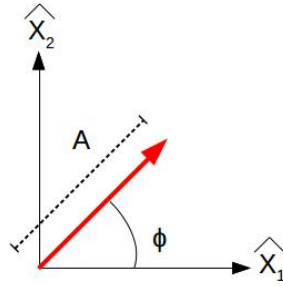


Figure 3.1 – Classical phasor diagram with amplitude A proportional to ψ_0 and phase ϕ represented in the amplitude and phase quadratures \hat{X}_1 and \hat{X}_2 plane.

3.2.2 The vacuum state

The vacuum state, noted $|0\rangle$ in Dirac notation is a state that has no coherent amplitude, containing no photons on average, $\alpha = 0$. Nevertheless, this does not mean that the amplitude and phase quadratures uncertainties are zero, violating the Heisenberg's relation. According to Equation (3.11), we have for the amplitude quadrature of the vacuum state:

$$\begin{aligned} \Delta\hat{X}_1 &= \sqrt{\langle\hat{X}_1^2\rangle - \langle\hat{X}_1\rangle^2} \\ &= \sqrt{\langle 0|\hat{X}_1^2|0\rangle - \langle 0|\hat{X}_1|0\rangle^2}. \end{aligned} \quad (3.17)$$

Then according to Equation (3.6):

$$\Delta\hat{X}_1 = \sqrt{\langle 0|(\hat{a} + \hat{a}^\dagger)^2|0\rangle - \langle 0|\hat{a} + \hat{a}^\dagger|0\rangle^2}. \quad (3.18)$$

Finally, using Equation (3.4), we get:

$$\Delta\hat{X}_1 = 1. \quad (3.19)$$

Similarly for the phase quadrature of the vacuum state, we obtain:

$$\Delta\hat{X}_2 = 1. \quad (3.20)$$

3.2.3 Coherent states

Coherent state is an important state of light for quantum optics experiments because it is a good approximation for the light generated by a frequency and intensity stabilized laser source as it is the quantum-mechanical equivalent of a classical monochromatic electromagnetic wave.

According to Heisenberg's relation, the amplitude and phase quadratures of the electromagnetic field are not known with an absolute precision. At best, for a coherent state we have:

$$\Delta\hat{X}_1 = \Delta\hat{X}_2 = 1. \quad (3.21)$$

This field can be represented in the amplitude and phase quadrature plane, i.e. a *quantum phasor diagram*, as a disc centered on the mean value of the field, of width the uncertainty on phase and amplitude as shown on the left of Figure 3.2. The trace of a typical measurement result of the electric field of a coherent state is represented on the right of Figure 3.2 showing the associated uncertainty on the phase and amplitude of the wave field.

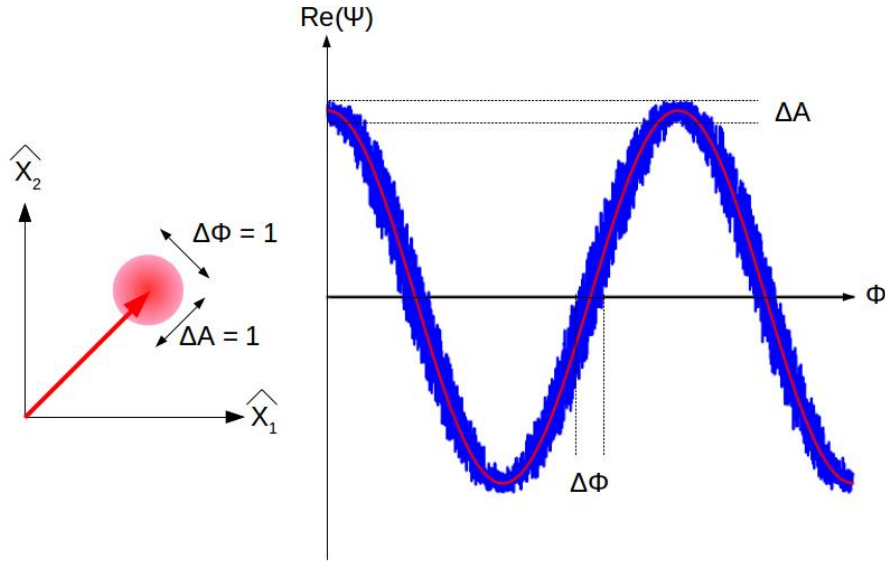


Figure 3.2 – Representation of a coherent state. *Left*: Quantum phasor diagram in the amplitude and phase quadratures. *Right*: Real part of the electric field featuring a typical measurement result of a coherent state.

In Dirac notation, coherent states are denoted by $|\alpha\rangle$, where α is a dimensionless complex number, sometimes called the *coherent amplitude* of the state. They are generated from the vacuum state $|0\rangle$ using the unitary displacement operator $\hat{D}(\alpha)$ [75]:

$$\hat{D}(\alpha) = \exp\left(\alpha\hat{a}^\dagger - \alpha^*\hat{a}\right), \quad (3.22)$$

$$|\alpha\rangle = \hat{D}(\alpha)|0\rangle, \quad (3.23)$$

where $\alpha = Ae^{i\phi}$ is a complex number.

Let's note some properties of the displacement operator $\hat{D}(\alpha)$ which will further be useful:

$$\hat{D}^\dagger(\alpha)\hat{D}(\alpha) = \hat{D}(\alpha)\hat{D}^\dagger(\alpha) = 1 \Rightarrow \hat{D}^\dagger(\alpha) = \hat{D}^{-1}(\alpha), \quad (3.24)$$

$$\hat{D}^\dagger(\alpha)\hat{a}\hat{D}(\alpha) = \hat{a} + \alpha, \quad (3.25)$$

$$\hat{D}^\dagger(\alpha)\hat{a}^\dagger\hat{D}(\alpha) = \hat{a}^\dagger + \alpha^*. \quad (3.26)$$

Coherent states are left eigenstates of the annihilation operator and right eigenstates of the creation operators [75]:

$$\hat{a}|\alpha\rangle = \alpha|\alpha\rangle, \quad (3.27)$$

$$\langle\alpha|\hat{a}^\dagger = \langle\alpha|\alpha^*. \quad (3.28)$$

Let's introduce the number operator \hat{N} to describe the mean photon number \bar{N} within a state. The mean optical power is then, as in Equation (2.36):

$$P_{opt} = \bar{N} \frac{\hbar\omega_0}{\tau}, \quad (3.29)$$

where τ is the observation time of the \bar{N} photons.

The number operator is defined from the creation and annihilation operators [76]:

$$\hat{N} = \hat{a}^\dagger \hat{a}. \quad (3.30)$$

Then, the mean photon number within a coherent state is:

$$\begin{aligned} \bar{N} &= \langle\hat{N}\rangle \\ &= \langle\alpha|\hat{a}^\dagger \hat{a}|\alpha\rangle \\ &= \alpha^* \alpha \\ &= |\alpha|^2. \end{aligned} \quad (3.31)$$

3.2.4 Squeezed states

As the Heisenberg uncertainty relation of Equation (3.14) involves a multiplicative term, coherent states are not the only type of minimum uncertainty state. It only requires that there is a minimum area for the phasor dispersion.

It is possible, for instance, to have a minimum uncertainty state increasing the uncertainty in one quadrature and decreasing it in the other. These kind of states are called *quadrature squeezed states*.

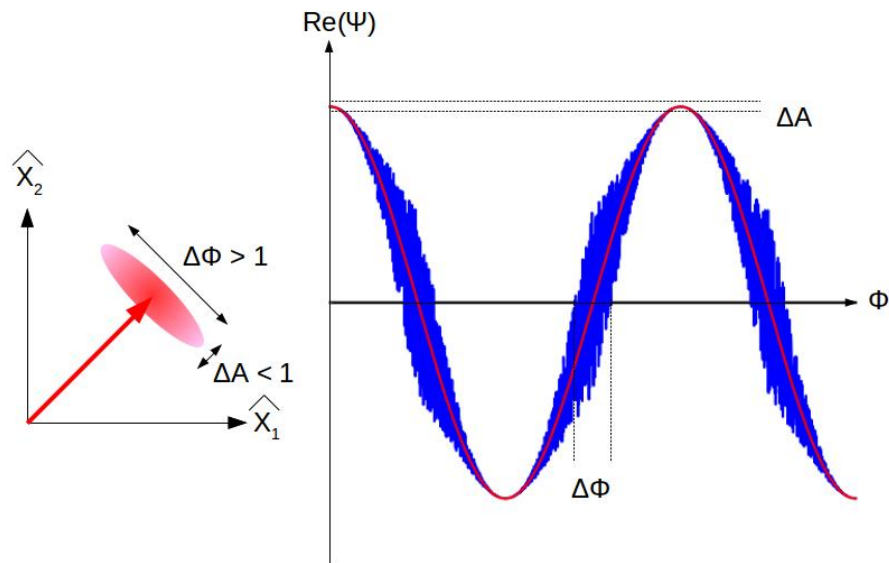


Figure 3.3 – Representation of an amplitude squeezed state. *Left*: Quantum phasor diagram in the amplitude and phase quadratures. *Right*: Real part of the electric field featuring a typical measurement result of an amplitude squeezed state.

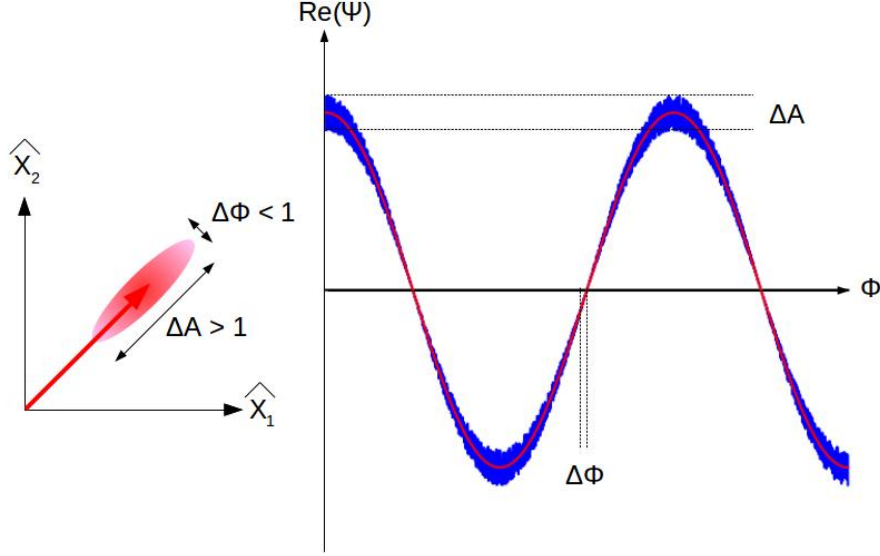


Figure 3.4 – Representation of a phase squeezed state. *Left*: Quantum phasor diagram in the amplitude and phase quadratures. *Right*: Real part of the electric field featuring a typical measurement result of a phase squeezed state.

Two forms of squeezed states are illustrated in Figures 3.3 and 3.4: *amplitude squeezed states* and *phase squeezed states* depending on the reduced quadrature. As a consequence, using such kind of light states, it is possible to reduce the measurement uncertainty in one quadrature at the cost of increasing the other one.

In Dirac notation, squeezed states are denoted $|\alpha, \epsilon\rangle$, where ϵ is the *squeezing parameter*. They are generated by first squeezing the vacuum through the unitary squeeze operator $\hat{S}(\epsilon)$ and then displacing it through the unitary displacement operator $\hat{D}(\alpha)$.

The squeezing operator is defined by [77]:

$$\hat{S}(\epsilon) = \exp\left(\frac{1}{2}[\epsilon^* \hat{a}^2 - \epsilon \hat{a}^{\dagger 2}]\right), \quad (3.32)$$

where $\epsilon = \sigma e^{2i\theta}$ with σ the squeeze factor giving the degree of squeezing and θ the quadrature angle of the squeezing. The squeezing operator acts by creating or destroying photons in pairs. These pairs of photons are the actual source of squeezing.

As for Equation (3.23), the squeezed state can be written:

$$|\alpha, \epsilon\rangle = \hat{D}(\alpha)\hat{S}(\epsilon)|0\rangle. \quad (3.33)$$

Some features of squeezed states can be noted. For any arbitrary quadrature \hat{X}_α and its complementary quadrature $\hat{X}_{\alpha+\pi/2}$, their uncertainty can be described by:

$$\Delta\hat{X}_\alpha = e^{-\sigma}, \quad (3.34)$$

$$\Delta\hat{X}_{\alpha+\pi/2} = e^{\sigma}. \quad (3.35)$$

satisfying the Heisenberg uncertainty relation.

Moreover, the mean photon number within a squeezed state can be determined using some properties of the squeezing operator $\hat{S}(\epsilon)$:

$$\hat{S}^\dagger(\epsilon)\hat{S}(\epsilon) = \hat{S}(\epsilon)\hat{S}^\dagger(\epsilon) = 1 \Rightarrow \hat{S}^\dagger(\epsilon) = \hat{S}^{-1}(\epsilon) = \hat{S}(-\epsilon), \quad (3.36)$$

$$\hat{S}^\dagger(\epsilon)\hat{a}\hat{S}(\epsilon) = \hat{a} \cosh(\sigma) - \hat{a}^\dagger e^{2i\theta} \sinh(\sigma), \quad (3.37)$$

$$\hat{S}^\dagger(\epsilon)\hat{a}^\dagger\hat{S}(\epsilon) = \hat{a}^\dagger \cosh(\sigma) - \hat{a} e^{-2i\theta} \sinh(\sigma). \quad (3.38)$$

Then using Equations (3.24), (3.25), (3.26), (3.36), (3.37) and (3.38), we have:

$$\begin{aligned}
 \bar{N} &= \langle \alpha, \epsilon | \hat{a}^\dagger \hat{a} | \alpha, \epsilon \rangle \\
 &= \langle 0 | \hat{S}^\dagger \hat{D}^\dagger \hat{a}^\dagger \hat{D} \hat{S} | 0 \rangle \\
 &= \langle 0 | \hat{S}^\dagger (\hat{a}^\dagger + \alpha^*) (\hat{a} + \alpha) \hat{S} | 0 \rangle \\
 &= |\alpha|^2 + \langle 0 | \hat{S}^\dagger \hat{a}^\dagger \hat{S} \hat{S}^\dagger \hat{a} \hat{S} | 0 \rangle \\
 &= |\alpha|^2 + \sinh^2(\sigma).
 \end{aligned} \tag{3.39}$$

Squeezed vacuum state

The vacuum state can also be squeezed to a *squeezed vacuum state*. According to Equation (3.39), the mean photon number within a squeezed vacuum state is non zero and depends on the squeeze factor σ . This non-zero mean photon number translates into optical power in the squeezed vacuum beam that can be interpreted as the energy necessary to obtain a squeezed vacuum state from a vacuum state.

3.3 Quantum noise in gravitational wave detectors

The quantum noise in gravitational wave detectors has been classically described in Section 2.3.3. I will here give a description of the shot noise and of the radiation pressure noise with respect to the amplitude and phase quadrature uncertainties and how they affect the detection of gravitational waves.

Quantum noise arises from vacuum fluctuations entering the interferometer through the antisymmetric port [60]. The fluctuations are amplified by the laser power inside the interferometer and then reflected back to the photodiode as shown in Figure 3.5.

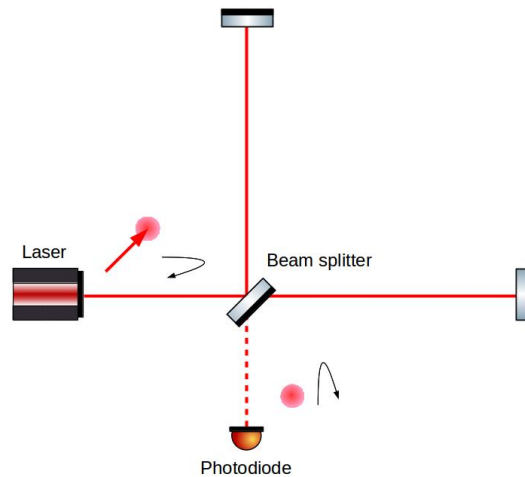


Figure 3.5 – Simple Michelson interferometer operated near dark fringe. The input laser is reflected back to the laser and the input vacuum field is reflected back to the photodiode.

As mentioned in Section 2.2.2, gravitational waves are detected as a phase shift $\Delta\phi_{GW}$. Consequently to detect them we have to compare the phase shift they induce to the noise in the phase quadrature.

The shot noise arises from the uncertainty in the arrival time of photons on the photodiode and from the uncertainty on the number of photon measured on the photodiode. Consequently the shot noise shows up in both phase and amplitude quadrature. It has the same uncertainty as the input vacuum field.

The radiation pressure noise arises from the differential fluctuations in the amplitude of the beam power on the mirrors that modifies the radiation pressure force exerted on the mirrors. As the radiation pressure force causes a displacement of the mirrors, its fluctuations causes variations in the position of the mirrors leading to a phase shift between the beams coming back from the two arms and combining on the beam splitter. Thus, the radiation pressure noise shows up in the phase quadrature but correlated to the amplitude quadrature fluctuations of the field. Moreover, as explained in Chapter 2, the radiation pressure force is inversely proportional to the square of the frequency, i.e. it is negligible compared to the shot noise at high frequencies.

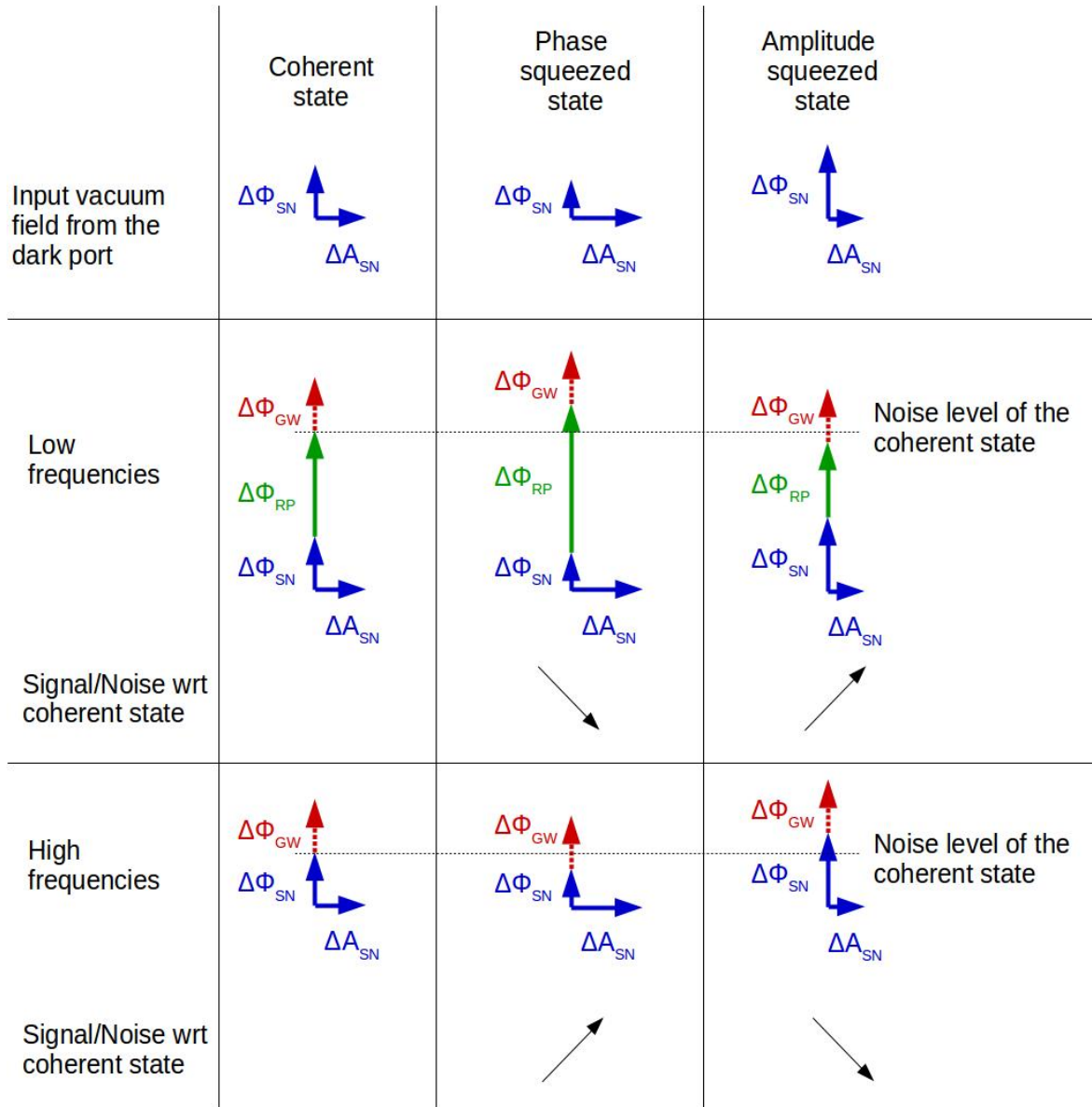


Figure 3.6 – Schematic view of the quantum noise decomposition at low (below $100Hz$) and high (above $100Hz$) frequencies for input vacuum fields from the antisymmetric port as coherent state, phase squeezed state and amplitude squeezed state. The blue arrows represent the amplitude A and phase Φ noise due to shot noise (SN), the green arrows represent the phase noise due to radiation pressure noise (RP) and the red arrows represent the phase change due to a gravitational wave (GW) that is independent of the type of vacuum field entering the dark port. The evolution of the signal to noise ratio from a coherent state to a phase or amplitude squeezed state is also represented. The aim of squeezing is to increase the signal to noise ratio.

These descriptions are summarized in the first column of Figure 3.6, corresponding to the usual state of the interferometer vacuum fluctuations entering through the antisymmetric port. The effect of the gravitational wave is shown with a red arrow in the phase quadrature. The shot noise is independent on the frequency and is represented with a blue arrow. The radiation pressure noise is inversely proportional to the frequency and correlated to the amplitude fluctuations. It is represented in green for the low frequency case and is not represented for high frequencies because it becomes negligible.

In this representation, what is important to detect gravitational waves is the relative length of the red arrow due to gravitational waves with respect to the sum of the noises green and blue arrow in the phase quadrature. One can see that as shown on the Advanced Virgo design simulated sensitivity curve in Figure 2.6, we have a better sensitivity at high frequencies than at low frequencies.

The two right columns represent the effect of the injection of phase or amplitude squeezed field from through antisymmetric port. One can see that a phase squeezed state improves the sensitivity at high frequencies but decreases it at low frequency and inversely for the amplitude squeezed state. This effect can also be represented with the detector sensitivity as shown in Figure 3.7.

These representations are done for a simple Michelson interferometer, but it can be extended to the full configuration of a dual recycled Fabry-Perot Michelson interferometer as Advanced Virgo and LIGO [78]. The total quantum noise is represented in Figure 3.8 for this full configuration without squeezing and with different types of squeezing.

The type of squeezing is defined by the squeezing angle θ of the ellipse with respect to the amplitude uncertainty axis. Consequently, $\theta = 0$ corresponds to an amplitude squeezed state, $\theta = -\pi/2$ corresponds to a phase squeezed state and $\theta = -\pi/4$ corresponds to an intermediate squeezed state improving the sensitivity around a narrow frequency band. An optimal squeezing angle $\theta_{\text{opt}}(f)$ can be defined for each frequency leading to an improved sensitivity in the whole bandwidth of the gravitational wave detector.

At high frequencies, gravitational waves detectors are shot noise limited, while radiation pressure noise is not completely the dominant noise at low frequencies. Consequently, it is possible to use phase squeezed states to improve the detector sensitivity. This has already been done and I will give an overview of the experimental work done on that subject in Section 3.7.

Nevertheless, as improvements are also done on reducing the other noises at low frequencies, it is important to reduce quantum noise at both low and high frequencies, using frequency dependent squeezing. This is the object of this thesis that will be introduced in Section 3.4.

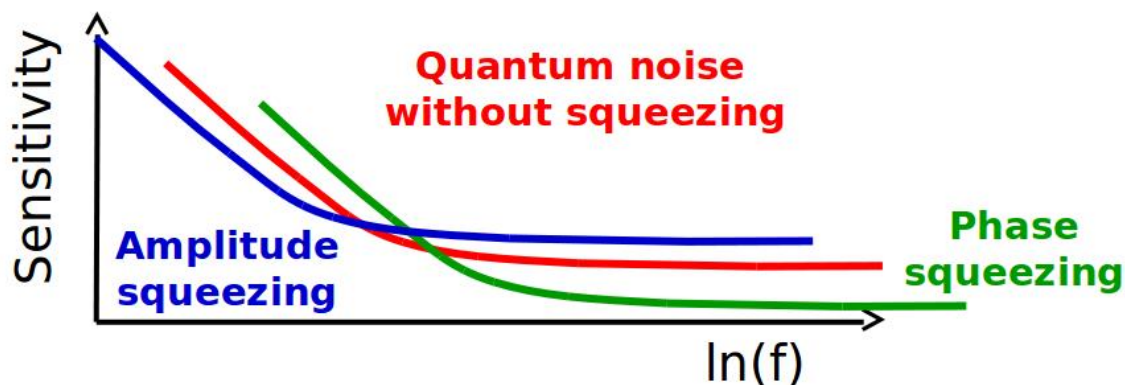


Figure 3.7 – Plot of the quantum noise limit sensitivity without squeezing and with phase and amplitude squeezing.

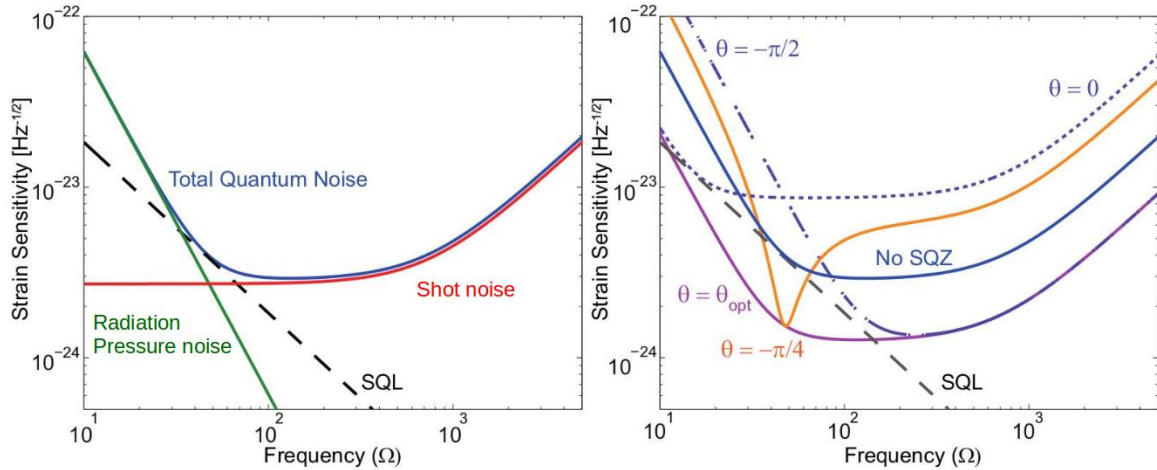


Figure 3.8 – *Left*: Total quantum noise and its contributions for a Dual Recycled Fabry-Perot Michelson interferometer. *Right*: Total quantum noise with injected squeezing at various squeezing angle [78].

3.4 Frequency dependent squeezing

Lasers emit photons one at a time, in the sense they are *one-photon devices*. Nevertheless it exists *two-photon devices* generating light by the simultaneous emission of two photons into two output modes. As we will see in Section 3.5.1, squeezed states are generated using a two-photon device.

To explain frequency dependent squeezing, I will first introduce the two-photon formalism presented by Caves and Schumaker in 1985 [79] and then explain how we can use a *filter cavity* to rotate the ellipse angle of the squeezed state in a frequency dependent way.

3.4.1 Two-photon formalism

The easiest way to understand the two-photon formalism is to start with the example of an *optical parametric generator*. As shown in Figure 3.9, this device converts a $2\omega_0$ pump photon onto *signal* and *idler* photons at frequencies $\omega_0 \pm \Omega$ with a correlated complex amplitude.

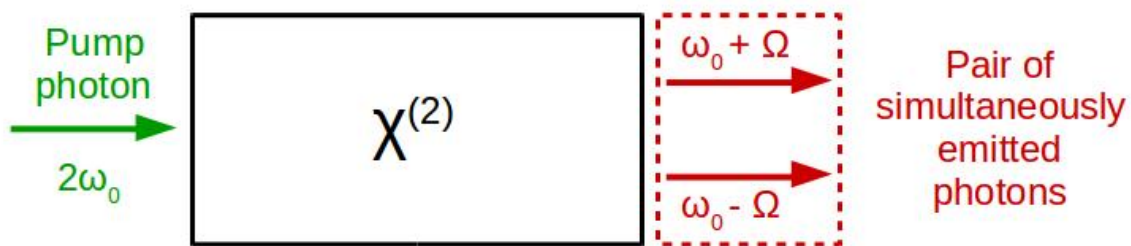


Figure 3.9 – Scheme of an optical parametric generator.

The fact that the two photons are emitted simultaneously as a correlated pair means that they cannot be described in terms of independently excited single modes as we usually do for laser light. In the two-photon formalism, a laser beam can be described as a classical carrier at frequency ω_0 and small quantum fluctuations at frequencies $\omega_0 \pm \Omega$ with $\Omega \ll \omega_0$. In the case of a vacuum state we only have the quantum fluctuations at frequencies $\pm\Omega$.

The electric field at the output of the optical parametric generator is given by [80]:

$$E(t) = E_1(t) \cos(\omega_0 t) + E_2(t) \sin(\omega_0 t) \quad (3.40)$$

$$= (\cos(\omega_0 t) \sin(\omega_0 t)) \begin{pmatrix} E_1(t) \\ E_2(t) \end{pmatrix}, \quad (3.41)$$

where $E_1(t)$ and $E_2(t)$ are real quadrature phases describing modulation of waves $\cos(\omega_0 t)$ and $\sin(\omega_0 t)$. We can write the quadrature phases in terms of their Fourier components [79]:

$$E_m(t) = \int \frac{d\Omega}{2\pi} \left[\tilde{E}_m(\Omega) e^{-i\Omega t} + \tilde{E}_m^*(\Omega) e^{i\Omega t} \right], \quad m = 1, 2, \quad (3.42)$$

where the Fourier components can be written:

$$\tilde{E}_1(\Omega) = \tilde{E}(\omega_0 + \Omega) + \tilde{E}^*(\omega_0 - \Omega), \quad (3.43)$$

$$\tilde{E}_2(\Omega) = -i\tilde{E}(\omega_0 + \Omega) + i\tilde{E}^*(\omega_0 - \Omega). \quad (3.44)$$

In this description, the fluctuations in the quadrature phases are due to random emission of pairs of photons, exciting the quadrature phases at various modulation frequencies Ω but the fluctuations in the electric field are not distributed randomly in phase relatively to the carrier frequency ω_0 .

It is useful to define a conversion between the one-photon and the two-photon pictures by replacing E by:

$$\mathbf{E} = \begin{pmatrix} E_1 \\ E_2 \end{pmatrix}. \quad (3.45)$$

For an arbitrary optical system, we then define transfer coefficients for positive and negative sidebands, $\tau_+ = \tau(\Omega)$ and $\tau_- = \tau(-\Omega)$ to construct the two-photon transfer matrix by [81]:

$$\mathbf{T} = \mathbf{A}_2 \begin{pmatrix} \tau_+ & 0 \\ 0 & \tau_-^* \end{pmatrix} \mathbf{A}_2^{-1}, \quad (3.46)$$

with:

$$\mathbf{A}_2 = \frac{1}{\sqrt{2}} \begin{pmatrix} 1 & 1 \\ -i & i \end{pmatrix} \text{ and } \mathbf{A}_2^{-1} = \frac{1}{\sqrt{2}} \begin{pmatrix} 1 & i \\ 1 & -i \end{pmatrix}. \quad (3.47)$$

An input field \mathbf{E}_i on the optical system is transformed into an output field \mathbf{E}_o such that:

$$\mathbf{E}_o = \mathbf{T}\mathbf{E}_i. \quad (3.48)$$

Finally, the two photon formalism can be constructed in an similar way than the one-photon formalism [82]. The annihilation and creation operators for the two modes $\omega_0 \pm \Omega$ are noted \hat{a}_\pm and \hat{a}_\pm^\dagger . They satisfy the boson commutation relations of Equations (3.2), (3.3) and (3.4).

Similarly to Equation (3.32), we can define the *two-mode squeeze operator* by [82]:

$$\hat{S}(\epsilon) = \exp\left(\epsilon^* a_+ a_- - \epsilon a_+^\dagger a_-^\dagger\right) = \exp\left[\sigma \left(a_+ a_- e^{-2i\theta} - a_+^\dagger a_-^\dagger e^{2i\theta}\right)\right] = \hat{S}(\sigma, \theta). \quad (3.49)$$

3.4.2 Filter cavity

A filter cavity is a Fabry-Perot cavity for which the one-photon transfer coefficient is just the amplitude reflectivity of the cavity which can be rewritten from Equation (2.66):

$$r_{fc}(\Omega) = r_1 - \frac{t_1^2}{r_1} \frac{r_{rt} e^{-i\Phi(\Omega)}}{1 - r_{rt} e^{-i\Phi(\Omega)}}, \quad (3.50)$$

with $r_{rt} = r_1 r_2$ the round-trip reflectivity and $\Phi(\Omega)$ the round-trip phase:

$$\Phi(\Omega) = (\Omega - \Delta\omega_{fc}) \frac{2L_{fc}}{c}. \quad (3.51)$$

L_{fc} is the length of the filter cavity and $\Delta\omega_{fc} = \omega_{fc} - \omega_0$ is the cavity detuning, i.e. the difference between the laser frequency ω_0 and the cavity resonance frequency ω_{fc} .

To understand the effect of a filter cavity on a squeezed field we need to convert its one-photon response into the two-photon picture following Equation (3.46) with the coefficient for the positive and negative sidebands $r_+ = r_{fc}(\Omega)$ and $r_- = r_{fc}(-\Omega)$:

$$\mathbf{T}_{fc} = \mathbf{A}_2 \begin{pmatrix} r_+ & 0 \\ 0 & r_-^* \end{pmatrix} \mathbf{A}_2^{-1}. \quad (3.52)$$

This expression can be rewritten using the complex phase α_{\pm} and magnitude ρ_{\pm} of the coefficients r_{\pm} :

$$\alpha_{\pm} = \arg(r_{\pm}) \text{ and } \rho_{\pm} = |r_{\pm}|, \quad (3.53)$$

and defining:

$$\alpha_p = \frac{\alpha_+ \pm \alpha_-}{2} \text{ and } \rho_p = \frac{\rho_+ \pm \rho_-}{2}. \quad (3.54)$$

Finally, the transfer matrix of the filter cavity is [83]:

$$\mathbf{T}_{fc} = e^{i\alpha_m} \mathbf{R}_{\alpha_p} \left(\rho_p \mathbf{I} - i\rho_m \mathbf{R}_{\frac{\pi}{2}} \right), \quad (3.55)$$

where we define:

$$\mathbf{R}_{\theta} = \begin{pmatrix} \cos(\theta) & -\sin(\theta) \\ \sin(\theta) & \cos(\theta) \end{pmatrix} \text{ and } \mathbf{I} = \begin{pmatrix} 1 & 0 \\ 0 & 1 \end{pmatrix}. \quad (3.56)$$

Let's now analyze Equation (3.55). The first term $e^{i\alpha_m} \mathbf{R}_{\alpha_p}$ corresponds to the rotation operation of angle α_p and an overall phase α_m for a lossless filter cavity. Consequently, the effect of the filter cavity is to introduce a **frequency dependent rotation** between the upper and lower sidebands leading to a rotation of the squeezing ellipse angle according to the frequency: *frequency dependent squeezing*.

Thus the ellipse of the squeezing rotates with an angle $\alpha_p(\Omega) \neq 0$ if $\alpha_+ \neq -\alpha_-$ according to Equation (3.54). If the cavity is not detuned, i.e. $\Delta\omega_{fc} = 0$, we have:

$$\Phi(\Omega) = -\Phi(-\Omega) \Rightarrow r_+ = r_-^* \Rightarrow \alpha_+ = \alpha_-. \quad (3.57)$$

This is why we need to have a detuned cavity to get frequency dependent squeezing.

For a lossless filter cavity, the expression of the squeezed quadrature rotation $\alpha_p(\Omega)$ is [83]:

$$\alpha_p(\Omega) = \arctan \left(\frac{2\gamma_{fc}\Delta\omega_{fc}}{\gamma_{fc}^2 - \Delta\omega_{fc}^2 + \Omega^2} \right), \quad (3.58)$$

with γ_{fc} the half-width-half-maximum-power linewidth such that, according to Equation (2.74):

$$\gamma_{fc} = 2\pi \frac{\delta\nu}{2} = \frac{\pi c}{2L\mathcal{F}}. \quad (3.59)$$

From Equation (3.58), one can say that:

- to have a squeezed quadrature rotation of $\pi/2$ between $\Omega = 0$ and $\Omega = +\infty$ we need to have an *optimally detuned filter cavity* with:

$$\Delta\omega_{fc} = \gamma_{fc} \quad (3.60)$$

- if $\Delta\omega_{fc} > \gamma_{fc}$, we obtain a rotation of more than $\pi/2$,
- if $\Delta\omega_{fc} < \gamma_{fc}$, we obtain a rotation of less than $\pi/2$.

Moreover in the case of an *optimally detuned filter cavity*, the $\pi/4$ rotation of the squeezing ellipse occurs at a frequency Ω_t defined by:

$$\Omega_t = \sqrt{2}\gamma_{fc}. \quad (3.61)$$

Consequently we can adjust the frequency at which the tilt occurs by changing the length of the filter cavity and its finesse. To have a shift at low frequency, which is what matters for gravitational wave detectors, we have to use long and high finesse filter cavities. In Figure 3.10, I represented the squeezed rotation quadrature $\alpha_p(f)$ for a 50 m-long filter cavity with a finesse $\mathcal{F} = 3000$ and $\mathcal{F} = 30000$. The second one leads to a tilt frequency $f_t = 70.7$ Hz corresponding to the need for gravitational wave detectors.

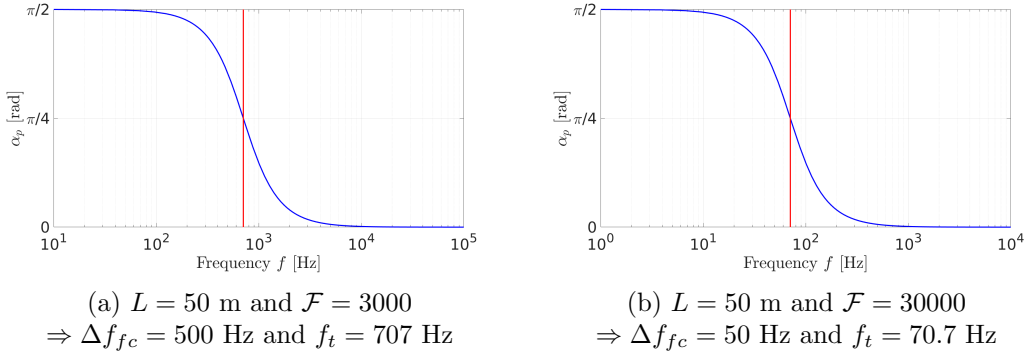


Figure 3.10 – Squeezed rotation quadrature $\alpha_p(f)$ for two optimally detuned filter cavities. The red line corresponds to the tilt frequency of the squeezing angle.

Finally, to analyze the parenthesis of Equation (3.55), I will first give an expression of ρ_{\pm} :

$$\rho_{\pm} = \sqrt{1 - \frac{(2 - \varepsilon)\varepsilon}{1 + \xi^2(\pm\Omega)}}, \quad (3.62)$$

with:

$$\varepsilon = \frac{2\Lambda_{rt}^2}{t_1^2 + \Lambda_{rt}^2} \text{ and } \xi(\Omega) = \frac{2\Phi(\Omega)}{t_1^2 + \Lambda_{rt}^2}, \quad (3.63)$$

where Λ_{rt}^2 accounts for the power lost during one round-trip in the cavity and $\Phi(\Omega) \ll 1$.

Consequently, for a lossless filter cavity we have $\rho_p = 1$ and $\rho_m = 0$ and the filter cavity only rotates the squeezing ellipse without any other change. Nevertheless, any loss will introduce mixing between the quadratures of the squeezed state leading to antisqueezing. Thus, to maximize the benefit from squeezed states we need to **minimize all sources optical loss**.

3.5 Experimental squeezed states of light

3.5.1 Generation of squeezed states

Squeezed states are produced through second order non-linear interaction in a crystal. First, I will recall the effect on a medium of an electric field such as laser light. I will then introduce non linear and anisotropic effects to explain possible second order non-linear interactions. Finally, I will present second order non linear processes including squeezed state generation.

Dielectric response of a medium

An electric field interacting with a medium has the effect of exerting a force on the electrons of the atoms composing the medium. The electrons oscillate around the nucleus as dipoles

at the angular frequency of the incoming electric field ω_0 . In turn, these electrons radiate an electric field at angular frequency ω_0 leading to the propagation of the electric field in the medium.

The electric displacement \vec{D} is related to the electric field \vec{E} and the electric polarization \vec{P} by:

$$\vec{D} = \epsilon_0 \vec{E} + \vec{P}, \quad (3.64)$$

where ϵ_0 is the electric permittivity of free space. In an isotropic medium, under low power electric field, the electric polarization can be written:

$$\vec{P} = \epsilon_0 \chi_e \vec{E}, \quad (3.65)$$

with χ_e the electric susceptibility of the medium. This expression conveys the fact that the microscopic dipoles align along the direction of the incoming electric field.

In an anisotropic medium, there are privileged directions for the displacement of the electrons. Consequently the electric polarization acquired by the medium depends on the direction of \vec{E} . This can be expressed by replacing the electric susceptibility χ_e by a tensor χ :

$$\chi = \begin{pmatrix} \chi_{xx} & \chi_{xy} & \chi_{xz} \\ \chi_{yx} & \chi_{yy} & \chi_{yz} \\ \chi_{zx} & \chi_{zy} & \chi_{zz} \end{pmatrix}. \quad (3.66)$$

Moreover, in nonlinear crystals the polarization depends on higher powers of the electric field. Writing it in term of modulus P and E , we have:

$$P = \epsilon_0 \left[\chi^{(1)} E + \chi^{(2)} E^2 + \chi^{(3)} E^3 + \dots \right]. \quad (3.67)$$

We can identify the first term to the linear one, thus $\chi^{(1)} = \chi_e$. The other terms describe the nonlinear response of the crystal. The third order term in E^3 and higher orders are orders of magnitude lower than the second order term in E^2 we are interested in.

Second order interactions

Consider a high power electric field, composed of cosinusoidal waves at angular frequency ω_1 and ω_2 with amplitude E_1 and E_2 , impinging on a nonlinear crystal. The second order nonlinear polarization term is then:

$$\begin{aligned} P^{(2)}(t) &= \epsilon_0 \chi^{(2)} [E_1 \cos(\omega_1 t) + E_2 \cos(\omega_2 t)]^2 \\ &= \epsilon_0 \chi^{(2)} \left\{ E_1^2 + E_2^2 + \frac{1}{2} [E_1^2 \cos(2\omega_1 t) + E_2^2 \cos(2\omega_2 t) \right. \\ &\quad \left. + E_1 E_2 \cos((\omega_1 + \omega_2)t) + E_1 E_2 \cos((\omega_1 - \omega_2)t)] \right\} \end{aligned} \quad (3.68)$$

According to Equation (3.68), the response of the nonlinear crystal to a high power field is to generate an oscillating polarization at the sum and difference frequencies of the input fields, thus emitting light at angular frequencies $(\omega_1 + \omega_2)$ and $|\omega_1 - \omega_2|$. These processes are called **sum** and **difference frequency generation** (SFG and DFG). The photons effectively emitted and transmitted through the crystal depend on the properties of the medium and must respect the conservation of energy.

The sum frequency mixing is an *up-conversion process*, that means that photons at lower frequency ω_1 and ω_2 combine to produce photons at higher frequency. In the special case where $\omega_1 = \omega_2$ the sum frequency is at twice the input frequency leading to **frequency doubling** often called **second harmonic generation**. This process is represented in Figure 3.11.

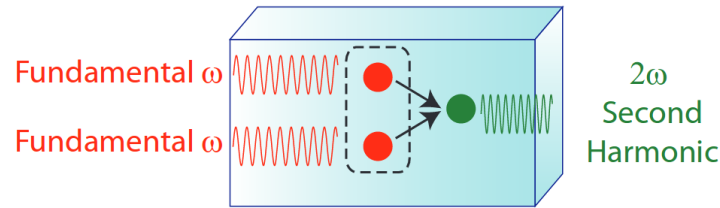


Figure 3.11 – Scheme of a second harmonic generator converting 2 photons at angular frequency ω into a photon at angular frequency 2ω [84].

Optical parametric oscillator

Squeezed states are produced using parametric *down-conversion process* in a non linear crystal. This device is called **Optical Parametric Oscillator (OPO)** and is represented in Figure 3.12. Taking the notation of Equation (3.68), $\omega_1 = 2\omega$ is the angular frequency of the *pump* beam and $\omega_2 = \delta$ is the angular frequency of photons produced by vacuum fluctuations.

Here we are interested in the difference frequency mixing leading to the emission of a photon of angular frequency $\omega_1 - \omega_2 = 2\omega - \delta$. For energy conservation, a photon of angular frequency δ is also emitted. These two photons form a correlated sideband pair as the one introduced in Section 3.4.1 to define the two-photon formalism.

The photon pairs reduce the quantum noise in the output field. They are the source of squeezing. The alignment of the correlated sidebands pairs depends on the phase of the pump field. Thus, a rotation of the pump phase leads to a rotation of the squeezing quadrature.

Vacuum fluctuations exist at all frequencies. Consequently the angular frequency δ is fluctuating randomly and the generated $2\omega - \delta$ fluctuates with it. It can be rewritten with respect to the carrier and sideband frequencies used in Section 3.4.1:

$$\delta = \omega_0 + \Omega \quad (3.69)$$

$$2\omega - \delta = \omega_0 - \Omega, \quad (3.70)$$

where ω_0 corresponds to the angular frequency ω in Figure 3.12. The names of upper and lower sidebands come from these two equations.

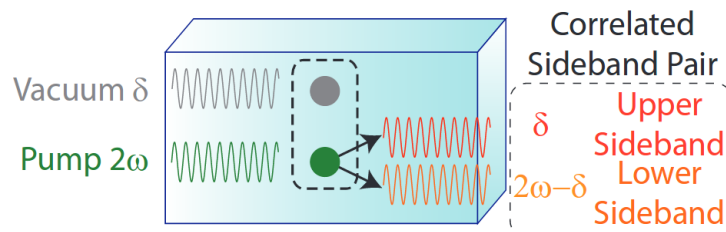


Figure 3.12 – Scheme of an optical parametric oscillator [84].

Random fluctuations of δ lead to random fluctuations of Ω . As a consequence, an OPO generates correlated photon pairs with random frequency separations from the carrier, changing over time and hence populating all frequencies.

Most of the time, the nonlinear medium generating optical parametric oscillation is placed inside an optical cavity to enhance the squeezing signal by increasing the number of passages inside the crystal. Only frequencies which are resonant inside the cavity will be enhanced.

Phase matching

Until now, I only considered energy conservation. Nevertheless, another quantity has to be conserved: momentum. If we note \vec{k}_p , \vec{k}_s and \vec{k}_i the wave-vectors of the pump, upper sideband (*signal*) and lower sideband (*idler*) photons, they must obey the relation:

$$\vec{k}_p = \vec{k}_s + \vec{k}_i. \quad (3.71)$$

More generally, the sum of the input wave-vectors must be equal to the output ones. If we consider that the input and output fields are propagating collinearly with each other, we can drop the vector notation and obtain that all photons must propagate with the same phase velocity through the non linear media. This means that all photons emitted must see the same refractive index. For instance in second harmonic generator we must have $n^{(\omega)} = n^{(2\omega)}$.

The refractive index of a crystal changes with the frequency. Consequently, most of the time, photons at different frequencies travel at different speeds and are not phase matched. However it is possible to achieve good phase matching in a dispersive medium using the birefringence of the nonlinear crystal. The birefringence is a property of some anisotropic medium leading to a dependence of the refractive index on the incoming field polarization. In this case the phase matching depends on the angle of incidence of the incoming photons on the crystal.

The phase mismatch Δk is defined as the difference between input and output photons wave-vectors magnitudes:

$$\Delta k = \sum_{\text{input}} k_{\text{input}} - \sum_{\text{output}} k_{\text{output}}. \quad (3.72)$$

To understand the impact of phase mismatch on the generated field power, we can take the example of a second harmonic generator. The expression of the generated field power at 2ω , $\mathcal{P}^{(2\omega)}$, depends on the input field power at ω , $\mathcal{P}^{(\omega)}$ as [85]:

$$\mathcal{P}^{(2\omega)} = \frac{1}{2} \frac{(\mu_0 c)^3}{n^{(2\omega)}(n^{(\omega)})^2} \frac{d^2 l^2 (2\omega)^2}{S} \left(\mathcal{P}^{(\omega)}\right)^2 \frac{\sin^2\left(\frac{\Delta k l}{2}\right)}{\left(\frac{\Delta k l}{2}\right)^2}, \quad (3.73)$$

where μ_0 is the permeability of free space, d a nonlinear coefficient, l the distance inside the crystal and S the area of the beam inside the crystal. The variation of this power with respect to phase mismatch is represented in Figure 3.13. One can see that moving away from perfect matching, corresponding to $\Delta k = 0$ leads to a large decrease of the generated second harmonic power and consequently to the efficiency of the non linear process.

Quasi-phase matching

Another solution to achieve a quasi-phase matching is to periodically invert the non linear coefficient of the crystal. This method is called *periodic poling* and allows for the input and output fields to have the same polarization which is not the case when using birefringence.

Taking again the example of a second harmonic generator, the refractive index of the fundamental and second harmonic beams are not the same inside the crystal. Note n_1 the refractive index of the fundamental beam at $\lambda_0 = 1064$ nm and n_2 the refractive index of the second harmonic beam at $\lambda_2 = 532$ nm. We can define the coherence length l_c :

$$l_c = \frac{\lambda_0}{4(n_2 - n_1)}. \quad (3.74)$$

The coherence length is the distance over which the second harmonic field accumulates a phase shift of π with respect to the fundamental field. Consequently, for non poled material, if $n_1 \neq n_2$, after two coherence lengths, the newly generated photons interfere destructively

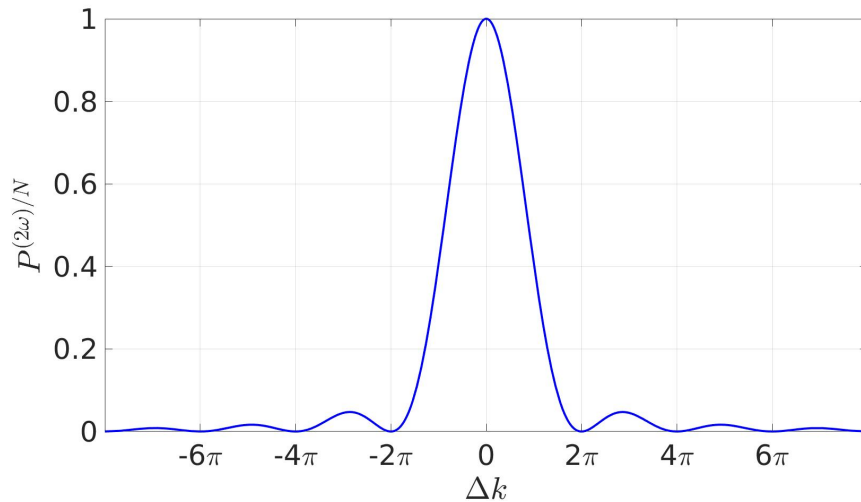


Figure 3.13 – Generated power field by a second harmonic generator with respect to phase mismatch Δk , at a distance $l = 1$ inside the crystal, normalized by the factor before the sinc function of Equation (3.73).

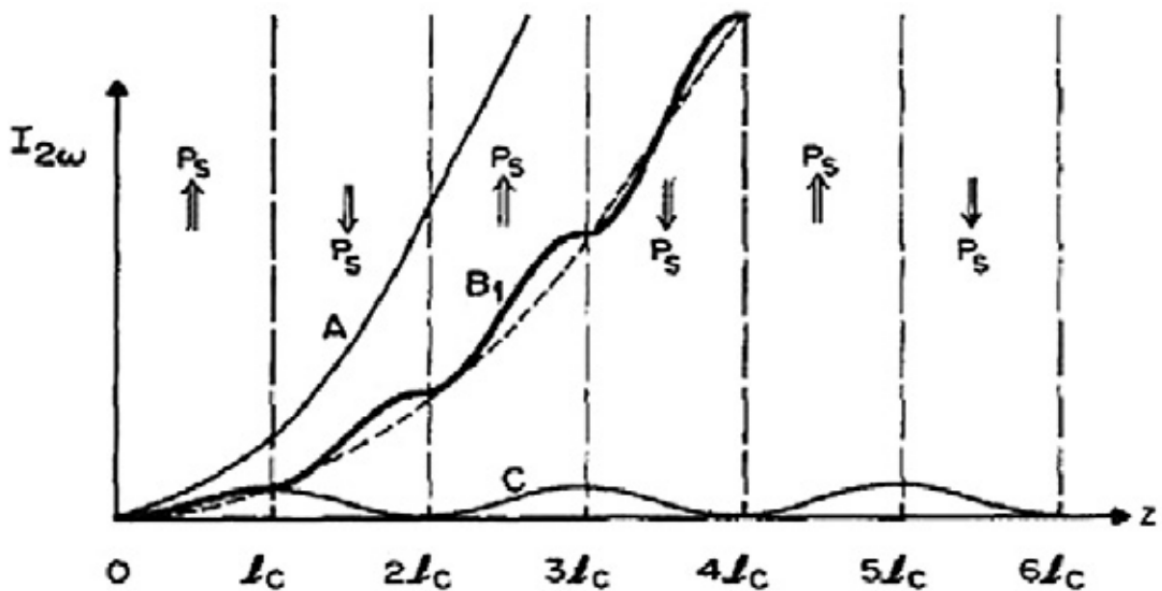


Figure 3.14 – Plot of the second harmonic beam intensity as a function of the distance in a nonlinear crystal. A: Perfect phase matching in a uniformly poled crystal. B: Quasi-phase matching by flipping the sign of the spontaneous polarization of the crystal every coherence length. C: Non-phase matched interaction [86].

with the previously generated photons, leading to no power on the second harmonic beam as shown on case C of Figure 3.14.

Nevertheless, by flipping the orientation of the polarization of the crystal every coherence length the newly generated photons interfere constructively with the previously generated photons increasing the number of second harmonic photons generated by the nonlinear process through the crystal.

3.5.2 Detection of squeezed states

As the squeezed field is generated through a second order nonlinear process, it has a low optical power making difficult its direct detection. A solution to measure it is to use a

balanced homodyne detection scheme amplifying the low-power squeezed signal with a high power *local oscillator*.

A general balanced homodyne detection scheme is represented in Figure 3.15. A 50:50 beam splitter mixes two fields: the one we want to measure, squeezed field in our case, noted A and a high power local oscillator, noted B . The relative phase between the two fields is noted ϕ . Two photodetectors measure the resulting fields C and D and their measurements are combined via electronic subtraction and addition to obtain a difference photocurrent i_- and a sum photocurrent i_+ which give information about the properties of the input fields.

In the balanced homodyne detection scheme, the local oscillator is a bright coherent field at the same wavelength as the signal we want to measure.

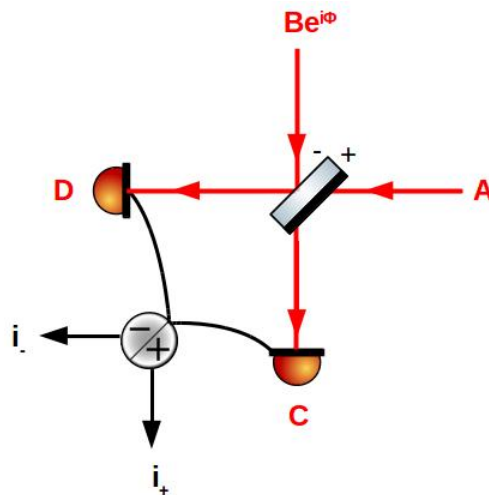


Figure 3.15 – Scheme of a balanced homodyne detection. A is the low power squeezed signal we want to measure and B is the high power local oscillator field with a relative phase ϕ with respect to A .

According to Figure 3.15, and using the convention defined in Section 2.2.2, we can write the two output fields C and D with respect to input fields A and B :

$$C = \frac{1}{\sqrt{2}} (A + Be^{i\phi}), \quad (3.75)$$

$$D = \frac{1}{\sqrt{2}} (A - Be^{i\phi}), \quad (3.76)$$

and the difference and sum photocurrents are given by:

$$i_- = C^\dagger C - D^\dagger D, \quad (3.77)$$

$$i_+ = C^\dagger C + D^\dagger D. \quad (3.78)$$

Then, the input fields A and B can be linearized separating them into two components, a steady-state one and fluctuations:

$$A = \bar{A} + \delta A, \quad (3.79)$$

$$B = \bar{B} + \delta B. \quad (3.80)$$

Now, we can rewrite the photocurrents in terms of the linearized A and B :

$$i_- = (\bar{A} + \delta A)^\dagger (\bar{B} + \delta B) e^{i\phi} + (\bar{B} + \delta B)^\dagger e^{-i\phi} (\bar{A} + \delta A), \quad (3.81)$$

$$i_+ = (\bar{A} + \delta A)^\dagger (\bar{A} + \delta A) + (\bar{B} + \delta B)^\dagger (\bar{B} + \delta B). \quad (3.82)$$

As δA and δB are negligible compared to \bar{A} and \bar{B} , we neglect the cross fluctuation terms such as $\delta A \delta B$. We also assume that the mean field amplitudes are real, i.e. $\bar{A} = \bar{A}^*$ and

$\bar{B} = \bar{B}^*$. Finally the local oscillator has a much higher amplitude than that of the signal we want to measure. Thus we have $\bar{A} \ll \bar{B}$. Under these assumptions the photocurrents become:

$$i_- \simeq 2\bar{A}\bar{B} \cos(\phi) + \bar{B} \left(\delta A^\dagger e^{i\phi} + \delta A e^{-i\phi} \right), \quad (3.83)$$

$$i_+ \simeq \bar{B}^2 + \bar{B} \left(\delta B + \delta B^\dagger \right). \quad (3.84)$$

Finally we can use the definitions of the quadratures of Equations (3.6) and (3.7), with the notations X_1^A and X_2^A for the A field and X_1^B and X_2^B for the B field and the fluctuations associated. We obtain:

$$i_- \simeq 2\bar{A}\bar{B} \cos(\phi) + \bar{B} \left(\delta X_1^A \cos(\phi) + \delta X_2^A \sin(\phi) \right), \quad (3.85)$$

$$i_+ \simeq \bar{B}^2 + \bar{B} \delta X_1^B. \quad (3.86)$$

According to Equation (3.85), the difference of the photocurrents contains information about the amplitude and phase quadratures of the signal we want to measure, amplified by the local oscillator field. Moreover, the observed quadrature depends on the relative phase ϕ of the local oscillator with respect to the signal. This phase can be tuned and this is how we can completely characterized the squeezed state quadratures.

Concerning the sum of the photocurrents, according to Equation (3.86), its measure is equivalent to a direct measurement of the local oscillator field.

3.6 Squeezing degradation budget

Losses are an important factor to take into account when designing a squeezing experiment as any source of loss will degrade the squeezing level. There are several sources of squeezing degradation arising at different points of the squeezing propagation that I will present now using a model adapted from [83].

To compute the quantum noise, we propagate two different vacuum fields through the optical system: v_1 which passes through the squeezer and becomes the squeezed field and v_2 which enters after the squeezer.

$$v_1 = v_2 = \sqrt{2\hbar\omega_0} \mathbf{I}, \quad (3.87)$$

where \mathbf{I} is the identity matrix. Optical systems can be defined by 2×2 transfer matrix \mathbf{T} . The interaction v_{out} of the vacuum fields with an optical system is then obtained by multiplying its transfer matrix \mathbf{T} by the squeezed field v_{in} :

$$v_{out} = \mathbf{T} v_{in}. \quad (3.88)$$

The noise N on the homodyne detector can be written [83]:

$$N = |\bar{\mathbf{b}}_\phi v|^2, \quad (3.89)$$

where v is the vacuum field that recombines on the homodyne detection with the local oscillator and

$$\bar{\mathbf{b}}_\theta = A_{LO} \begin{pmatrix} \cos(\theta) & \sin(\theta) \end{pmatrix}, \quad (3.90)$$

is the local oscillator field with amplitude A_{LO} and relative phase θ with the vacuum field v determining the readout quadrature. If there are multiple vacuum fields beating with the local oscillator on the homodyne detection, the total noise is then the sum of the contributions due to each vacuum source:

$$N = \sum_n |\bar{\mathbf{b}}_\theta \mathbf{T}_n v_n|^2. \quad (3.91)$$

The shot noise level is obtained directly applying the local oscillator to the vacuum field without interaction through optical system:

$$N_{SN} = |\bar{\mathbf{b}}_{\theta} v_1|^2 = 2\hbar\omega_0 A_{LO}^2. \quad (3.92)$$

Finally, we define the normalized noise power \hat{N} used to characterize the squeezing degradation by:

$$\hat{N} = \frac{N}{N_{SN}}. \quad (3.93)$$

I will now present the different sources of losses and how they are taken into account in the noise budget and I will conclude this section showing the squeezing degradation they give rise and a noise budget for achievable losses values.

3.6.1 Injection and readout losses

The optics on the squeezing path are not perfect. These imperfections can cause scattering and absorption leading to losses for the squeezed field. Moreover the residual transmission of the steering mirrors is added to these losses. These losses can be seen as a loss of one entangled photon of a pair.

Generally, the losses outside the filter cavity are frequency independent. In the absence of non linear element between the squeezer and the readout, there is no mixing between upper and lower sidebands and we can combine all input losses together.

We define the injection losses Λ_{inj}^2 which represent the total power loss between the squeezer and the homodyne detection, and the readout losses Λ_{ro}^2 which represent the total power loss at the homodyne readout, coming from the non perfect photodiodes quantum efficiency.

3.6.2 Filter cavity losses

The effect of the filter cavity is described in Section 3.4.2 in the absence of losses. We define the round trip losses of the cavity Λ_{rt}^2 by:

$$\Lambda_{rt}^2 = L_1 + L_2 + T_2, \quad (3.94)$$

where L_1 and L_2 account for the absorption and scattering power losses respectively at the input and end mirrors of the filter cavity and T_2 is the power transmissivity of the end mirror. Taking into account the power round trip losses we can approximate the round-trip reflectivity r_{rt} of Equation (3.50) by:

$$r_{rt} \simeq 1 - \frac{T_1 + \Lambda_{rt}^2}{2}, \quad (3.95)$$

with $T_1 + \Lambda_{rt}^2 \ll 1$. The reflectivity of the filter cavity at the frequency $2\pi \times \Omega$ can then be rewritten:

$$r_{fc}(\Omega) = \frac{\varepsilon - 1 + i\xi(\Omega)}{1 + i\xi(\Omega)}, \quad (3.96)$$

with

$$\varepsilon = \frac{2\Lambda_{rt}^2}{t_1^2 + \Lambda_{rt}^2}, \quad (3.97)$$

$$\xi(\Omega) = \frac{\Omega - \Delta\omega_{fc}}{\gamma_{fc}}. \quad (3.98)$$

The half-width-half-maximum-power linewidth is then approximated by:

$$\gamma_{fc} = \frac{T_1 + \Lambda_{rt}^2}{2} \frac{c}{2L_{fc}}, \quad (3.99)$$

and the squeezed quadrature rotation α_p produced by the filter cavity becomes:

$$\alpha_p = \arctan \left(\frac{(2 - \varepsilon)\gamma_{fc}\Delta\omega_{fc}}{(1 - \varepsilon)\gamma_{fc}^2 - \Delta\omega_{fc}^2 + \Omega^2} \right). \quad (3.100)$$

Finally, I recall the transfer matrix of the filter cavity defined in Equation (3.55):

$$\mathbf{T}_{fc} = e^{i\alpha_m} \mathbf{R}_{\alpha_p} \left(\rho_p \mathbf{I} - i\rho_m \mathbf{R}_{\frac{\pi}{2}} \right). \quad (3.101)$$

3.6.3 Mode matching losses

An important source of losses is the mode matching of the squeezed beam both to the filter cavity and to the local oscillator at the homodyne detection readout. In fact if the overlap between the filter cavity mode and the incident beam is not perfect, only the fraction of the incident beam that is matched to the cavity resonates inside the cavity and undergoes the frequency dependent rotation. Consequently the mismatched fraction of the incident beam is lost for frequency dependent squeezing.

Moreover as the filter cavity is locked near resonance of the fundamental mode, the mismatched fraction of the incident beam that is composed of higher order modes is completely reflected by the cavity and goes through the path towards the readout.

Using the notations of [83], we define a_0^2 the power mode coupling between the squeezed field and the filter cavity and c_0^2 the power mode coupling between the squeezed field and the local oscillator. The overlap b_0 between the local oscillator and the filter cavity modes is then:

$$b_0 = a_0 c_0 + \sqrt{(1 - a_0^2)(1 - c_0^2)} e^{i\phi_{mm}}, \quad (3.102)$$

where ϕ_{mm} is an arbitrary phase. The spatial overlap of the reflected field from the filter cavity and the local oscillator is then:

$$U_{mm} = t_{00} r_{fc}(\Omega) + t_{mm}, \quad (3.103)$$

whith $t_{00} = a_0 b_0^*$ and $t_{mm} = c_0 - t_{00}$.

Finally, the transfer matrix \mathbf{T}_{mm} of the field mismatched to the filter cavity and to the local oscillator is then defined by:

$$\mathbf{T}_{mm} = |t_{mm}| \mathbf{R}_{\arg(t_{mm})}. \quad (3.104)$$

3.6.4 Phase noise

There are two sources of phase noise: the squeezing ellipse jitter and the filter cavity length noise.

When the squeezed field is produced in an Optical Parametric Oscillator (OPO), the squeezing angle produced depends on the relative phase of the pump field to the OPO. Consequently, any fluctuation of the pump phase will lead to squeezing ellipse jitter. As this noise arises directly in the squeezing generation, it is not frequency dependent.

Otherwise, when the filter cavity is locked to be kept at optimal detuning $\Delta\omega_{fc}$ defined in Equation (3.60), any residual length fluctuation δL_{fc} will add a detuning $\delta\Delta\omega_{fc}$ to the filter cavity with:

$$\delta\Delta\omega_{fc} = \frac{\omega_0}{L_{fc}} \delta L_{fc}, \quad (3.105)$$

where ω_0 is the angular frequency of the squeezed field and L_{fc} the nominal length of the filter cavity. The phase noise arising from the filter cavity length noise is frequency dependent.

3.6.5 Linear noise transfer and noise budget

From the above, we obtain the full expressions of the transfer matrices \mathbf{T}_1 and \mathbf{T}_2 of the vacuum fields v_1 and v_2 towards the readout:

$$\mathbf{T}_1 = \tau_{inj}\tau_{ro}(t_{00}\mathbf{T}_{fc} + \mathbf{T}_{mm})\mathbf{S}, \quad (3.106)$$

$$\mathbf{T}_2 = \tau_{ro}\Lambda_2 + \Lambda_{ro}, \quad (3.107)$$

where the transfer coefficient τ_{inj} and τ_{ro} are defined by $\tau = \sqrt{1 - \Lambda^2}$,

$$\mathbf{S} = \begin{pmatrix} \cos(\theta) & -\sin(\theta) \\ \sin(\theta) & \cos(\theta) \end{pmatrix} \begin{pmatrix} e^\sigma & 0 \\ 0 & e^{-\sigma} \end{pmatrix} \begin{pmatrix} \cos(\theta) & \sin(\theta) \\ -\sin(\theta) & \cos(\theta) \end{pmatrix}, \quad (3.108)$$

is the two-photon transfer matrix for the squeezed state of squeeze factor σ and quadrature angle θ , and

$$\Lambda_2 = \sqrt{1 - \frac{|\tau_2(\Omega)|^2 + |\tau_2(-\Omega)|^2}{2}}, \quad (3.109)$$

$$\tau_2(\Omega) = (t_{00}r_{fc}(\Omega) + t_{mm})\tau_{inj}. \quad (3.110)$$

I will now give the squeezing degradation of a frequency dependent squeezing experiment starting from $\sigma_{dB} = 10$ dB of injected squeezing, corresponding to a 10 dB reduction of the noise level with respect to the shot noise, with:

$$\sigma_{dB} = 20 \log_{10}(e^\sigma), \quad (3.111)$$

with a 50-meter long filter cavity of finesse $\mathcal{F} = 3000$ at the squeezing wavelength, corresponding to the aim of this thesis. I will first represent all types of losses independently and then the total noise budget and the effect depending on the quadrature measurement that corresponds to what we can experimentally measure.

Frequency independent losses

There are 4 sources of losses that do not depend on the frequency: injection and readout losses, phase noise arising from the squeezing ellipse jitter at the squeezing production and mode matching of the squeezed beam with the local oscillator. Their respective effect is represented in Figure 3.16

Going through the details of the plots, we can see that the squeezing measurement is quickly degraded by any losses on the squeezing path. With 9% of injection losses there is already less than 7.5 dB of squeezing left out of 10 dB produced. This shows the importance to have the best coatings available and the best quality optics on the squeezing path to reduce injection losses. From simulation of the whole set-up of a squeezing experiment, it is hard to go under 9% of injection losses.

The detection efficiency of the homodyne photodiodes is also important as 5% of losses gives rise to more than 1.5 dB of squeezing degradation. However, high quantum efficiency photodiodes with conversion efficiency of the order of 99% exist commercially.

The squeezing ellipse jitter noise is more difficult to evaluate. However, values of the order of 30 mrad are achievable [87–89] and give rise to less than 0.5 dB of squeezing degradation.

Finally, the mode matching between the squeezed beam and the local oscillator has to be carefully done as 10% of mismatch (meaning 90% of fringe visibility) leads to almost 4.5 dB of squeezing degradation. This is something we really have to take care in a squeezing experiment.

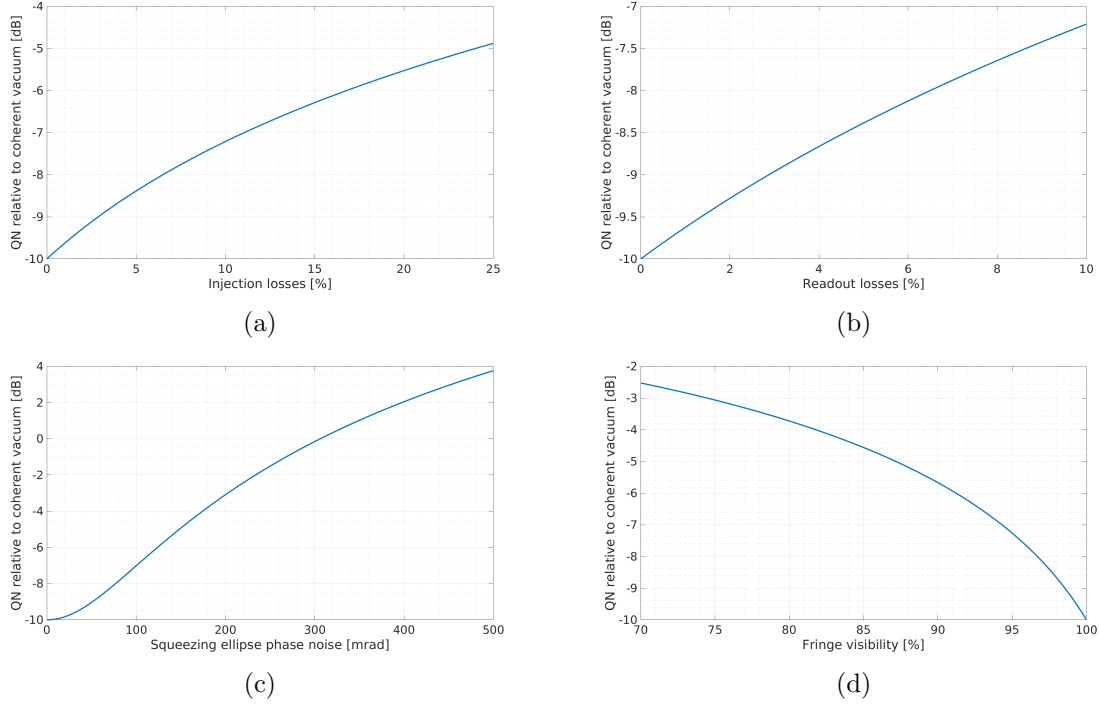


Figure 3.16 – Simulation of the effect of frequency independent losses on the squeezing level. (a) Injection losses, (b) readout losses, (c) losses due to the squeezing ellipse jitter and (d) losses from the mode mismatch of the local oscillator beam with the squeezed beam, measured at the homodyne detection. The simulation starts from 10 dB injected squeezing.

Frequency dependent losses

There are 3 sources of losses that are frequency dependent because they occur at the filter cavity level: filter cavity round trip losses, mode matching of the squeezed beam to the filter cavity and filter cavity length noise. Their respective effect is represented in Figure 3.17.

First of all, we can clearly see that frequency dependent losses have a significant impact on the squeezing degradation around and below the tilt frequency $f_t \simeq 700$ Hz in this simulation.

It is important to limit the filter cavity round trip losses to few tens of *ppm* in order not to degrade too much the squeezing at low frequency. For instance $\Lambda_{rt}^2 = 50$ ppm leads to around 1.5 dB of squeezing degradation at low frequency.

More important the mode matching of the squeezed beam to the filter cavity has to be tuned as much as possible as 10% of mismatch gives rise to around 4 dB of squeezing degradation at low frequency with a maximum of 5.5 dB squeezing degradation close to the tilt frequency.

Finally, the lock of the filter cavity has to be robust and less noisy as possible. To stay in reasonable loss values, lower than 4 dB of squeezing degradation, the filter cavity length noise for a 50 m long cavity has to stay below 10 pm.

Noise budget

Finally, I plotted the squeezing degradation taking into account reasonably achievable values for all noise sources summarized in Table 3.1.

In Figure 3.18a, one can see the squeezing measurement at the homodyne detection for different measurement quadrature angles ϕ and the resulting squeezing measurement in dashed corresponding to the minimum envelope of the different measurement angles.

The noise content of the same measurement is shown in Figure 3.18b. One can clearly see that the dominant noises are the filter cavity length noise, the squeezed field mode mismatch to the filter cavity and the injection losses.

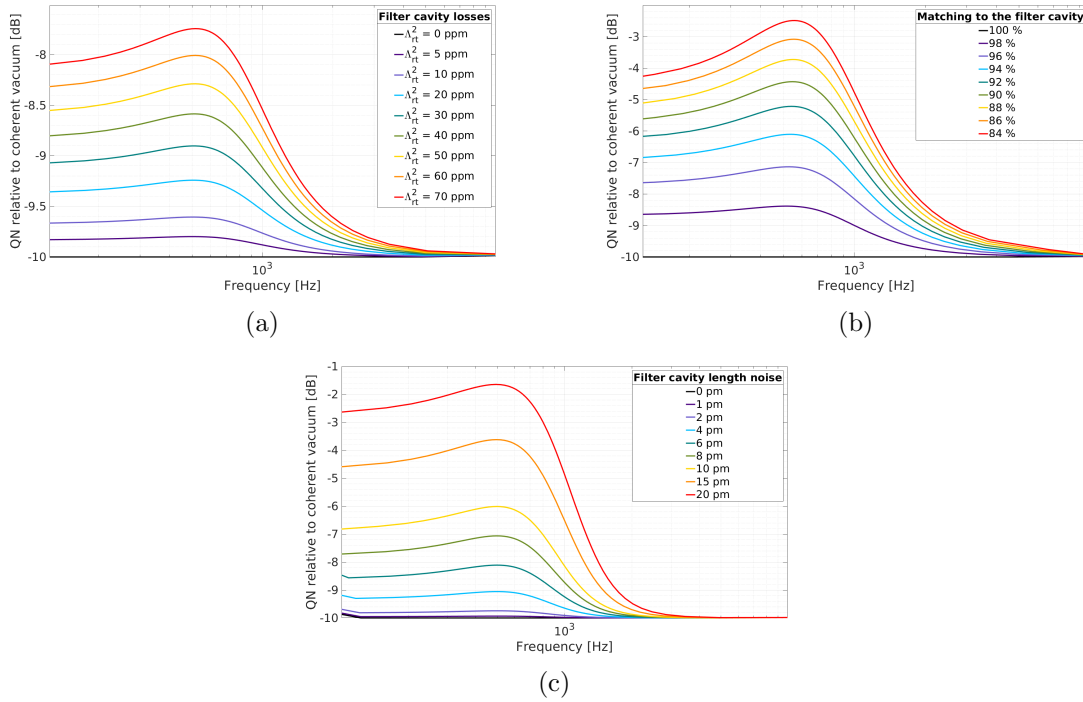


Figure 3.17 – Simulation of the effect of frequency dependent losses on the squeezing level. (a) Filter cavity round trip losses, (b) losses from the mode mismatch of the squeezed beam to the filter cavity and (c) losses due to filter cavity length noise, measured at the homodyne detection taking at each frequency the measurement quadrature angle ϕ that gives the minimal noise value. The simulation starts from 10 dB injected squeezing.

Noise source	Value
Injection losses	11.5%
Readout losses	1%
Squeezing ellipse phase noise	30 mrad
Homodyne detection fringe visibility	97.5%
Filter cavity round trip losses	50 ppm
Mode matching of the squeezed field to the filter cavity	95%
Filter cavity length noise	10 pm

Table 3.1 – Losses parameter chosen for the simulation results presented in Section 3.6.5.

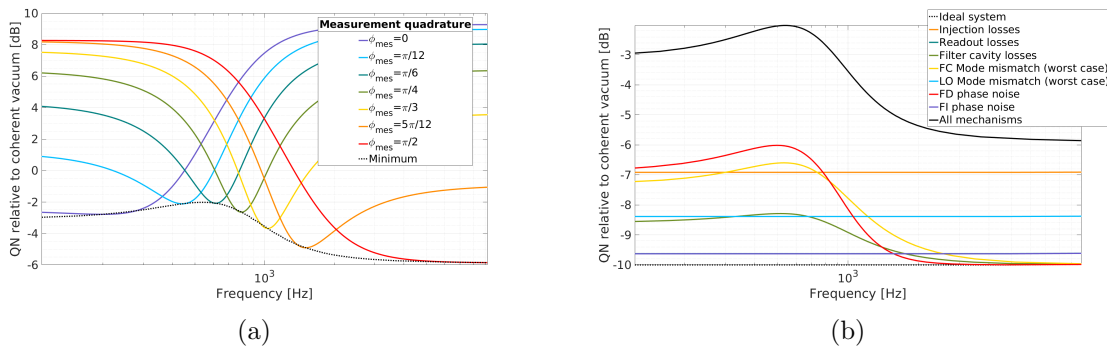


Figure 3.18 – Simulation of the frequency dependent squeezing measured at the homodyne detection (a) total losses for different measurement quadrature angle ϕ (b) all losses sources taking at each ϕ the measurement quadrature angle ϕ that gives the minimal noise value. The simulation starts from 10 dB injected squeezing and takes the losses values given in Table 3.1. The black dashed line of (a) is the black continuous line of (b).

3.7 State of the art

3.7.1 Squeezing production

The use of squeezing to enhance gravitational wave detectors sensitivity was first proposed in 1981 by Caves [74] while squeezing was not yet experimentally observed. The first measurement of squeezing was published in 1985 by Slusher *et al.* [90]. A 7% noise reduction was observed at about $4 \cdot 10^8$ Hz corresponding to about 20% of squeezing produced. Most of the time, noise reduction and squeezing production are expressed in dB. In this unit, the first measurement was of 0.3 dB noise reduction for about 1 dB of produced squeezing.

Since this first measurement, a huge progress has been made [91] until the first squeezing in the audio-band, that is between 10 Hz and 10 kHz, corresponding to the detection frequency band of gravitational wave detectors. This was done in 2004 by McKenzie *et al.* [92] achieving a broadband squeezing from 280 Hz to above 100 kHz. They reached about 5.5 dB of produced squeezing and 7 dB antisqueezing as the phase ϕ of the homodyne detection varies.

In 2007, Vahlbruch *et al.* [93] achieved the first squeezing production across the whole audio gravitational wave band, down to 1 Hz reaching 6.5 dB of produced squeezing. This was improved to 11.6 dB of squeezing produced by Stefszky *et al.* [94] in 2012 as shown in Figure 3.19a. The highest level of squeezing until now has been achieved in 2016 by Vahlbruch *et al.* [95] with 15 dB of produced squeezing at 5 MHz as shown in Figure 3.19b.

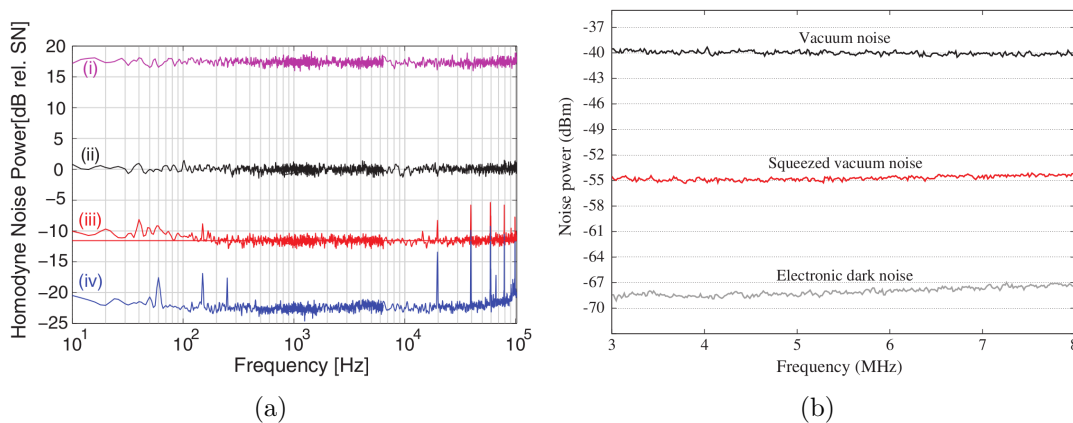


Figure 3.19 – (a) Measured squeezing by Stefszky *et al.* [94] in 2012 using a quantum noise limited balanced homodyne detector. (i) is the antisqueezing, (ii) is the shot noise level, (iii) is the squeezing with a line at -11.6 dB showing the average of the squeezing and (iv) is the dark noise. (b) Measured squeezing by Vahlbruch *et al.* [95]

3.7.2 Squeezing in gravitational wave detectors

Frequency independent vacuum squeezing has been tested and used on different gravitational wave interferometers.

Since 2010, squeezing has been routinely used to increase the sensitivity of the gravitational wave detector GEO 600 [87], an interferometric gravitational wave detector like Virgo and LIGO but with only 600 m long arms to test the new technologies. They measured the best gain sensitivity for a gravitational wave detector with a reduction of quantum noise up to 6 dB.

Squeezing was also tested on Enhanced LIGO Hanford gravitational wave detector at the end of 2011 [96]. It was then used in the direct measurement of gravitational waves on both Advanced LIGO Livingston and Hanford detectors [97] for the third Observing Run (O3) with up to 3 dB quantum noise reduction measured.

Advanced Virgo also used squeezing during the O3 with a sensitivity enhancement up to 3dB like in the Advanced LIGO detectors. A simplified layout of the implementation

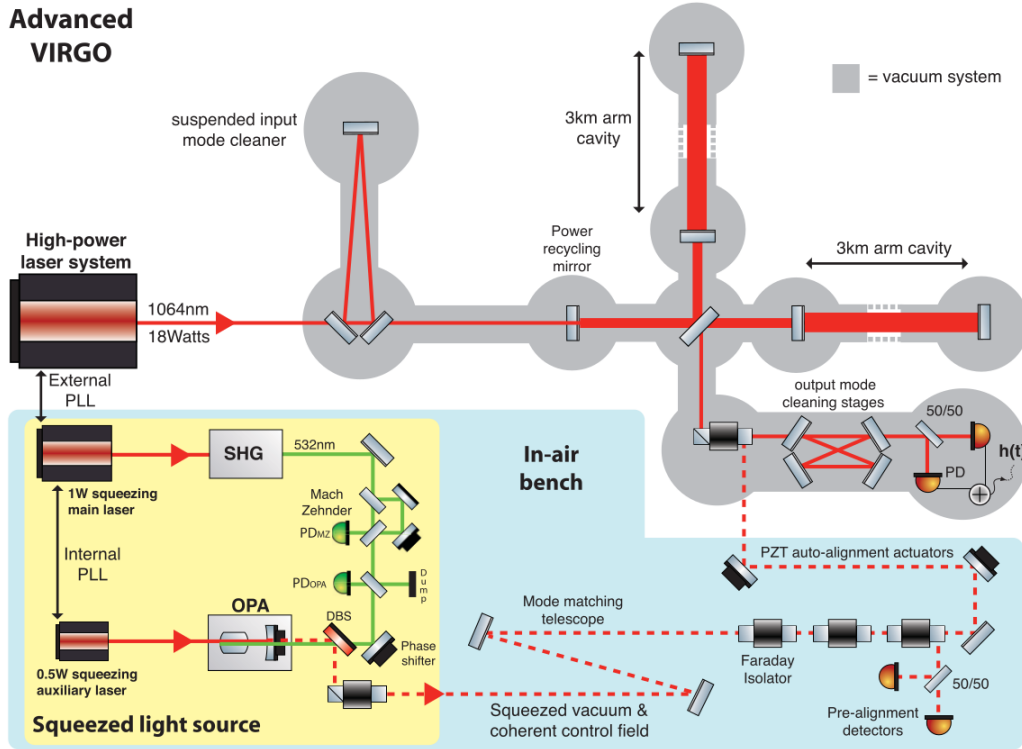


Figure 3.20 – Simplified scheme of the squeezed light enhanced gravitational wave detector Advanced Virgo [98].

of squeezing in Advanced Virgo is represented in Figure 3.20, showing how the squeezed vacuum enters the interferometer dark port. The Advanced LIGO and GEO 600 layouts are very similar to the Advanced Virgo one.

The measured spectral strain sensitivity of Advanced Virgo, Advanced LIGO Livingston and GEO 600 are represented for comparison in Figure 3.21 with and without frequency independent vacuum squeezing.

3.7.3 Frequency dependent squeezing

To enhance gravitational wave detectors in their whole bandwidth we have to use frequency dependent squeezing with a rotation of the squeezing ellipse occurring at about 50 Hz. This is the object of the work done at CALVA in the framework of the ANR Exsqueez that will be described in the rest of this thesis.

However other teams are working in parallel on similar approaches and published their results at the beginning of 2020. I will give a brief overview of their work and compare them with this thesis work.

The first demonstration of a frequency dependent squeezing with a rotation of the squeezing ellipse below 100 Hz was done using the infrastructure of the former TAMA300 interferometer with a squeezing source in-air and a 300-meter filter cavity [89] with 4 dB quantum noise reduction at high frequencies and 2 dB at low frequencies. At MIT, another team demonstrated a frequency dependent squeezing with a rotation of the squeezing ellipse at 30 Hz using an in-vacuum squeezing source and a 16-meter filter cavity [88] with 4 dB quantum noise reduction at high frequencies and no reduction at low frequencies.

Both results are presented in Figure 3.22 and a summary of the main differences between the experiments done at TAMA and MIT is given in Table 3.2 with the same parameters given for the Exsqueez project that is closer to the MIT one but adapted to the Advanced Virgo framework.

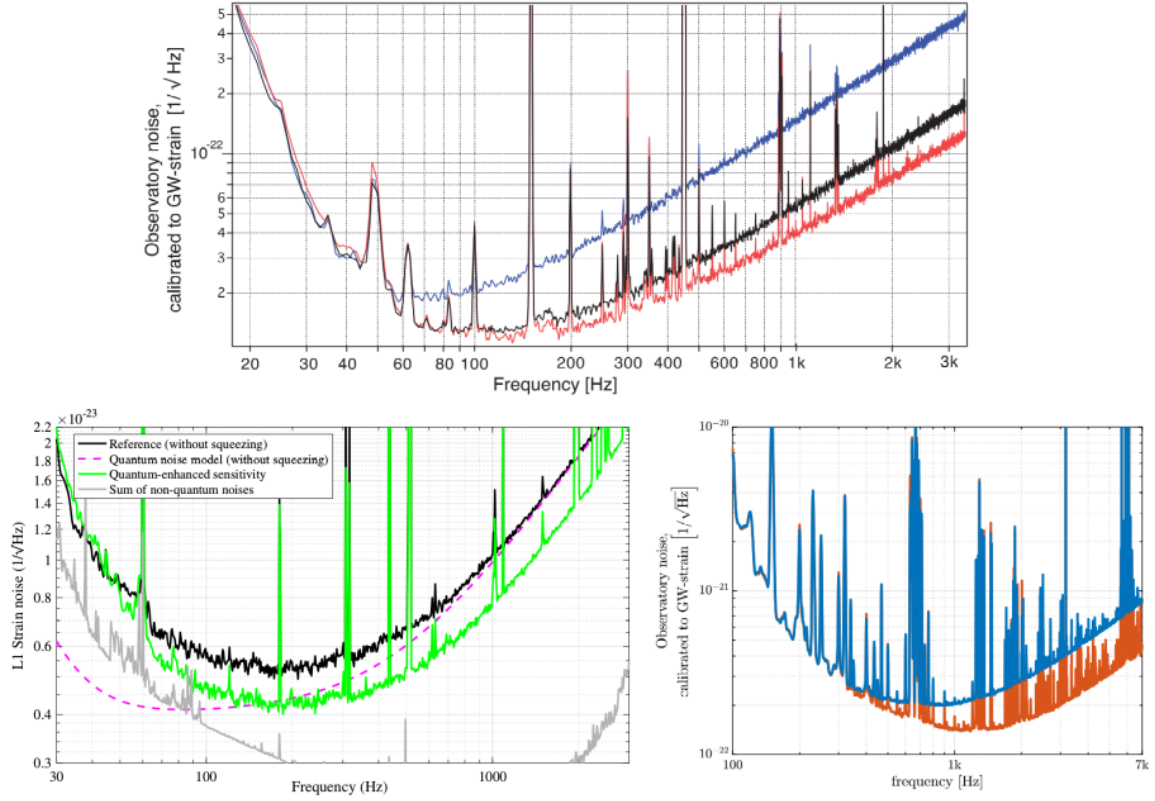


Figure 3.21 – Measured spectral strain sensitivity: (*upper*) for Advanced Virgo during the O3 observation run with in black the reference without squeezing in red with squeezing and in blue with antisqueezing [98], (*lower left*) for Advanced LIGO Livingston during the O3 observation run with in black the reference without squeezing and in green with squeezing [97], (*lower right*) for GEO600 in 2020 with in blue without squeezing and in red with squeezing [87].

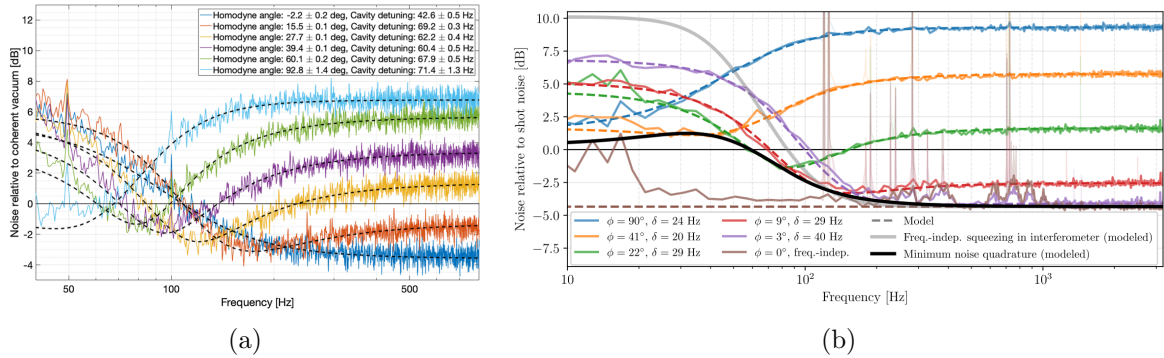


Figure 3.22 – Frequency dependent squeezing measured at (a) TAMA [89] and (b) MIT [88] showing the noise spectra measured for different homodyne angles.

Parameter	TAMA	MIT	Exsqueeze
Squeezer cavity geometry	Linear hemilithic	Bow-tie	Bow-tie
Squeezer environment	In-air	In-vacuum	In-vacuum
Filter cavity length	300 m	16 m	50 m
Squeezing ellipse rotation frequency	90 Hz	30 Hz	700 Hz and then 70 Hz

Table 3.2 – Summary of some main differences between the frequency dependent experiment done at TAMA and MIT and the Exsqueeze project.

Chapter 4

Design of a Frequency Dependent Squeezing Experiment: Exsqueez

The Exsqueez project is conducted by 4 laboratories: LKB, LAL/IJCLab, LMA/IP2I and LAPP [99]. It is two-sided and aims at demonstrating frequency dependent squeezing along two bands of frequencies, i.e. at high frequencies (of the order of the MHz) and at low frequencies (in the audio band from 10 Hz to 10 kHz). The high frequency side of this project is conducted at LKB [100] while the object of this thesis is the demonstration of the low frequency dependent squeezing with a squeezing source under vacuum.

As presented in Chapter 2, the sensitivity of the advanced generation of gravitational wave detectors should soon reach the Standard Quantum Limit, defined in Section 2.3.3. The implementation of low frequency dependent squeezing would allow to further improve the detectors sensitivities. Moreover, the Standard Quantum Limit is also investigated in optomechanical systems such as micropillar resonators [101] and the high frequency side of the Exsqueez project takes place in this framework.

Both parts of the project share common features, in particular the design of a robust squeezed light source and the use of a filtering cavity for the rotation of the squeezing ellipse. In addition, there are also control loops required for both systems that will be described later in this chapter.

The main differences between the two sides of the project are summarized in Table 4.1. In the rest of the thesis I will refer to the low frequency dependent squeezing experiment as *Exsqueez*. This experimentation is done at LAL/IJCLab on the CALVA facility shown in Figure 4.1, using the existing 50-meter suspended cavity as a filtering cavity.

	High Frequency	Low Frequency
Environment	In-air	Under vacuum
Type of seeding	Bright	Vacuum
Corner frequency	165 kHz	1 kHz
Target system	Optomechanical resonator	Gravitational wave interferometer

Table 4.1 – Main differences between the low frequency and the high frequency parts of the Exsqueez project

In this chapter I will first present an overview of Exsqueez using a simplified scheme and introduce the needed beams and systems to fully control the experiment. I will then go through the details of the different subsystems to construct the full conceptual design and present the chosen parameters. Finally I will summarize the different beam paths and parameters of interest for Exsqueez.



Figure 4.1 – First clean room of CALVA with the red tank, named Ferrarix, used for the in-vacuum preparation bench of the Exsqueeze experiment and the grey tank where the first mirror of the filter cavity stands.

4.1 Exsqueeze experiment overview

4.1.1 Simplified conceptual design

The squeezed state generator used for Exsqueeze aims at generating frequency dependent vacuum squeezed state such as the one that could be applicable to gravitational wave detectors. A simplified scheme of the experiment is shown in Figure 4.2. It presents the main parts of the experiments as a first sketch.

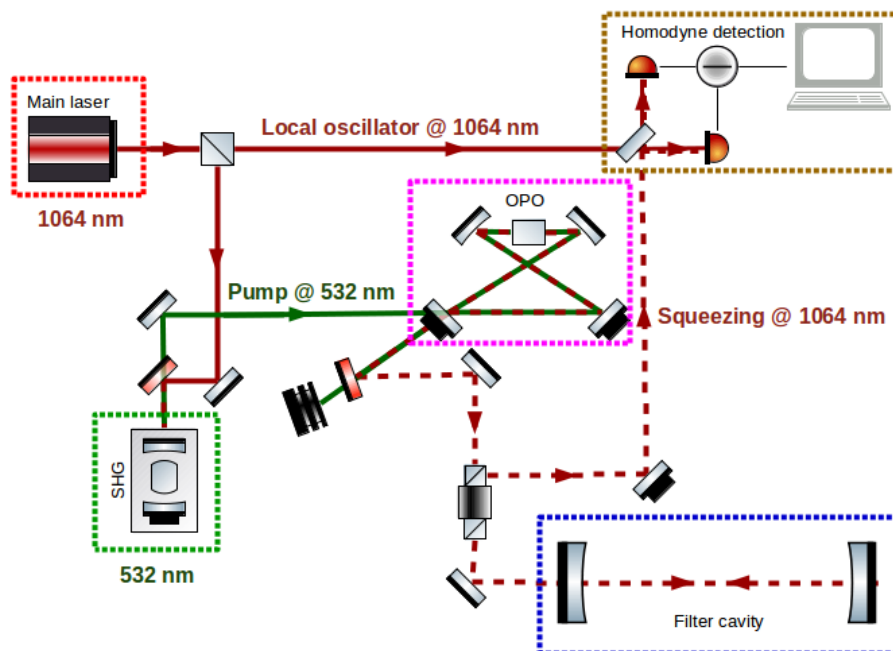


Figure 4.2 – Simplified conceptual scheme of Exsqueeze including only the main parts of the frequency dependent squeezing production and measurement in dashed boxes. In red: the main laser at 1064 nm, in green: the Second Harmonic Generator (SHG) producing light at 532 nm, in pink: the Optical Parametric Oscillator (OPO), in blue: the filter cavity and in brown: the homodyne detection.

The main important device to generate squeezing is the Optical Parametric Oscillator (OPO). As explained in Section 3.5.1, the non-linear medium of the OPO downconverts

photons of the pump field at 532 nm (after frequency doubling) into correlated sideband pairs, generating a squeezed state of light. From Figure 3.12, one can see that vacuum squeezing is produced in the crystal at all frequencies up to the pump frequency, centered at half the pump frequency.

The characteristics of the non-linear medium will be presented in Section 4.3.1. Moreover, it is placed inside an optical cavity that will be described in Section 4.3.2 to filter the squeezed photons frequency.

To obtain frequency dependent squeezing, the squeezed beam is then injected into a filter cavity that will rotate the squeezing ellipse in a frequency dependent manner, as explained in Section 3.4.2. The parameters chosen for the Exsqueeze filter cavity will be given in Section 4.5.

Finally, the squeezing measurement is done using the balanced homodyne detection scheme presented in Section 3.5.2. It needs to combine the squeezed beam with a local oscillator beam at the same wavelength. To ensure this condition, the pump beam, that is used to produce the squeezed field, is obtained by frequency doubling a main laser with a Second Harmonic Generator (SHG) that will be described in Section 4.2. A tap off of this main laser is then used as local oscillator for the squeezing measurement.

4.1.2 Introduction of the full conceptual design

To fully control the squeezing production at the maximum possible level, we have to introduce more beams and systems. In this section I will only give a short overview of all the beams that are used and I will go through the details in the next sections of this chapter.

The full conceptual design, represented in Figure 4.3, comprises 8 different beams, named when they enter the Ferrarix in-vacuum tank (red tank in Figure 4.1), while the in-air part corresponds to the beam preparation stage. Due to the complexity of this scheme, I will do some round trips between the generation of the beams and the explanation of their use. I will list here a summary in alphabetic order of the different beams with their usefulness:

- **Filter Cavity Control (FCC):** green beam used to lock the filter cavity.
- **Filter Cavity Verification (FCV):** infrared beam used to verify the lock of the filter cavity in the infrared for the squeezed beam.
- **Local Oscillator (LO):** infrared beam used to measure the squeezing level.
- **Modified Coherent Locking (MCL):** infrared beam, frequency shifted from the squeezed beam, used to control the squeezing ellipse angle.
- **Phase Locking (PL):** green beam used to phase lock the MCL and squeezed beams.
- **Pump¹:** green beam used to generate the squeezed beam.
- **Seed:** infrared beam used to characterize the OPO and the homodyne detection.
- **Squeezed:** infrared beam generated in the in-vacuum tank from the pump beam.

All these beams are summarized in table 4.2 with their wavelength and simplified sideband diagrams and reviewed in Section 4.6. To generate all these beams we use two infrared laser sources at 1064 nm: a main laser that delivers 2 W and an auxiliary laser that delivers 200 mW. The auxiliary laser is frequency shifted from the main laser and both lasers are phase locked with each other, as it will be explained in Section 4.4.2.

On both infrared paths, we placed a Second Harmonic Generator (SHG) that produces a green beam. The specific features and use of these SHG stages will be presented later in this chapter, but we can already notice that both of them are placed inside an optical cavity.

¹All over this thesis the term of *pump* beam will refer to this 532 nm beam used to generate the squeezing. In particular I won't use it for the infrared beam that generates green beam via frequency doubling.

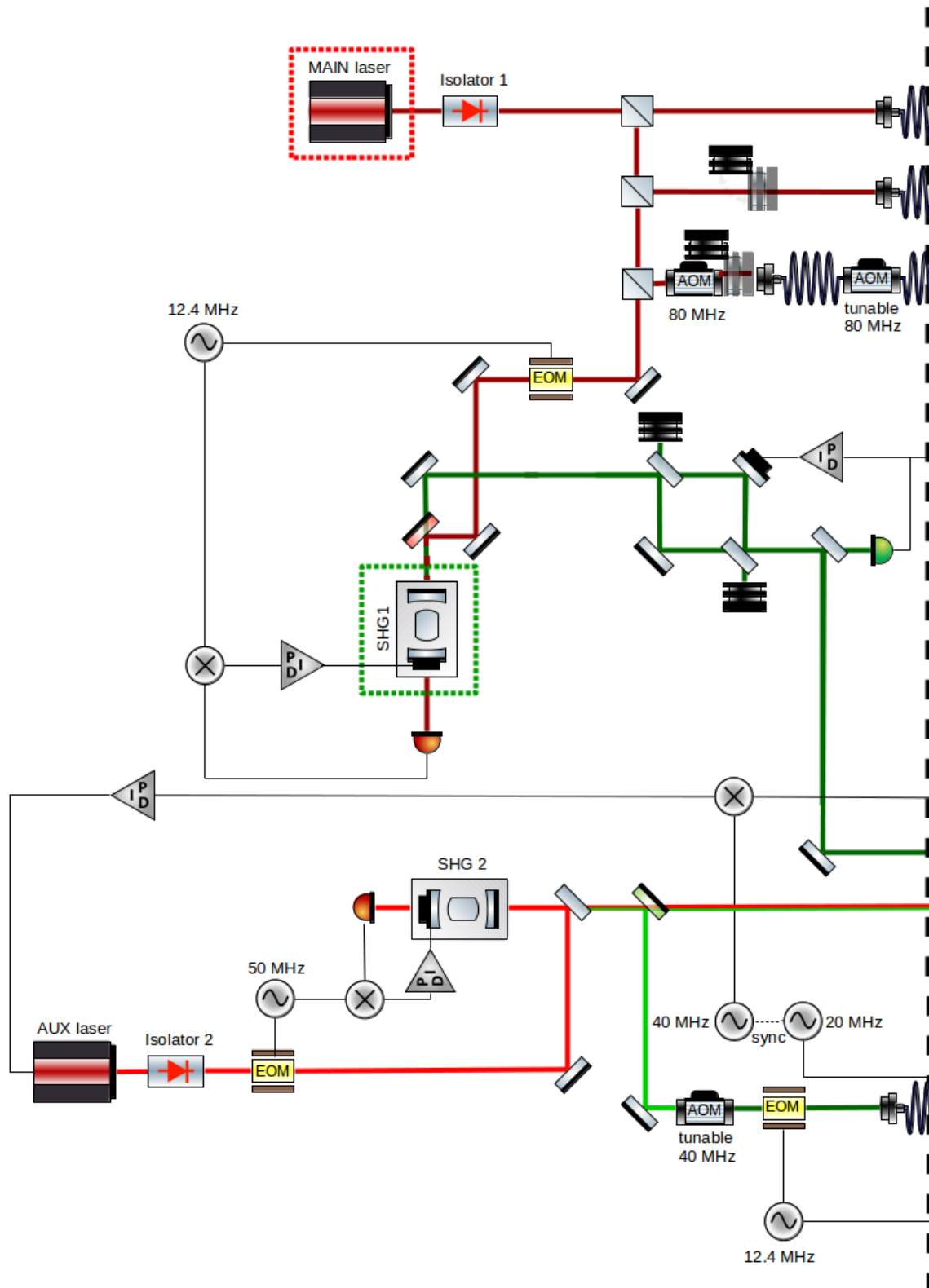
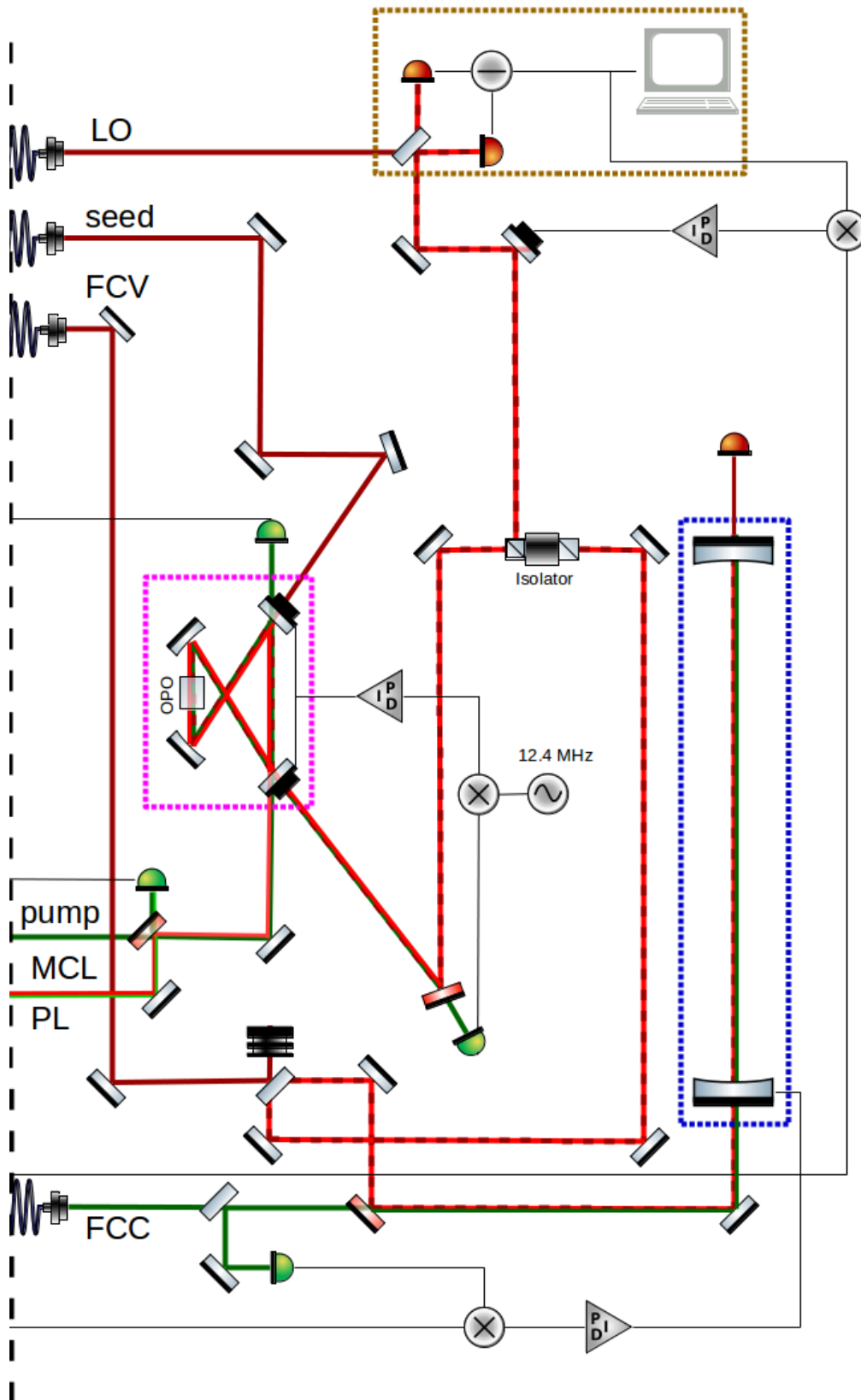


Figure 4.3 – Full conception design of Exsqueeze. Left: In-air part.



Right: In-vacuum part.

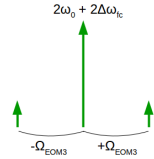
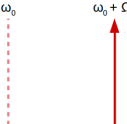
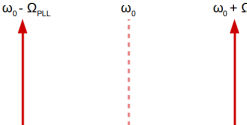
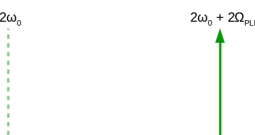
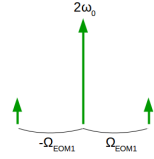
Beam name and laser source	Wavelength	Sideband diagram
Filter Cavity Control (FCC) from the auxiliary laser	532 nm	
Filter Cavity Verification (FCV) from the main laser	1064 nm	
Local Oscillator (LO) from the main laser	1064 nm	
Modified Coherent Locking (MCL) from the auxiliary laser before the OPO	1064 nm	
Modified Coherent Locking (MCL) from the auxiliary laser after the OPO	1064 nm	
Phase Locking (PL) from the auxiliary laser	532 nm	
Pump from the main laser	532 nm	
Seed from the main laser	1064 nm	
Squeezed from the main laser	1064 nm	

Table 4.2 – Summary of the beams used for Exsqueez presenting there wavelength and simplified sideband diagrams. The IR laser source at 1064nm is precised and the beams at 532nm are obtained after interacting through a Second Harmonic Generator (SHG) which is SHG1 on the path of the main laser and SHG2 on the path of the auxiliary laser.

4.1.3 Pound-Drever-Hall Locking technique

In the full conceptual design there are 4 optical cavities : for the Optical Parametric Oscillator (OPO), for the main and the auxiliary Second Harmonic Generator (SHG1 and SHG2) and for the filter cavity. All these cavities need to be length controlled and locked on resonance for a given wavelength. These locks will be done using the Pound-Drever-Hall (PDH) technique.

The principle of the Pound-Drever-Hall technique [102] is to modulate the incoming ω field in phase at a frequency Ω_{EOM} and a modulation depth m creating sidebands at $\omega \pm \Omega_{EOM}$. This is done by adding an Electro-Optic Modulator (EOM) in the path of the incoming beam.

Considering again the classical field at a given position in space of Equation (2.1), the field of the beam before the EOM is written:

$$\psi = \psi_0 e^{i\omega t}. \quad (4.1)$$

And after the EOM, the field entering the Fabry-Perot cavity is:

$$\psi_{in} = \psi e^{im \sin(\Omega_{EOM} t)} = \psi \sum_{n=-\infty}^{n=+\infty} J_n(m) e^{in\Omega_{EOM} t}, \quad (4.2)$$

where $J_n(m)$ are the Bessel functions.

Consequently, at first order we have:

$$\psi_{in} = \psi \left[J_0(m) + J_1(m) e^{i\Omega_{EOM} t} + \underbrace{J_{-1}(m)}_{=-J_1(m)} e^{-i\Omega_{EOM} t} \right]. \quad (4.3)$$

From Equation (4.3), we see that we have now 3 separated frequencies entering the Fabry-Perot cavity: the carrier at ω and 2 sidebands at $\omega \pm \Omega_{EOM}$.

According to Equations (2.65) and (2.66), the complex amplitude reflectivity and transmissivity of the cavity depend on the frequency. Consequently the field of the beam containing a carrier and sidebands that is filtered by the cavity is just the sum of the field associated to each frequency multiplied by the complex amplitude effect $F(\omega)$ of the cavity, at this frequency:

$$\psi_F = \psi \left[J_0(m) F(\omega) + J_1(m) F(\omega + \Omega_{EOM}) e^{i\Omega_{EOM} t} - J_1(m) F(\omega - \Omega_{EOM}) e^{-i\Omega_{EOM} t} \right]. \quad (4.4)$$

For instance in reflection of the cavity, $F(\omega)$ is the complex amplitude reflectivity and in transmission of the cavity, $F(\omega)$ is the complex amplitude transmissivity. Finally, a photodiode measures the power of the field that is:

$$P_F = |\psi_F|^2 = P_{DC} + P_{AC_{\Omega_{EOM}}} + P_{AC_{2\Omega_{EOM}}}, \quad (4.5)$$

with:

$$P_{DC} = |\psi_0|^2 \left[J_0(m)^2 |F(\omega)|^2 + J_1(m)^2 \left(|F(\omega + \Omega_{EOM})|^2 + |F(\omega - \Omega_{EOM})|^2 \right) \right], \quad (4.6)$$

$$P_{AC_{\Omega_{EOM}}} = 2P_{AC_q} \cos(\Omega_{EOM} t) + 2P_{AC_p} \sin(\Omega_{EOM} t), \quad (4.7)$$

$$P_{AC_{2\Omega_{EOM}}} = |\psi_0|^2 J_1^2(m) \left(F(\omega + \Omega_{EOM}) F^*(\omega - \Omega_{EOM}) e^{2i\Omega_{EOM} t} + c.c. \right), \quad (4.8)$$

where:

$$P_{AC_q} = |\psi_0|^2 J_0(m) J_1(m) \operatorname{Re} [F(\omega) F^*(\omega + \Omega_{EOM}) - F^*(\omega) F(\omega - \Omega_{EOM})], \quad (4.9)$$

$$P_{AC_p} = |\psi_0|^2 J_0(m) J_1(m) \operatorname{Im} [F(\omega) F^*(\omega + \Omega_{EOM}) - F^*(\omega) F(\omega - \Omega_{EOM})]. \quad (4.10)$$

P_{DC} is the DC power measured by a photodiode. To obtain the demodulated signal, the power measured by the photodiode is mixed with a phase-delayed version of the original modulation to obtain P_F^m :

$$P_F^m = P_F \cos(\Omega_{EOM} t + \varphi), \quad (4.11)$$

where φ is the phase delay introduced. By developing Equation (4.11), we get:

$$\begin{aligned} P_F^m = & P_{DC} \cos(\Omega_{EOM}t + \varphi) \\ & + P_{AC_q} \cos(2\Omega_{EOM}t + \varphi) + P_{AC_p} \sin(2\Omega_{EOM}t + \varphi) \\ & + P_{AC_q} \cos(\varphi) + P_{AC_p} \sin(\varphi) \\ & + P_{AC_{2\Omega_{EOM}}} \cos(\Omega_{EOM}t + \varphi). \end{aligned} \quad (4.12)$$

And after low-pass filtering we only have the demodulated AC signal $P_F^{\Omega_{EOM}}$:

$$P_F^{\Omega_{EOM}} = P_{AC_q} \cos(\varphi) + P_{AC_p} \sin(\varphi). \quad (4.13)$$

By tuning the phase delay φ we can observe either the signal demodulated in quadrature P_{AC_q} , or the signal demodulated in phase P_{AC_p} or a combination of both.

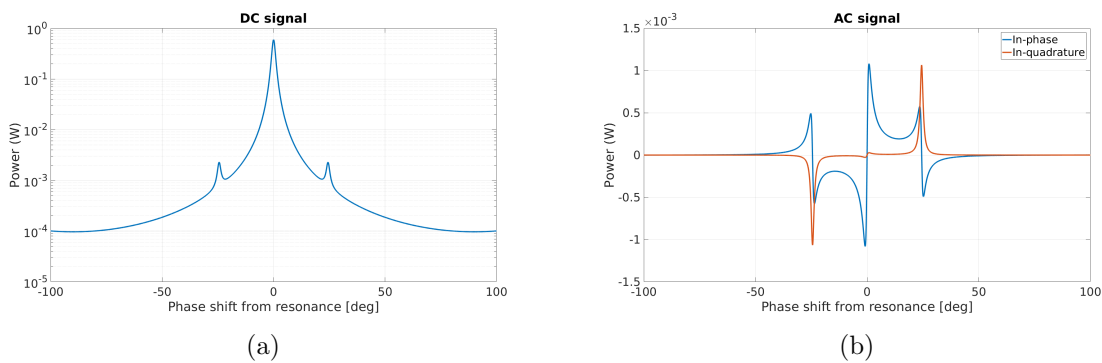


Figure 4.4 – Signals measured in transmission of a cavity showing the carrier and the sidebands (a) DC signal. (b) AC in-phase and in-quadrature signals.

The signal demodulated in phase is linear and centered on zero around the resonance of the cavity. That is a good error signal for a locking loop to keep the cavity on resonance.

4.2 Second Harmonic Generators

There are primarily 4 beams generated on the in-air preparation bench of Figure 4.3 that give rise to the 8 beams entering the Ferrarix in-vacuum tank, defined in Section 4.1.2 and Table 4.2: 2 infrared beams at 1064 nm and 2 green beams at 532 nm.

We use 2 laser heads and 2 Second Harmonic Generators (SHG) [103] to generate these beams. The reason why we use SHGs on beams at 1064 nm to obtain beams at 532 nm and not directly laser head at 532 nm will become clearer in the rest of the chapter. For now, I will only say that SHG1 ensures that on the homodyne detection the local oscillator from the main laser and the squeezed beam generated from the pump beam are exactly at the same frequency. SHG2, on its side, is used to phase lock the main and auxiliary laser. The necessity of the phase lock and the method to phase lock the lasers will be detailed in Section 4.4.3.

Both SHGs share the same properties that I will describe now.

4.2.1 Non linear medium

The non linear medium used for the second harmonic generators is a magnesium oxide doped periodically-poled lithium niobate (MgO:PPLN) crystal. This is a quasi-phase matched material in which the spontaneous polarization of the lithium niobate crystal is periodically inverted (poled).

The refractive index of light in the crystal depends on the temperature. Consequently, according to Section 3.5.1, the coherence length l_c of the medium depends on the temperature.

Recalling Equation (3.74), we can express the coherence length according to the fundamental wavelength $\lambda_0 = 1064$ nm and the refractive index n_1 and n_2 , respectively at the fundamental wavelength and at the second harmonic wavelength $\lambda_2 = 532$ nm:

$$l_c = \frac{\lambda_0}{4(n_2 - n_1)}. \quad (4.14)$$

The best quasi-phase matching is obtained when flipping the orientation of the polarization of the medium every coherence length. From Equation (4.14), the period of the poling at a given fundamental wavelength λ_0 depends on the refractive index at both fundamental and second harmonic wavelengths.

To increase the available tuning of the phase matching we use crystals that have several gratings of periodically poled medium with different poling periods separated by non poled medium of the same material as shown in Figures 4.5a and 4.5b.

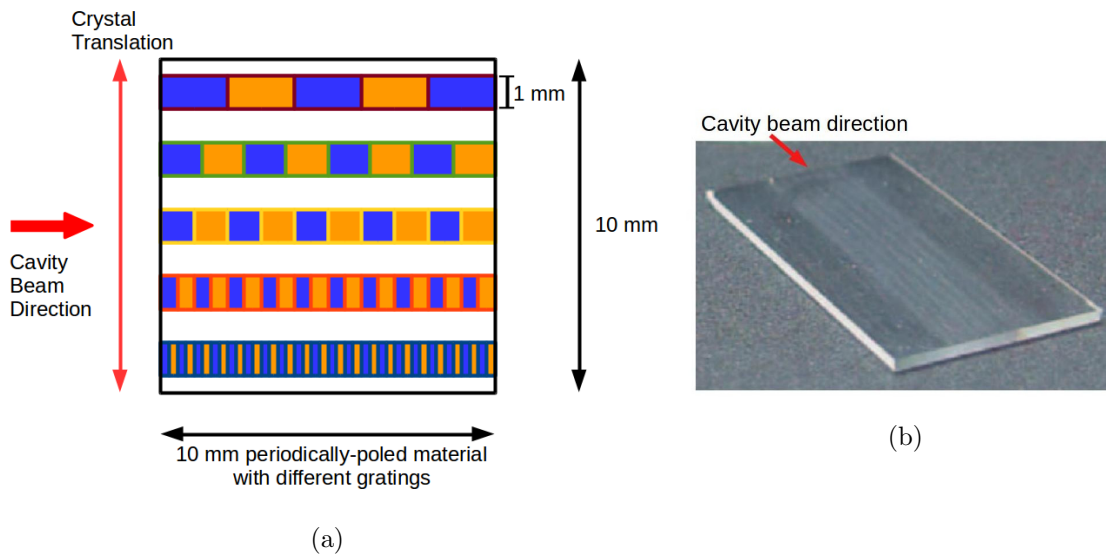


Figure 4.5 – (a) Scheme of the PPLN crystal showing the 5 gratings that can be used as Second Harmonic Generators (SHG). The periodic poling is represented by the blue and orange boxes and the non poled material is represented in white. (b) Picture of a PPLN crystal showing the gratings [104].

The crystal we are using is 1 mm thick, 10 mm wide and 10 mm long. It is composed of non poled material surrounding 5 lines of periodically poled material with 5 different periods that are exaggerated in Figure 4.5a. Each grating is 1 mm wide and the fundamental beam is then sent through one grating that have a given optimal temperature for phase matching as shown in Figure 4.6.

4.2.2 Temperature control

The control of the crystal temperature is done using a Thermistor to measure the temperature and obtain an error signal and a Peltier unit to increase or lower the temperature and maintain it to the best phase matching value.

We decided to use the second grating with the highest period of poling, that is $6.93 \mu\text{m}$ on both SHG because it allows a phase matching temperature at 1064 nm of 50°C that is not too high with respect to the room temperature. We decided not to use the first one at 33°C because it was too close to the beginning of the operating temperature range.

The first difference between SHG1 and SHG2 stands in the temperature controller unit. For SHG1 we use a commercial oven, that contain the thermistor and the Peltier, with its associated temperature controller unit. It has been chosen for its easy handling.

However, for the Optical Parametric Oscillator (OPO), that I will describe in Section 4.3, we won't be able to use a commercial oven and temperature controller unit to control the

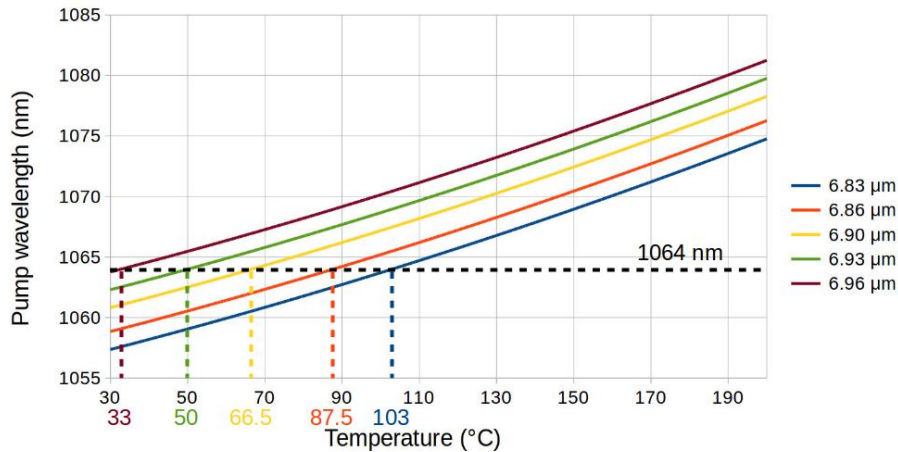


Figure 4.6 – Quasi-phase matching curves of the PPLN crystal used [105]. The pump wavelength is the wavelength of the fundamental beam (1064 nm) and the curves correspond to the different poling periods of the gratings.

OPO crystal temperature as it will be placed under vacuum and classical commercial systems are not vacuum compatible.

To limit the costs, for the OPO, we will use a home made system with a thermistor and a Peltier unit connected to the acquisition system provided by LAPP for Exsqueez¹.

To test this type of home made system before the OPO, and to reduce the costs, we decided to use the same home made system for SHG2.

4.2.3 Cavity

As the second harmonic generation is a second order process its efficiency is quite low, even using a periodically poled crystal. A single passage inside the crystal produces few tens of μW of second harmonic beam from few hundreds of mW of fundamental beam.

To increase the produced power of the second harmonic beam, we place the crystal inside a resonant Fabry-Perot cavity that is resonant for the fundamental frequency but not for the second harmonic one that escapes the cavity through the input mirror.

Both SHG share the same cavity properties. The SHG cavities are 45 mm long with the coating specifications given in Table 4.3 resulting in a finesse at 1064 nm of $\mathcal{F} = 57$ and a linewidth of 58 MHz.

Wavelength	$\lambda = 1064 \text{ nm}$	$\lambda = 532 \text{ nm}$
Input mirror	$R = 0.9$	$R < 0.01$
End mirror	$R = 0.995$	$R > 0.999$

Table 4.3 – Coating specifications for the Exsqueez Second Harmonic Generators SHG1 and SHG2.

The end mirror of the cavity is placed on a piezoelectric actuator controlled remotely to be able to adjust the length of the cavity and keep it on resonance for the fundamental 1064nm beam using the Pound-Drever-Hall technique described in Section 4.1.3.

The second difference between SHG1 and SHG2 stands in the modulation frequency chosen to lock the cavities. The SHG1 cavity uses a modulation frequency of 12.4 MHz, while the SHG2 cavity uses a modulation frequency of 50 MHz. To fully understand the choice of modulation frequencies, we have to keep in mind the whole conceptual design. Consequently I will come back to the modulation frequency choice in Section 4.6.

¹Note that the acquisition system provided by LAPP for Exsqueez is the same one as what they provide for Advanced Virgo, meaning that it would be easier to transfer to Advanced Virgo what have been done in CALVA.

To summarize this part on the main and auxiliary SHG, I represented in Figures 4.7a and 4.7b the conceptual design of SHG1 and SHG2 with their locking schemes and the origin of the 8 beams defined in Section 4.1.2 and Table 4.2.

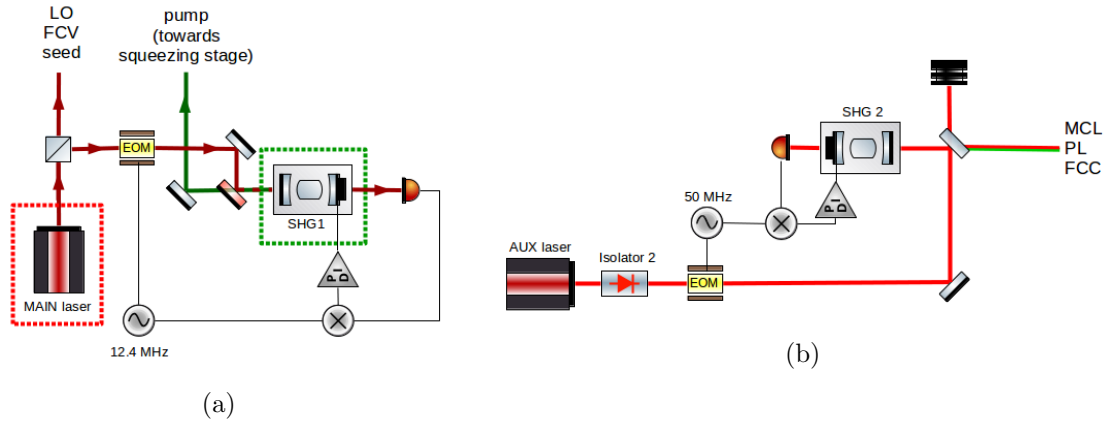


Figure 4.7 – Scheme of the (a) main Second Harmonic Generator (SHG1) and (b) auxiliary Second Harmonic Generator (SHG2) including the locking schemes and the name of the beams generated according to Table 4.2. Note that the squeezed beam is not produced at this stage but will be generated from the pump beam.

4.3 Optical Parametric Oscillator

4.3.1 Non linear medium

For Exsqueeze we use a periodically-poled potassium titanyl phosphate (PPKTP) crystal as Optical Parametric Oscillator (OPO). The periodic poling, represented by the blue and orange portions in the crystal scheme of Figure 4.8, allows a quasi-phase matching as explained in Section 3.5.1.

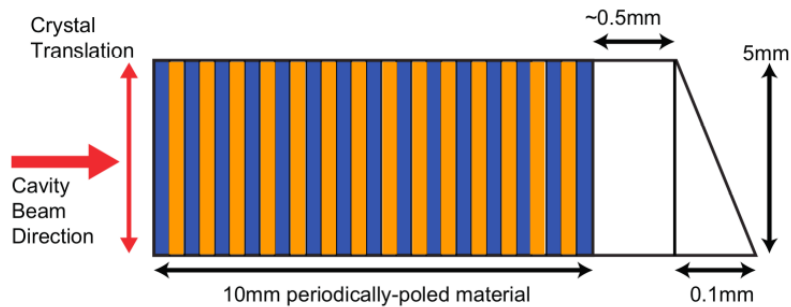


Figure 4.8 – Schematic of the OPO non linear wedged crystal [78]. The periodically poled material is represented by the blue and orange boxes while the non poled material is represented in white.

The PPKTP crystal that we use is 1 mm thick, 5 mm wide and 11.2 mm long before polishing. It is composed of 10.2 mm of periodically poled KTP with a period of $9 \mu\text{m}$ and 1 mm of non poled KTP with a 1.43° wedge. The reason of the use of non poled material and wedge will be detailed on Section 4.3.2.

The refractive index of light in the crystal depends on the temperature, consequently, for a given crystal there is an optimum of temperature to obtain the best phase matching of the input beam to the crystal. For the crystal we are using, the optimum temperature is between 28°C and 37°C , which is quite low and easy to reach and maintain. The PPKTP crystal used as an OPO has a high non linear gain coefficient and has been found to achieve the highest efficiency [106].

4.3.2 The doubly resonant bow-tie cavity

Doubly resonant cavity

The PPTKP crystal is placed inside an optical cavity of total length 255 mm, that is resonant at the pump field frequency to increase the number of passages of the beam inside the crystal and as a result to increase the squeezing production.

Moreover, the resonance of the pump field inside the cavity allows to use the pump field to lock the cavity using the Pound-Drever Hall technique described in Section 4.1.3, using a photodiode in reflection of the cavity. The finesse of the cavity at the pump frequency is 28 and the modulation frequency to lock the OPO is 12.4 MHz.

The cavity is also resonant at the fundamental frequency of the squeezed field with a finesse of 35 allowing the selection of the squeezed photons frequency inside the linewidth of 17 MHz of the cavity, as represented in Figure 4.9.

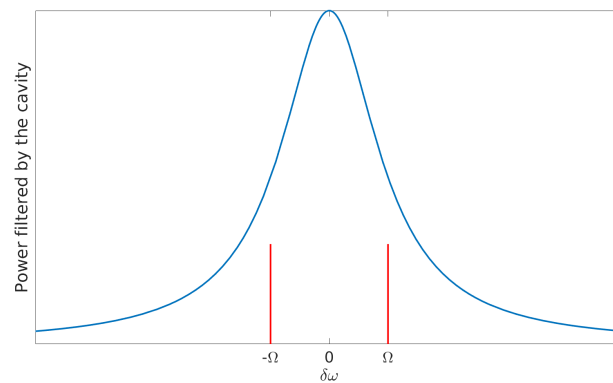


Figure 4.9 – In blue: Power filtered by the cavity according to the frequency separation from the fundamental frequency ω_0 . In red: example of $\omega_0 \pm \Omega$ squeezed photons frequencies resonating inside the cavity.

This doubly resonant system also ensures a good overlap between the pump field and the fundamental field. Nevertheless, the intra-cavity dispersion of the fundamental and harmonic fields due to the PPKTP crystal leads to a slight offset between the resonance frequency of the two fields. This can be compensated by leaving a wedged non periodically poled section at the end of the crystal [106] as represented in Figure 4.8. One can then change the effective path length and consequently the phase relationship between the two beams by lateral translation of the crystal position perpendicular to the beam propagation direction.

Bow-tie travelling wave cavity

The cavity used is a bow-tie travelling cavity as represented in Figure 4.10 with two flat mirrors M_1 and M_2 to scan and lock the cavity and two curved mirrors M_3 and M_4 with a radius of curvature of 38 mm to focus the beam inside the crystal. The first advantage of this configuration is the number of potential ports available for input and output of optical fields used for OPO operation and characterization.

Nevertheless this increased number of mirrors is also a drawback as it increases optical losses, thus reducing the squeezing escape efficiency. It also reduces the total mechanical stability with respect to a linear cavity.

Moreover, the beam is not in normal incidence on the mirrors but has a small angle of $\theta = 12^\circ$ that introduces beam astigmatism. To reduce this effect, the smallest possible angles of incidence are used without clipping the beam. The astigmatism causes problems to matched the squeezed beam first to the filter cavity and then to the homodyne detection (or in the case of gravitational wave detector, to the interferometer itself).

However, another advantage of the bow-tie configuration is the isolation to backscattered light [84]. For instance scattered light coming from the homodyne detection will not be reflected back from the OPO to the homodyne detection. In addition, backscattered light propagates in the reverse direction inside the OPO with respect to the pump one and consequently it does not seed the OPO. The seeding of the OPO will be explained in Section 4.4.4.

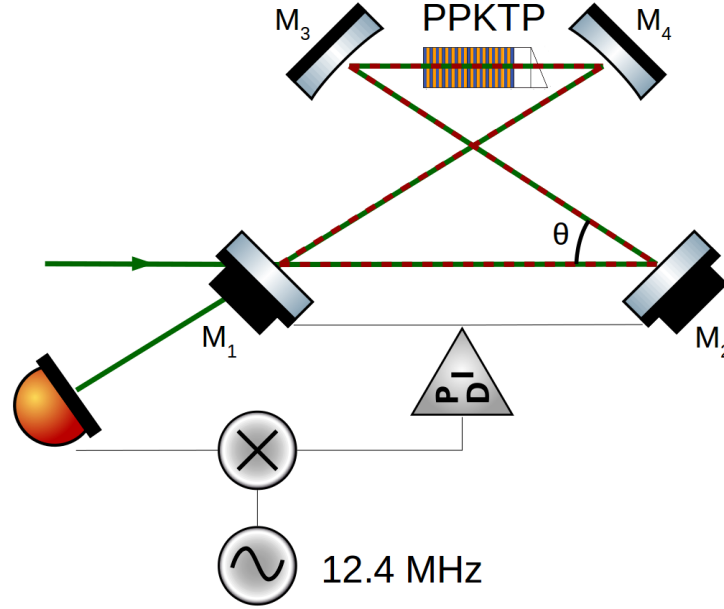


Figure 4.10 – Scheme of the OPO cavity.

Cavity mirrors positioning

To explain and define the choices made in dimensioning the OPO cavity, I first have to give some features of Gaussian optics. A Gaussian beam is fully described by its complex radius of curvature $q(z)$ at the z position:

$$\frac{1}{q(z)} = \frac{1}{R(z)} - i \frac{\lambda}{\pi n w(z)^2}, \quad (4.15)$$

where $R(z)$ is the beam radius of curvature and $w(z)$ the beam radius at the z position, λ the beam wavelength and n the refractive index of the medium. The beam radius $w(z)$ can be determined from its minimal radius w_0 , called waist:

$$w(z) = w_0 \sqrt{1 + \left(\frac{z}{z_R}\right)^2}, \quad (4.16)$$

with z_R the Rayleigh length, corresponding to the longitudinal distance, since the waist, after which the radius of the beam has increased by a factor $\sqrt{2}$:

$$z_R = \frac{\pi w_0^2}{\lambda}. \quad (4.17)$$

The ABCD matrix method [107] allows to determine the relationship between an input an output complex radius of curvature q_i and q_o after going through an optical system defined by a matrix M :

$$\begin{pmatrix} q_i \\ 1 \end{pmatrix} = kM \begin{pmatrix} q_o \\ 1 \end{pmatrix}, \quad (4.18)$$

with k a normalization factor and the M matrix can be written in its general form:

$$M = \begin{pmatrix} A & B \\ C & D \end{pmatrix}. \quad (4.19)$$

From Equation (4.18) and the ABCD coefficients of the M matrix, we can then write the direct relation between the input and the output complex radius of curvature:

$$q_o = \frac{Aq_i + B}{Cq_i + D}. \quad (4.20)$$

The beam radius is not necessary the same in the x and y direction because some optical systems, especially curved mirrors not in normal incidence, do not act in the same way in both directions. We have to define the tangential direction, corresponding to the x axis and the sagittal direction, corresponding to the y axis and we will add the subscripts t and s to the beams parameters.

To write the matrix corresponding to the OPO system, we first have to decompose it into a succession of simpler systems of known ABCD matrices. The 4 matrices $M_f(d)$, $M_i(n_1, n_2)$, $M_{rt}(R, \theta)$ and $M_{rs}(R, \theta)$ that are used to describe the OPO are given in Table 4.4. Note that for the reflection on a flat mirror, the corresponding matrix is the unity matrix both for the tangential and sagittal reflection at every angle of incidence.

Propagation	Interface	Tangential reflection	Sagittal reflection
$M_f(d) =$	$M_i(n_1, n_2) =$	$M_{rt}(R, \theta) =$	$M_{rs}(r, \theta) =$
$\begin{pmatrix} 1 & d \\ 0 & 1 \end{pmatrix}$	$\begin{pmatrix} 1 & 0 \\ 0 & \frac{n_1}{n_2} \end{pmatrix}$	$\begin{pmatrix} 1 & 0 \\ -\frac{2}{R \cos(\theta)} & 1 \end{pmatrix}$	$\begin{pmatrix} 1 & 0 \\ -\frac{2 \cos(\theta)}{R} & 1 \end{pmatrix}$

Table 4.4 – ABCD matrices used for the description of the OPO. The matrix of propagation over a distance d , the matrix of the refraction on an interface from a medium of refractive index n_1 to a medium of refractive index n_2 and the matrix of the tangential and sagittal reflection on a mirror of radius of curvature R with a angle of incidence θ with respect to the normal of the mirror.

From Figure 4.10 and Table 4.4, we can write the full round-trip matrix M_{OPO} of the OPO cavity as a multiplication of the elementary matrices. To do so, we note d_1 the flat mirror separation, i.e. the distance between M_1 and M_2 and d_3 the curved mirror separation, i.e. the distance between M_3 and M_4 . The crystal length is noted d_c , the refractive index of the crystal is n and the distance between M_2 and M_3 , which is by design the same as the one between M_1 and M_4 , is noted d and fixed by d_1 , d_3 , and the angle θ :

$$d = \frac{d_1 + d_3}{2 \cos(\theta)}. \quad (4.21)$$

Starting from the first mirror of the OPO, M_1 , the matrix of the OPO M_{OPO_p} where p stands for the tangential (t) or sagittal (s) plane, is written:

$$M_{OPO_p} = M_f(d) M_{rp} \left(R, \frac{\theta}{2} \right) M_f \left(\frac{d_3 - d_c}{2} \right) M_i(n, 1) M_f(d_c) \quad (4.22)$$

$$\times M_i(1, n) M_f \left(\frac{d_3 - d_c}{2} \right) M_{rp} \left(R, \frac{\theta}{2} \right) M_f(d_1 + d)$$

$$M_{OPO_p} = \begin{pmatrix} A_{OPO_p} & B_{OPO_p} \\ C_{OPO_p} & D_{OPO_p} \end{pmatrix}. \quad (4.23)$$

The OPO cavity is stable and resonates if the complex radius of curvature of the beam at a specific position inside the cavity remains the same after one round trip. From Equation

(4.20), the complex radius of curvature q_{1p} on the input mirror of the OPO, M_1 is the solution of:

$$\frac{B_{OPO_p}}{q_{1p}^2} + \frac{(A_{OPO_p} - D_{OPO_p})}{q_{1p}} - C_{OPO_p} = 0. \quad (4.24)$$

Equation (4.24) gives a complex radius of curvature if its discriminant is negative. This condition can be written using a stability factor m_p defined as:

$$m_p = \frac{Tr(M_{OPO_p})}{2} = \frac{A_{OPO_p} + D_{OPO_p}}{2}. \quad (4.25)$$

The stability condition is then:

$$-1 \leq m_p \leq 1, \quad (4.26)$$

for both the tangential and sagittal plane and for both wavelength of the pump beam and the squeezed beam. Under this condition the complex radius of curvature q_{1p} on the input mirror of the OPO, M_1 is defined by:

$$\frac{1}{q_{1p}} = \frac{D_{OPO_p} - A_{OPO_p} + i\sqrt{4 - Tr(M_{OPO_p})^2}}{2B_{OPO_p}}. \quad (4.27)$$

Then from Equation (4.27), we can obtain the beam radius all along its path inside the OPO cavity for a given set of d_1 , d_3 , d_c , R and θ values. When the cavity is stable there are two waists: one in the middle of the curved mirrors, and one in the middle of the flat mirrors. To improve the squeezing production, there is an optimal waist size of 30 μm inside the crystal for the infrared squeezed beam [108].

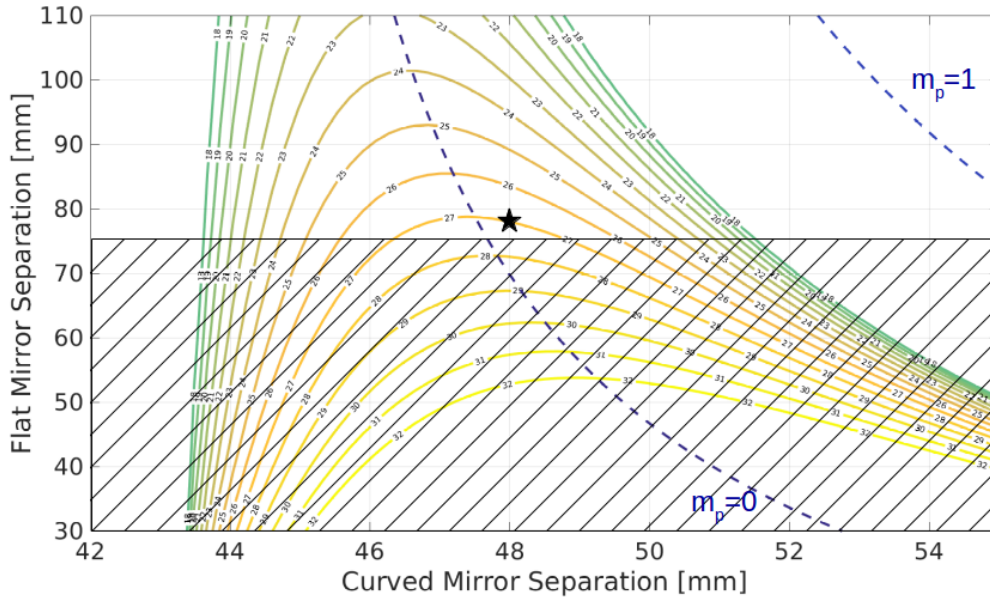


Figure 4.11 – Simulation of the sagittal beam waist radius of the infrared beam inside the crystal when scanning the flat and curved mirrors separations. The solid lines corresponds to the waist radius, the dashed line represent the stability factor. The dashed region is not accessible with our experimental set up that fixed the minimal flat mirror separation and the black star is the value we chose to use for our OPO: $d_1 = 78$ mm and $d_3 = 48$ mm leading to an infrared sagittal waist radius inside the crystal of 27 μm .

We already fixed the value of $\theta = 12^\circ$ to minimized the beam astigmatism. The length d_c of the crystal and the radius of curvature R of the curved mirrors were fixed in previous works [84]. Consequently, the parameter space is given by d_1 and d_3 . In Figure 4.11, I simulated the sagittal beam waist radius of the infrared beam inside the crystal.

From this simulation we can see that an infrared waist size of $30\ \mu\text{m}$ inside the crystal is not achievable on our experimental set-up due to physical constraints as we are limited to a flat mirror separation above $75\ \text{mm}$. To not be too close to our limitation, but as close as possible to the $30\ \mu\text{m}$ waist radius, we decided to chose an infrared sagittal waist radius inside the crystal of $27\ \mu\text{m}$ with $d_1 = 78\ \text{mm}$ and $d_3 = 48\ \text{mm}$ (a larger curved mirror separation was better in our physical system to keep the $\theta = 12^\circ$ angle for the OPO).

For these values I simulated the beam radius all along its trajectory inside the OPO in Figure 4.12 for the infrared and green beams in the tangential and sagittal planes. This enabled us to check that the beam width stayed below 1/2-inch mirrors radius to avoid beam clipping. With this simulation we obtained the second cavity waist radius that is out of the crystal and that is experimentally measurable: $115.5\ \mu\text{m}$ for the green beam and $159.9\ \mu\text{m}$ for the infrared beam in the sagittal plane.

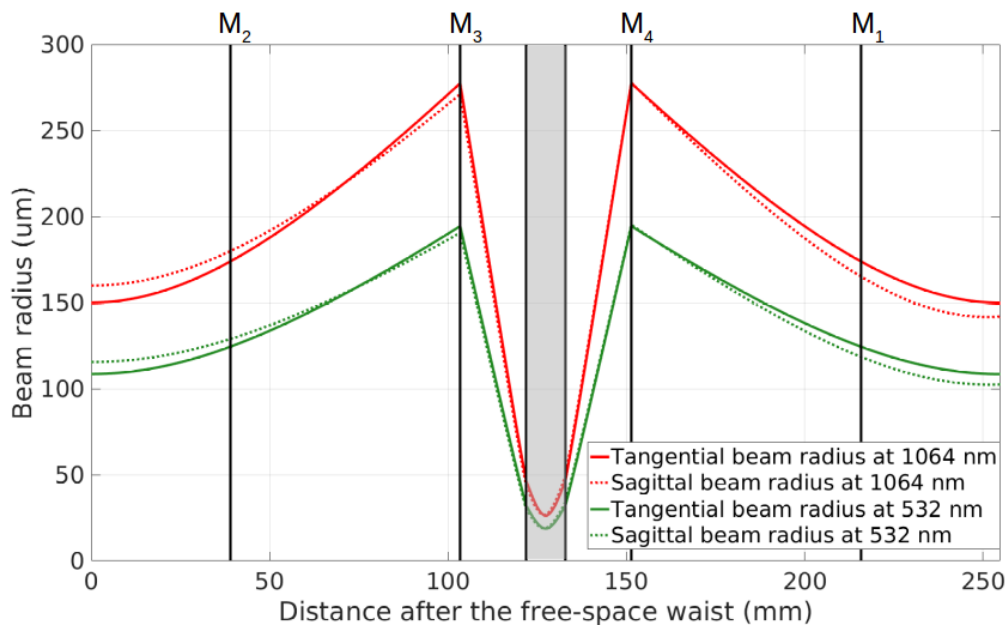


Figure 4.12 – Simulation of the beam radius all along its trajectory inside the OPO for the infrared and green beams in the tangential and sagittal planes.

4.4 Control of the squeezing production

4.4.1 Power fluctuation reduction using a Mach-Zehnder

The squeezing produced from the $532\ \text{nm}$ pump beam depends on the power of this beam. Power fluctuations can affect the degree of measured squeezing and anti-squeezing [109] and therefore lead to squeezing ellipse jitter causing losses as described in Section 3.6.4.

Nevertheless, the infrared beam power from the main laser is not stabilized in power. Moreover, the conversion efficiency of the second harmonic generator described in Section 4.2 also depends on the infrared power as fluctuations of input power change the temperature and consequently the phase matching condition. This two factors lead to power fluctuations of the pump beam generating the squeezing. We have to reduce these power fluctuations.

A solution to stabilize the beam power is to use a Mach-Zehnder interferometer schematized in Figure 4.13.

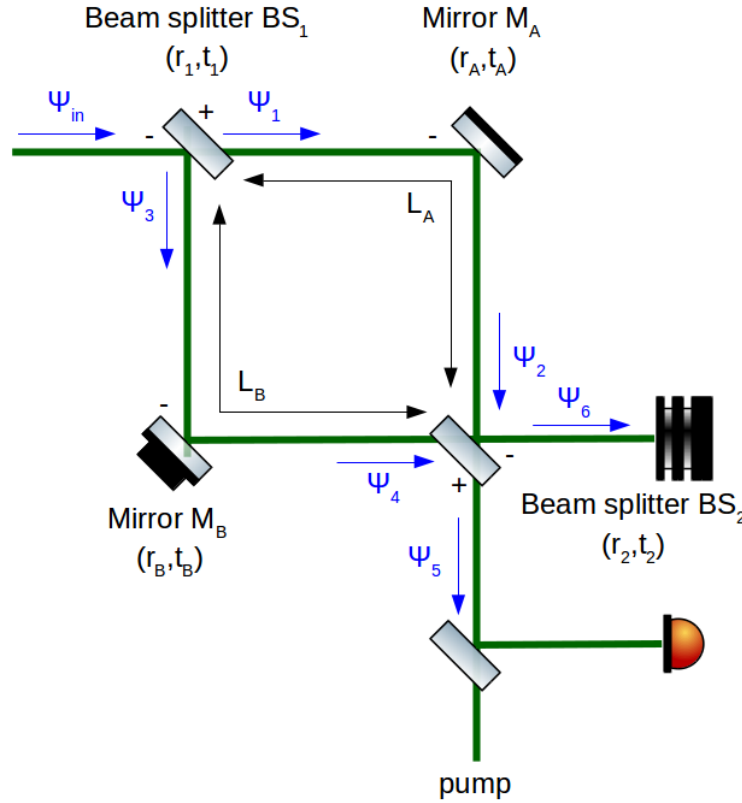


Figure 4.13 – Scheme of a Mach-Zehnder interferometer.

Using the same rules as in Section 2.2.2 and the scheme of Figure 4.13, we can write the electromagnetic field, for a beam of wave vector k , at several points in the interferometer with respect to the incoming field ψ_{in} on the first beam splitter:

$$\psi_1 = t_1 \psi_{in}, \quad (4.28)$$

$$\psi_2 = -r_A t_1 \psi_{in} e^{-ikL_A}, \quad (4.29)$$

$$\psi_3 = -r_1 \psi_{in}, \quad (4.30)$$

$$\psi_4 = r_B r_1 \psi_{in} e^{-ikL_B}, \quad (4.31)$$

$$\psi_5 = t_2 \psi_2 + r_2 \psi_4, \quad (4.32)$$

$$\psi_6 = -r_2 \psi_2 + t_2 \psi_4. \quad (4.33)$$

The two important beams are the ones going out of the second beam splitter. We can write their fields ψ_5 and ψ_6 with respect to the incoming field ψ_{in} :

$$\psi_5 = \left(-r_A t_1 t_2 e^{-ikL_A} + r_B r_1 r_2 e^{-ikL_B} \right) \psi_{in}, \quad (4.34)$$

$$\psi_6 = \left(r_A r_2 t_1 e^{-ikL_A} + r_B r_1 t_2 e^{-ikL_B} \right) \psi_{in}. \quad (4.35)$$

Consequently the power in the two beams going out of the Mach-Zehnder interferometer are:

$$P_5 = P_{in} \left[r_A^2 t_1^2 t_2^2 + r_B^2 r_1^2 r_2^2 - 2r_A r_B r_1 r_2 t_1 t_2 \cos(k\delta L) \right], \quad (4.36)$$

$$P_6 = P_{in} \left[r_A^2 r_2^2 t_1^2 + r_B^2 r_1^2 t_2^2 + 2r_A r_B r_1 r_2 t_1 t_2 \cos(k\delta L) \right], \quad (4.37)$$

where $\delta L = L_A - L_B$ is the difference between the two arms lengths.

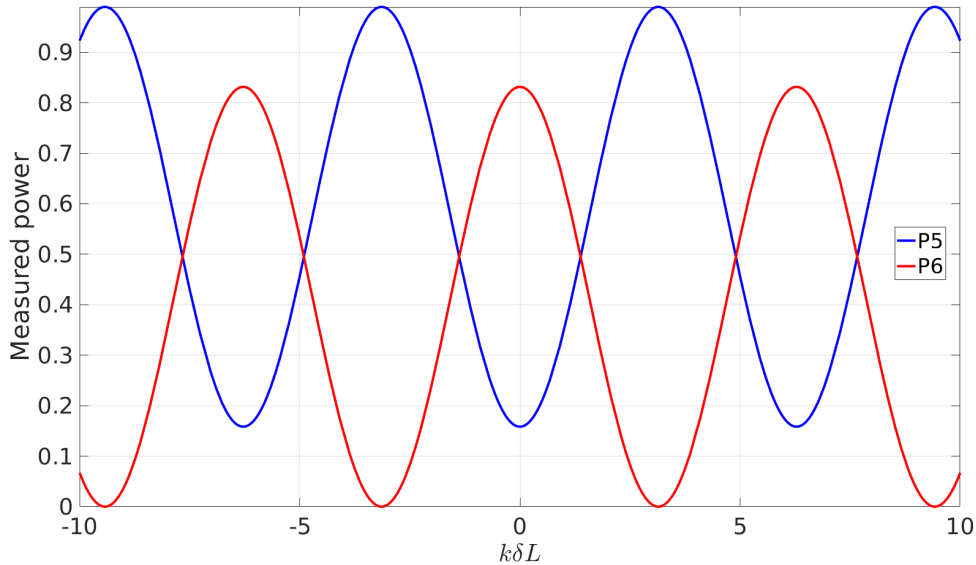


Figure 4.14 – Power exiting the two arms of an asymmetric Mach-Zehnder interferometer with 70:30 beam splitters according to Equations (4.36) and (4.37) and corresponding to Figure 4.13, when varying the relative length between both arms of the interferometer.

From Equations (4.36) and (4.37), the power going out of each arm of the Mach-Zehnder interferometer depends on δL , the difference between the two arm lengths. They are represented in Figure 4.14 for an asymmetric Mach-Zehnder interferometer with 70:30 beam splitters.

We chose an asymmetric Mach-Zehnder with two beam splitters that reflect 70% of green power to ease the alignment by blocking the A arm of the Mach-Zehnder. Indeed, in that case, there is most of the power in the output P_5 of the Mach-Zehnder that is sent to the squeezer. Moreover some measurements will be described in Chapter 6 to characterize the OPO nonlinear gain using the Mach-Zehnder with one arm blocked.

To lock the Mach-Zehnder and stabilize the pump beam power, we place on the pump path a beam sampler that reflects 8% of green power towards a photodiode. The mirror M_B is placed on a piezoelectric to slightly change the difference between the two arm lengths δL . The Mach-Zehnder is then locked so that the beam power on the photodiode is fixed, via a DC subtraction locking loop. The power fluctuation of the pump beam entering the squeezer are then reduced.

Note that the second output P_6 of the interferometer cannot be used to stabilize the power on the first output P_5 as long as the input power P_{in} is not constant.

A second stage of stabilization can be achieved if needed using as error signal the pump power measured either in transmission or reflexion of the Optical Parametric Oscillator (OPO).

4.4.2 Modified Coherent Locking scheme

Now that we produce a stable green beam to pump the Optical Parametric Oscillator (OPO) and generate a squeezed beam, the next step is to control the squeezing ellipse phase with respect to the measurement quadrature. The quadrature angle of the produced squeezing depends on the phase of the pump beam at the interaction point inside the crystal of the OPO.

Several techniques have been developed to control the ellipse phase like quantum noise locking [110] or the coherent sideband locking [111]. For Exsqueezez, we use a modified coherent sideband locking technique [112] that I will describe hereafter.

Modified Coherent Locking beam

The modified coherent locking scheme uses a new control field, the Modified Coherent Locking beam (MCL), that is coherent with the squeezed field but frequency shifted in order not to interfere with it. This ensures that noise from the control field does not deteriorate the non classical performance of the squeezed field. Nevertheless, the frequency shift of the MCL beam should stay in the linewidth of the OPO cavity so that it escapes from the cavity after sensing the crystal nonlinearity.

The simplified conceptual scheme presenting the modified coherent locking technique is shown in Figure 4.15. I will now go through its details.

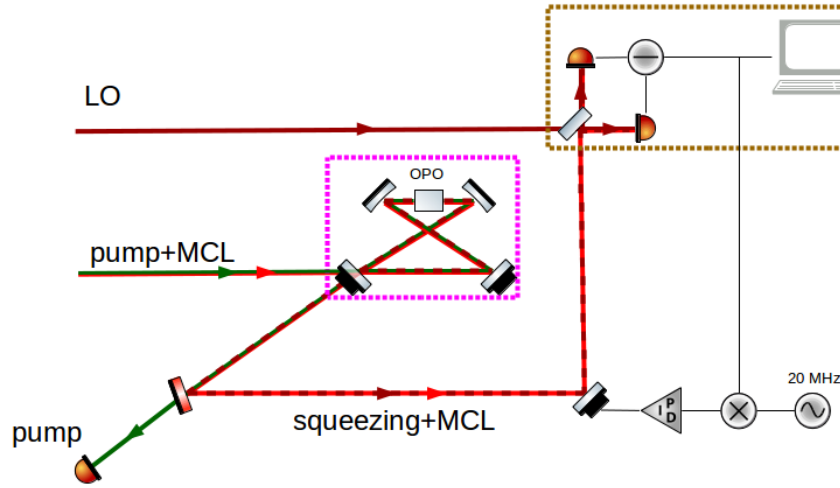


Figure 4.15 – Simplified conceptual scheme of the Modified Coherent Locking technique.

Before entering the OPO, one can consider the MCL beam as a single sideband field with respect to the fundamental frequency of the squeezed beam ω_0 . Its frequency is $\omega_0 + \Omega_{PLL}$ and its amplitude is noted $\alpha_{\Omega_{PLL}}$.

After going through the OPO, the electric field of the MCL beam E_{MCL} is [111]:

$$E_{MCL}(t) \propto \frac{1+g}{\sqrt{2g}} \alpha_{\Omega_{PLL}} \cos(\omega_0 t + \Omega_{PLL} t) - \frac{1-g}{\sqrt{2g}} \alpha_{\Omega_{PLL}} \cos(\omega_0 t - \Omega_{PLL} t - 2\theta), \quad (4.38)$$

where θ is the quadrature angle of the squeezing and $\exp(\sigma) = \sqrt{g}$ with σ the squeeze factor as defined in Equation (3.32).

From Equation (4.38), one can see that after interacting through the OPO, the MCL beam is composed of two sidebands at $\omega_0 \pm \Omega_{PLL}$. Note that if there is no non linear interaction, i.e. no squeezing, we have $r = 0$ and thus $g = 1$, in this case, the $\cos(\omega_0 t - \Omega_{PLL} t - 2\theta)$ term disappear and there is only the initial sideband at $\omega_0 + \Omega_{PLL}$ left.

The MCL beam has to resonate inside the OPO cavity, consequently its frequency must not be too far from the OPO linewidth in infrared given in Section 4.3, which is 17 MHz. We chose to use $\Omega_{PLL} = 20$ MHz.

Then the MCL beam is sent to the homodyne detection where it is recombined with the Local Oscillator beam (LO), that is a tap off from the main laser at the squeezing frequency ω_0 with amplitude α_{LO} . The difference photocurrent i_- of the homodyne photodiodes is given by [111]:

$$i_- \propto \frac{2\sqrt{2}\alpha_{LO}\alpha_{\Omega_{PLL}}(g-1)}{\sqrt{g}} \cos(\Omega_{PLL} t + 2\theta + \phi), \quad (4.39)$$

where ϕ is the phase between the MCL and LO beams. After demodulating i_- at Ω_{PLL} , applying a low-pass filter and tuning the demodulation phase delay, as done for the PDH

technique in Section 4.1.3, we obtain the error signal:

$$S_{err}^{MCL-LO} \propto \frac{\sqrt{2}\alpha_{LO}\alpha_{\Omega_{PLL}}(g-1)}{\sqrt{g}} \sin(2\theta + \phi). \quad (4.40)$$

From equation (4.40), the error signal depends on the squeezing angle θ and on the relative phase ϕ between the MCL and LO beams.

Then if we fix the phase relationship between the MCL beam and the pump beam, meaning we fix the squeezing angle θ , we are able to fix the measurement quadrature ϕ of the squeezing using a mirror on a piezoelectric mount on the MCL path as shown in Figure 4.15. Note that the piezo could also have been placed on the LO path.

To fix the phase relationship between the MCL beam and the pump beam, we chose to use an auxiliary infrared laser frequency shifted from the main laser and phase locked with the main laser. The details of the phase locking of the main and auxiliary lasers will be given in Section 4.4.3.

The important thing to note is that we use a Second Harmonic Generator (SHG), described in Section 4.2 to obtain a green beam frequency shifted from the pump beam, the Phase Locking beam (PL). The MCL and the PL beams co-propagate from the SHG and then they are recombined with the pump beam on a dichroic plate.

From this point, the MCL and the pump beam are superposed and co-propagate towards the OPO. From this same point, in another direction, the PL and a pick off of the pump beams co-propagate towards the phase locking loop photodiode which allows to phase lock both main and auxiliary lasers as shown in Figure 4.16. This lock fixes the phase relationship on the dichroic plate and later on their propagation of the MCL beam, coming from the auxiliary laser, and the pump beam, coming from the main laser.

4.4.3 Phase Locking Loop

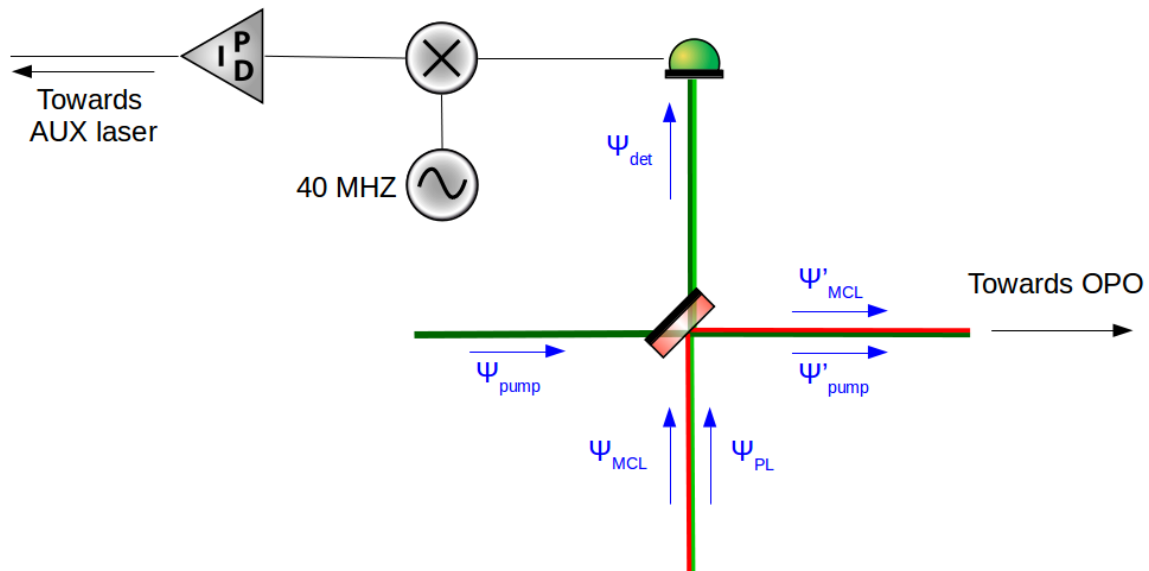


Figure 4.16 – Optical scheme of the Phase Locking Technique.

To phase lock the main laser and the auxiliary laser we use the green beams produced by the Second Harmonic Generators (SHG), described in Section 4.2, on both main and auxiliary paths. They are the pump and the Phase Locking (PL) beams.

As described before and represented in Figure 4.16, the Modified Coherent Locking beam (MCL) and the frequency doubled PL beam co-propagate towards a dichroic plate that reflects 12% of the infrared MCL beam towards the OPO and transmits 96% of the green PL beam

towards a photodiode. On the same dichroic plate, the pump beam is transmitted towards the OPO and superposed with the MCL but 2% of the pump power, representing few mW in operation, are reflected towards the photodiode.

Before the beam splitter, the two green incoming fields ψ_{pump} and ψ_{PL} can be written:

$$\psi_{pump} = \psi_{pump}^0 e^{2i\omega_0 t}, \quad (4.41)$$

$$\psi_{PL} = \psi_{PL}^0 e^{2i\omega_0 t + 2i\Omega_{PLL} t}. \quad (4.42)$$

Then, using the same rules as in Section 2.2.2 and the scheme in Figure 4.16, noting, r_{DC} , and t_{DC} the amplitude reflectivity and transmissivity of the dichroic beam splitter for the green beam, we can write the electromagnetic field that goes to the photodiode ψ_{det} :

$$\psi_{det} = r_{DC}\psi_{pump} + t_{DC}\psi_{PL}. \quad (4.43)$$

Consequently, the power measured P_{det} is:

$$P_{det} = r_{DC}^2 |\psi_{PL}^0|^2 + t_{DC}^2 |\psi_{pump}^0|^2 + 2 \operatorname{Re} \left(r_{DC} t_{DC} \psi_{PL}^0 \psi_{pump}^0 \right) \cos(2\Omega_{PLL} t). \quad (4.44)$$

After demodulation at ω_{ref} applying a low-pass filtering and choosing the appropriate demodulation phase delay, as explained for the PDH technique in Section 4.1.3, the error signal measured is:

$$P_{det}^{err} \propto \sin(2(\Omega_{PLL} - \omega_{ref})t). \quad (4.45)$$

The error signal of Equation (4.45) is represented in Figure 4.17. One can see that around $\Omega_{PLL} = \omega_{ref}$ the error signal is linear and centered on zero, making it a good error signal.

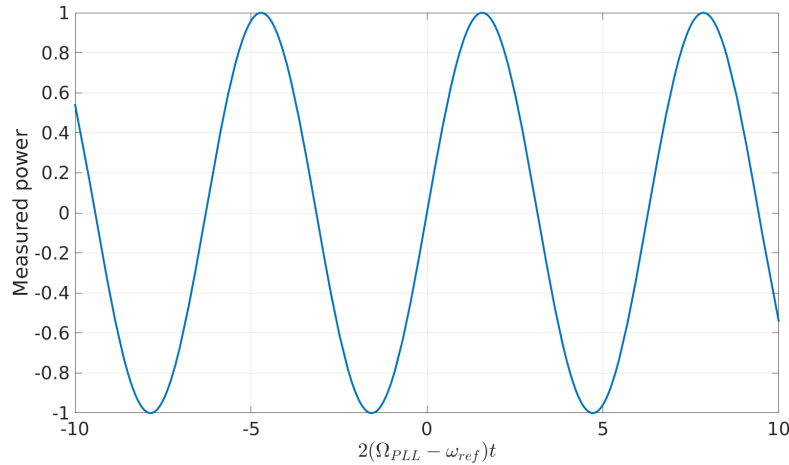


Figure 4.17 – Error signal for the Phase Locking Loop.

4.4.4 Seed beam

To characterize the non linear interaction in the Optical Parametric Oscillator (OPO), a seed beam is sent to the OPO as represented in Figure 4.18. This seed beam won't be used during the production of squeezing but only for characterization of the OPO and homodyne detection efficiencies that will be done in Chapter 6.

The seed field is a tap off beam from the main laser and is consequently at the squeezing fundamental frequency like the local oscillator (LO) beam. Thus, it undergoes non linear interaction when going through the crystal of the OPO. It acts as a bright seed field leading to degenerate optical parametric amplification as represented in Figure 4.19.

The bright seed field acts as a catalyst for the reaction of the pump photon down conversion. Only a small portion of the pump field undergoes this down conversion process leading

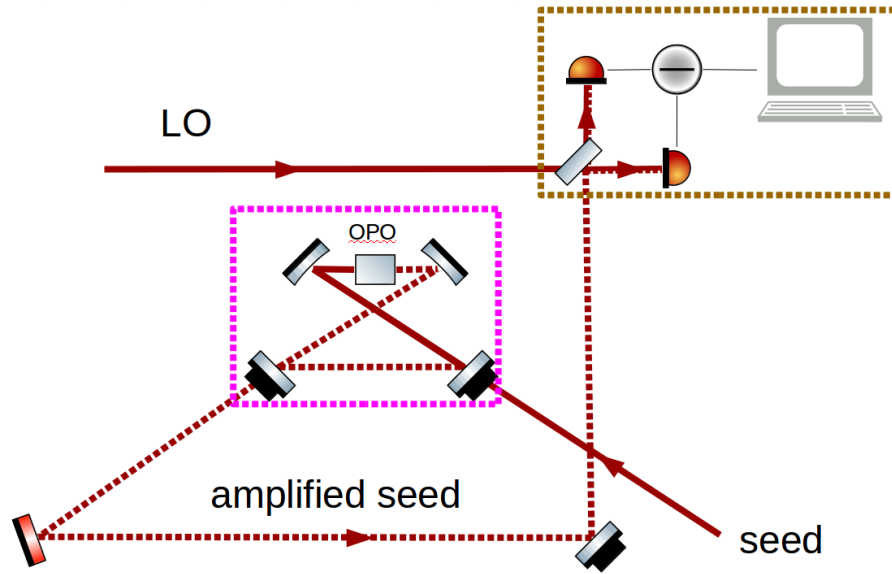


Figure 4.18 – Simplified conceptual scheme of the OPO with the seed field and the homodyne detection with the local oscillator (LO) field.

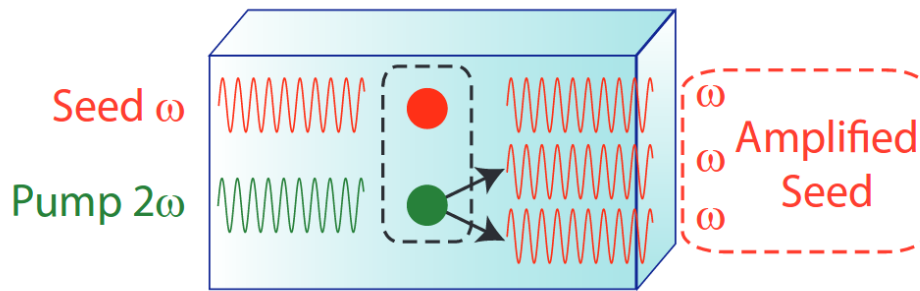


Figure 4.19 – Scheme of a degenerate optical parametric amplifier [84].

to a small amplification of the seed field. By changing the pump power and measuring the amplification and de-amplification of the seed field on one of the homodyne photodiodes, this allows us to determine the pump threshold power of the OPO.

Moreover, the waist size and position of the LO and squeezed beams should be exactly the same on the beam splitter before the two homodyne detection photodiodes to achieve complete destructive or constructive interference. The visibility \mathcal{V} quantifies the spatial mode mismatch between the signal (squeezed or seed) and local oscillator beams. It is defined by:

$$\mathcal{V} = \frac{P_{max} - P_{min}}{P_{max} + P_{min}}, \quad (4.46)$$

where P_{max} and P_{min} are respectively the maximum and minimum power measured as the relative phase between the two beams is varied.

The seed beam goes through the OPO cavity and has the same frequency as the squeezed beam, thus the seed field has the same mode shape than the squeezed field. Consequently, we can characterize the homodyne detection efficiency by measuring the visibility of the homodyne detection system with the seed beam.

4.5 Filter cavity

The filter cavity of Exsqueez is composed of two suspended spherical mirrors separated by 50 m. It takes advantage of the existing 50 m cavity of the CALVA facility.

The main parameters of the mirrors are their sizes, radius of curvature and coating specifications. The size of the mirrors is fixed by the CALVA facility on which the mirror mounts for the suspended mirrors are designed for 2-inch optics. I will present now the choices of radius of curvature and coating specifications of the mirrors.

4.5.1 Mirrors radius of curvature

There are several criteria to take into account to choose the mirrors radius of curvature: the stability of the cavity, the clipping loss on the mirrors and round trip losses of the cavity. I will detail them now.

Stability of the cavity

First of all the resulting cavity should be stable in order to keep the beam refocusing inside the cavity. To characterize this stability, we can define a stability parameter g_i for each mirror of the cavity:

$$g_i = 1 - \frac{L}{R_i}, \quad (4.47)$$

with L the length of the cavity and R_i the radius of curvature of the mirrors. Then the stability criterion is:

$$0 \leq g_1 g_2 \leq 1. \quad (4.48)$$

In practice we avoid to have $R_i = L$ because this is marginally stable and any imperfection on the mirror radius of curvature leads to an unstable cavity.

Clipping losses

To reduce the clipping losses we use the same radius of curvature R on both input and end mirrors of the cavity. This leads to a waist in the middle of the cavity and the same beam diameter on both mirrors. The waist of a resonating beam of wavelength λ inside the cavity of length L is then:

$$w_0 = \sqrt{\frac{\lambda L}{2\pi} \sqrt{\frac{2R}{L} - 1}}, \quad (4.49)$$

leading to beam radius w_m on the mirrors of the cavity:

$$w_m = w_0 \sqrt{1 + \left(\frac{\lambda L}{2\pi w_0^2}\right)^2}. \quad (4.50)$$

Moreover, the CALVA facility has in-vacuum suspension mounts for 2-inch mirrors that will be used for Exsqueez. The beam waist size on the cavity mirrors is represented according to the radius of curvature R of the cavity mirrors in Figure 4.20 for a beam of wavelength $\lambda = 1064$ nm and a cavity of length $L = 50$ m. One can see that radius of curvature from 29 m to 189 m lead to beams radius of less than one fifth of the 2-inch mirror radius on it.

Round trip losses

An estimation of the round trip losses of the cavity according to the mirrors radius of curvature has been done using the technique described in [113]. It is represented in Figure 4.21. It seems to be no special place to avoid the resonances of higher order modes. Nevertheless, the peak density seems to reduce with the increase of the radius of curvature. In addition, it is easier to polish flatter mirrors. Consequently radius of curvature of $R = 150$ m have been chosen for the filter cavity mirrors.

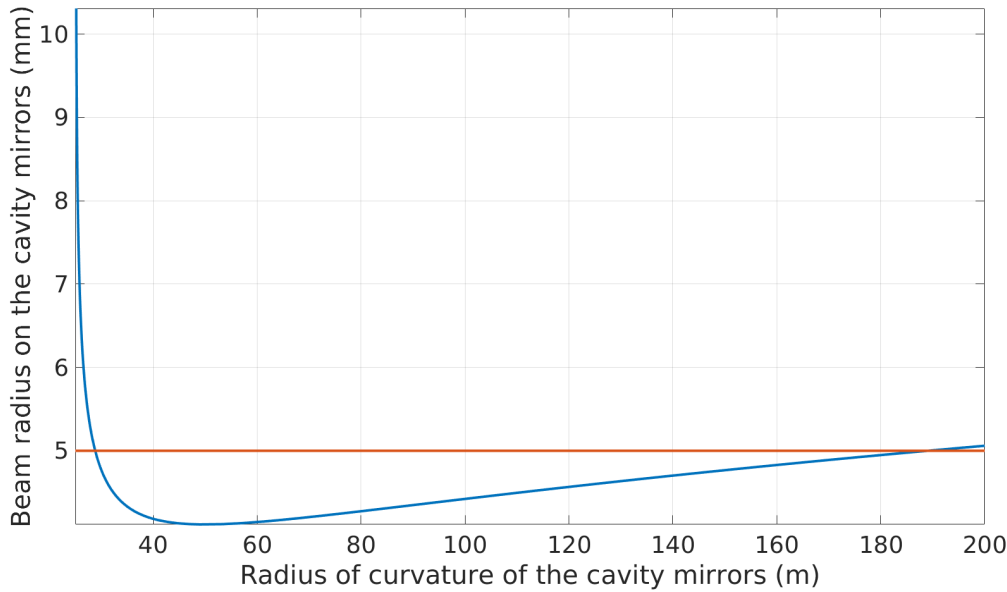


Figure 4.20 – In blue: plot of the beam radius on the mirrors of a 50 m length cavity for $\lambda = 1064$ nm. In red: upper limit on the beam radius to limit the clipping losses by having $5w_m$ on the 2-inch mirror.

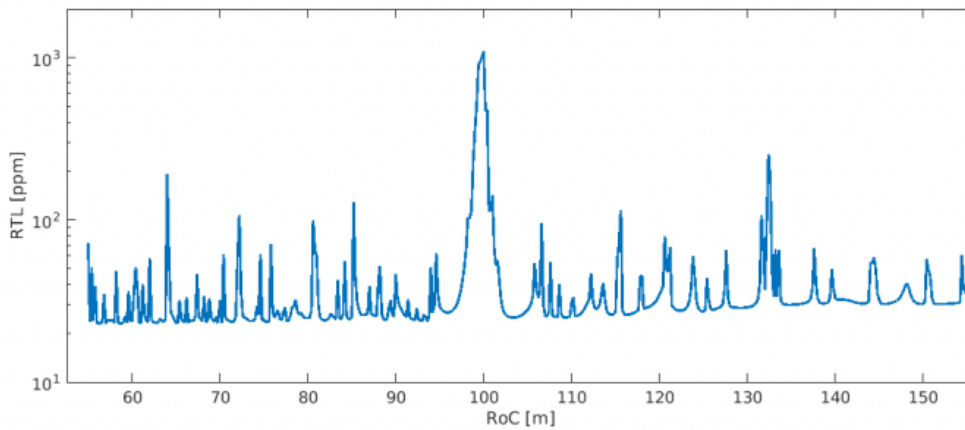


Figure 4.21 – Simulation of the round trip losses with respect to the cavity mirrors radius of curvature.

4.5.2 Mirrors coating specifications

The coating specifications will depend on the beams that have to resonate inside the cavity. The first beam is the squeezed beam with a wavelength $\lambda = 1064$ nm. According to Section 3.4.2, the finesse of the filter cavity depends on the corner frequency we want to achieve as defined by Equations (3.61) and (3.59).

The first goal of Exsqueezez is to demonstrate frequency dependent squeezing with a corner frequency below 1 kHz. We chose a finesse of the filter cavity $\mathcal{F}_{IR} \simeq 3000$ leading to a corner frequency $\Omega_t \simeq 700$ Hz¹.

However the finesse of the cavity will be too high at $\lambda = 1064$ nm to acquire the lock of the suspended cavity in an easy and reproducible way. The solution will be to lock the cavity using a green auxiliary laser at $\lambda = 532$ nm as it will be explained on Section 4.5.3.

¹Note that here and all over the rest of the thesis we use the usual convention to write the frequencies with the angular frequency ω letter while they are not angular frequencies and should not be multiplied by 2π to recover the frequency.

The finesse of the cavity for this beam will be $\mathcal{F}_{\text{green}} \simeq 150$ with a linewidth of 20 kHz and a separation of 800 kHz between two high order modes. Consequently, this finesse is high enough to degenerate higher order modes and lock on the fundamental mode but low enough to easier acquire the lock. Moreover, the coating formula for the finesse $\mathcal{F}_{\text{green}} \simeq 150$ is already known by LMA/IP2I, as it is the one used on Virgo, and can be done in a robust way.

According to Equation (2.75), the finesse of a cavity depends on the reflectivity of both mirrors. Moreover, as explained on Section 2.4.1, the phase shift in reflection induced by the cavity is enhanced around the resonance for an over coupled cavity. Thus we use an over coupled filter cavity with an end mirror almost perfectly reflective.

However, the mirrors are not theoretical one surface but a medium with two surfaces and an anti-reflective coating has to be done on the second surface outside of the cavity to limit losses. The coating specifications for both wavelengths are summarized in Table 4.5.

Wavelength	$\lambda = 1064 \text{ nm}$	$\lambda = 532 \text{ nm}$
AR of the input mirror	$R < 100 \text{ ppm}$	$R < 1 \%$
HR of the input mirror	$T = 2000 \pm 200 \text{ ppm}$	$T = 4 \pm 1 \%$
HR of the end mirror	$T = 5 \pm 2 \text{ ppm}$	$T < 1 \%$
AR of the end mirror	$R < 500 \text{ ppm}$	$R < 1 \%$
Resulting finesse	$\mathcal{F}_{IR} = 3131_{-287}^{+350}$	$\mathcal{F}_{\text{green}} = 140 \pm 38$

Table 4.5 – Coating specifications for the Exsqueeze filter cavity mirrors. AR: Anti-reflective coating outside of the cavity. HR: High-reflective coating inside the cavity.

4.5.3 Control of the filter cavity

The mirrors of the filter cavity are suspended and their position is controlled using magnets at each corner of the mirror mount that are placed in 4 coils on the suspension as it will be shown in Section 5.3.3. By changing the current in the coils, we can steer the mirror position.

The filter cavity should be locked for the squeezed beam. However the squeezed beam has really low power due to the second order non linear interaction efficiency and the finesse of the cavity at the squeezing fundamental frequency is too high to lock the cavity directly on the squeezed beam.

Consequently we use a green beam to lock the cavity with a lower finesse. Moreover, as explained on Section 3.4.2, to have a squeezed quadrature rotation of $\pi/2$ in reflection of the filter cavity we need to optimally detuned the filter cavity by:

$$\Delta\omega_{fc} = \frac{\Omega_t}{\sqrt{2}}, \quad (4.51)$$

where $\Omega_t \simeq 700 \text{ Hz}$ is the corner frequency. That leads to a cavity detuning at the wavelength $\lambda = 1064 \text{ nm}$ of $\Delta\omega_{fc}^{IR} \simeq 500 \text{ Hz}$ and thus we should have $\Delta\omega_{fc}^{\text{green}} \simeq 1 \text{ kHz}$ at the control wavelength $\lambda = 532 \text{ nm}$.

We use the frequency doubled beam from the auxiliary laser to obtain a Filter Cavity Control beam (FCC). As shown in Figure 4.22, the beam reflected from the auxiliary Second Harmonic Generator is composed of the infrared Modified Coherent Locking beam (MCL) and the green Phase Locking beam (PL).

There is no need of high power on the PL beam for the phase lock of the lasers. Consequently, we place a dichroic beam splitter on the path of the MCL and PL beams that transmits only green. We now have a green beam that is $2\Omega_{PLL} = 40 \text{ MHz}$ down-shifted from the pump beam. Consequently we add an AOM that up-shifts the green beam frequency of $40 \text{ MHz} + \Delta\omega_{fc}^{\text{green}}$ and form the Filter Cavity Control (FCC) beam that is recombined in

vacuum on a dichroic beam splitter with the squeezed and MCL beams coming from the Optical Parametric Oscillator (OPO).

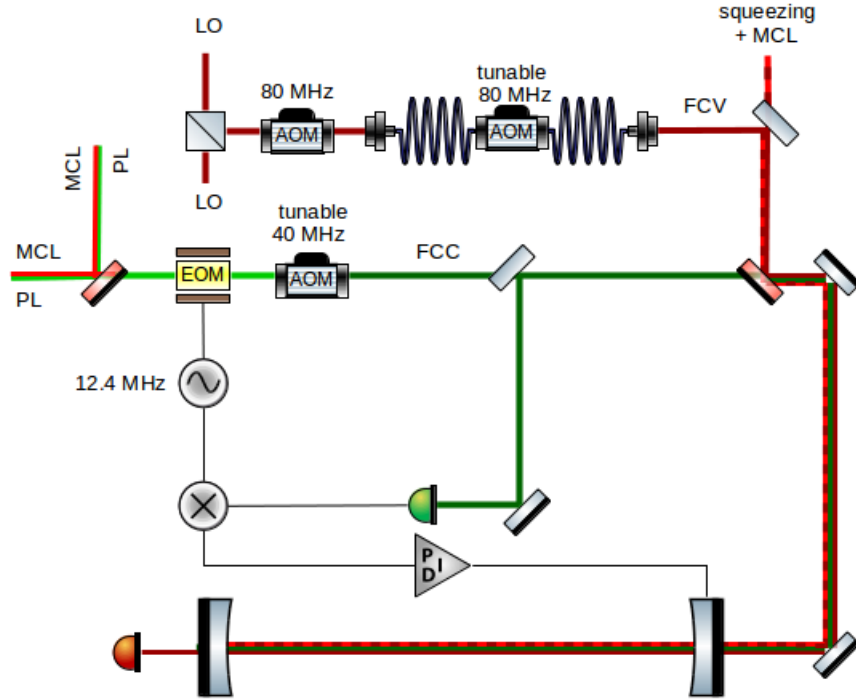


Figure 4.22 – Control scheme of the filter cavity.

Modulation frequency

The lock of the filter cavity is done using the Pound-Drever-Hall technique described in Section 4.1.3. The photodiode is placed in reflection of the cavity using a beam splitter.

The modulation frequency f_{mod} has to be chosen such as the sidebands don't resonate at the same time as the carrier inside the filter cavity. The separation between two consecutive fundamental resonances inside the cavity is the free spectral range:

$$\Delta\nu_{FSR} = \frac{c}{2L}. \quad (4.52)$$

The free spectral range of our 50 m filter cavity is $\Delta\nu_{FSR} = 3$ MHz. The separation f_{sep} between two consecutive high order TEM_{nm} resonances is:

$$f_{sep} = \frac{\Psi_{rt}c}{4\pi L}, \quad (4.53)$$

where $\Psi_{rt} = 2 \times 841 \times 10^{-3}$ rad is the round trip Gouy phase in the filter determined using FINESSE [114]. Thus we obtain $f_{sep} = 0.8$ MHz.

Finally we chose $f_{mod} = 12.4$ MHz which exactly in-between two high order modes resonances and which can be achieved using a commercial free space EOM at 12 MHz. Note that this is the same modulation frequency as the one for the main Second Harmonic Generator described in Section 4.2 allowing to use the same high frequency generator.

Filter Cavity Verification beam

In order to verify the lock of the cavity for the infrared squeezed beam, we add another infrared beam that is a tap off from the main laser such as the local oscillator beam used for the measurement of the squeezed beam on the homodyne detection. As shown in Figure

4.22, this tap off is down-shifted by 80 MHz using a free space AOM and up-shifted again by 80 MHz using a tunable fibered AOM.

This new beam is the Filter Cavity Verification (FCV) beam. By varying the frequency of the second AOM from ± 4 MHz, we can scan the cavity in frequency when locked with the green beam. This allows us to verify the resonance condition of the squeezed beam and check the stability of the lock in infrared as its resonance is thinner than the one of the green.

4.6 Summary

I will now come back to the full conceptual design through each of the 8 beams defined in Table 4.2 that enter the in-vacuum Ferrarix tank and give a full description of their characteristics and interactions with the optical systems of Exsqueez, following the full conceptual design scheme in Figure 4.3. Finally I will summarize the parameters used for Exsqueez, for instance the frequencies or the cavity parameters.

4.6.1 Filter Cavity Control beam

The Filter Cavity Control beam (FCC) starts from the auxiliary laser as an infrared beam of frequency $\omega_0 + \Omega_{PLL}$. An EOM is placed on this beam with a modulation frequency $\Omega_{EOM_2} = 50$ MHz used to lock the auxiliary Second Harmonic Generator (SHG2) described in Section 4.2.

Then SHG2 generates a green beam of frequency $2\omega_0 + 2\Omega_{PLL}$ with sidebands at modulation frequency Ω_{EOM_2} (coming from the sum-frequency generation of a carrier photon and a sideband photon) and $2\Omega_{EOM_2}$ (coming from the sum-frequency generation of two sideband photons). This green beam is reflected by a dichroic plate and goes through a free space AOM of central frequency $2\Omega_{PLL} = 40$ MHz that is supplied by a frequency generator at $2\Omega_{PLL} + 2\Delta\omega_{fc}$ to obtain a green beam at the frequency $2\omega_0 + 2\Delta\omega_{fc}$ where $\Delta\omega_{fc}$ is the detuning of the filter cavity for the squeezed beam as defined in Section 3.4.2.

After the AOM, an EOM is placed with a modulation frequency $\Omega_{EOM_3} = 12.4$ MHz used to lock the filter cavity. The choice of this modulation frequency has been motivated in Section 4.5.3. The modulation is added both for the carrier at $2\omega_0 + 2\Delta\omega_{fc}$ and for the already existing sidebands from the previous EOM as represented on the full sideband scheme of Figure 4.23.

However, the sidebands from EOM_2 have already a power proportional to $J_1^2(m_{EOM_2})$, according to Section 4.1.3. Consequently the modulation from EOM_3 adds to them sidebands with a power proportional to $J_1^2(m_{EOM_2})J_1^2(m_{EOM_3})$ which is negligible in front of the other sidebands.

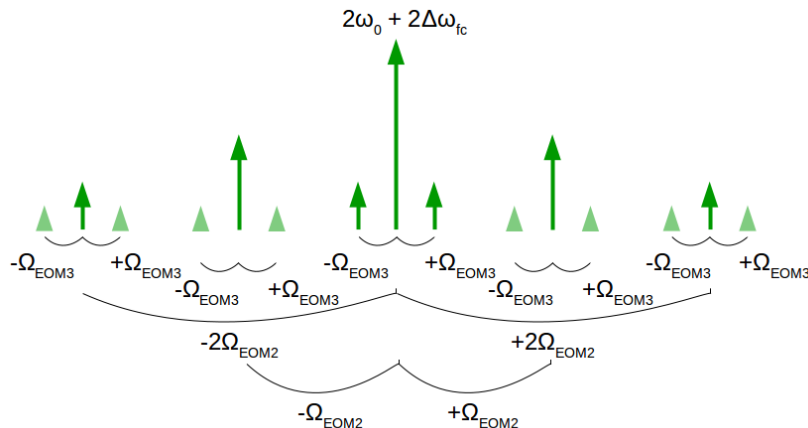


Figure 4.23 – Full sideband scheme of the Filter Cavity Control beam (FCC).

The FCC beam is then injected through a fiber to the in-vacuum Ferrarix tank where it is superposed to the squeezed beam on a dichroic plate and sent to the filter cavity. A 50:50 beam splitter placed on the FCC path only allows to send the FCC beam reflected from the filter cavity to a photodiode where the measured signal is demodulated as explained in Section 4.1.3 to obtain an error signal. We then act on the coils currents of one of the filter cavity mirror to keep it on resonance.

4.6.2 Filter Cavity Verification beam

The Filter Cavity Verification beam (FCV) starts from the main laser as an infrared beam of frequency ω_0 . A pick off takes ~ 100 mW that are sent towards 2 successive AOM of central frequency 80 MHz. The first AOM is free space while the second one is fibered to be able to tune the shift frequency on the AOM bandwidth $\Delta\Omega_{AOM_2} = 8$ MHz without shifting the beam positioning. The full sideband scheme of the FCV beam is represented in Figure 4.24.

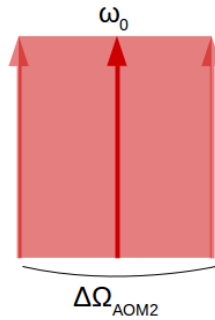


Figure 4.24 – Full sideband scheme of the Filter Cavity Verification beam (FCV).

Then, at the output of the fibered AOM, ~ 30 mW of the FCV beam enters the in-vacuum Ferrarix tank and are recombined with the squeezed beam on a beam splitter plate that reflects 99% and transmits 1% of the infrared light. This choice was done to limit the losses on the squeezing path added by the beam splitter to only 1% as it has been shown in Section 3.6.5 that any source of injection losses degrades the squeezing. However, for the FCV, we lose 99% of the incoming 30 mW before entering the filter cavity. Indeed, as both FCV and squeezed beams have the same wavelength, we cannot use a dichroic plate to recombine them as done for the Filter Cavity Control beam (FCC).

Then the DC signal of the FCV beam is measured in transmission of the filter cavity on a photodiode. While locking in green the cavity with the FCC beam, we scan the infrared cavity mode of the filter cavity by changing the frequency of the fibered AOM on the FCV path. As the free spectral range of the filter cavity is $\Delta\nu_{FSR} = 3$ MHz and the AOM bandwidth is $\Delta\Omega_{AOM_2} = 8$ MHz, we are able to scan a whole free spectral range of the filter cavity to verify its detuning in infrared at the frequency of the squeezed beam.

Note that there is no commercial AOM that can shift the frequency below few MHz. Thus, to scan the cavity on few MHz we have to use 2 AOMs, one that up-shifts the frequency and the other that down-shifts it from the same amount plus the few MHz of difference needed. We chose a frequency shift of 80 MHz because it was the lower frequency commercially and easily available for the fibered AOM.

4.6.3 Local Oscillator beam

The Local Oscillator beam (LO) starts from the main laser as an infrared beam of frequency ω_0 . A small amount of the main laser is picked off and injected through a fiber to the in-vacuum Ferrarix tank so that ~ 5 mW of LO beam goes out of the fiber and are directly sent to the homodyne detection photodiodes for the squeezing measurement. The fiber acts as a

mode cleaner so that the LO beam is mostly a fundamental gaussian beam. The sideband scheme of the local oscillator is simple, as it is not modulated, and is represented in Figure 4.25.



Figure 4.25 – Full sideband scheme of the Local Oscillator beam (LO).

4.6.4 Modified Coherent Locking beam

The Modified Coherent Locking beam (MCL) has the same start as the Filter Cavity Control beam (FCC). It starts from the auxiliary laser as an infrared beam of frequency $\omega_0 + \Omega_{PLL}$. An EOM is placed on this beam with a modulation frequency $\Omega_{EOM2} = 50$ MHz used to lock the auxiliary Second Harmonic Generator (SHG2) described in Section 4.2.

In reflection of SHG2, the MCL beam is co-propagating with the FCC beam until the dichroic plate which transmits the MCL beam towards the in-vacuum Ferrarix tank. The beam enter the tank through a window and is then superposed to the pump beam on a dichroic plate. The full sideband scheme of the MCL beam before entering the Optical Parametric Oscillator (OPO) is represented in Figure 4.26a.

As the linewidth at ω_0 of the OPO cavity is 17 MHz, as defined in Section 4.3.2, the MCL carrier at $\omega_0 + \Omega_{PLL}$ should enter the OPO cavity while its sidebands should almost be reflected. Nevertheless, I will still take them into account in the full sideband scheme of the MCL beam after interacting inside inside the crystal of the OPO. As explained in Section 4.4.2, the non-linearity of the crystal generates MCL sidebands symmetrical to the squeezed frequency ω_0 as shown in Figure 4.26b.

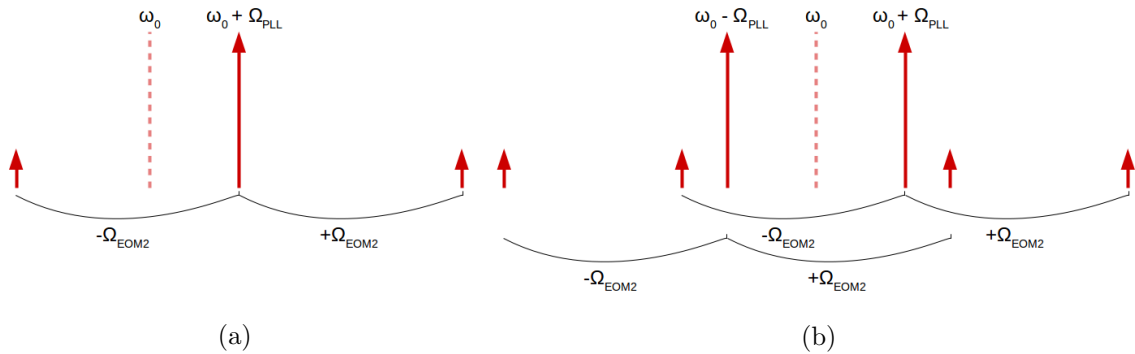


Figure 4.26 – Full sideband scheme of the Modified Coherent Locking beam (MCL): (a) before the Optical Parametric Oscillator (OPO) and (b) after the OPO.

After interacting inside the OPO, the MCL beam co-propagates with the squeezed beam to the filter cavity. The parameters of the filter cavity are given in Section 4.5. At ω_0 , the free spectral range of the cavity is 3 MHz, its linewidth is 1 kHz with a detuning of 500 Hz. Consequently, the MCL beam does not resonate inside the filter cavity but is directly reflected when the cavity is locked.

Finally, the MCL beam reflected from the filter cavity is sent to the homodyne detection photodiode using a Faraday Isolator.

4.6.5 Phase Locking beam

The Phase Locking beam (PL) has the same start as the Filter Cavity Control beam (FCC) and the Modified Coherent Locking beam (MCL). It starts from the auxiliary laser as an infrared beam of frequency $\omega_0 + \Omega_{PLL}$. An EOM is placed on this beam with a modulation frequency $\Omega_{EOM_2} = 50$ MHz used to lock the auxiliary Second Harmonic Generator (SHG2) described in Section 4.2.

Then SHG2 generates a green beam of frequency $2\omega_0 + 2\Omega_{PLL}$ with sidebands at modulation frequency Ω_{EOM_2} (coming from the sum-frequency generation of a carrier photon and a sideband photon) and $2\Omega_{EOM_2}$ (coming from the sum-frequency generation of two sideband photons). 1% of this green beam is transmitted through the dichroic plate that separates the FCC and MCL beams.

The PL beam then co-propagates with the MCL beam until the dichroic plate where the MCL and pump beams are recombined. It is transmitted by this dichroic plate and sent to a photodiode with 2% of the pump beam to generate the error signal to phase lock the main and auxiliary lasers as explained in Section 4.4.3. The full sideband scheme of the PL beam is represented in Figure 4.27.

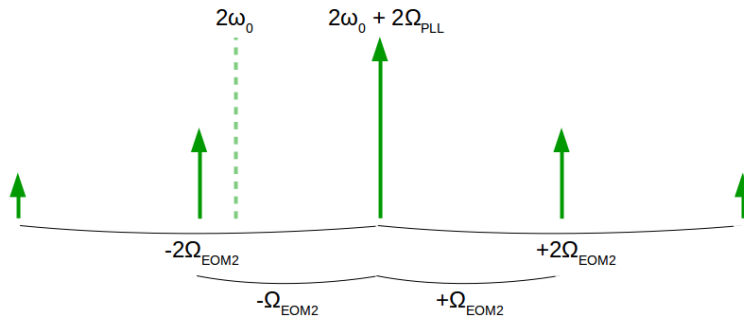


Figure 4.27 – Full sideband scheme of the Phase Locking beam (PL).

4.6.6 Pump beam

The pump beam starts from the main laser as an infrared beam of frequency ω_0 . An EOM is placed on this beam with a modulation frequency $\Omega_{EOM_1} = 12.4$ MHz used to lock the main Second Harmonic Generator (SHG1) described in Section 4.2.

Then SHG1 generates a green beam of frequency $2\omega_0$ with sidebands at modulation frequencies Ω_{EOM_1} (coming from the sum-frequency generation of a carrier photon and a sideband photon) and $2\Omega_{EOM_1}$ (coming from the sum-frequency generation of two sideband photons). Indeed, the linewidth of the SHG1 cavity in infrared is 58 MHz, allowing the sidebands to resonate inside the locked SHG1 cavity and convert infrared photons onto green photons.

The pump beam goes then through the Mach-Zehnder interferometer described in Section 4.4.1 to be locked in power, via a photodiode on a pick-off, before entering the in-vacuum Ferrarix tank through a window.

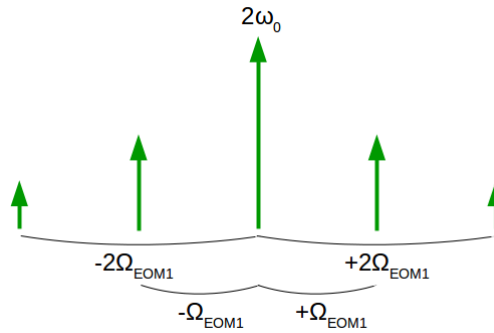


Figure 4.28 – Full sideband scheme of the pump beam.

Before entering the Optical Parametric Oscillator (OPO), the pump beam is superposed with the Modified Coherent Locking beam (MCL) on a dichroic where it loses 2% of power that superposed to the Phase Locking beam (PL) to phase lock the main and auxiliary laser as detailed in Section 4.4.3, and another 2% reflected on the second surface of the dichroic and blocked with a dump.

The OPO is locked using the pump beam on a photodiode in reflection. The error signal is obtained using the same modulation sidebands as for the lock of SHG1 as shown on the full sideband scheme of the pump beam in Figure 4.28. Consequently, the demodulation of the error signal for the PDH lock of the OPO, as explained in Section 4.1.3, is done at $\Omega_{EOM_1} = 12.4$ MHz. The DC pump power in reflection or transmission of the OPO cavity can also be used to stronger lock the Mach-Zehnder interferometer.

4.6.7 Seed beam

The seed beam starts from the main laser as an infrared beam of frequency ω_0 . A pick off takes ~ 100 mW that are injected through a fiber to the in-vacuum Ferrarix tank. The seed beam enters the Optical Parametric Oscillator (OPO) via a high reflective mirror and follow in OPO the same path as the squeezed beam and in the same direction.

The seed beam escaping the OPO through its input/output coupler is then sent to the homodyne detection photodiodes for characterization of the OPO non linear gain and the matching of the seed beam with the Local Oscillator (LO) beam.

The sideband scheme of the seed beam is simple, as it is not modulated and has the same frequency as the squeezed beam. It is represented in Figure 4.29. The seed beam is only used for characterization, it will be blocked before its injection into the fiber during squeezing operation.



Figure 4.29 – Full sideband scheme of the seed beam.

4.6.8 Squeezed beam

The squeezed beam is generated inside the Optical Parametric Oscillator (OPO) crystal by non linear down-conversion of the pump beam. It escapes the OPO cavity through an input/output coupler and is sent into the filter cavity where it senses frequency dependent rotation. After reflection of the filter cavity the squeezed beam is sent to the homodyne detection photodiode, via a Faraday Isolator, for homodyne measurement with the Local Oscillator beam.

The sideband scheme of the squeezed beam is represented in Figure 4.30 with its carrier and the two sidebands at Ω_{EOM1} coming from the modulation of the pump field and the initial infrared field to lock the SHG1 and OPO cavities. Nevertheless, as the squeezing generation is low efficiency non-linear process, the power in the sidebands will be negligible.

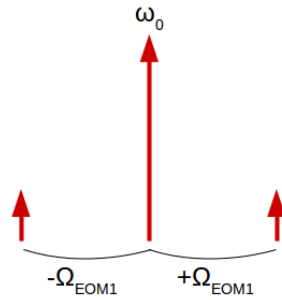


Figure 4.30 – Full sideband scheme of the squeezed beam.

4.6.9 Parameters summary

I summarized in Table 4.6 the 7 frequencies that need to be generated for Exsqueez with their use.

Frequency	Use
12.4 MHz	Lock of the SHG1, OPO and filter cavities
20 MHz	Lock of the squeezing ellipse measurement ϕ
40 MHz	Phase lock of the main and auxiliary lasers
tunable 40 MHz	Fix the detuning of the filter cavity
50 MHz	Lock of the SHG2 cavity
80 MHz	Down-shift frequency for the FCV beam
tunable 80 MHz	Up-shift frequency to scan the filter cavity with the FCV beam

Table 4.6 – Summary of the frequencies generated for Exsqueez with their use.

Finally, I give in Table 4.7 the main parameters of the cavities used for Exsqueez.

Cavity	Length	Finesse	Free Spectral Range	Linewidth
SHG1 at 1064 nm	45 mm	57	3.3 GHz	58 MHz
SHG2 at 1064 nm	45 mm	57	3.3 GHz	58 MHz
OPO at 532 nm	255 mm	28	59 MHz	21 MHz
OPO at 1064 nm	255 mm	35	59 MHz	17 MHz
Filter cavity at 532 nm	50 m	140	3 MHz	21 kHz
Filter cavity at 1064 nm	50 m	3100	3 MHz	1 kHz

Table 4.7 – Summary of the cavities parameters of Exsqueez.

Chapter 5

Integration of the Exsqueez experiment on the CALVA facility

The CALVA facility is composed of two clean rooms and of a control room. Most of the integration is done in the first clean room where the in-air beams preparation bench, the in-vacuum Ferrarix tank and the filter cavity input mirror are located. The filter cavity end mirror is in the second clean room, 50 m away and the electronics is spread between the two clean rooms and the control room.

The integration of the Exsqueez experiment on the CALVA facility was separated into three main parts: the upgrade of the existing electronics with the new LAPP electronics, the in-air preparation bench and the Optical Parametric Oscillator (OPO) that generates the squeezing designed at LKB and installed jointly by LKB and LAL/IJCLab teams and finally the in-vacuum bench designed and installed by the LAL/IJCLab team.

In this chapter, I will first present the electronics that is used for the data acquisition and control. Then, I will go through the installation of the in-air bench with the characterization of its subsystems leading to the 7 beams, presented in Table 4.2, that are send towards the in-vacuum bench. And finally I will detail the simulations done to prepare and design the in-vacuum bench, followed by the installations done. The installation and characterization of the OPO and homodyne detection will be presented in Chapter 6.

5.1 Acquisition electronics

The acquisition electronics used for Exsqueez on CALVA has been developed by LAPP and is the same one as for Advanced Virgo. A simplified scheme of the electronics used for the data acquisition and the driving of the actuators is represented in Figure 5.1.

There are two types of data acquisition depending on the type of photodiodes used : in-air commercial photodiodes or in-vacuum LAPP photodiodes. The commercial photodiodes are composed of an active detector surface followed by a preamplifier that amplifies the current measured and converts it into voltage. The bandwidth of the data acquired by the photodiode goes from DC to 150 MHz. Then, a commercial splitter separate the DC and RF signal with a cutoff frequency of 100 kHz.

The DC signal of the in-air photodiodes is sent to an Analog to Digital Converter (ADC) channel on an ADC7674 board from LAPP [115] where it is down sampled at 10 kHz before being sent to the real time PC.

The RF signal of the in-air photodiodes is sent to a demodulation channel on a LAPP DaqBox [116]. The demodulation frequency is sent by a generator to another demodulation channel on the same demodulation mezzanine of the DaqBox and both of them are sampled at 400 MHz before being demodulated at a given reference frequency. The comparison between the demodulated RF signal and generator results in the demodulated signals in-phase and in-quadrature AC_p and AC_q that are down sampled at 10 kHz and sent to the real time PC.

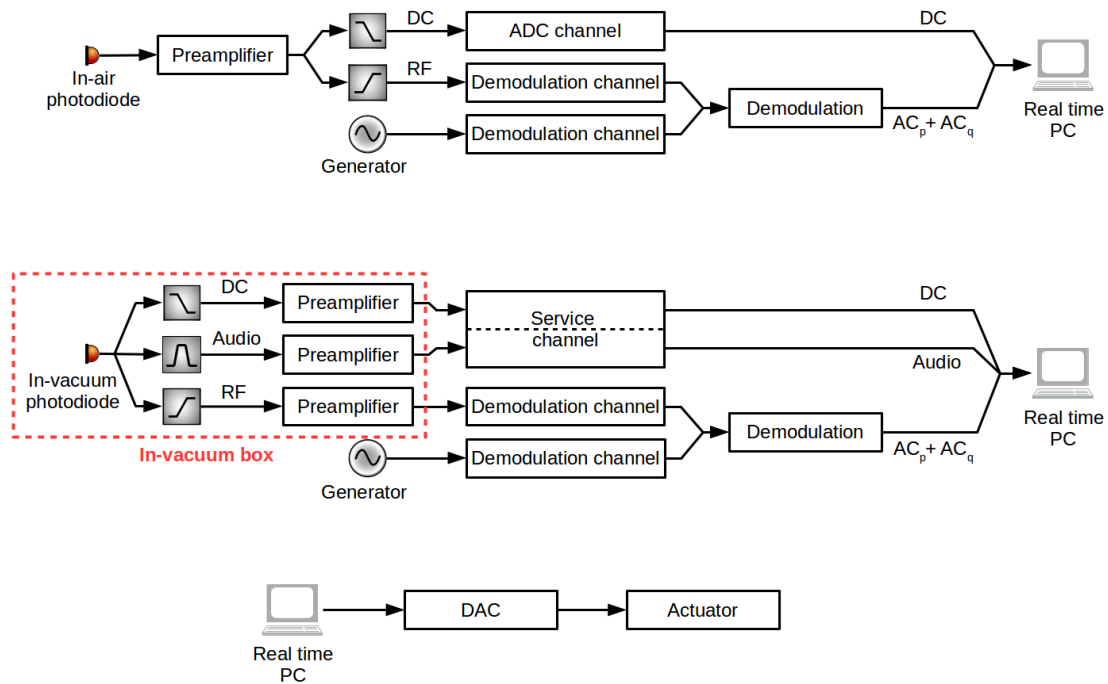


Figure 5.1 – Simplified scheme of the electronics building blocs of the Exsqueez experiment showing (*top*) the acquisition scheme of in-air commercial photodiodes, (*middle*) the acquisition scheme of in-vacuum LAPP photodiodes and (*bottom*) the driving scheme. Note that the low-pass filter cutoff frequency defining the DC signal is not the same for the in-air photodiodes (100 kHz) and the in-vacuum photodiodes (~ 2 Hz). The in-vacuum photodiodes have an additional Audio channel that is band-pass filter between ~ 2 Hz and ~ 16 kHz and amplified by a factor 100. The sampling of the RF channels is done at 400 MHz while the data sent to the real time PC (DC, Audio and AC) are down sampled at 10 kHz. The real time PC sends data to the DAC for actuation at 100 kHz.

The used demodulation frequency is the same as the frequency at which the measured photodiode signal is modulated either from an EOM on the beam path before the photodiode or a beat note between two beams superposed on the photodiode. In the case of a modulation frequency from an EOM, the used frequency generator channel is the same for both the modulation on the EOM and the demodulation on the demodulation mezzanine.

The in-vacuum LAPP photodiodes have a similar behavior as the in-air photodiodes except that before the preamplifier, the signal from the active detector is split into 3 parts that undergo different filters. The bandwidth of the data acquired by the photodiode ranges from DC to 80 MHz. A low-pass filter with a cut-off frequency ~ 2 Hz generates a DC signal, a high-pass filter with a cut-off frequency ~ 16 kHz generates a RF signal and a band-pass filter between ~ 2 Hz and ~ 16 kHz generates an audio signal. Note that the bandwidth of the DC and RF signals are not the same depending on the type of photodiode used (in-air or in-vacuum).

The DC and audio signals of the in-vacuum LAPP photodiodes are sent via a micro-subd15 connector to a service channel of a LAPP DaqBox [116] while the RF signal is sent via SMA to a demodulation channel. The method for the demodulation is then exactly the same as for the in-air photodiode describe above. Finally the DC, audio and demodulated signals in-phase and in-quadrature AC_p and AC_q are down sampled at 10 kHz and sent to the real time PC.

From the real time PC, the data can be visualized using a Data Display [117] or filtered by the control loops to drive actuators with the calculated corrections via DAC channels at 100 kHz on a LAPP DaqBox [116]. The control loops are defined using the Algorithms for Control and Locking (Acl) server [118] developed at LAPP, usually at 10 kHz.

5.2 In-air beams preparation bench

The aim of the in-air bench is to prepare the 7 beams that need to be used in the in-vacuum Ferrarix tank to produce, lock and measure frequency dependent squeezing as detailed in Chapter 4.

The full real life scheme of the in-air bench is represented in Figure 5.2. We can roughly divide the table into 4 quadrants. The top quadrants correspond to the green beams production while the bottom quadrants are used for the beam injections into the fibers that go towards the in-vacuum tank. The left quadrants produce beams from the main laser and the right quadrants produce beams from the auxiliary laser.

I will now present the installation of the 4 quadrants of the in-air table and the characterization of the optical systems done.

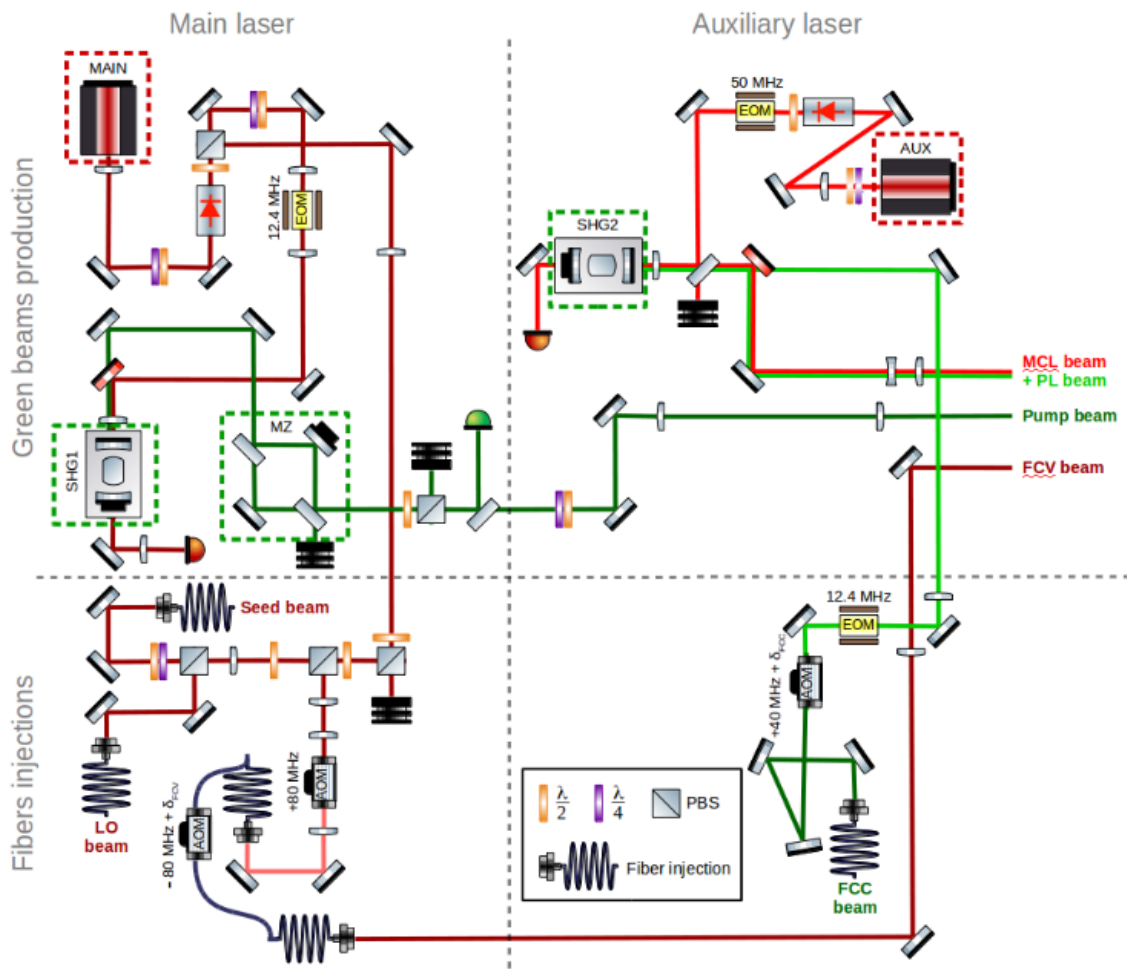


Figure 5.2 – Scheme of the in-air bench full real life optical set-up with red boxes for the laser heads and green boxes for the green beam production subsystems : main and auxiliary Second Harmonic Generators (SHG) and Mach-Zehnder (MZ). The boundaries of the 4 quadrants defined for the in-air table are shown in grey.

5.2.1 Main laser green beam production

The main laser green beam production quadrant scheme is represented along with its picture on the CALVA facility at LAL/IJCLab in Figure 5.3. Its installation starts from the main laser Coherent Mephisto that have been measured to deliver 2.3 W of infrared light at 1064 nm with a waist radius of $120 \mu\text{m} \pm 5 \mu\text{m}$ at a distance of $95 \text{mm} \pm 2 \text{mm}$ before the front end of the laser head, inside the laser box.

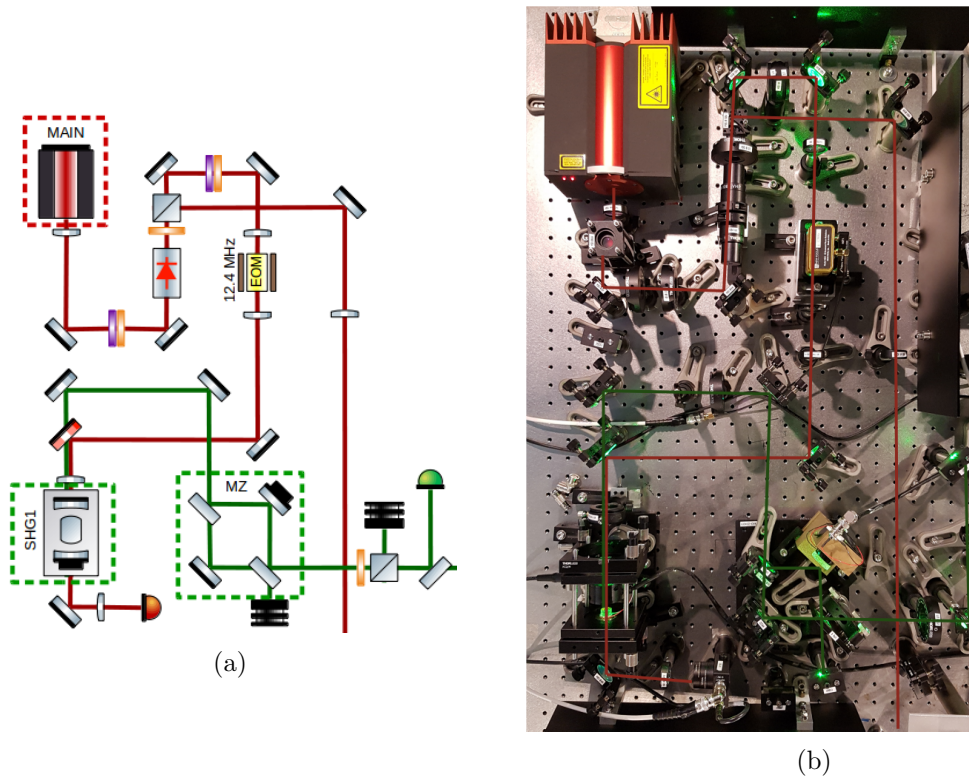


Figure 5.3 – Main laser green production quadrant scheme (a) and picture on the CALVA facility at LAL/IJCLab (b).

A system composed of a quarter-wave plate and a half-wave plate is then placed on the beam to obtain a laser field s-polarized that is sent to a Faraday isolator to protect the laser head from back reflection. The Faraday isolator transmits 95.5% of the incoming field.

A half-wave plate and a polarizing cube beam splitter are placed after the Faraday isolator to pick off part of the infrared beam towards the main laser fibers injections quadrant and the other part is used to produce the green pump beam. The amount of power sent in both paths can be chosen by rotating the half-wave plate. 1070 mW s-polarized of the main laser are reflected by the cube beam splitter towards the main laser fibers injections quadrant which installation will be described in Section 5.2.2.

Main Second Harmonic Generator

The field transmitted by the cube beam splitter is p-polarized. A quarter and a half-wave plates are placed to obtain a s-polarized field that is sent through the EOM generating the sidebands at 12.4 MHz for the lock of the Main Second Harmonic Generator (SHG1) as described in Section 4.2. The EOM transmits 85% of the incoming field, leading to 780 mW of 1064 nm beam arising on SHG1.

The SHG1 cavity length is locked using the Algorithms for Control and Locking (AcL) server [118] used on Advanced Virgo and developed by LAPP. The error signal is obtained from the in-air photodiode in transmission as described in Section 5.1. The demodulation frequency is the same one used to drive the EOM, i.e. 12.4 MHz.

The scanning of the cavity length is done using a piezo ring on the end mirror of the SHG1 cavity. The piezo is driven by a DAC channel amplified by a High Voltage (HV) amplifier by a factor ~ 30 . For the piezo safety, the HV amplifier channel cannot deliver more than 100 V to the piezo.

Feedback system

The feedback loop can be schematized using a block diagram as shown in Figure 5.4. This is a general feedback loop that is used for all the plants that need to be locked as SHG1 for which the actuator is a piezo ring. In our scheme we gather together the DAC channel, the HV amplifier and the piezo inside the actuator transfer function. The corrector is digitally applied to the error signal using Acl.

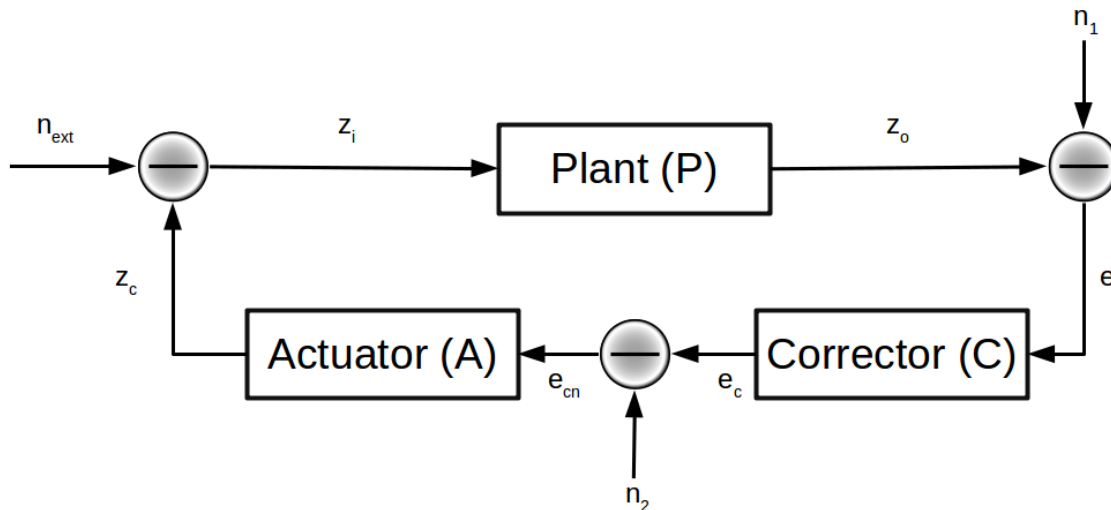


Figure 5.4 – General feedback loop scheme used for the Exsqueez experiment. The plant is usually one of the optical cavity, the Mach-Zehnder interferometer, or the laser heads, the corrector is the transfer function applied to the error signal before sending it to the actuator, generally a piezo except for the 50 m filter cavity where the actuators are coils. There are two possible digital noise input n_1 and n_2 used to characterize the system.

By injecting noise at different places of the feedback loop, we measured a flat transfer function for the system composed of the DAC and the HV amplifier. The electrical transfer function of the piezo was measured to be an order 1 low-pass filter with a cutoff frequency of ~ 320 Hz. Finally, the optical transfer function of the cavity is flat on the actuation bandwidth.

The control loop filter of the corrector was then chosen to obtain a stable lock starting from a simple integrator to first acquire the lock and improved after some trials into a “best” filter that is more robust:

$$C(s) = \frac{1 + \frac{s}{2\pi f_0} + \frac{s^2}{(2\pi f_1)^2}}{s^4}, \quad (5.1)$$

with $f_0 = 0.1$ Hz and $f_1 = 1$ Hz. The Bode diagram of this filter is shown in Figure 5.5. With respect to the simple integrator filter, it has more gain at DC and a larger bandwidth.

These are the same filters, only adjusting a gain factor, that are used for all the control loops except for the temperature controller and the 50 m filter cavity control.

Lock of the Main Second Harmonic Generator

An example of scan and lock of the SHG1 cavity is given in Figure 5.6 showing the instruction scanning ramp and correction along with the DC and demodulated in-phase error signals defined in Section 4.1.3.

The locking strategy is in two steps. First when the DC signal exceed 5 V the frequency of the ramp sent to the piezo is decreased by a factor 10 to approach the resonance more slowly. Then we start trying to lock when the in-phase error signal is in the linear part between -0.3 V and 0.3 V.

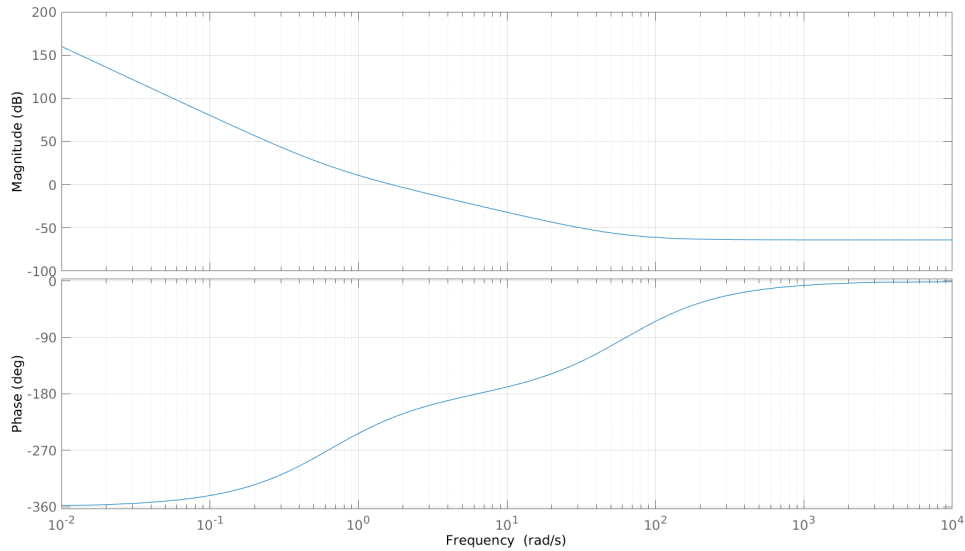


Figure 5.5 – Bode diagram of the *best* filter used to control the optical cavities and Mach-Zehnder interferometer on the Exsqueez experiment. Only a gain factor is adjusted for each plant.

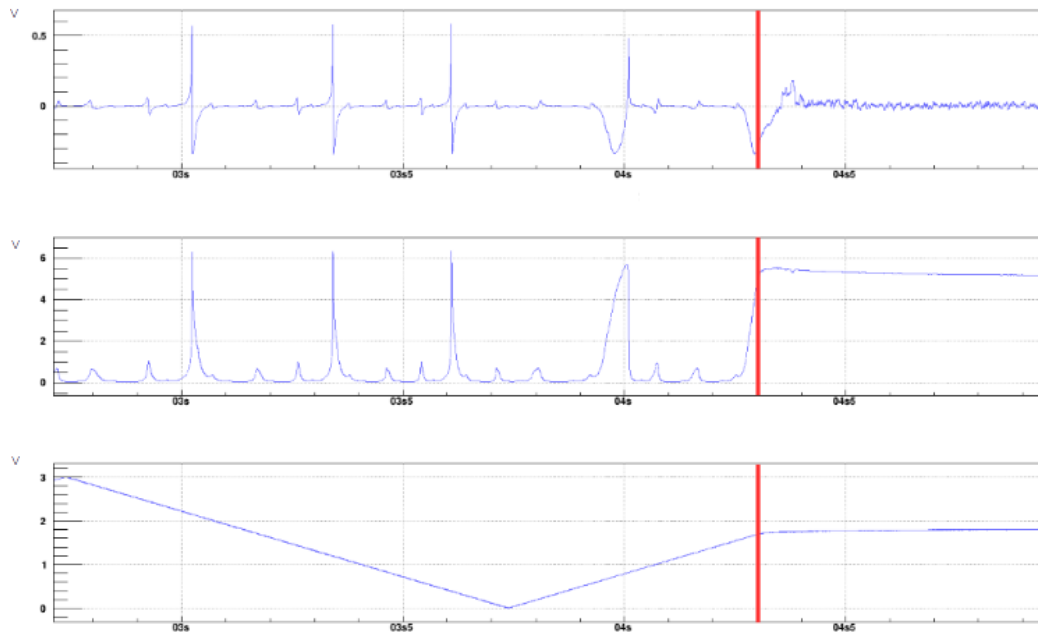


Figure 5.6 – Example of scan and lock of the SHG1 cavity separated by the red line: (*upper*) error signal from the in-phase demodulation at 12.4 MHz of the signal from the in-air photodiode in transmission of the SHG1 cavity, (*middle*) DC signal from the in-air photodiode in transmission of the SHG1 cavity, (*lower*) actuation order sent by the DAC to the piezo on the end mirror of the SHG1 cavity.

The FFT of the error signal when the SHG1 cavity is locked is represented in Figure 5.7. It shows the residual noise spectrum with in particular spectral lines at 50 Hz and harmonics and unknown noises at ~ 250 Hz, ~ 750 Hz and ~ 2 kHz. The cut-off at high frequency is due to the acquisition frequency of 10 kHz with a butterworth filter of order 8 leading to an attenuation of 20 dB at 5 kHz.

The green beam at 532 nm produced by SHG1 is separated from the infrared beam at 1064 nm reflected by the SHG1 cavity using a dichroic plate that reflects the infrared beam and transmits the green beam. A power meter has been placed on this green beam to characterize the green beam production from SHG1.

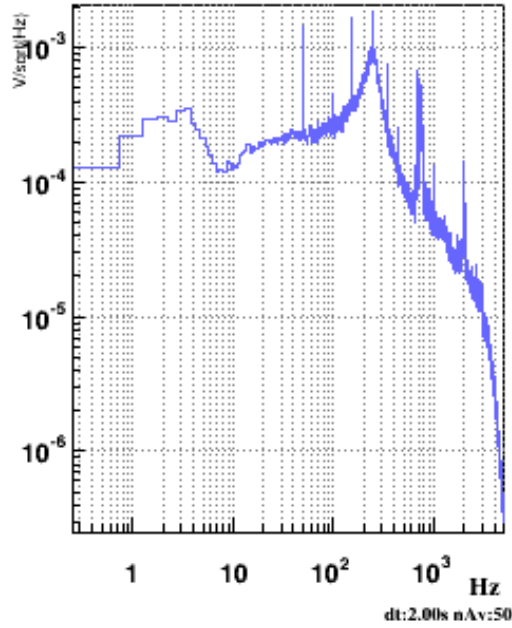


Figure 5.7 – FFT of the error signal when the main Second Harmonic Generator (SHG1) cavity is locked.

The temperature of the SHG1 crystal is controlled using a commercial oven shown in Figure 5.8a. The temperature was then varied with the SHG1 cavity locked and the generated green power at 532 nm was measured with the power-meter. The resulting phase-matching temperature plot is shown in Figure 5.8b. As expected from Equation 3.73, it follows a sinc^2 function with a maximum power generated at 50.6° C at the moment of this measurement. The optimal temperature depends on the room temperature and should be adjusted of about 1° C.

Finally after some alignment and matching improvement we measured ~ 200 mW of generated green beam from 780 mW of infrared beam injected to the SHG1 cavity leading to a green beam production efficiency of $\sim 25\%$.

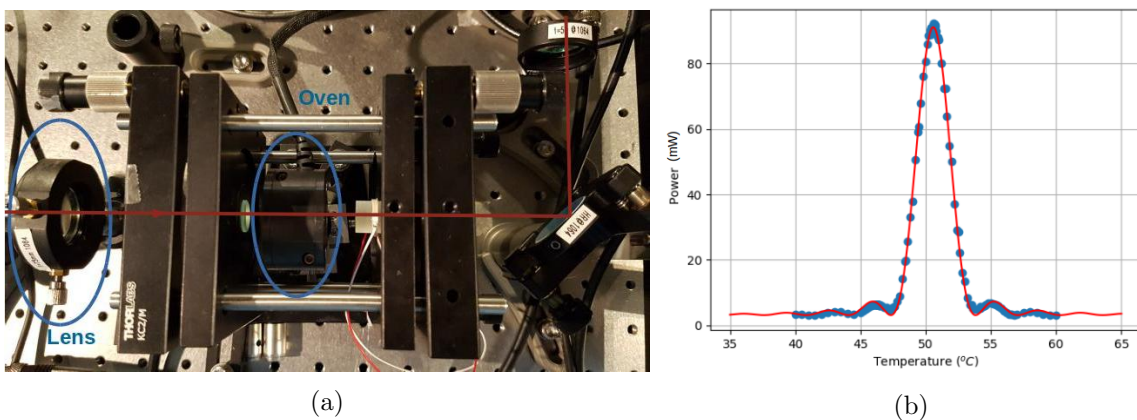


Figure 5.8 – (a) Picture of the main Second Harmonic Generator (SHG1) showing, the lens before the cavity to mode match the beam to the cavity, the two mirrors of the cavity with the piezo on the end mirror and the oven of the MgO:PPLN crystal. (b) Plot of the phase-matching temperature measurement superposed with a sinc^2 fit.

Mach-Zehnder interferometer

The green beam produced by the Main Second Harmonic Generator (SHG1) is then sent to the Mach-Zehnder interferometer shown in Figure 5.9a. The beam splitters of the Mach-Zehnder reflect 70% of the green beam to allow some measurements, that will be described in Section 6.2.3, without the Mach-Zehnder interferometer by adding a beam dump on the lower arm but keeping most of the green power. Note that the mirror mounted on a piezo is placed on the Mach-Zehnder arm with the highest power that is always used.

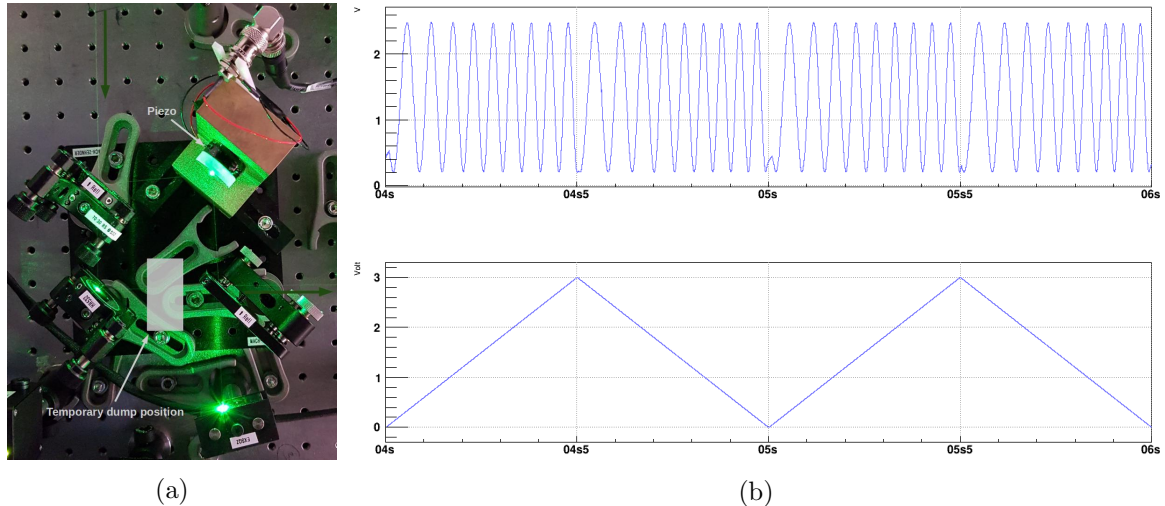


Figure 5.9 – (a) Picture of the Mach-Zehnder interferometer on the ExsqueeZ experiment showing the mirror on which the piezo actuation is done, the dumped arm and the position of the temporary beam dump used for some measurements. (b) Example of scan of the Mach-Zehnder interferometer with (*top*) the DC signal measured in transmission of the Mach-Zehnder and (*bottom*) the actuation scanning order sent by the DAC to the Mach-Zehnder piezo.

As shown in Section 4.4.1, one of the two output beams of the Mach-Zehnder interferometer is not used and a beam dump is placed on it to avoid spurious reflections. The other output beam is sent to a half-wave plate and a polarizing cube beam splitter to allow a beam power control by hand. The beam reflected by the polarizing cube beam splitter is not used and blocked by a beam dump while the beam transmitted will become the pump beam defined in Chapter 4.

A pick off that reflects less than 1% of the green beam is added on the pump beam with a photodiode on the reflected beam. This photodiode is used to lock the Mach-Zehnder interferometer length via the Acl server. Without locking or scanning the interferometer, and blocking one arm to ensure no interference pattern, one can observe in Figure 5.10 power fluctuations in the pump beam correlated with the voltage fluctuations of a free ADC channel that has been checked to be correlated to the room temperature fluctuations.

We calibrated the pump beam power sent to the in-vacuum bench, and more specifically at the entrance of the Optical Parametric Oscillator (OPO), with respect to the Mach-Zehnder photodiode measured voltage. The calibration plot is shown in Figure 5.11.

The error signal for the Mach-Zehnder interferometer is defined by the difference between the measured power on the photodiode and the requested power. The actuation is done on the piezo of the Mach-Zehnder driven by a DAC channel amplified by a HV amplifier by a factor ~ 130 . This piezo can support up to 1000 V actuation.

In the same way as for SHG1, we measured a flat transfer function for the system composed of the DAC and the HV amplifier. The electrical transfer function of the piezo was measured to be an order 1 low-pass filter with a cutoff frequency of ~ 1.1 kHz. Finally, the optical transfer function of the cavity is flat on the actuation bandwidth. The control loop filter was then optimized to obtain a stable lock using the *best* filter defined in Figure 5.5.

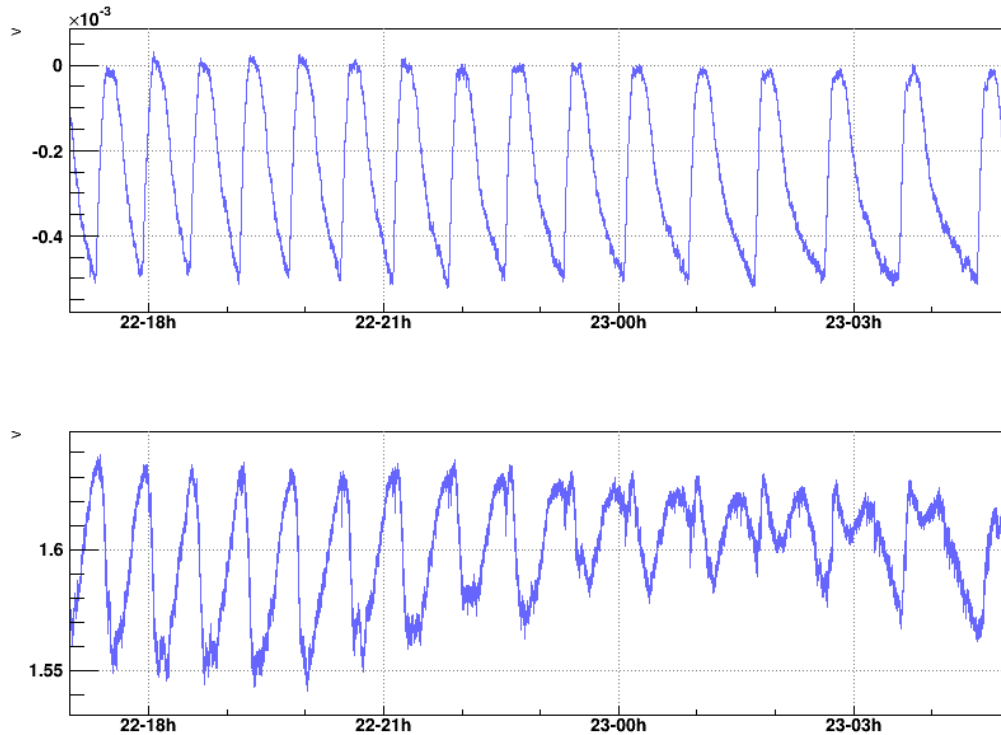


Figure 5.10 – Power fluctuations over a night of the pump beam measured using the Mach-Zehnder photodiode (bottom), blocking one arm of the interferometer. The power fluctuations are clearly correlated with room temperature fluctuations measured on a free ADC channel (top).

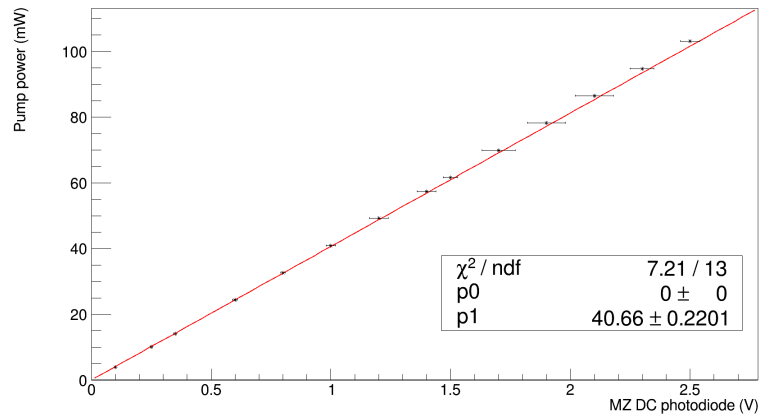


Figure 5.11 – Calibration of the pump beam power sent to the in-vacuum bench with respect to the Mach-Zehnder photodiode measured voltage.

An example of scan of the Mach-Zehnder is given in Figure 5.9b and the FFT of the error signal when the Mach-Zehnder interferometer is locked is represented in Figure 5.12. It shows the residual noise spectrum with in particular spectral lines at 50 Hz and harmonics, unknown noises between ~ 300 Hz and ~ 700 kHz and some residual noise at low frequencies. It is quite difficult to reduce the noise above few hundreds of Hz because of the actuation loop limited at 10 kHz.

When the Mach-Zehnder was locked, we checked on its photodiode over few hours that the effect of the room temperature fluctuations on the pump power is corrected ensuring a constant pump power as shown in Figure 5.13, even if we still see noise RMS changes linked to the room temperature.

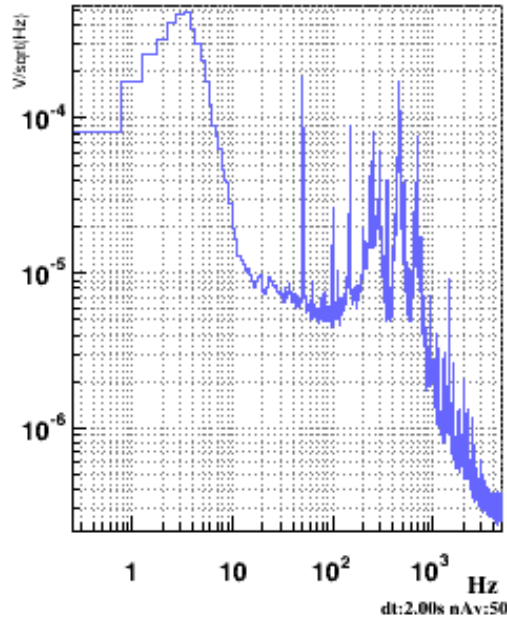


Figure 5.12 – FFT of the error signal when the Mach-Zehnder interferometer is locked.

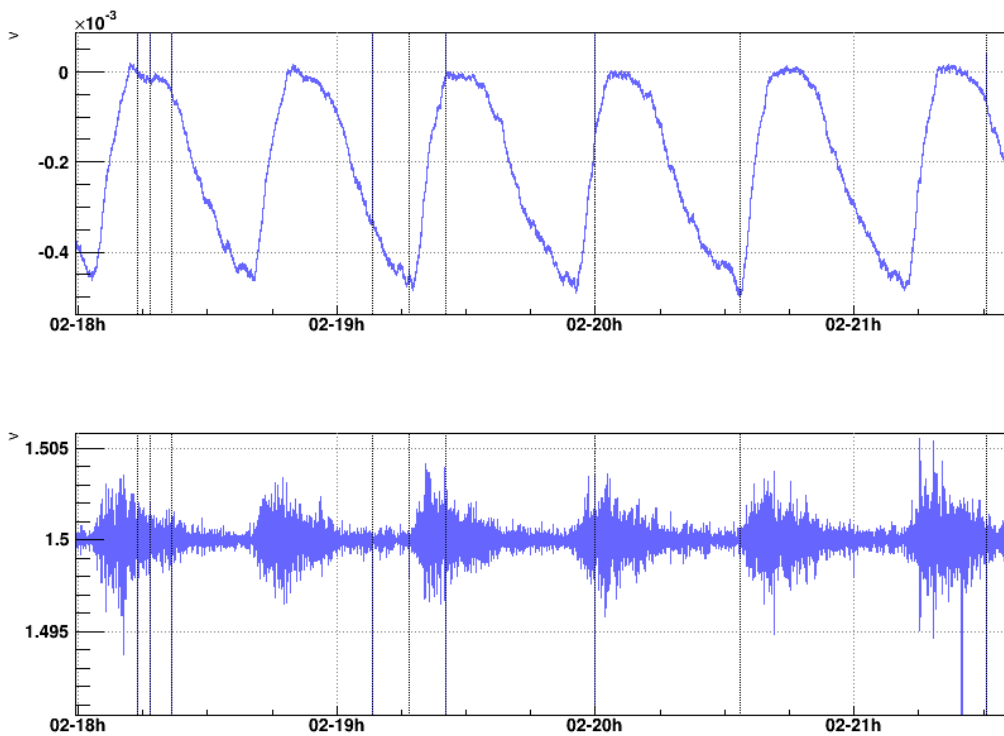


Figure 5.13 – Power fluctuations over a night of the pump beam measured using the Mach-Zehnder photodiode (bottom), locking interferometer. The effect of the room temperature fluctuations measured on a free ADC channel (top) is reduced compared to Figure 5.10. The grey lines corresponds to loss of data on the acquisition system.

5.2.2 Main laser fibers injections

The main laser fibers injections quadrant scheme is represented along with its picture on the CALVA facility at LAL/IJCLab in Figure 5.14. The infrared s-polarized beam coming from the main laser green beam production quadrant goes through a half-wave plate and a polarizing cube beam splitter to adjust the total beam power sent to the fiber injections.

The beam transmitted by the cube beam splitter is not yet used and sent to a beam dump. We could use it to add a reference cavity to stabilize the main laser frequency in a next step of the experiment. The beam reflected by the cube beam splitter will be divided into three parts via two systems of half-wave plates and polarizing cube beam splitters. The beam power on each path is adjusted by rotating the half-wave plates.

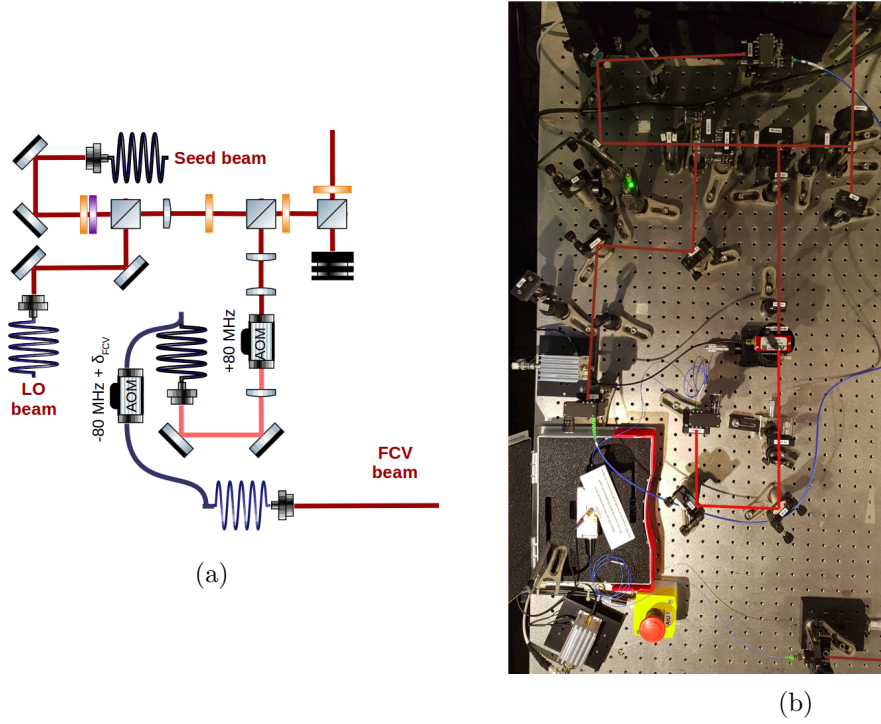


Figure 5.14 – Main laser fibers injections quadrant scheme (a) and picture on the CALVA facility at LAL/IJCLab (b).

Filter Cavity Verification beam injection

The first reflected s-polarized beam is injected through a free space AOM aligned on the +1 order to have a positive frequency shift at the applied RF modulation of 80 MHz. The transmission efficiency of the beam to the +1 order of the AOM output was measured to be 69%.

This beam is then injected through a fibered AOM designed to transmit the order -1 to have a negative frequency shift at the applied RF modulation of 80 MHz + δ_{FCV}. The δ_{FCV} frequency shift is a small variable shift used to scan the 50-m filter cavity spectrum at the squeezing frequency as defined in Section 4.5.3 with:

$$-4 \text{ MHz} = -\frac{\Delta\Omega_{AOM_2}}{2} \leq \delta_{FCV} \leq \frac{\Delta\Omega_{AOM_2}}{2} = 4 \text{ MHz}. \quad (5.2)$$

A lens is placed on a translation stage before the fiber injection to adjust the mode matching of the beam to the optical fiber. Finally we measured that 45% of the power arising on the fibered AOM injection is coupled inside of it and exists the fiber output.

At first we aligned the free space and fibered AOM and measured the total propagation efficiency between the cube beam splitter and the output of the fibered AOM. Then this beam will be recombined with the squeezed beam on a plate reflecting 99% of the infrared light (to limit losses on the squeezing). Consequently, we needed to have as much as possible power on the FCV beam entering the in-vacuum Ferrarix tank without damaging the AOMs. For safety we chose to have 30 mW going out of the fiber for this beam, leading to 98 mW reflected by the second cube beam splitter.

Note that even if there is a fibered AOM on this beam, it is not injected to the cavity through a fiber to allow some matching and position adjustment in operation without adding any in-vacuum motorized translation stage.

Local Oscillator beam injection

The second reflected s-polarized beam is injected to a fiber to be sent to the in-vacuum tank as the Local Oscillator (LO) beam. It will be used on the homodyne detection photodiodes that can support at maximum 5 mW of infrared light on each detector. We decided, for safety to send 6 mW of LO beam out of the fiber, leading to 3 mW on each photodiode.

We optimized the injection of the infrared beam to the LO fiber using the steering mirror and the translation on the fiber mount and obtained a coupling efficiency of 42%. Consequently, we adjusted the half-wave plates to have 15 mW reflected by the third cube beam splitter.

Seed beam injection

Finally the transmitted p-polarized beam from the third polarizing cube beam splitter goes through the system of quarter-wave plate and half-wave plate to rotate its polarization into a s-polarization. This beam is then injected to a fiber to become the seed beam on the in-vacuum bench.

The seed beam will have to enter the Optical Parametric Oscillator (OPO) cavity through one of its high reflective mirror. Thus the beam should be powerful enough to be detected on a photodiode after transmission through the input/output coupler of the OPO cavity. We send 92 mW of infrared light onto the fiber injection.

After alignment of the injection of the infrared beam to the seed fiber as for the LO injection fiber, we obtained a coupling efficiency of 25% leading to 23 mW of seed beam at the output of the fiber inside the in-vacuum Ferrarix tank. As we were limited to maximum 30 mW going out of the fiber for the fiber safety, and had enough input power, we did not have to further optimize this fiber injection to better coupling efficiency.

The final adjustment of the three half wave-plates before the polarizing cube beam splitter is done when all injection efficiencies are measured.

5.2.3 Auxiliary laser green beam production

The auxiliary laser green beam production quadrant is represented along with its picture in the CALVA facility at LAL/IJCLab in Figure 5.15. Its installation starts from the auxiliary laser Coherent Mephisto S that have been measured to deliver 194 mW of infrared light at 1064 nm with a waist radius of $130.5 \mu\text{m} \pm 0.5 \mu\text{m}$ at a distance of $75 \text{ mm} \pm 2 \text{ mm}$ before the front end of the laser head, inside the laser box.

As for the main laser, a system composed of a quarter-wave plate and a half-wave plate is placed on the beam to obtain a laser field s-polarized that is sent to a Faraday isolator to protect the laser head. The Faraday isolator transmits $88.7\% \pm 0.1\%$ of the incoming field.

The beam transmitted by the Faraday isolator is linearly polarized at 45° angle and we use a half-wave plate to s-polarize it before entering an EOM. The EOM generates sidebands at 50 MHz for the lock of the Auxiliary Second Harmonic Generator (SHG2) as described in Section 4.2. It transmits 97.1% of the incoming field.

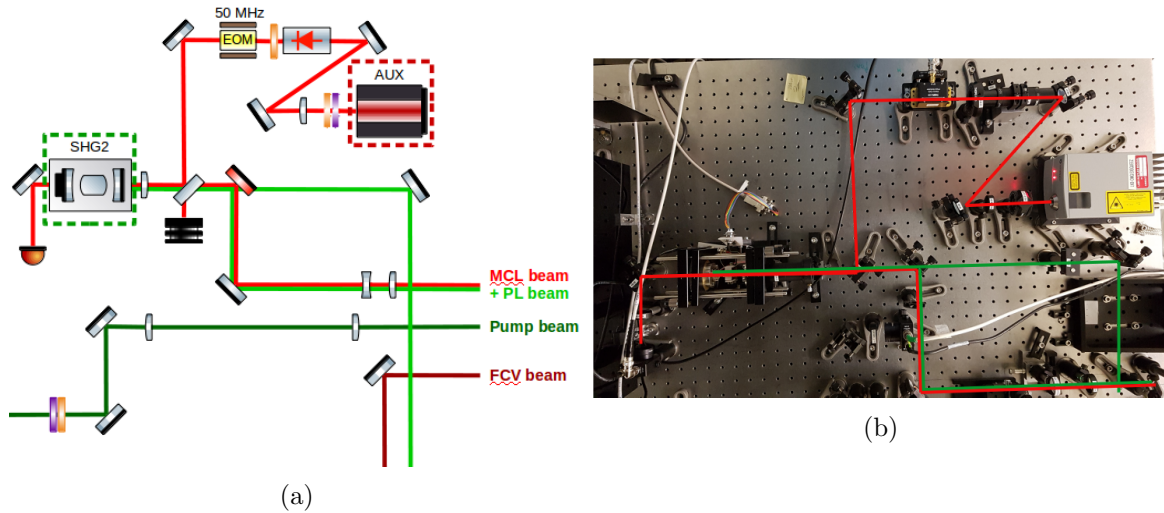


Figure 5.15 – Auxiliary laser green production quadrant scheme (a) and picture on the CALVA facility at LAL/IJCLab (b).

Auxiliary Second Harmonic Generator cavity

Before entering the auxiliary Second Harmonic Generator (SHG2) cavity, the infrared beam is reflected by a dichroic plate that transmits 96% of green beam while reflecting 79% of infrared beam. This dichroic plate is used to propagate towards the in-vacuum bench both infrared and green beams. The unused transmitted infrared beam before the SHG2 cavity is blocked by a beam dump, but can be used to monitor the power fluctuations of the auxiliary laser or test the laser phase lock in infrared.

The scanning of the cavity length is done using a piezo ring on the end mirror of the SHG2 cavity. The piezo is driven by a DAC channel amplified by a HV amplifier by a factor ~ 30 . For the piezo safety, the HV amplifier channel cannot deliver more than 100 V to the piezo.

We measured a flat transfer function for the system composed of the DAC and the HV amplifier. The electrical transfer function of the piezo was measured to be an order 1 low-pass filter with a cutoff frequency of ~ 220 Hz. Finally, the optical transfer function of the cavity is flat on the actuation bandwidth. The control loop filter was then optimized to obtain a stable lock.

The SHG2 cavity length is locked exactly as the SHG1 cavity length, except that the RF signal from the photodiode in transmission is demodulated at 50 MHz which is the frequency that drives the EOM. An example of scan and lock of the SHG2 cavity is given in Figure 5.16 showing the instruction scanning ramp and correction along with the DC and demodulated in-phase error signals defined in Section 4.1.3.

The locking strategy is in two steps. First when the DC signal exceed 3 V the frequency of the ramp sent to the piezo is decreased by a factor 10 to approach the resonance more slowly. Then we start trying to lock when the in-phase error signal is in the linear region between 1.5 V and -1.5 V.

The FFT of the error signal when the SHG2 cavity is locked is represented in Figure 5.17. It shows the residual noise spectrum with in particular spectral lines at 50 Hz and harmonics and unknown noises between ~ 200 Hz and ~ 700 Hz.

We observed that this noise presents some similarities with the noise of the Mach-Zehnder interferometer shown in Figure 5.12, while being different from the noise of SHG1 shown in Figure 5.7. To test this we measured the coherence between the error signals of the 3 optical systems of the in-air table. The coherence plots are shown in Figure 5.18.

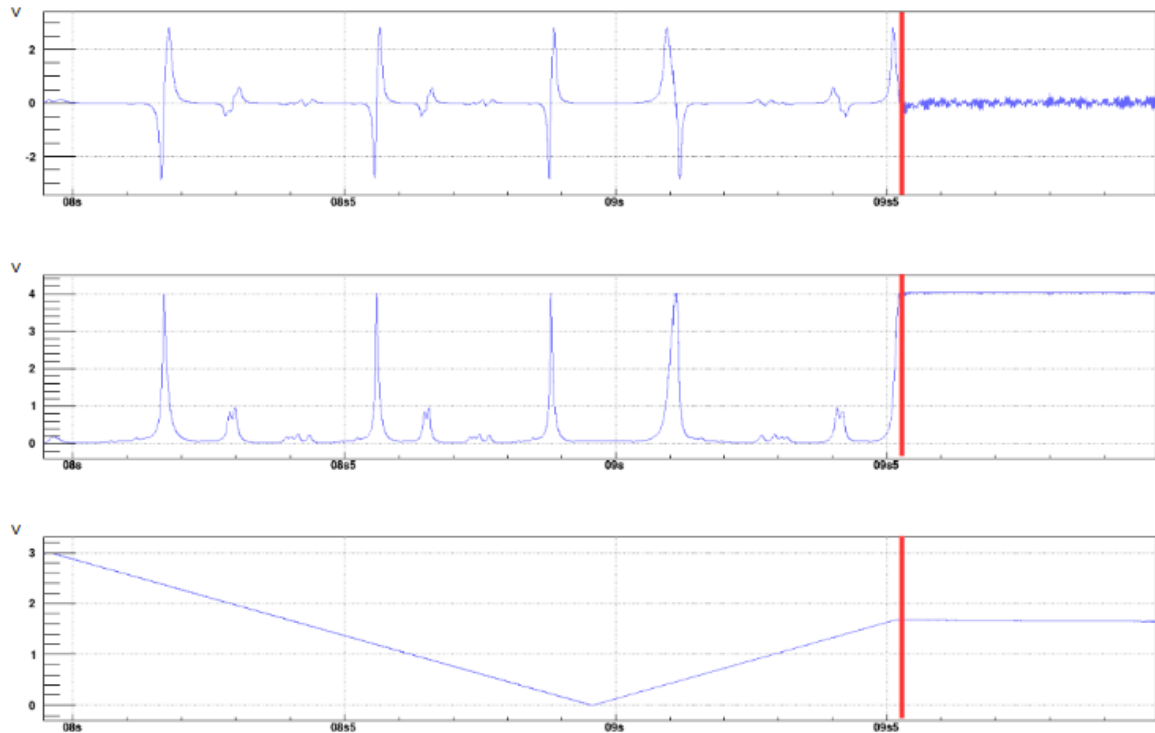


Figure 5.16 – Example of scan and lock of the SHG2 cavity separated by the red line: (*upper*) error signal from the in-phase demodulation at 50 MHz of the signal from the in-air photodiode in transmission of the SHG2 cavity, (*middle*) DC signal from the in-air photodiode in transmission of the SHG2 cavity, (*lower*) actuation order sent by the DAC to the piezo on the end mirror of the SHG2 cavity.

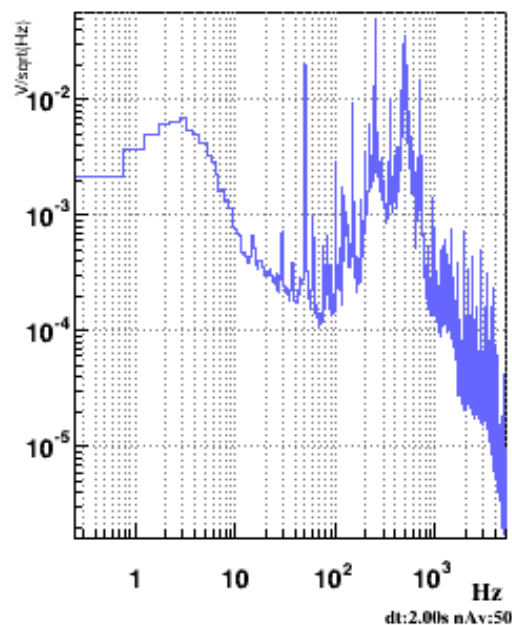


Figure 5.17 – FFT of the error signal when the auxiliary Second Harmonic Generator (SHG2) cavity is locked.

The coherence between SHG1 and SHG2 is very low except for the 50 Hz and harmonics lines while there is some coherence between SHG1 and the Mach-Zehnder which seems reasonable as the residual noise on the pump beam coming from SHG1 go through the Mach-Zehnder interferometer. The coherence between the Mach-Zehnder and SHG2 is quite important, es-

pecially between 200 Hz and 1 kHz even though they are not on the same beam. This seems to indicate that this noise may be due to a noise in the room (such as air movements or table defect) that has not been investigated yet, but that impact less SHG1.

The green beam at 532 nm produced by SHG2 is then transmitted by the SHG2 dichroic plate through another dichroic plate that that transmits green and reflects infrared. The powermeter or a photodiode are placed after this second dichroic plate to measure the green power produced by SHG2.

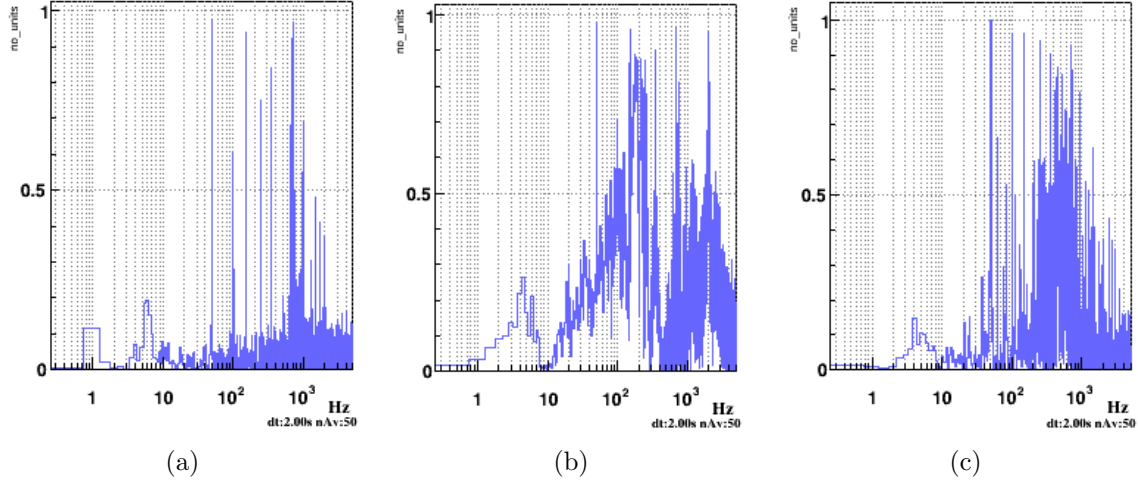


Figure 5.18 – Coherence plots of the FFT of the error signal between the 3 optical systems of the in-air bench: (a) coherence between SHG1 and SHG2, (b) coherence between SHG1 and the Mach-Zehnder, (c) coherence between SHG2 and the Mach-Zehnder.

Auxiliary Second Harmonic Generator temperature controller

The temperature of the SHG2 crystal is controlled using a homemade oven with a Peltier cell and a thermistor as shown in Figure 5.19a. The thermistor used is a TCS650 Thermistor [119], the same one with the same electronics will be used in-vacuum to control the temperature of the crystal of the Optical Parametric Oscillator (OPO). When the temperature on the thermistor T_{th} changes, it changes the resistor value R_{th} of the thermistor according to the Steinhart-Hart equation:

$$\frac{1}{T_{th}} = A + B \times \ln(R_{th}) + C \times (\ln(R_{th}))^3, \quad (5.3)$$

where A, B and C are coefficients given by the thermistor datasheet [119], R_{th} is expressed in Ohm and T_{th} is expressed in Kelvin. Then the LAPP Temperature Control Box transform the measured resistor R_{th} onto a measured voltage U_{mes} sent to an ADC for data acquisition. U_{mes} is electronically comprised between -4 V and +4 V and is obtained via:

$$U_{mes} = \left(0.25 - \frac{0.5 \times R_{th}}{R_{box} + R_{th}}\right) \times \left(1 + \frac{50000}{511}\right), \quad (5.4)$$

where the numerical values come from fixed electronics components and R_{box} is a resistor that can be changed inside the temperature controller box to adjust the range of measurable temperatures around the optimal designed temperature range. For the SHG2 crystal the optimal temperature should be around $50^\circ \text{C} \pm 5^\circ \text{C}$ according to Figure 4.6. So we decided to use $R_{box} = 15 \text{ k}\Omega$ to have an available temperature range measurement of from 45°C to 61°C .

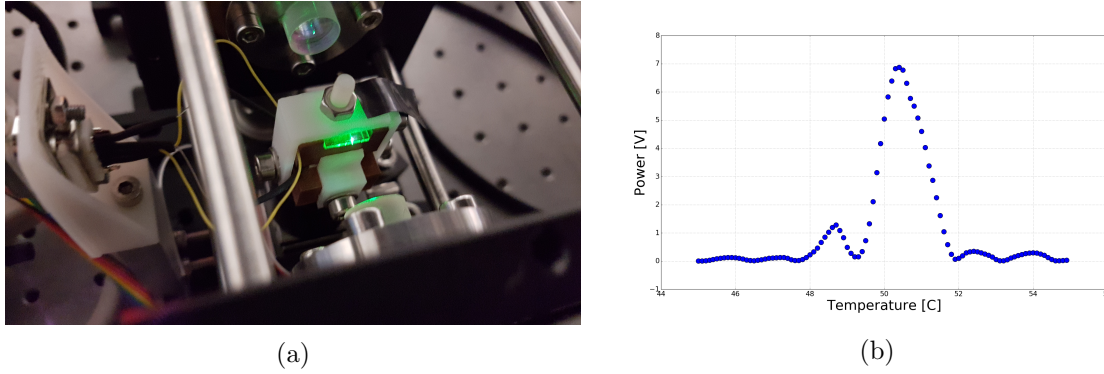


Figure 5.19 – (a) Picture of the auxiliary Second Harmonic Generator (SHG2) showing, the MgO:PPLN crystal and its homemade oven. (b) Plot of the phase-matching temperature measurement.

Then, to reconstruct the temperature T_{th} measured by the thermistor, we approximate it by a quadratic polynomial in U_{mes} adjusted depending on the R_{box} resistor value. For the SHG2 temperature control, the measured temperature T_{th} is obtained from the measured voltage U_{mes} via:

$$T_{th} \simeq 52.84 + 2.029 \times U_{mes} + 0.0109 \times U_{mes}^2. \quad (5.5)$$

The Peltier cell is driven using the Acl server to send instruction voltage via a DAC to lock the crystal temperature to the desired value. To find the optimal value, we locked the SHG2 cavity and scan the SHG2 crystal temperature. The green power produced was measured with a photodiode connected to an ADC. The resulting phase-matching temperature plot is shown in Figure 5.19b. It almost follows a sinc^2 function with a maximum power generated at 50.3° C. However one can see that for an unknown reason it is not as symmetrical as for SHG1 in Figure 5.8b.

The stability of the temperature lock was tested over a day in Figure 5.20. For the test, the temperature actuation order was 52.5° C and it was stable with a RMS of 0.02° C. Moreover, we were able to check that the lock corrects the crystal temperature variations due to the room temperature fluctuations. In fact the correction actuation follows the voltage fluctuations of a free ADC channel that has been checked to be correlated to the room temperature fluctuations.

Finally after some alignment and matching improvement we measured 33 mW of generated green beam from 141 mW of infrared beam injected to the SHG1 cavity leading to a green beam production efficiency of 23%.

Beams injections towards the in-vacuum tank via the window

On this quadrant of the in-air bench, there are 4 beams that are propagated towards the Ferrarix in-vacuum tank through its window. The in-air and in-vacuum benches are not at the same height in the room. Consequently we have to use periscopes to change the beam height and send the beams to the in-vacuum tank.

99.8% of the green beam is sent to the auxiliary laser fiber injection quadrant while 0.2% is used for the Phase Locking (PL) beam, superposed with the Modified Coherent Locking (MCL) beam.

The pump beam that comes from the main laser green beam production quadrant goes through a quarter-wave plate and a half-wave plate to ensure a good s-polarization of the beam before the Optical Parametric Oscillator (OPO).

Finally the Filter Cavity Verification (FCV) beam is sent to the in-vacuum tank after in-air propagation through the main and auxiliary lasers fibers injections quadrants.

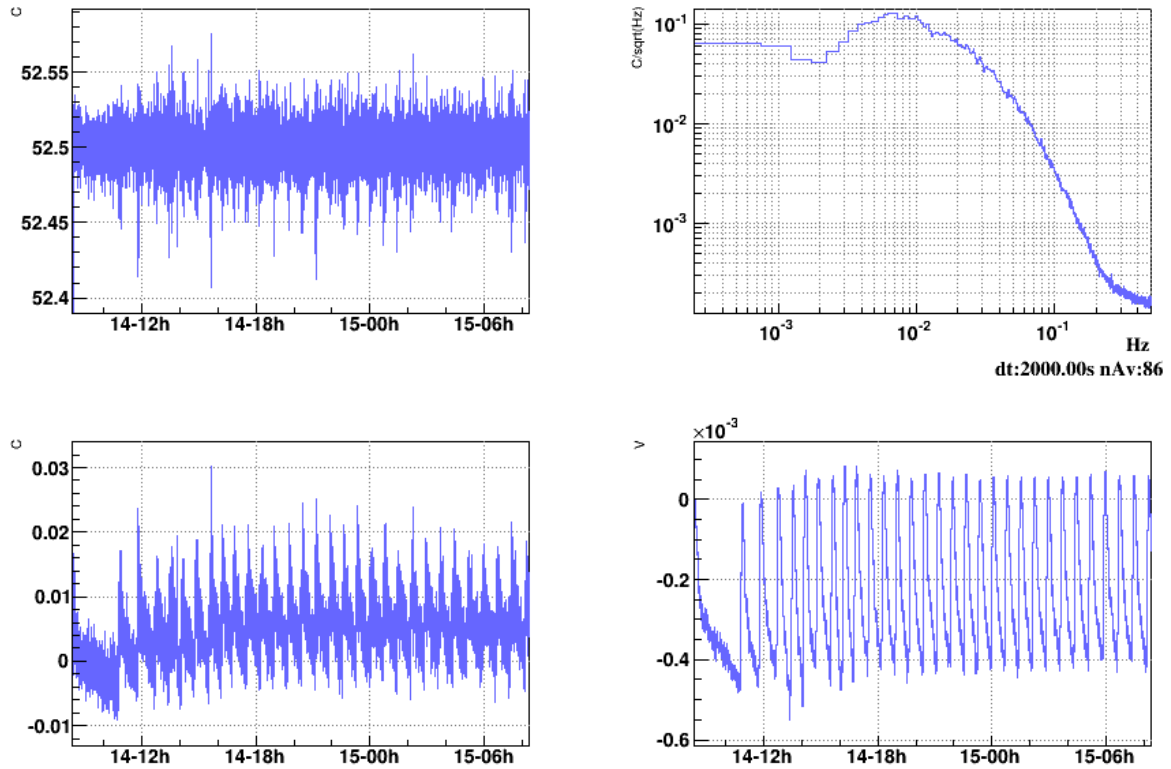


Figure 5.20 – Test of the stability of the temperature lock of the SHG2 crystal over a day showing for the time channel minimal (green), maximal (blue) and mean (red) value of the channel each second. *Upper left:* Temperature of the SHG2 crystal. *Lower left:* Correction actuation sent to the Peltier of the SHG2 crystal *Upper right:* FFT of the correction actuation. *Lower right:* Free ADC channel sensitive to room temperature variations.

The power of the 4 beams send from the in-air bench to the in-vacuum bench through the window are summarized in table 5.1.

Beam	Wavelength	Power
Modified Coherent Locking (MCL)	1064 nm	18 mW
Phase Locking (PL)	532 nm	$\sim 160 \mu\text{W}$
Pump	532 nm	from 1 mW to 120 mW
Filter Cavity Verification (FCV)	1064 nm	30 mW

Table 5.1 – Summary of the beam power going through the Ferrarix in-vacuum tank window.

5.2.4 Auxiliary laser fiber injection

The auxiliary laser fiber injection quadrant is represented along with its picture in the CALVA facility at LAL/IJCLab in Figure 5.21. It is composed of two beams: the Filter Cavity Verification (FCV) beam coming from the main laser fibers injections quadrant and sent to the auxiliary laser green beam production quadrant and the Filter Cavity Control (FCC) beam coming from the auxiliary laser green beam production quadrant and injected to a fiber.

The FCV beam passes through one lens on this quadrant that is used to have an almost collimated beam on the ~ 3 m propagation before entering the in-vacuum tank with the need waist.

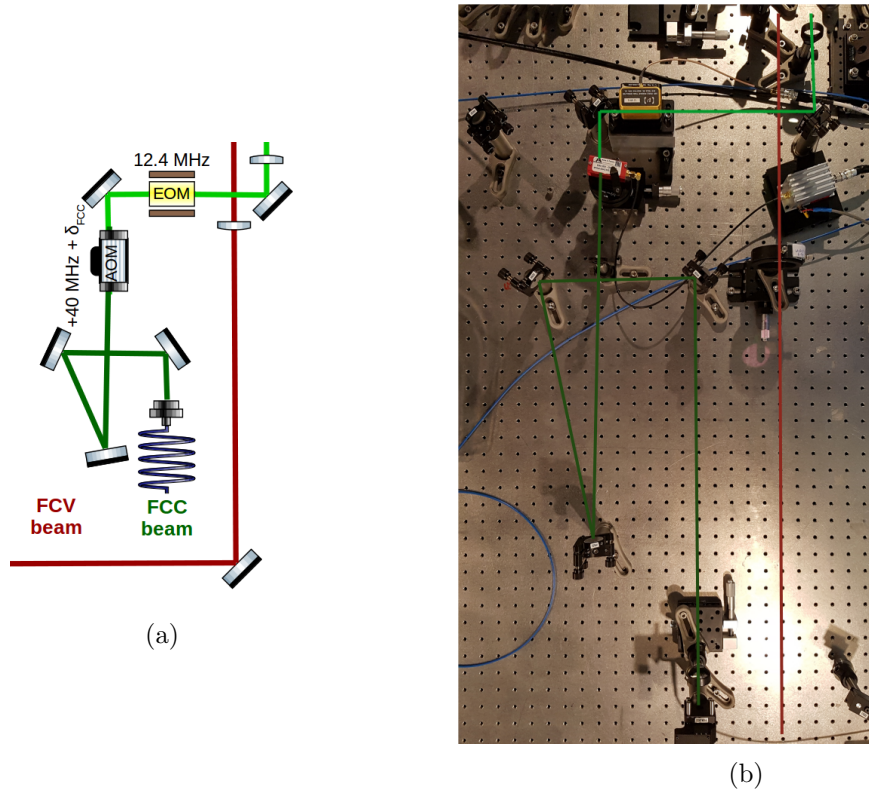


Figure 5.21 – Auxiliary laser fiber injection quadrant scheme (a) and picture on the CALVA facility at LAL/IJCLab (b).

The FCC beam passes through an EOM that generates sidebands at 12.4 MHz used for the lock of the 50 m filter cavity. It transmits 94% of the incoming field that is then injected through a free space AOM aligned on the +1 order to have a positive frequency shift at the RF modulation applied $40 \text{ MHz} + \delta_{FCC}$. The δ_{FCC} frequency shift is a small shift adjusted to lock the 50 m filter cavity with a detuning in infrared as define in Section 4.5.3:

$$\Delta\omega_{fc} = \frac{\delta_{FCC}}{2}. \quad (5.6)$$

In the first step of Exsqueez, we will have $\delta_{FCC} \sim 1 \text{ kHz}$. The transmission efficiency of the beam to the +1 order of the AOM output was measured to be 65%. This beam is then injected through a fiber with a transmission efficiency of 13% leading to a Filter Cavity Control beam inside the in-vacuum tank of 2 mW to lock the 50-m filter cavity. Further optimization should be done on this fiber injection to improve the beam power used to lock the filter cavity.

The power of the 3 beams send from the in-air bench to the in-vacuum bench using fibers are summarized in table 5.2.

Beam	Wavelength	Power
Local Oscillator (LO)	1064 nm	6.4 mW
Seed	1064 nm	23 mW
Filter Cavity Control (FCC)	532 nm	2 mW

Table 5.2 – Summary of the beam power going through the Ferrarix in-vacuum tank using fibers.

5.3 In-vacuum bench

The design of the in-vacuum bench was done at LAL/IJCLab using the OptoCad simulation tool [120], based on the conceptual design made by LKB. It is represented in Figure 5.22, showing all beams and optics on the Ferrarix in-vacuum tank, the in-air detection bench and the 50-meter filter cavity.

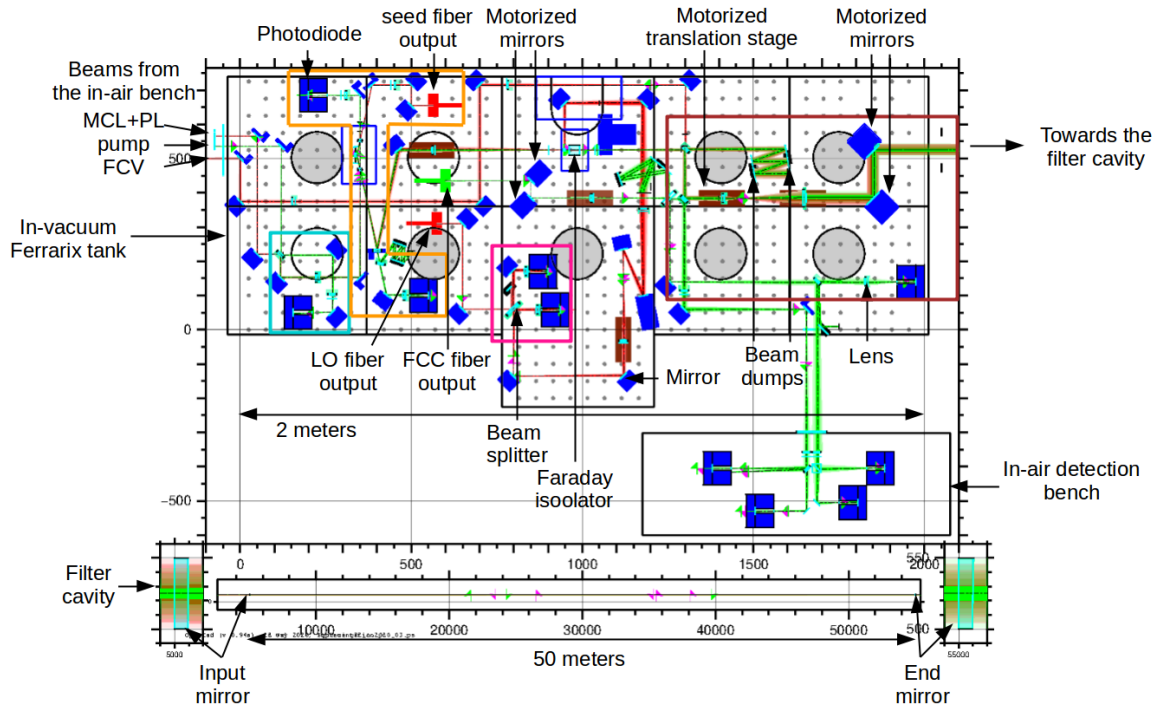


Figure 5.22 – OptoCad scheme showing the Ferrarix in-vacuum tank, the filter cavity and the in-air detection bench with all the optics and beams simulated. 4 areas are highlighted on the in-vacuum bench: in light blue for the laser phase locking, in orange of the Optical Parametric Oscillator (OPO), in pink for the homodyne detection and in brown for the filter cavity injection and control.

There are 4 main areas that have been highlighted on the in-vacuum bench simulated scheme: in light blue for the laser phase locking, in orange for the Optical Parametric Oscillator (OPO), in pink for the homodyne detection and in brown for the filter cavity injection and control.

I will first present simulations and experimental work preparing the integration and characterization of the main areas. Then I will go through the laser phase locking integration and characterization and finally I will present the preparation of the filter cavity integration. The integration and characterization of the squeezing related area OPO and homodyne detection will be described in Chapter 6.

5.3.1 Preparation of the in-vacuum bench integration

The first thing we had to take care when designing the in-vacuum tank real optical scheme was the over-crowding of the in-vacuum bench. To do so, we added in the OptoCad simulation the imprints of the optics mounts, especially for the fibers outputs, mirrors, photodiodes and translation stages.

Moreover, on the scheme of Figure 5.22, I also represented the screw holes, separated by 5 cm, to prepare the binding of the optical mounts and the circular removable parts of the bench with in grey the ones that we removed for the passage of electric cables. This simulation was used to define the installation procedure of the in-vacuum bench.

We decided to motorized 4 mirrors to adjust the beams alignments to the filter cavity and placed 5 lenses on translation stages to tune the matching of the beams to the filter cavity and to the homodyne detection.

Then when we received the first optical elements, we measured their properties that I will now summarized.

Faraday isolator

On the in-vacuum bench we use a Faraday isolator, shown in Figure 5.23 to recover the squeezed beam reflected by the 50-meter filter cavity. Its losses will be important for the squeezing measurement.

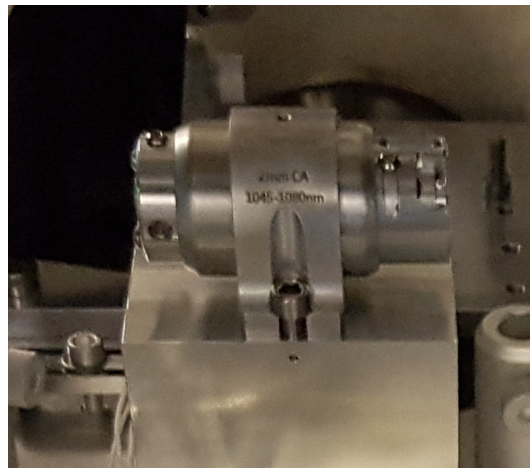


Figure 5.23 – In-vacuum Faraday isolator.

To obtain an isolated beam from the filter cavity reflected by the Faraday isolator in the bench plane, we have to send a p-polarized beam at the input of the Faraday isolator. However at the output of the Optical Parametric Oscillator (OPO), the squeezed beam is s-polarized. Consequently we add a half-wave plate before the Faraday isolator to rotate the polarization of the squeezed beam into a p-polarization.

Then the coating of the filter cavity are designed for s-polarized beams. Consequently we add another half-wave plate in transmission of the Faraday isolator to obtain a s-polarized beam. We did not used a quarter-wave plate before the half-wave plate as for the in-air bench because it is more restrictive to find vacuum compatible wave-plates.

The transmissivity of the Faraday isolator has been measured to be 98.2% from the OPO to the 50-meter filter cavity and 97.1% from the filter cavity to the isolated beam leading to a total loss of 4.6% of the squeezed light.

Fiber output collimators

We measured the beam size generated by the fibers output collimators and compared them to the values given by the manufacturer in Table 5.3. We observed huge differences between the values given by the manufacturer and the measured ones. Consequently we had to adjust the OptoCad simulation with the measured waist sizes generated by the fiber collimator.

Moreover, after few months in box, the Filter Cavity Verification (FCV) and Local Oscillator (LO) collimators were remeasured for installation and we observed respectively 6 % and 15% of waist radius changes while the Filter Cavity Control (FCC) collimator that was already mounted and installed showed no waist change. All the measurements were done with the same apparatus.

Beam	Measured waist (radius and position)	Manufacturer
Filter Cavity Control (FCC)	$103.8 \pm 0.2 \mu\text{m}$ at $231.2 \pm 0.3 \text{ mm}$	$400 \mu\text{m}$
Filter Cavity Verification (FCV)	$372 \pm 4 \mu\text{m}$ at $242 \pm 0.5 \text{ mm}$	$500 \mu\text{m}$
Local Oscillator (LO)	$297.9 \pm 0.5 \mu\text{m}$ at $274 \pm 1 \text{ mm}$	$500 \mu\text{m}$

Table 5.3 – Beam collimator waist radius measured after the collimator and manufacturer given beam radius with a waist at infinity.

Lenses focal lengths

We also measured the focal length of the in-vacuum lenses and observed a correct agreement with less than 1% of error with respect to the manufacturer values for the lenses with focal lengths above and equal to 250 mm. Then lenses with focal lengths between 50 mm and 175 mm presented up to 5% difference with respect to the manufacturer values. These differences were taken into account into the simulated OptoCad scheme, even though they did not generate important changes in the design.

Finally we have a lens with more than 10% discrepancy between the manufacturer value of 200 mm and the measured value of $174.7 \pm 1.1 \text{ mm}$. This lens is placed after the fiber output of the Filter Cavity Control (FCC) beam to mode match it to the 50 m filter cavity. Consequently we had to modify the simulation to take into account the real focal length value to define the design of the in-vacuum bench.

In-vacuum beam dumps

To block the ghost beams and the unused beams inside the in-vacuum tank we use dumps shown in Figure 5.24 that are basically made of black glass. We have two kind of dump: with and without anti-reflective coating in infrared. There properties are summarized in Table 5.4.

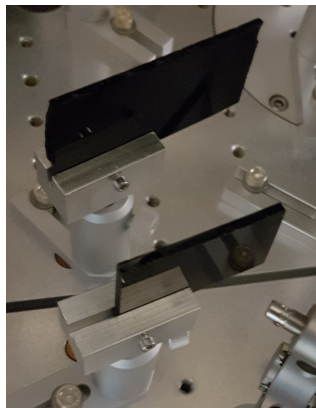


Figure 5.24 – In-vacuum beam dumps.

Dump	Reflectivity at 532 nm	Reflectivity at 1064 nm
With coating	$0.15 \pm 0.01\%$	$0.016 \pm 0.005\%$
Without coating	$0.043 \pm 0.001\%$	$0.083 \pm 0.007\%$

Table 5.4 – Beam dump reflectivity measurement with and without anti-reflective coating in infrared. The transmissivity couldn't be measure, only an upper limit of $T < 1\text{ppm}$ could be given.

We uses uncoated dump on green beams and coated dumps on infrared beams. When we need to dump few dozens of mW of a beam we place two beam dumps in parallel to have multiple reflections between them and better attenuate the beam.

5.3.2 Laser phase locking

The two green beams used to phase lock the main and auxiliary lasers, in the light blue area of Figure 5.22, are the Phase Locking (PL) and pump beams described in Chapter 4. They enter the in-vacuum Ferrarix tank through a window after their preparation on the in-air bench. Entering the tank, the PL beam is superposed to the infrared Modified Coherent Locking (MCL) beam.

The PL and pump beams are combined on a beam splitter that reflects on each side 2% at 532 nm and 12% at 1064 nm. This plate was chosen to have enough pump power combined to the PL beam to observe a beatnote and a reduction by a factor 10 of the MCL power sent to the homodyne detection photodiodes, after going through the Optical Parametric Oscillator (OPO), not to blow up the homodyne photodiodes.

Consequently, going towards the Phase Locking Loop (PLL) photodiode, there is 96% of the PL beam (corresponding to 150 μ W), 2% of the pump beam (corresponding to 10 μ W to 1 mW depending on the pump power) and 76% of the MCL beam (corresponding to 13 mW). Then as the two mirrors between the beam splitter and the PLL photodiode are designed to reflect green beam, there is no measurable MCL beam on the PLL photodiode. The PLL photodiode is an in-vacuum photodiode that supports up to 2.5 mW of green beam.

The laser phase locking is done using the open source software PyRPL [121] on a Red Pitaya [122] that has 2 inputs and 2 outputs. On the first input we connected the RF signal of the PLL photodiode. The second input is used for tests and connected to an in-air photodiode to check the beatnote between the main and auxiliary lasers in infrared.

The first output is connected to the PZT of the auxiliary laser allowing a 65 MHz tuning range and the second output is connected to the auxiliary laser crystal temperature controller allowing a ~ 6 GHz tuning. The pre-tuning of the auxiliary laser crystal temperature was done on a tuning screw so that the 20 MHz beatnote foreseen between both laser heads is in the 6 GHz range accessible with the Red Pitaya. Then the offset on the laser crystal temperature was tuned on the RedPitaya to observe the 20 MHz beatnote on the 65 MHz range of the laser PZT.

The sidebands pictures of the beam on the green and infrared photodiodes are shown in Figure 5.25. In infrared, the main laser is taken from a pick-off before the EOM used to control the main Second Harmonic Generator cavity and thus it has no sidebands while the auxiliary laser is taken from a pick-off after the EOM used to control the auxiliary Second Harmonic Generator cavity and thus is represented with its 50 MHz sidebands.

As a result when we look at the spectrum on the infrared photodiode using the spectrumanalyzer toolbox of PyRPL, if the laser are correctly phase locked, we can observe the beatnote between the carriers of the main and auxiliary lasers at 20 MHz and the beatnote between the carrier of the main laser and the lower sideband of the auxiliary laser at 30 MHz

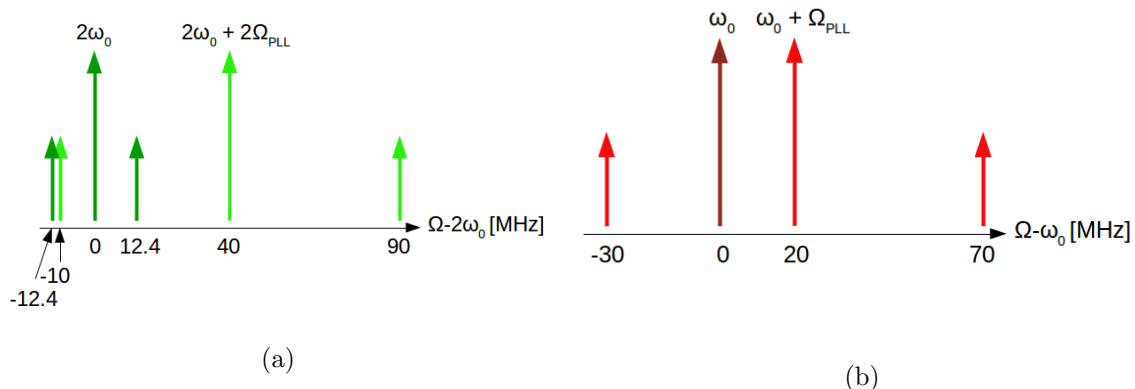


Figure 5.25 – Sidebands pictures (a) on the photodiode used to phase lock both main and auxiliary lasers in green (b) on an in-air test photodiode used to check the infrared spectrum.

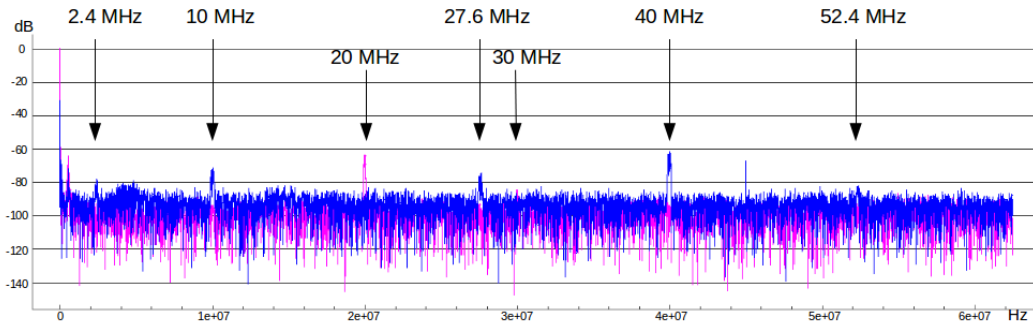


Figure 5.26 – Spectrum of the in-vacuum green photodiode (in blue) and in-air infrared photodiode (in pink) measured using the spectrumanalyzer toolbox of PyRPL and showing the visible beatnote between the carriers and sidebands of the main and auxiliary lasers.

with a lower amplitude as shown in Figure 5.26. The beatnote between the main carrier and the higher sideband of the auxiliary laser at 70 MHz is not in the range of measurement of the Red Pitaya.

The spectrum in green is more complex as both PL and pump beams have sidebands. The summary of the beatnote frequency observed when locked is given in Table 5.5. They are not all observables on the spectra shown in Figure 5.26 due to two reasons. First of all the bandwidth of the Red Pitaya spectrumanalyzer is comprised between 0 and 60 MHz. Then the beatnote signal to noise ratio is more important for carriers than sidebands as there is more power on the sideband. Finally, the PLL photodiode has a cutoff frequency of 20 MHz, thus the 22.4 MHz beatnote between two sidebands is not observable while the 2.4 MHz beatnote between two sidebands is close to noise but observable.

Frequency [MHz]	Main laser	Auxiliary laser	Observable
2.4	Lower sideband	Lower sideband	Close to noise
10	Carrier	Lower sideband	Yes
22.4	Higher sideband	Lower sideband	No
27.6	Higher sideband	Carrier	Yes
40	Carrier	Carrier	Yes
52.4	Lower sideband	Carrier	Close to noise
77.6	Higher sideband	Higher sideband	No
90	Carrier	Higher sideband	No
102.4	Lower sideband	Lower sideband	No

Table 5.5 – Beatnote frequencies on the PLL photodiode.

The presence of the sidebands beatnotes has an impact for the phase lock of the laser due to the way the error signal is derived using PyRPL. PyRPL doesn't demodulate the signal at the chosen frequency Ω_{PLL} , it uses a frequency comparison between the internal frequency reference at Ω_{PLL} and the input signal. Every time the measurement signal crosses 0, a timer on a 2^{14} basis is incremented and every time the internal signal crosses 0, the same timer is decremented. Thus if the two signals are at the same frequency, the error signal is at 0. Otherwise the voltage of the error signal is between -1 and +1 V.

However, when sweeping the auxiliary laser frequency on 65 MHz using the PZT, not only the carriers beatnote crosses the 40 MHz frequency leading to an error signal at 0, but sidebands beatnote too. The error signal gives no information on the beatnote amplitude and only the ones that have enough signal to noise ratio lead to a 0 crossing. Consequently we have to carefully chose the starting offset of the PZT when trying to phase lock the laser heads.

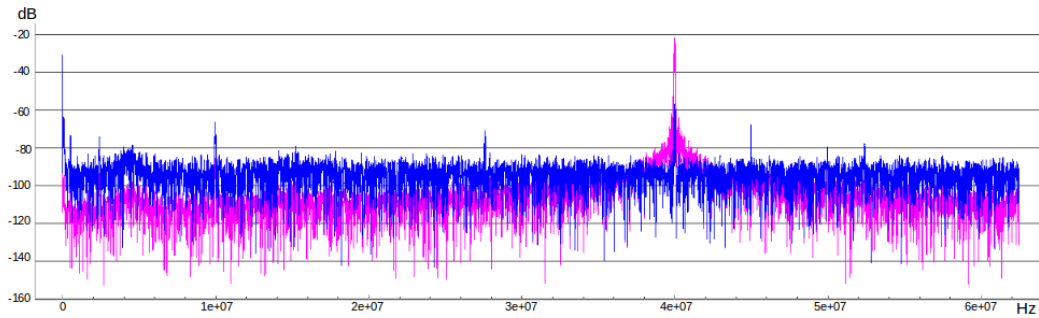


Figure 5.27 – Spectrum of the in-vacuum green photodiode without filtering (in blue) and with filter (in pink) measured using the RedPitaya spectrumanalyzer. The filtering improves the signal to noise ratio at 40 MHz.

To improve the signal to noise ratio of the 40 MHz beatnote and thus obtain a cleanest error signal, we filtered the PLL RF signal with a bandpass digital filter of 40 kHz around 40 MHz. The filtered signal is shown in Figure 5.27 along with the non filtered signal for the PLL photodiode.

Finally a example of input RF signal from the PLL photodiode and derived error signal is shown in Figure 5.28 showing the phase lock acquisition of the main and auxiliary laser heads at $\Omega_{PLL} = 20$ MHz.

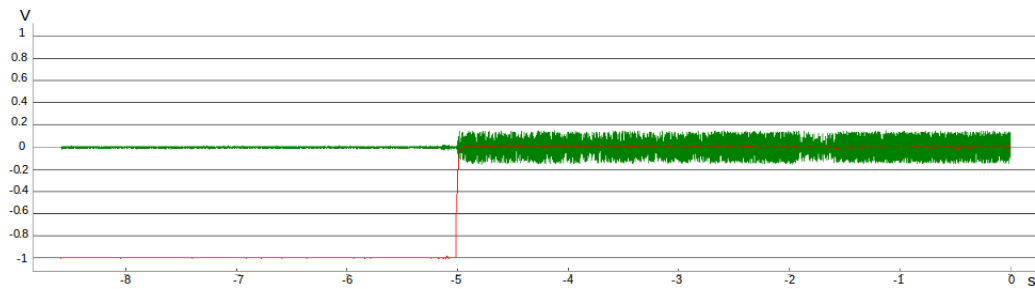


Figure 5.28 – Temporal plots of the RF signal from the in-vacuum green photodiode (in green) and phase lock error signal (in red) when scanning and locking.

5.3.3 Filter cavity

During the time of my thesis, the filter cavity was not used and the beams were not sent through it. However we prepared the beams injections and the control of the suspended mirrors that I will present now.

Beams injection

There are 3 independent beams that need to be injected through the 50-meter filter cavity: the squeezed beam – superposed to the Modified Coherent Locking (MCL) beam –, the Filter Cavity Control (FCC) beam and the Filter Cavity Verification (FCV) beam.

The beams are sent towards the filter cavity via a mode matching lens telescope composed of two lenses on motorized translation stages and 2 motorized mirror to be able to adjust the matching of the beams to the filter cavity and their alignment even under vacuum.

However, the beams should be superposed before the mode matching lens telescope on dichroic plates and beam splitters. To ensure this superposition, we will send the fourth port of the splitters, where the beams should also be superposed, into an in-air detection table

through a window of the in-vacuum tank. 2 quadrant photodiodes with 90° Gouy phase shift will then be used to check the superposition of the beams.

Moreover, as the telescope is common to both beams with two different wavelength, there should be another motorized mode matching lens on at least 2 beams to adjust separately the mode matching of each beam to the 50-meter filter cavity. Note also that due to the variation of refractive index, the focal length of the lenses is not the same for the green and infrared beams. We took that into account in the simulation of the mode matching lens telescope.

Control of the suspended mirrors

The 50-meter filter cavity is composed of two suspended mirrors that are controlled using magnet and coils shown with the mirror suspension in Figure 5.29.

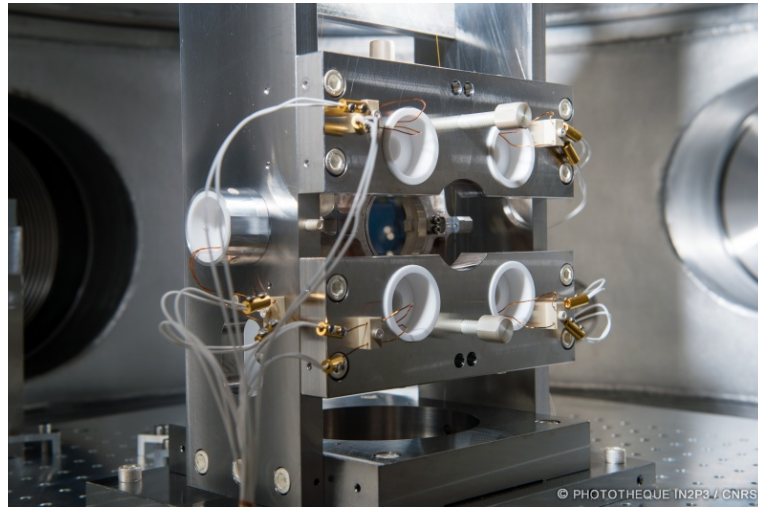


Figure 5.29 – Filter cavity mirror showing the suspension wires and the coils used to control the mirror position.

The first step to control the mirror of the filter cavity is to use local control with red lasers that are sent with 45° of incidence on both mirror as shown in Figure 5.30. The reflected beams are then sent to two quadrant photodiodes with 90° Gouy phase shift to control the pitch and yaw of the mirrors.

Then the length of the cavity is controlled using the Filter Cavity Control (FCC) beam with a photodiode in reflection of the cavity, in the Ferrarix in-vacuum tank. The detuning of the filter cavity for the squeezing frequency is verified using the Filter Cavity Verification (FCV) beam which frequency can be scan in a range of 8 MHz greater than the Free Spectral Range of 3 MHz of the cavity. The photodiode to measure the FCV beam is placed in transmission of the filter cavity to have enough power and contrast on the Airy peak as shown on the simulated plots of Figure 5.31.

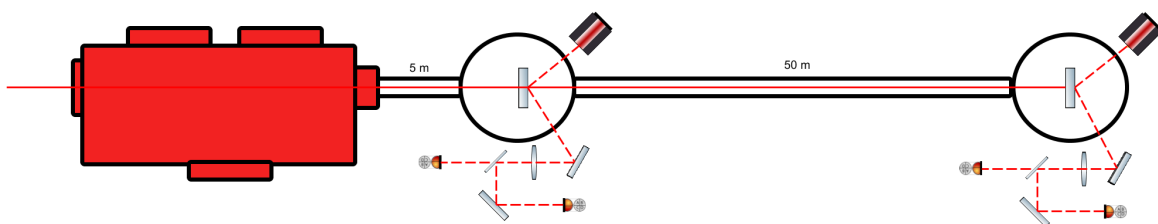


Figure 5.30 – Scheme of the CALVA in-vacuum system showing the Ferrarix tank in red, and the two tanks where the mirror of the 50-m filter cavity are. The local control lasers and photodiodes of both mirrors are also represented.

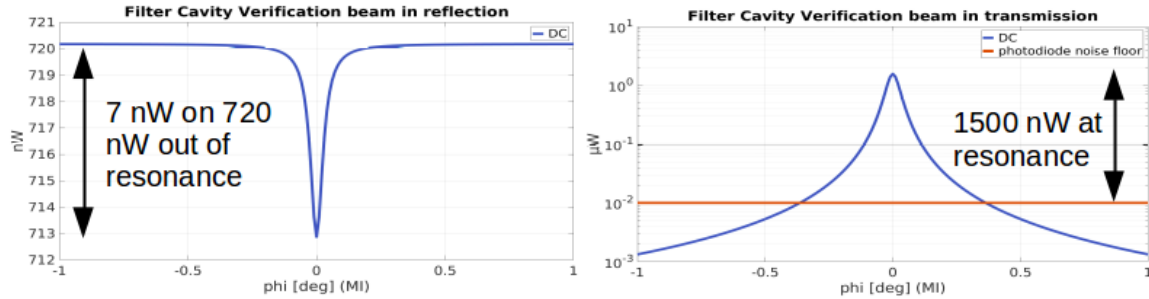


Figure 5.31 – Simulation of the signal measured for the Filter Cavity Verification (FCV) beam: (*left*) in reflection, (*right*) in transmission. The noise floor and RMS of the photodiode is at least 10 nW.

5.4 Conclusion

During the time of my thesis we installed and characterized the whole final in-air bench set-up. However we observed some slow, long time scale drifts of the alignment for unknown reasons (part of the drifts are due to thermal effect), in particular of the Second Harmonic Generator cavities that needed to be readjusted at week scale.

The injection of the Filter Cavity Control beam, even though installed, was not fully optimized due to these drifts, knowing that we would not use it for months.

The installation of the in-vacuum bench was dependent on the in-air beams generation and characterization. It was thus delayed and only a part of it was installed, starting from the beams entering the tank via fibers as we did not need the final in-air completion but could use temporary infrared and green beams injected on fibers.

However the phase lock of the laser heads in its final configuration was installed and characterized and the mode matching of the beam towards the 50-meter filter cavity and the filter cavity control were prepared and all optics mounts have been installed inside the in-vacuum tank to check the over-crowding of the bench.

The installation and characterization of the squeezing generation and measurement related area of the in-vacuum tank (the Optical Parametric Oscillator and the homodyne detection) will be described in Chapter 6.

Chapter 6

Preparation of the squeezing measurement

The first squeezing measurements on the CALVA facility are done without the 50 m filter cavity with a modified scheme shown in Figure 6.1. The aim of these measurements is to characterize the in-air frequency independent squeezing source. The next steps are to measure frequency independent squeezing under vacuum and then inject it into the 50-meter filter cavity to measure frequency dependent squeezing.

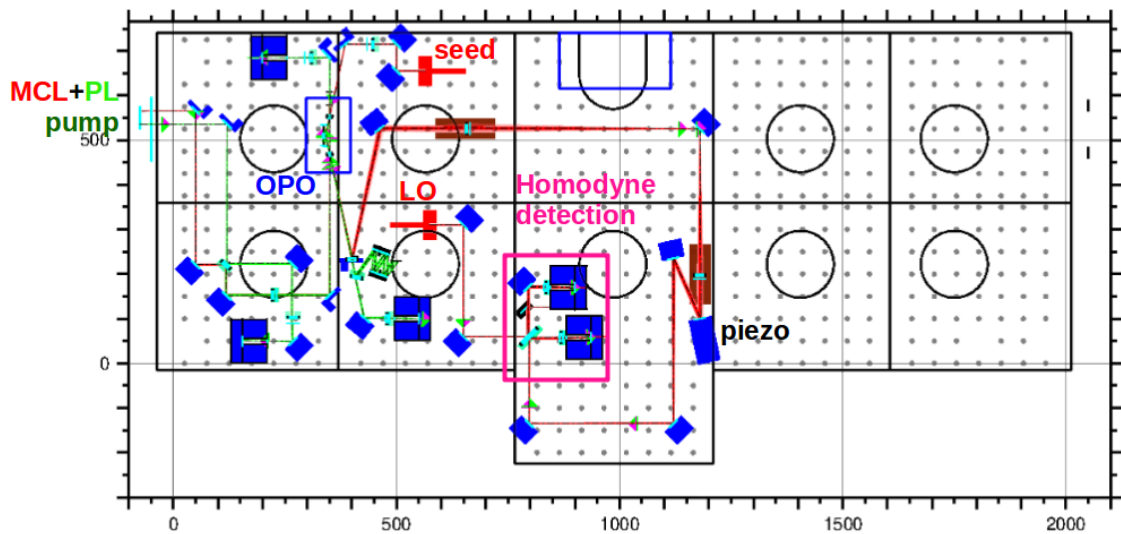


Figure 6.1 – OptoCad scheme of the experimental set-up used for the first squeezing measurement on the CALVA facility.

On this scheme, the squeezed beam generated by the Optical Parametric Oscillator (OPO) is directly sent to the homodyne detection photodiodes for measurement with the Local Oscillator (LO) beam. I will now present the alignment of the OPO cavity with the pump beam and the superposition of the Modified Coherent Locking (MCL) beam and the seed beam to the pump beam. Then I will explain the OPO characterization using the seed beam before detailing the homodyne detection efficiency.

6.1 Alignment of the Optical Parametric Oscillator cavity

The first alignment of the Optical Parametric Oscillator (OPO) cavity was done using 1 mW of green pump beam and a camera in transmission of the cavity.

The matching of the pump and MCL beams to the OPO cavity is obtained using a lens

in-vacuum (common to both pump and MCL beams) and two lenses in-air on each beam path with for each beam a lens on a manual translation stage to tune the matching.

Then, for the first alignment the procedure was the following:

- First we used the two pump steering mirrors to roughly ensure that, on the path towards the OPO, the pump beam stays at the design height of 10 cm above the in-air bench.
- We removed the OPO cavity input coupler (flat mirror) and placed the OPO mechanical board shown in Figure 6.2, so that the waist of the pump beam is in the middle of the two flat mirrors expected positions.
- We placed the thin flat mirror and the two curved mirrors on the mechanical board at there theoretical position.
- We placed a camera on the beam transmitted by the thin flat mirror.
- We oriented the thin flat mirror to reflect the pump beam on the first curved mirror and then oriented the first curved mirror to reflect the beam through the crystal up to the second curved mirror.
- We placed the input coupler at its theoretical position and oriented it so that the first round trip beam is visible on the camera and then we oriented the second curved mirror so that the direct beam and the first round trip beam are superposed on the camera leading to fringes.
- We started scanning the cavity with the piezo rings on the flat mirrors and used the two pump steering mirrors to widen the fringes until observing modes on the camera.
- We placed an in-vacuum photodiode in reflection of the cavity to see the spectrum while scanning and we fine tuned the pump steering mirrors alignment by increasing the fundamental mode and decreasing the first high order mode on the spectrum.

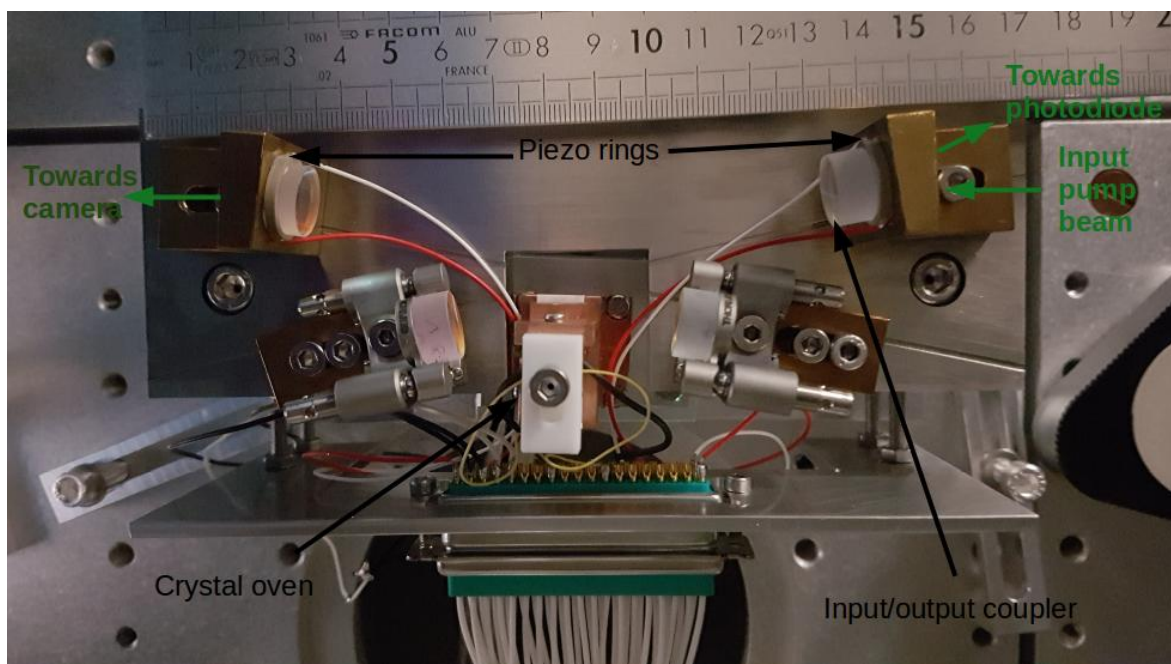


Figure 6.2 – Photo of the Optical Parametric Oscillator (OPO) mechanical board (before alignment at the definitive mirror positions) showing the input/output coupler and the position of the photodiode and camera used for the alignment.

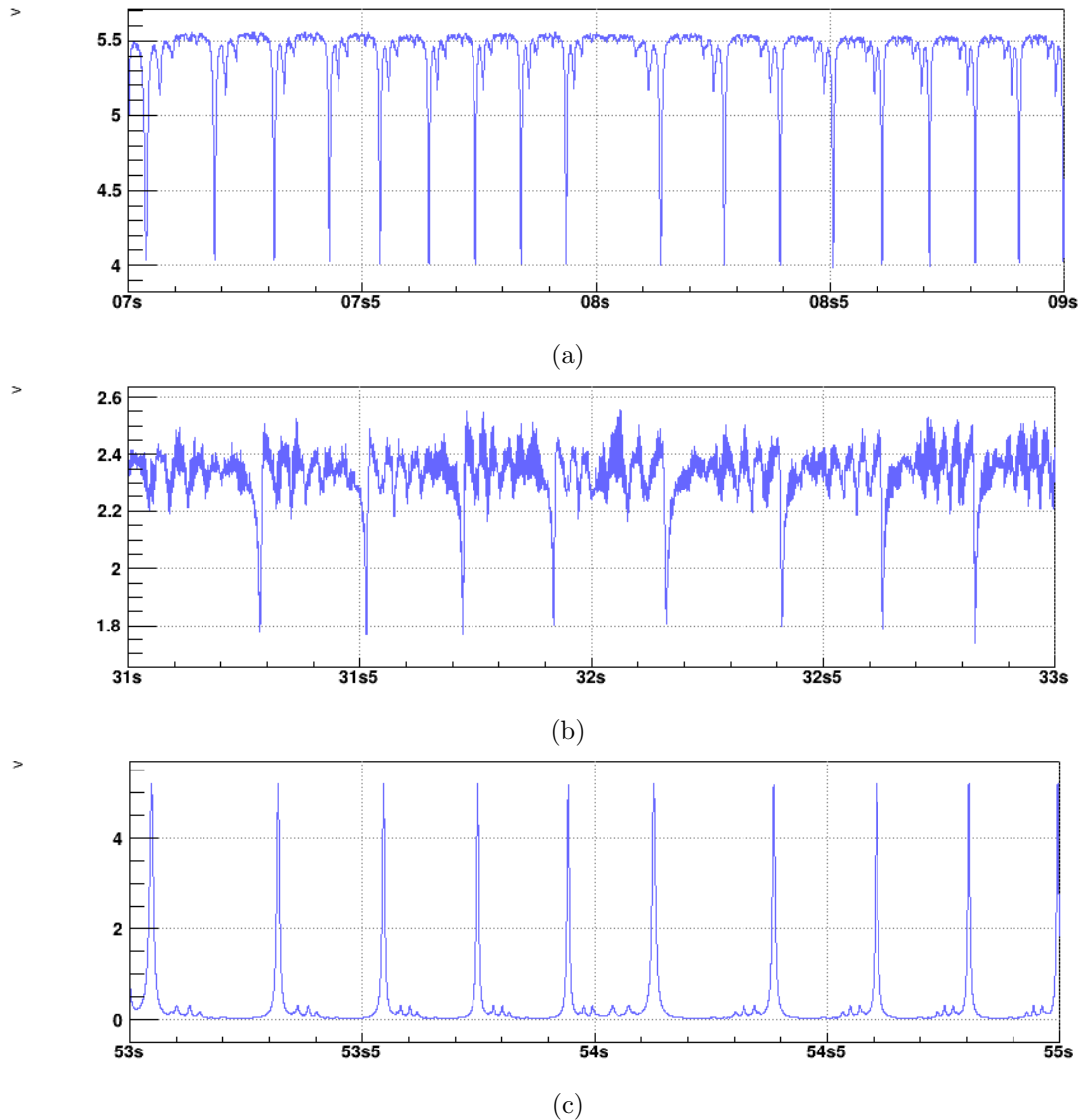


Figure 6.3 – Measurement of (a) the pump beam reflected by the OPO cavity, (b) the MCL beam reflected by the OPO cavity and (c) the seed beam transmitted by the OPO cavity while scanning it, at 3 different times, after optimization of their respective alignments on the cavity.

Once this first alignment was done, we never removed the OPO cavity mirrors again, only using the steering mirrors on the beam to make it resonates onto the cavity. The cavity became our reference and the criteria to define the superposition of the seed, pump and Modified Coherent Locking (MCL) beams was their resonance on the OPO cavity shown in Figure 6.3.

The locking strategy of the OPO cavity is in three steps. First we adjusted the OPO crystal position so that the green and infrared beams are co-resonant. Then, as shown in Figure 6.3, due to the frequency doubling, two green resonances are crossed meanwhile only one in infrared. Thus we adjusted the actuation range of the scanning ramp so that it crosses only one green resonance, co-resonant with an infrared resonance. Finally the threshold on the pump reflected DC signal is chosen such as we start the lock acquisition in the linear region of the error signal. This value is adjusted each time we change the pump power. An example of scan and lock of the OPO cavity is given in Figure 6.4 at low pump power (below 1 mW), in the absence of highly non linear interactions. The effect of non linear interactions will be given later on.

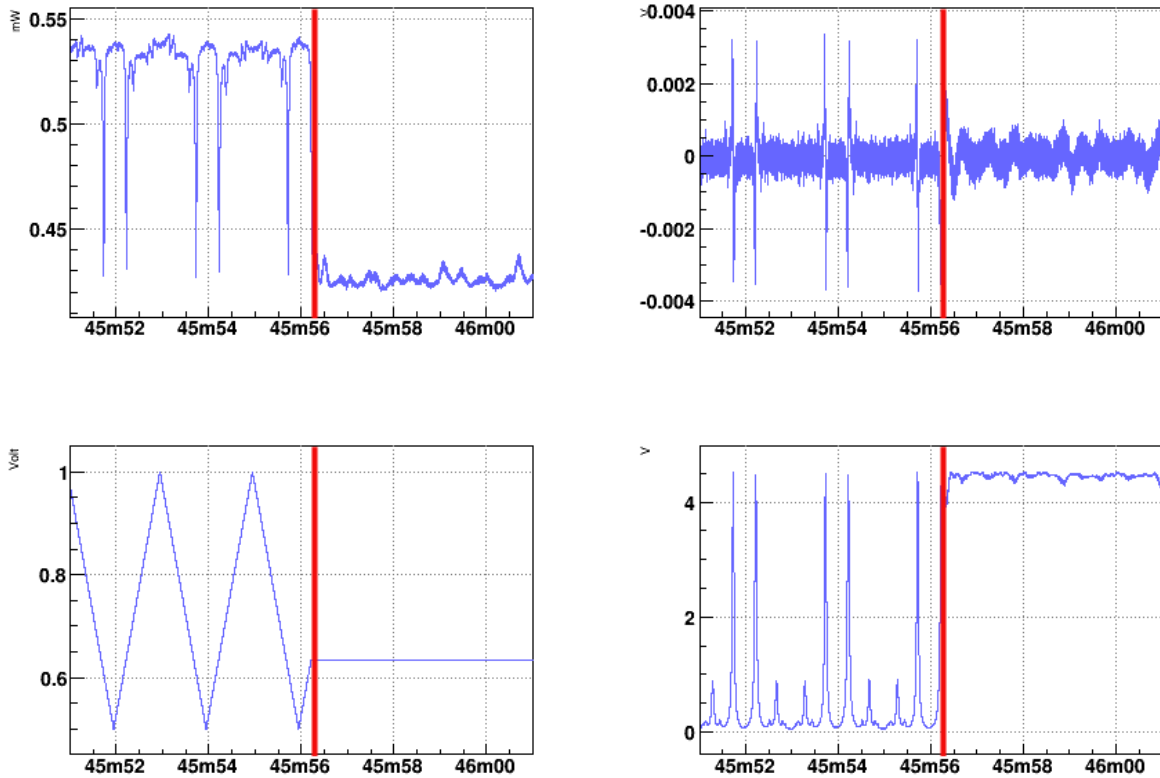


Figure 6.4 – Example of a scan and lock of the OPO cavity separated by the red line with 660 μ W of pump power: (*upper left*) DC signal from the in-vacuum photodiode on the pump beam reflected by the cavity, (*upper right*) error signal from the in-phase demodulation at 12.4 MHz of this same photodiode, (*lower left*) actuation order sent by the DAC to the piezos on the flat mirrors of the OPO cavity, (*lower right*) DC signal from the temporary Thorlabs photodiode on the seed beam transmitted by the cavity.

Finally, the in-vacuum photodiode on the pump beam reflected by the cavity can support up to 10 mW of green beam. However, the OPO will be run with much more power, up to 100 mW for some characterization measurements. Thus we added a beam splitter reflecting 90% of the green power before the photodiode to keep the photodiode safe with only 10% of the power. Dumps were placed on the path of the 90% reflected power to trap it.

6.2 Characterization of the Optical Parametric Oscillator

The characterization of the Optical Parametric Oscillator (OPO) was done using the seed and pump beams as shown in Figure 6.5. We used the in-vacuum photodiode on the pump reflected by the OPO cavity and added two temporary Thorlabs switchable gain photodiodes non-vacuum compatible: on the pump beam transmitted by the cavity and on the seed beam transmitted by the cavity. Filters have been added in front of the photodiodes to select the measurement wavelength.

The characterization can be decomposed into 3 main steps:

- measurement of the intra-cavity losses,
- observation of the nonlinear effects,
- measurement of the parametric gain.

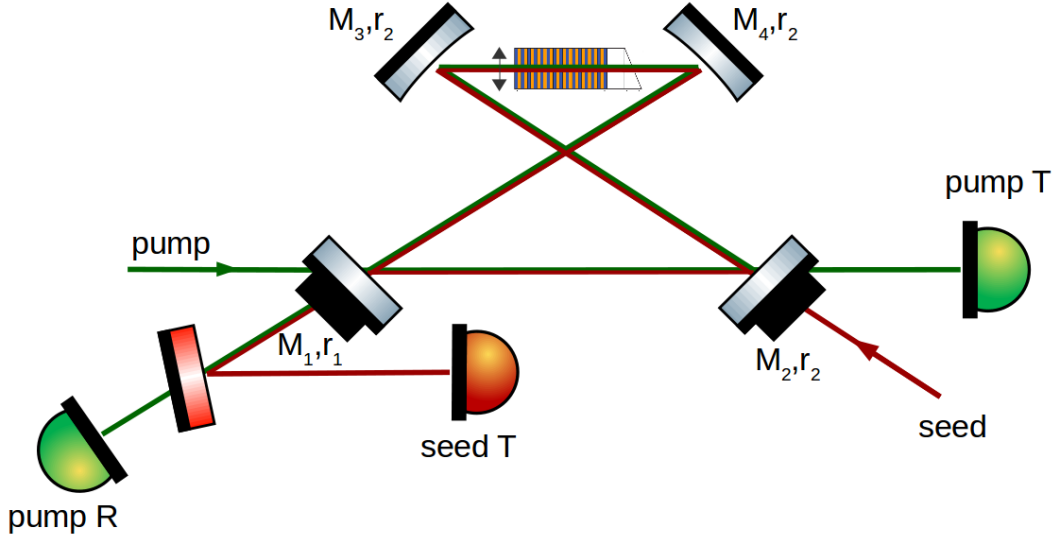


Figure 6.5 – Simplified scheme of the optical set-up used to characterize the Optical Parametric Oscillator (OPO). The crystal movement is shown by the black arrow.

6.2.1 Intra-cavity losses

Following the developments of the Fabry-Perot cavity equations in Section 2.4.1, we can derive the theoretical reflection depth D and transmission amplitude A of the pump beam on the OPO cavity defined in Figure 6.6:

$$D = \frac{4r_1r_2^3(1-r_1^2)\sqrt{1-L_c}[1-r_2^6(1-L_c)]}{[1-r_1^2r_2^6(1-L_c)]^2}, \quad (6.1)$$

$$A = \frac{4(1-r_1^2)(1-r_2^2)r_1r_2^3\sqrt{1-L_c}}{[1-r_1^2r_2^6(1-L_c)]^2}, \quad (6.2)$$

where r_1 is the amplitude reflectivity of the input coupler, r_2 is the amplitude reflectivity of each of the 3 high reflective mirrors and L_c are the intra-cavity power losses. For these expressions, we make the assumption that the beam is optimally coupled to the optical cavity, which is not completely the case in real life. For the pump beam we observed a matching of 80% to the OPO cavity, making the optimally coupled assumption reasonable with respect to other uncertainty sources to characterize intra-cavity losses. Moreover, in the rest of this part we won't do the difference between crystal losses and other intra-cavity losses such as scattering or absorption, and we will use the term of crystal losses for intra-cavity losses as we will be interested on mapping the crystal losses.

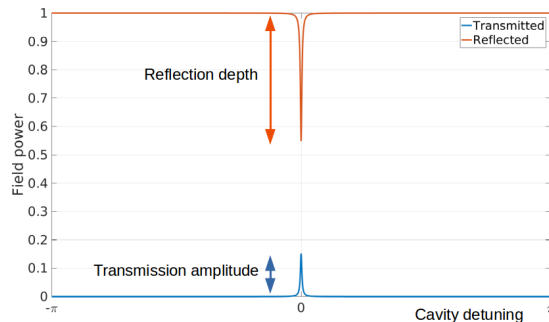


Figure 6.6 – Definition of the reflection depth and transmission amplitude of a bow-tie cavity. Note that the transmission is taken at only 1 of the 3 outputs.

From Equations (6.1) and (6.2), we should be able to measure both the intra-cavity losses and the input coupler reflectivity, assuming a perfect matching of the pump beam to the OPO cavity and the reflectivity of the high reflective mirror in green $R_2 = 0.999$. However, at high power the pump beam undergoes non-linear effects that will be described in Section 6.2.2 and that modifies its spectrum when scanning the cavity.

Consequently, the measurements had to be done at low pump power even though the power on the pump transmitted by the OPO is too low for the pump transmission amplitude measurement. Plotting Equation 6.1 for a fixed reflectivity r_1 and crystal losses between 0 and 100% in Figure 6.7 we found 2 possible crystal power losses for a given reflection depth. Nevertheless, for unharmed crystal, we expect not too high losses and we can consider only the left part of the plot.

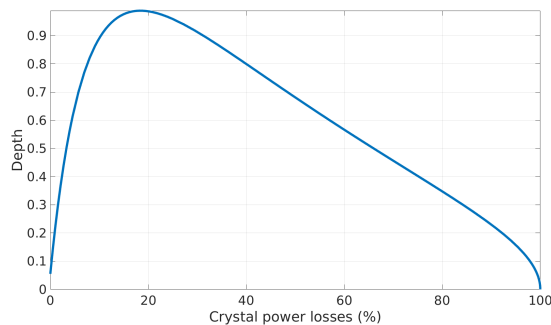


Figure 6.7 – Pump reflection depth of a bow-tie cavity with $R_1 = 0.81$ and $R_2 = 0.999$ with respect to the crystal losses.

The input/output coupler has a theoretical power transmissivity of 19% at 532 nm. However its reflectivity and absorption could only be measured at 1064 nm at LMA. We tried to measure it at LAL/IJCLab while it was already mounted onto the OPO and were limited by the measurement precision of our powermeter. In particular, we found that the measured power is dependent on the powermeter angle with respect to the measured beam. We measured a power reflectivity between 72% and 81%.

We don't expect high losses inside the crystal and according to Figure 6.7, below 15% of crystal losses, a given pump reflection depth corresponds to a unique value of crystal losses. Thus we plotted in Figure 6.8, the crystal losses with respect to the pump reflection depth for the two extremal input/output coupler reflectivities. This shows that the uncertainty on the crystal losses is higher for higher pump reflection depths.

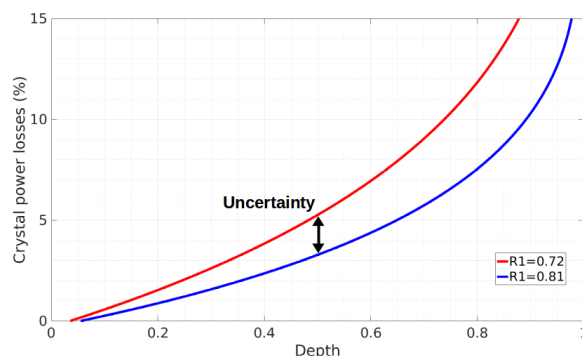


Figure 6.8 – Crystal losses with respect to the pump reflection depth for $R_1 = 72\%$ in red and $R_1 = 81\%$ in blue, the extremal values of our uncertainty on R_1 .

We finally measured the pump reflection depth shown in Figure 6.9a for different crystal positions using a vacuum compatible motorized translation stage. Then we took into account the uncertainty on the input/output coupler power reflectivity R_1 to map the crystal losses, as shown in Figure 6.9b.

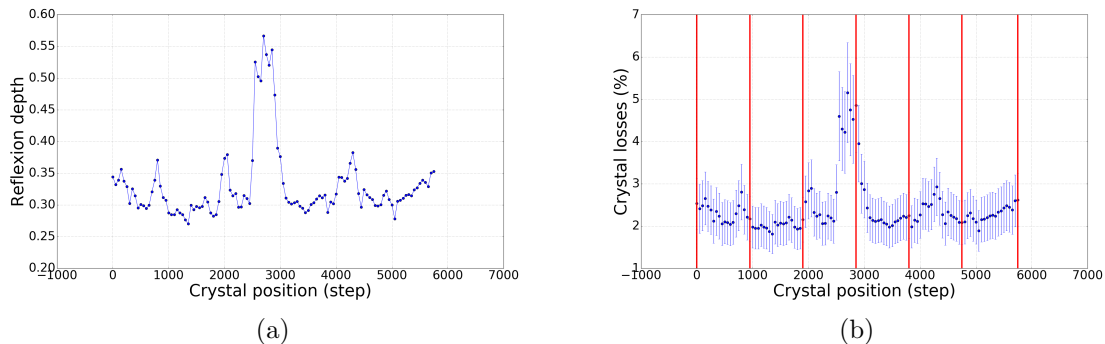


Figure 6.9 – (a) Measurement of the pump beam reflection depth on the Optical Parametric Oscillator. The error bars are present but too small to be visible as the precision measurement was of the order of promille. (b) Inferred crystal losses. The error bars are mostly due to the uncertainty on the input/output coupler reflectivity. The red vertical lines correspond to the crystal positions where the infrared and green beams are co-resonants.

The measurements were done with the crystal at 31.3°C , which was first measured to be an optimum temperature. The crystal translation stage does not allow access to its absolute positioning. Thus, the crystal was moved between the first observable infrared and green beams co-resonance inside the OPO cavity, arbitrarily chosen as step 0, and the last visible co-resonance at step 5750. Each translation step corresponds to a $\sim 1.75\ \mu\text{m}$ displacement and we did a measurement every 50 steps.

We observed that the crystal losses are most of the time below 3% except on a 500 steps area almost in the middle of the crystal where losses are around 5%. Thus we will chose a co-resonance that is farther from this area. We observed 7 co-resonances inside the crystal. Their relative position with respect to the higher loss area depends on the crystal temperature and we took care to avoid this area for our next measurements.

6.2.2 Nonlinear effects

The first thing that had to be checked to be able to observe nonlinear effects inside the OPO cavity was the polarization of the pump beam that has to be s-polarized. Indeed, the OPO crystal is made to nonlinearly interact with s-polarized beam.

Then we observed a nonlinear effect on the pump spectrum when scanning the OPO cavity with high pump power (above 10mW). The shape of the pump reflection dip shown in Figures 6.10 and 6.11 becomes asymmetrical¹. That have been understood to come from third-order non linear effects that I will describe now.

Optical Kerr effect

When a laser field goes through a nonlinear medium, the refractive index of the medium depends on the beam power going through it via a third order nonlinear effect called optical Kerr effect [123]. The refractive index n can be rewritten:

$$n = n_0 + 2\bar{n}_2|E(\omega)|^2, \quad (6.3)$$

where n_0 is the classical refractive index in weak field, $E(\omega)$ the electric field of the laser beam interacting through the medium and \bar{n}_2 the second-order index of refraction :

$$\bar{n}_2 = \frac{3\pi\chi^{(3)}}{n_0}. \quad (6.4)$$

¹Note that the same kind of asymmetry was also observed on the Second Harmonic Generators cavity scans as shown in Figures 5.6 and 5.16.

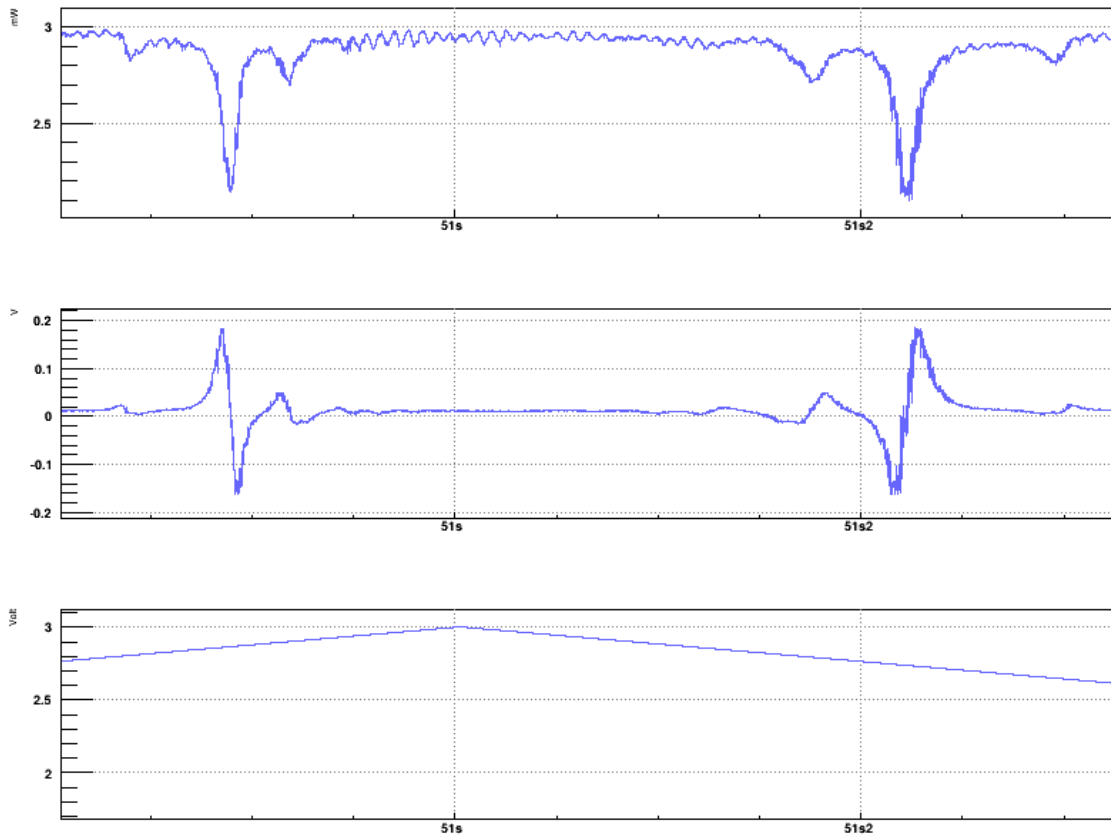


Figure 6.10 – Zoom on the spectrum of the pump beam in reflection of the OPO for low power on the pump beam. *Top*: DC signal, *middle*: error signal, *bottom*: scanning ramp.

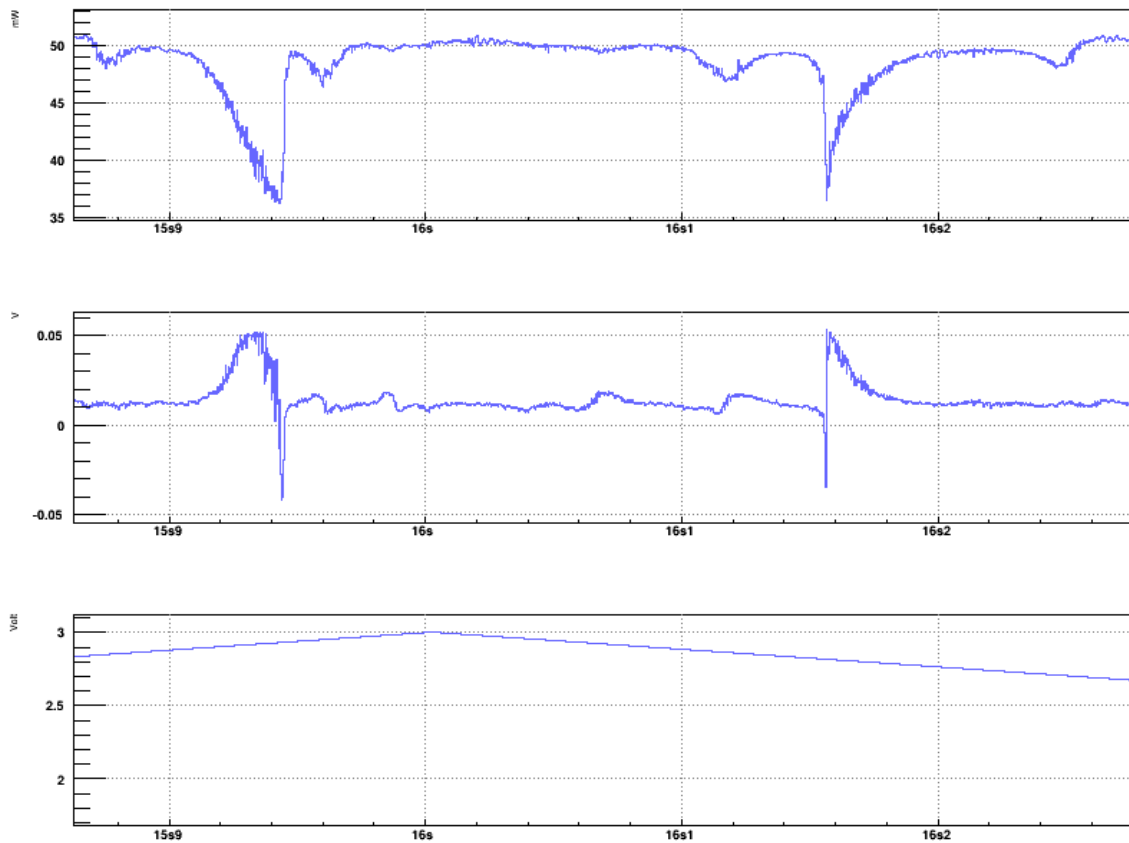


Figure 6.11 – Zoom on the spectrum of the pump beam in reflection of the OPO for high power on the pump beam. *Top*: DC signal, *middle*: error signal, *bottom*: scanning ramp.

Optical bistability

When the nonlinear medium is placed inside an optical resonator, the optical Kerr effects leads to optical bistability. To understand this we can go back to the Fabry-Perot cavity equations of Chapter 2, for instance Equation (2.69) in transmission of the cavity:

$$\frac{P_{tr}}{P_{in}} = \frac{t_1^2 t_2^2}{1 + r_1^2 r_2^2 - 2r_1 r_2 \cos(2k_0 L)}, \quad (6.5)$$

where P_{tr} is the power transmitted by the cavity, P_{in} the power at the input of the cavity, r_1 , r_2 , t_1 and t_2 are the respective amplitude reflectivity and transmissivity of the input and output mirror of the cavity, L is the length of the cavity and k_0 the wavenumber of the laser field, with:

$$k_0 = \frac{2\pi n}{\lambda_0}. \quad (6.6)$$

The refractive index n of Equation (6.3) can then be rewritten in terms of the cavity power parameters:

$$n = n_0 + 2\bar{n}_2 P_{cav} = n_0 + \frac{2\bar{n}_2}{t_2} P_{tr}. \quad (6.7)$$

Consequently, in the case of optical Kerr effect, it is not possible to invert Equation (6.5) to write the power transmitted by the cavity P_{tr} as a function of the input power of the cavity P_{in} [124]. However, it is possible to plot P_{in} as a function of P_{tr} and then swap the axis as shown in Figure 6.12.

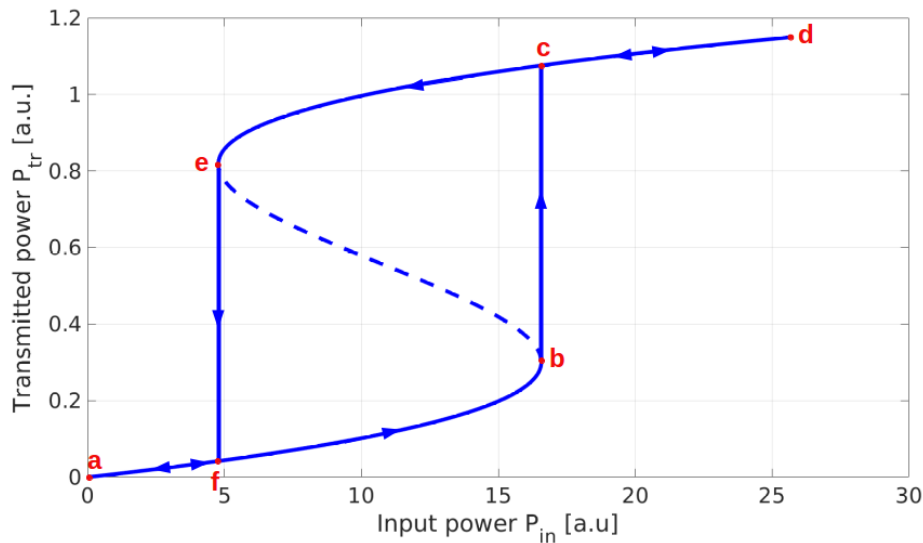


Figure 6.12 – Plot of the power transmitted by a Fabry-Perot cavity, at resonance with a nonlinear medium subject to Kerr effect, with respect to the input power. The system shows optical bistability: for a given input power, there are two possible transmitted power depending on the past history of the system. Starting from point a, when the input power increases, the transmitted power increases continuously up to point b where it rises to point c and then continuously increases up to point d. Starting from point d, when the input power decreases, the transmitted power decreases continuously down to point e where it drops to point f and then continuously decreases down to point a.

The optical bistability is characterized by the fact that for a given input power, there are two possible transmitted power depending on the past history of the system. For instance in Figure 6.12, the power transmitted by a Fabry-Perot cavity can be different for a same input power depending on the previous input power. In Figure 6.11, the pump power reflected by the OPO cavity at a given cavity length depends on the previous cavity length, leading to the asymmetry observed between the rising and the decreasing slope.

The optical bistability was not a problem to lock the main and auxiliary Second Harmonic Generator (SHG) cavities as the error signal was clean enough to have a good linear region on the Pound-Drever-Hall signal. However, the sidebands used to demodulate the error signal of the OPO are the same ones as the ones that are mainly transmitted to lock the main SHG. Consequently they are weaker on the pump beam that is reflected by the main SHG cavity and used to lock the OPO cavity. Moreover, the sidebands of the pump are also mainly transmitted by the OPO cavity, while the error signal for the lock is measured in its reflection.

All these losses on the sidebands added to the optical bistability complicate the lock of the OPO cavity. To obtain a stable lock we chose to lock not exactly at resonance but just nearby by adding an offset on the error signal.

6.2.3 Parametric gain

The measurement of the parametric gain was done using the set-up shown in Figure 6.5. The seed beam is a 23 mW beam that enters the OPO via a high reflective mirror and turns inside the OPO in the same direction as the pump beam. The seed beam is s-polarized as the pump to undergo nonlinear interaction inside the crystal. In the presence of the seed beam, the OPO crystal acts as an Optical Parametric Amplifier (OPA) as described in Section 4.4.4. We then measured the seed power transmitted by the input/output coupler using a temporary Thorlabs photodiode.

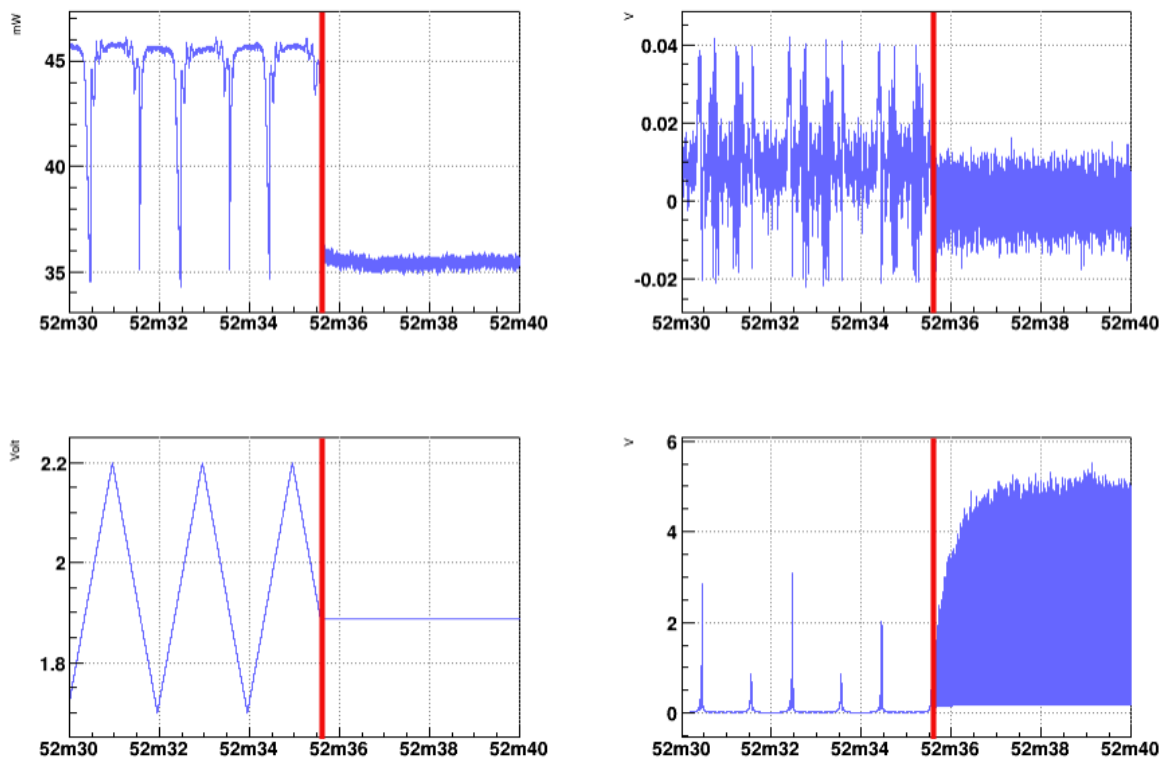


Figure 6.13 – Example of a scan and lock of the OPO cavity separated by the red line with 51.6 mW of pump power: (*upper left*) DC signal from the in-vacuum photodiode on the pump beam reflected by the cavity, (*upper right*) error signal from the in-phase demodulation at 12.4 MHz of this same photodiode, (*lower left*) actuation order sent by the DAC to the piezos on the flat mirrors of the OPO cavity, (*lower right*) DC signal from the temporary Thorlabs photodiode on the seed beam transmitted by the cavity, showing parametric gain.

For this measurement the pump beam was measured both in reflection of the OPO cavity with the in-vacuum LAPP photodiode and in transmission with a temporary Thorlabs photodiode to have a measurement of the pump beam with the same timing as the seed beam (we saw a 200 μs time shift between the Thorlabs and LAPP photodiodes due to the acquisition system) and with peaks instead of dips to ease the measurement of the co-resonance.

The nonlinear interaction of both the pump and seed beams inside the OPO crystal has for effect to amplify or deamplify the seed power. The regime of amplification or deamplification depends on the relative phase of the pump and seed beams inside the OPO crystal. Thus to more easily observe the nonlinear effect on the seed beam power, we scanned the pump phase using the piezo on the Mach-Zehnder interferometer, blocking the lower arm of the interferometer as mentioned in Section 5.2.1.

An example of scan and lock of the OPO cavity at high pump power and co-resonance is given in Figure 6.13. Comparing to Figure 6.4, the error signal is noisier and we clearly see parametric gain on the seed photodiode while locking the OPO cavity.

OPO crystal temperature optimization

The first thing to do to measure the OPO parametric gain was to optimized the OPO crystal temperature to achieve the best phase matching and thus the maximum parametric gain. This optimization is done by sending 50 mW of pump beam into the OPO cavity, which we know to be enough power to have clear amplification of the seed beam but not too high to avoid above threshold effects that will be described later on.

Then we translated the crystal using its motorized translation stage so that the pump and seed beams are both resonant inside the OPO cavity. When we reached the co-resonance we observed amplification of the seed beam shown in Figure 6.14, while scanning the OPO cavity.

The amplification depends on the phase of the pump beam on the OPO crystal. Thus if we don't change the pump phase we could be in a state were the seed beam is not maximally amplified with respect to its amplitude in absence of pump beam. To avoid this situation we scan the pump beam phase acting on the Mach-Zehnder piezo at a frequency different from all harmonics of the OPO scanning frequency. In Figure 6.14, two consecutive seed resonances are visible with different amplification factor.

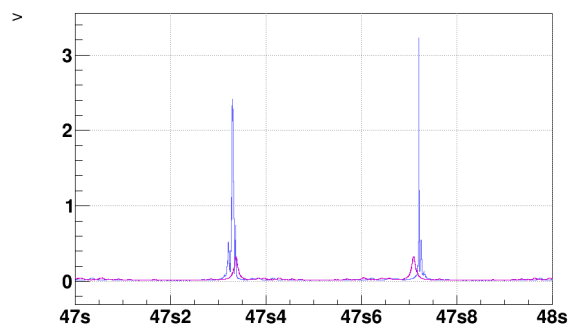


Figure 6.14 – Seed power transmitted by the OPO cavity measured without sending pump beam into the OPO in pink and with ~ 50 mW of pump beam entering the OPO in blue showing the amplification of the seed beam. The time shifts between both measurements is due to drift on the OPO PZT. The seed power in blue is not the same for both peaks because of the change in pump phase in-between when scanning the OPO at 1 Hz and the Mach-Zehnder piezo at 7 Hz.

Then we locked the OPO cavity with the in-vacuum pump beam photodiode in reflection of the cavity. The seed signal then oscillated between amplification and deamplification with respect to the seed power in the absence of parametric gain as shown in Figure 6.15. Then we fine tuned the crystal position to the co-resonance by optimizing the seed power oscillation amplitude.

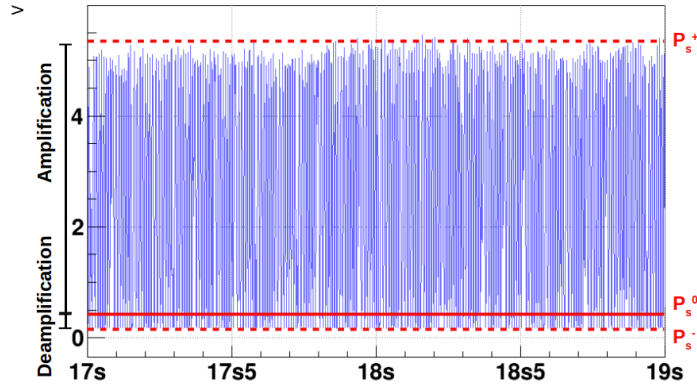


Figure 6.15 – Seed power transmitted by the OPO cavity, with 51.6mW of pump beam, when locking the OPO cavity at co-resonance. The red full line indicates the voltage measured on the seed photodiode while scanning the OPO cavity in absence of pump beam.

The parametric gain g is defined as the ratio between the seed measured power P_s in transmission of the OPO cavity at resonance while the pump beam interacts with the crystal and the seed measured power in the absence of pump beam P_s^0 . We can define its extremal values g^\pm using the seed power at maximal amplification P_s^+ and maximal deamplification P_s^- :

$$g^\pm = \frac{P_s^\pm}{P_s^0}. \quad (6.8)$$

We measured the parametric gain for different temperature between 20.5°C and 39.5°C . For each measurement, we adjusted the crystal position to keep the co-resonance as the refractive index of the crystal of the infrared and green beams depends differently on the temperature. Moreover, we ensured to stay in the left non damaged area of the crystal as parametric gain measurement is impacted by the crystal losses.

The measurement done at pump power $51 \pm 1\text{ mW}$ is shown in Figure 6.16. The optimum amplification of the seed beam is measured for an OPO crystal temperature of $29.5 \pm 0.5^\circ\text{C}$. The main uncertainty sources are due to the pump power variation and the crystal losses that are not homogeneous along the measurement. Moreover, we observed that the optimal temperature changes in a 2°C range on a long time scale (few months when the experiment is in operation and few weeks when the experiment is turned off). Thus before main measurements, we optimize the OPO crystal temperature.

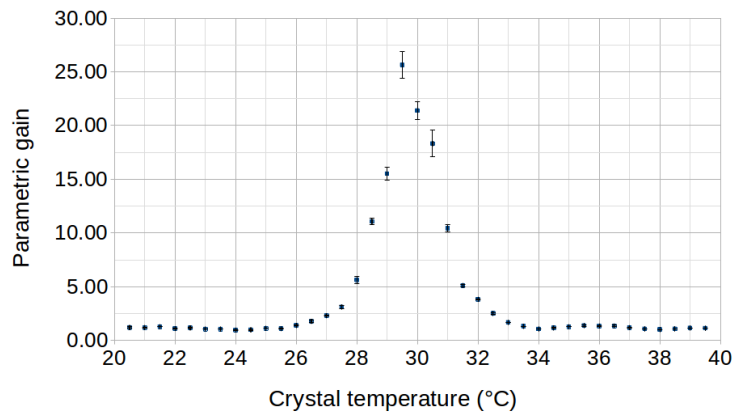


Figure 6.16 – Measurement of the parametric gain of the OPO crystal for temperatures between 20.5°C and 39.5°C showing an optimal phase matching for temperature between 29°C and 30°C .

OPO threshold measurement

To determine the threshold of the OPO where it enters a new mode of operation [84], we measured the parametric gain of the OPO for different pump powers as presented in Figure 6.17. It can be shown that the parametric gain in amplification and deamplification regimes at a given pump power P_p is related to the OPO pump threshold P_p^{th} as [78]:

$$g^{\pm} = \frac{(1 \pm \sqrt{P_p/P_p^{th}})^2}{(1 - P_p/P_p^{th})^2}, \text{ for } P_p < P_p^{th}. \quad (6.9)$$

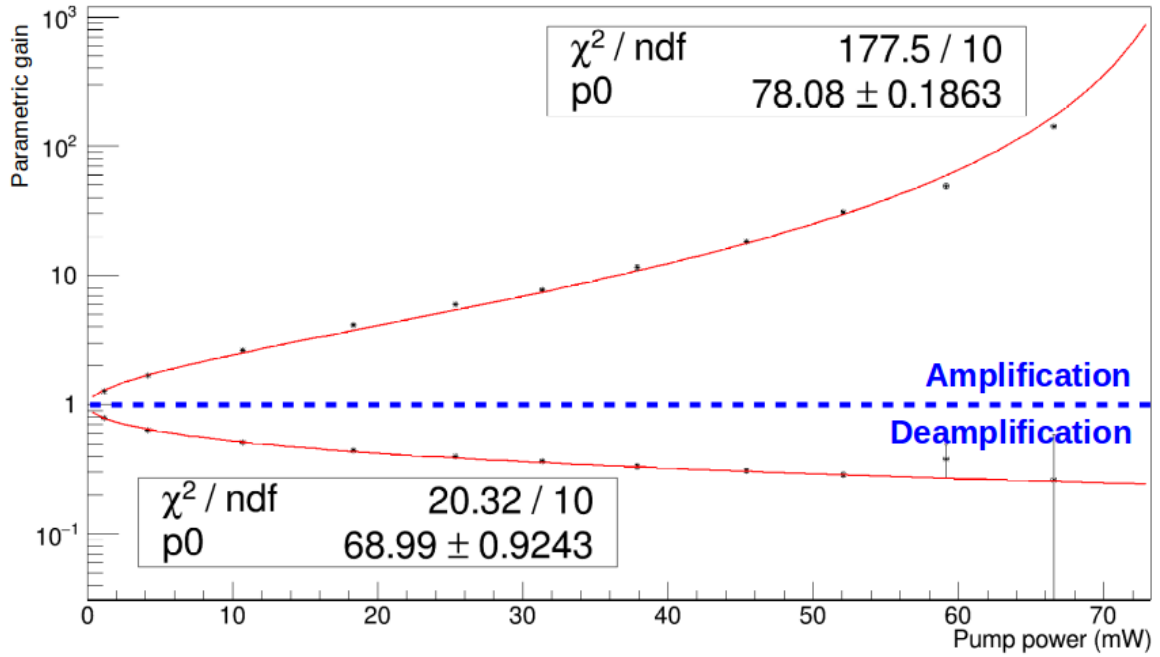


Figure 6.17 – Measurement of the OPO threshold in amplification and deamplification. p_0 is the pump power threshold fitted value in amplification and deamplification regime.

For each measurement we adjusted the gain of the Thorlabs photodiode measuring the seed beam so that the amplification does not saturate the photodiode but having the larger possible range for the deamplification measurement. However, at power above 55 mW the amplification became so important, reducing the gain of the photodiode too low to have an accurate measurement of the deamplification regime. This is why the error bars at high power in the deamplification regime become larger.

In the amplification regime we measured a pump OPO threshold of 78.1 ± 0.2 mW while in the deamplification regime we measured a pump OPO threshold of 69.0 ± 0.9 mW. The measured threshold in deamplification regime is lower than the one in amplification because intra-cavity losses affect more the deamplification than the amplification [84]. Moreover for deamplification, the signal to noise ratio is smaller than for amplification. Thus we can conclude that the OPO has a threshold of 78.1 ± 0.2 mW.

At a power higher than the threshold, as 90 mW, we observed in Figure 6.18 that infrared is produced inside the OPO even without the seed beam meaning the parametric gain is very high.

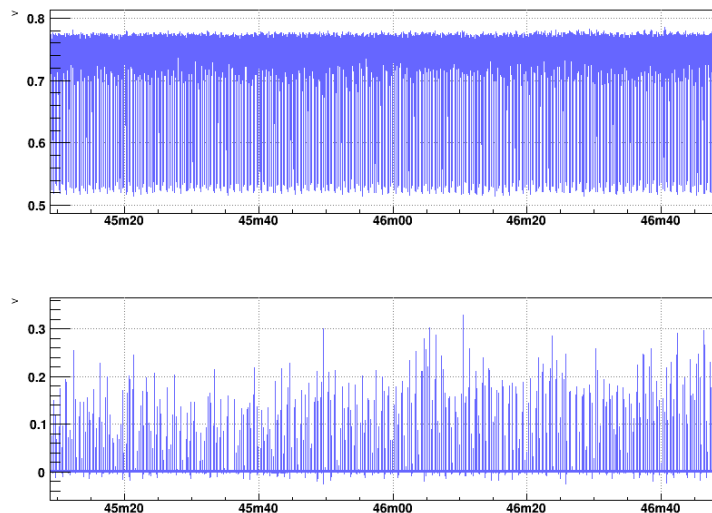


Figure 6.18 – Scan of the OPO at 1 Hz with 90 mW of pump beam and the Mach-Zehnder piezo scanning at 7 Hz. *Upper*: pump beam dips in reflection of the OPO. *Lower*: Infrared signal measured on the Thorlabs photodiode in the absence of seed beam.

6.3 Homodyne detection efficiency

The homodyne detection photodiodes have a quantum efficiency of 99% in infrared, a detector diameter of 500 μm and can measure up to 3 mW of infrared. They were first aligned using the Local Oscillator (LO) beam with lenses of focal length 50 mm in front of each photodiode to make the beam converging with a waist radius of 50 μm on the detector surface.

The recombination of the Local Oscillator (LO) beam and the Modified Coherent Locking (MCL) and squeezed beams is done using a 50:50 beam splitter as shown in Figure 6.19.

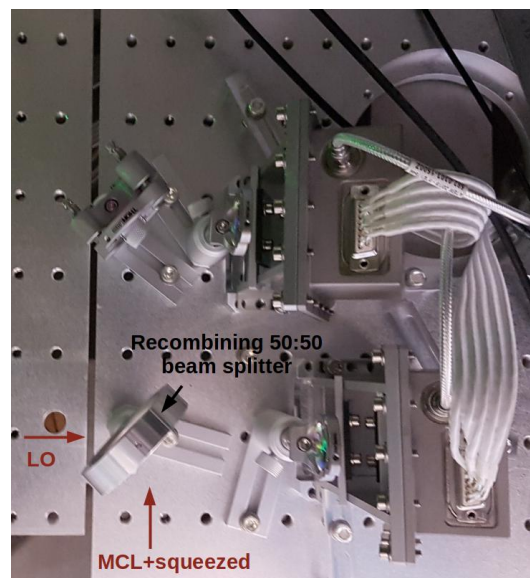


Figure 6.19 – Photo of the Homodyne Detection photodiodes showing the 50:50 beam splitter recombining the Local Oscillator (LO) beam and the Modified Coherent Locking (MCL) and squeezed beams.

To characterize the photodiodes we first measured their voltage without laser beam on them to numerically put the electronic offset to 0 on the Acl configuration. Then we aligned the LO beam on them. To be sure of the alignment we tested that we observed a plateau at the maximum value adjusting the beam position with the steering mirrors. We also ensure that the power on both photodiode was the same on the fluctuations uncertainties.

6.3.1 Beam splitter characterization

We observed that the beam splitter reflectivity was dependent on the beam polarization as shown on measurements made at LMA/IP2I in Figure 6.20. At the LO wavelength of 1064nm for 45° of incidence, it reflects $50.37 \pm 0.08\%$ of the s-polarized field and $35.34 \pm 0.08\%$ of the p-polarized field.

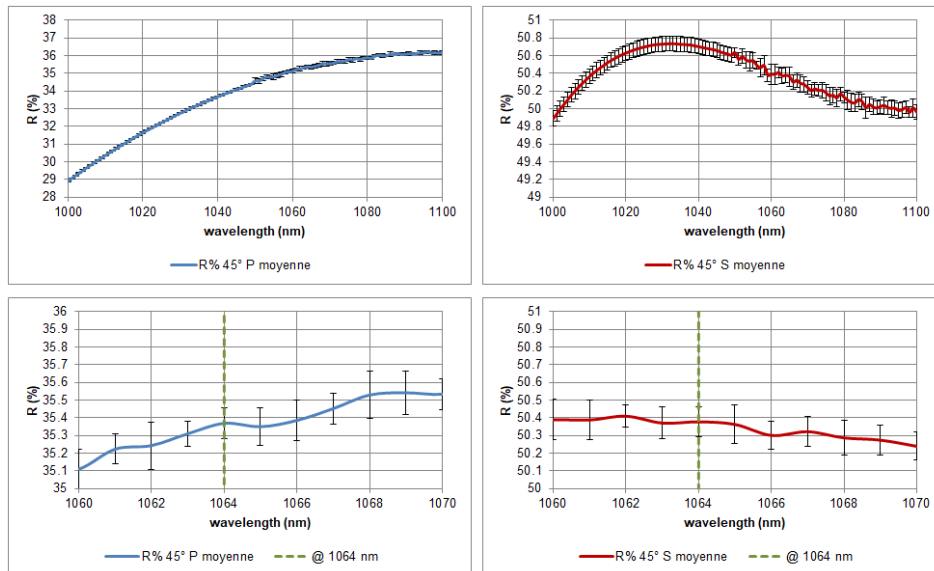


Figure 6.20 – Reflectivity of the 50:50 recombining homodyne detection beam splitter measured at LMA/IP2I for p and s polarization.

To propagate the LO beam from the in-air table to the in-vacuum Ferrarix tank we use a polarization maintaining fiber with the slow axis aligned for the s-polarization and a polarization maintaining feedthrough to enter the in-vacuum tank.

With the homodyne detection photodiodes, we observed 3% fluctuations on the beam splitter reflectivity with a periodicity compatible with the room temperature fluctuations.

To understand where the reflectivity fluctuations came, from we measured the beam polarization before the fiber input and at the output of the in-air fiber (before the feedthrough to the in-vacuum tank). We used polarizing cube beam splitters and placed photodiodes on the reflected s-polarized beam from the cubes. The measurements were done over half a day and are presented in Figure 6.21.

We can see that over the measurement time, there were known room temperature fluctuations with fast change when the cold block of the air conditioner activates and cools down the temperature on 2°C in few minutes followed by a slow drift when the room warms up on 2°C up to the next cold block activation, with a delay between two cold block activation depending on the outside temperature.

On the photodiode measuring the beam polarization before the fiber injection, we observed fluctuations of the s-polarized power of the order of 0.25%. However, on the photodiode measuring the beam polarization at the output of the in-air fiber, we observed 1.5% fluctuations on the s-polarized power with the same periodicity as the temperature fluctuations.

Consequently, from the measurements shown in Figures 6.20 and 6.21, there are polarization fluctuations in the fiber that leads to changes in the beam splitter reflectivity. To have a beam splitter reflectivity as close as possible to 50% we replaced one of the in-vacuum LO steering mirror by a polarizing plate transmitting the p-polarization that is dumped and reflecting the s-polarization towards the homodyne detection photodiodes.

The measurement of the homodyne beam splitter reflectivity is then more stable with less than 0.2% fluctuations mainly linked to polarization change at the output of the fiber due to room temperature change as shown in Figure 6.22.

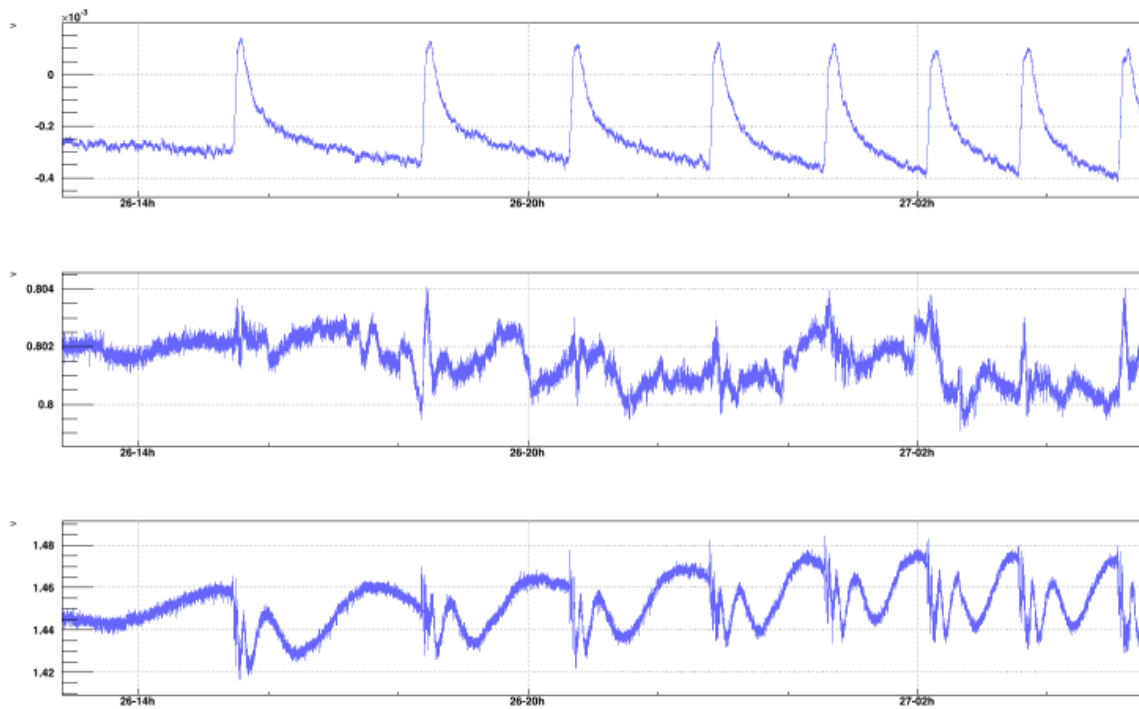


Figure 6.21 – Local Oscillator (LO) beam power in the s-polarization at the output of the in-air fiber (*bottom*), at the input of the in-air fiber (*middle*) and free ADC channel sensitive to room temperature variations (*upper*).

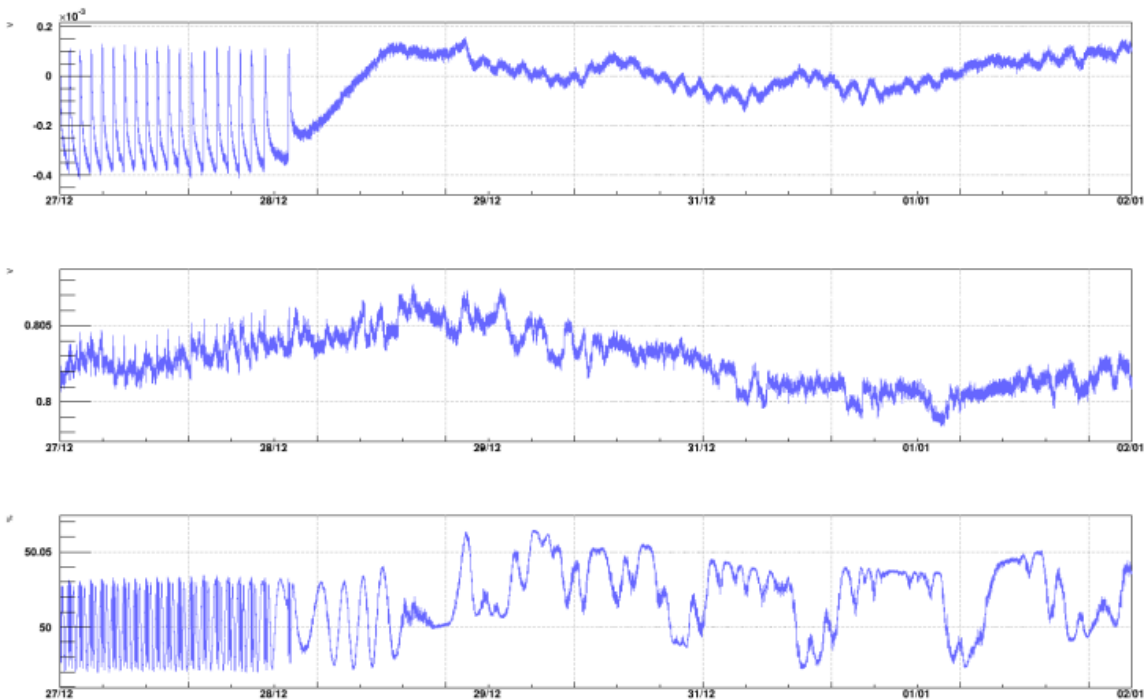


Figure 6.22 – Reflectivity of the 50:50 recombining homodyne detection beam splitter measured on the Local Oscillator (LO) beam (*bottom*), LO beam power in the s-polarization at the input of the in-air fiber (*middle*) and free ADC channel sensitive to room temperature variations (*upper*).

Characterization of the noise on the photodiodes

Before doing any squeezing measurement we had to characterize the dark noise and shot noise of homodyne detection photodiodes subtraction channel, that is the signal that will be used to measure squeezing as explained in Section 3.5.2.

Their measurement is shown in Figure 6.23 on the DC and Audio channels without beam and with 2.5 mW of LO beam. We observed on the DC channel that the dark noise is noisy at frequencies above 500 Hz where we want to measure the squeezing. Moreover, at these frequencies the dark noise is at the level of the shot noise or even higher. On the contrary, the Audio channel spectra is cleaner with only 50 Hz and harmonics lines on the dark noise and a shot noise one order of magnitude higher than the dark noise at 1 kHz due to an amplification factor of 100 on the Audio channel with respect to the DC channel.

On the shot noise limited Audio spectra with the LO beam we observed low frequency noise below 30 Hz that could be due to air turbulences but won't limit the squeezing measurement that will be done at higher frequencies. At frequencies between 100 Hz and 900 Hz there are some structures in the spectrum that could be due to mechanical resonances of optical elements.

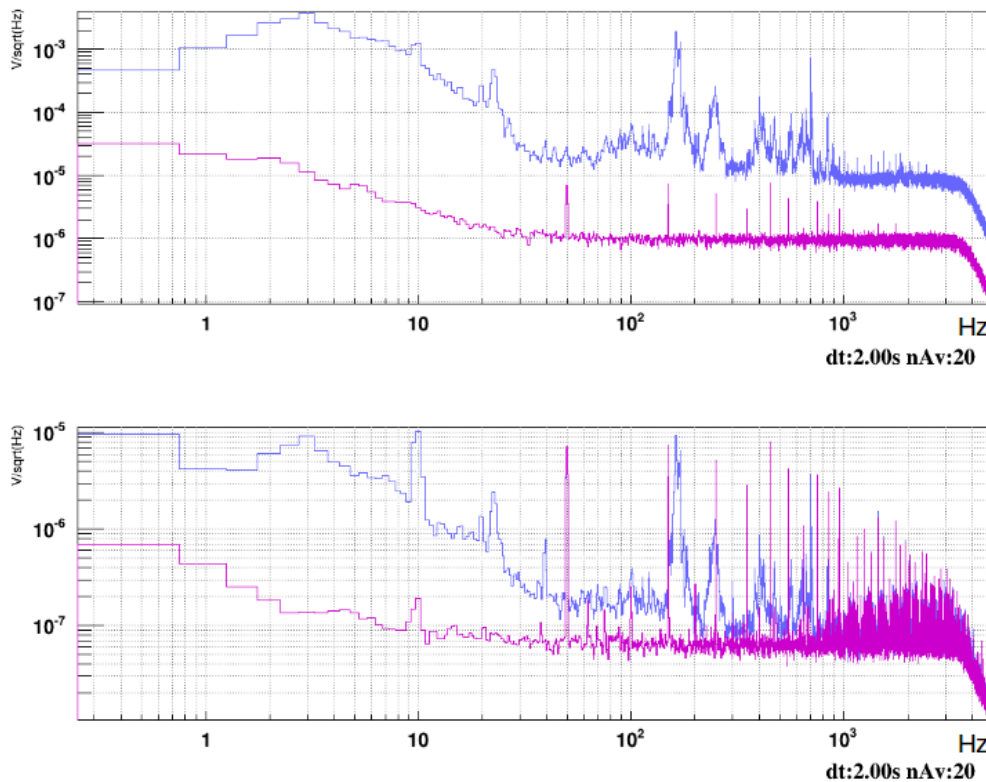


Figure 6.23 – FFT of homodyne detection subtraction channel on the Audio (upper) and DC (lower) signal without laser showing the electronic dark noise in pink and with 2.5 of the Local Oscillator (LO) on the photodiodes showing the shot noise in blue

Fringe visibility

When the LO beam was fully aligned on the homodyne detection photodiodes and the Optical Parametric Oscillator (OPO) fully characterized, we propagated the seed beam towards the homodyne detection photodiodes as shown on the OptoCad scheme of Figure 6.5.

The aim was to measure the fringe visibility on the homodyne detection photodiode between the LO beam and the squeezed beam that will have the same beam size and divergence as the seed beam. This fringe visibility measurement will be a measurement of the matching

between the LO and the squeezed beam allowing us to know the losses on the squeezing measurement due to the non perfect matching.

Considering two beams at the same frequency that have the same power on the photodiode, they lead to constructive and destructive interferences if they are well overlapped on the homodyne photodiodes, meaning that they have the same size, divergence and are superposed.

The visibility \mathcal{V} quantifies the spatial mode mismatch between the two beams. It is measured by scanning the relative phase of the two beams, in our case using a piezo on a mirror on the squeezed/seed path, leading to a sinusoidal signal with minimal power P_{min} and maximal power P_{max} . The visibility is then defined by Equation (4.46):

$$\mathcal{V} = \frac{P_{max} - P_{min}}{P_{max} + P_{min}}. \quad (6.10)$$

The first fringe visibility measurement that we done is shown in Figure 6.24. For this measurement we heated the OPO crystal to 35° C to be far from nonlinear interaction and locked the OPO cavity with the pump beam in co-resonance with the seed beam to maximized the seed power to ~ 6 mV on the homodyne detection photodiode, corresponding to ~ 7 μ W. Then we turned down the LO power to ~ 6 mV by adding a neutral density in-air before its injection into the fiber.

The measurement was done on one of the homodyne photodiodes, with both LO and seed beams on it. We scanned the seed phase at 14 Hz and determined that it corresponds to 14 periods of the seed phase, meaning that we expect to observe a 14 Hz signal. Afterwards, we optimized the superposition of the LO and seed beams and their mode matching to measure a fringe visibility of less about 70%.

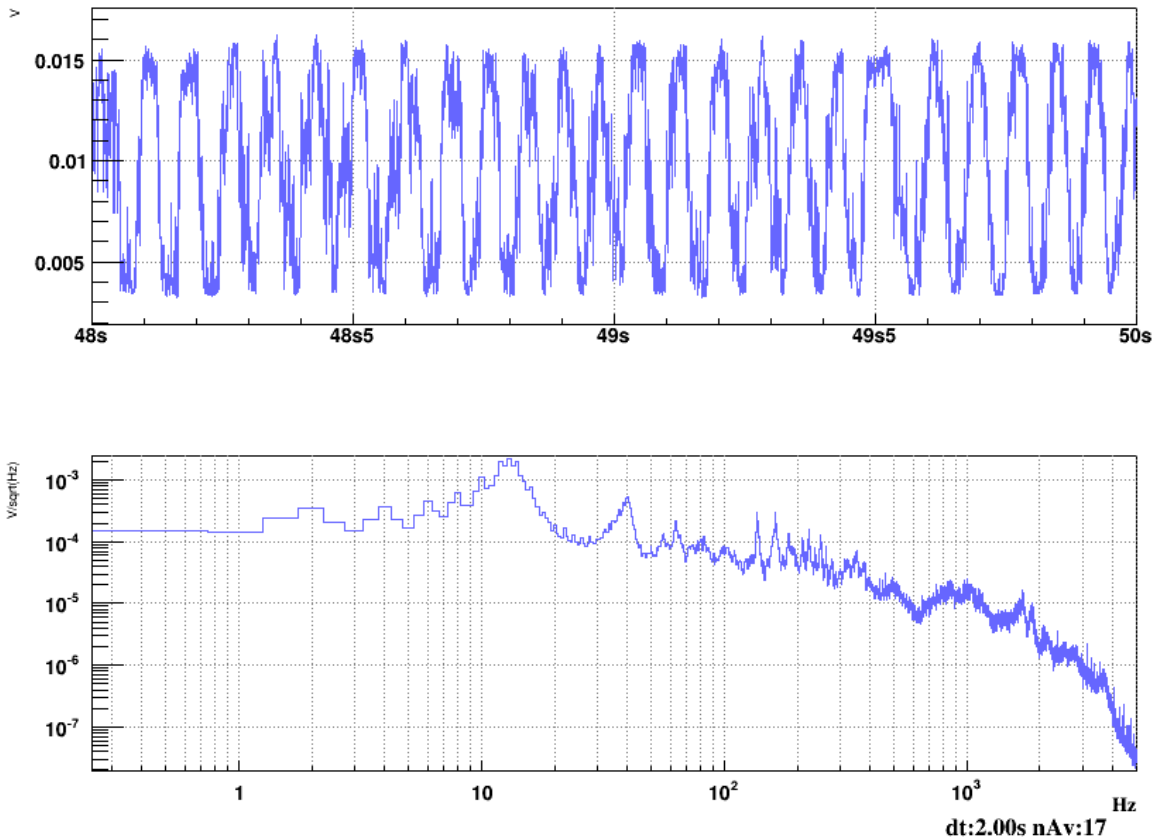


Figure 6.24 – First fringe visibility measurement done on between the LO and seed beams while scanning the seed phase at 14 Hz. *Upper*: DC signal on one of the homodyne photodiode. *Lower*: FFT of the same photodiode showing the measured signal at 14 Hz.

6.4 Conclusion

During the time of my thesis we aligned the Optical Parametric Oscillator (OPO) cavity first using the pump beam and then aligned the infrared beams on the cavity to superpose them to the pump beam.

Then we characterized the OPO, starting with the intra-cavity losses and more particularly their dependence on the OPO crystal position with respect to the cavity axis, showing an area that presents more losses in the middle of the crystal. We were then able to observe nonlinear effects and measure an OPO pump power threshold of 78.1 ± 0.2 mW.

Finally we aligned the homodyne detection and characterized the beamsplitter reflectivity and the noise of the photodiodes. We then started to propagate the beams from the OPO towards the homodyne detection and superposed them to the Local oscillator (LO) beam to be able to characterize the mode matching between the squeezed and LO beams.

We achieved a first visibility measurement of $\sim 70\%$ on the homodyne detection that we will then have to improve, mostly by moving lenses placed on the squeezed/seed beams path to adjust their mode matching to the LO beam. The next on-going step is to do a frequency independent squeezing measurement that first need to implement the Modified Coherent Locking control loop defined in Section 4.4.2.

Conclusion and outlooks

Frequency independent squeezing was already used on the O3 run of the Advanced LIGO and Advanced Virgo detectors. However to improve the detectors sensitivity in their whole bandwidth we will have to move on to frequency dependent squeezing with a corner frequency $\sim 50 - 70$ Hz.

Up to the end of 2019, frequency dependent squeezing had been achieved with a minimal corner frequency at 1.2 kHz [125] and much work has been done to reach corner frequencies below 100 Hz in 2020 [88, 89].

The Exsqueeze experiment aims at demonstrating under vacuum frequency dependent squeezing, first at a corner frequency of 700 Hz and in a second time at a corner frequency of 70 Hz, in the prospect of the Advanced Virgo detector O5 run.

During the time of my thesis I participated to the design of the full set-up of the Exsqueeze experiment to produce, control and measure frequency dependent squeezing. Then we started the installation and characterization of the optical devices. In particular, I characterized the Optical Parametric Oscillator (OPO) source of squeezing, determining a map of crystal losses and a pump threshold of 78.1 ± 0.2 mW. I also aligned and characterized the homodyne detection that will be used to measure the squeezing.

Nevertheless, many things still remain to be done before producing and measuring frequency dependent squeezing at a corner frequency of 70 Hz. First of all, we have to improve the mode matching between the Local Oscillator (LO) and squeezed beams on the homodyne detection to be able to do a first in-air frequency independent squeezing measurement and characterize the losses.

The Ferrarix in-vacuum tank, containing the OPO and homodyne detection, should then be placed under vacuum to check the movements due to pumping and the change of pressure. In fact, the passage under vacuum could slightly misalign the optics and we have to characterize and correct the alignments.

Then, the next important step will be to mode match and inject the Filter Cavity Control (FCC) and Filter Cavity Verification (FCV) beams to the 50-m filter cavity in order to lock the filter cavity at 532 nm and ensure its optimal detuning at 1064 nm.

The frequency independent squeezing produced in the OPO and previously measured will then be mode matched and injected into the filter cavity. Its reflection will be sent to the homodyne detection using a Faraday isolator. The mode matching of the squeezed beam to the LO beam on the homodyne detection will have to be tuned for this in-vacuum squeezed path and then the measurement of frequency dependent squeezing at corner frequency of 700 Hz will be done and the losses will be characterized.

Beyond Exsqueeze, the QFilter ANR aims at adding a short coupled cavity before the entrance mirror of the filter cavity. By adjusting the position of this new mirror and thus the detuning of the short cavity, we will be able to fine tune the finesse of the 50 m filter cavity and go to lower frequency. Having two cavities of lower finesse could ease the lock of the equivalent high finesse filter cavity.

To conclude, the use of frequency dependent squeezing with a 285 m filter cavity is foreseen for Advanced Virgo, with first an in-air squeezing source during the O4 run and then with an in-vacuum squeezing source during the O5 run [126].

Bibliography

- [1] Albert A. Michelson and Edward W. Morley. On a method of making the wave-length of sodium light the actual and practical standard of length. *The London, Edinburgh, and Dublin Philosophical Magazine and Journal of Science*, 24(151):463–466, 1887.
- [2] John A. Wheeler and Kenneth Ford. *Geons, Black Holes & Quantum Foam*. W. W. Norton & Company, 2000.
- [3] A. Einstein. Die grundlage der allgemeinen relativitätstheorie. *Annalen der Physik*, 14(1):517–571, 1916.
- [4] A. Einstein. Die Feldgleichungen der Gravitation. *Sitzungsberichte der Königlich Preußischen Akademie der Wissenschaften (Berlin)*, Seite 844-847., 1915.
- [5] Jolien DE Creighton and Warren G Anderson. *Gravitational-wave physics and astronomy: An introduction to theory, experiment and data analysis*. John Wiley & Sons, 2012.
- [6] Charles W. Misner, Kip S. Thorne, and John A. Wheeler. *Gravitation*. W.H. Freeman, 1973.
- [7] Felix Pirani. Measurement of classical gravitation fields. Report from the 1957 Chapel Hill Conference. <http://www.edition-open-sources.org/sources/5/21/index.html> (last accessed: 2018-08-01).
- [8] J. Weber. Detection and Generation of Gravitational Waves. *Phys. Rev.*, 117:306–313, Jan 1960.
- [9] Nicolas Arnaud. Gravitational waves: a taxonomy. <https://www.scienceinschool.org/content/gravitational-waves-taxonomy> (last accessed: 2018-07-12).
- [10] R. A. Hulse and J. H. Taylor. Discovery of a pulsar in a binary system. *Astrophysical Journal*, 195, Jan 1975.
- [11] B. P. Abbott et al. Observation of Gravitational Waves from a Binary Black Hole Merger. *Phys. Rev. Lett.*, 116:061102, Feb 2016.
- [12] B. P. Abbott et al. Properties of the Binary Black Hole Merger GW150914. *Phys. Rev. Lett.*, 116:241102, Jun 2016.
- [13] Bernard F. Schutz and Massimo Tinto. Antenna patterns of interferometric detectors of gravitational waves – I. Linearly polarized waves. *Monthly Notices of the Royal Astronomical Society*, 224(1):131–154, 1987.
- [14] B. P. Abbott et al. GW170814: A Three-Detector Observation of Gravitational Waves from a Binary Black Hole Coalescence. *Phys. Rev. Lett.*, 119:141101, Oct 2017.
- [15] B. P. Abbott et al. GW170817: Observation of Gravitational Waves from a Binary Neutron Star Inspiral. *Phys. Rev. Lett.*, 119:161101, Oct 2017.

- [16] B. P. Abbott et al. Gravitational Waves and Gamma-Rays from a Binary Neutron Star Merger: GW170817 and GRB 170817A. *The Astrophysical Journal Letters*, 848(2):L13, 2017.
- [17] B. P. Abbott et al. Multi-messenger Observations of a Binary Neutron Star Merger. *The Astrophysical Journal Letters*, 848(2):L12, 2017.
- [18] GCN CIRCULAR on LIGO/Virgo G298048. <https://gcn.gsfc.nasa.gov/other/G298048.gcn3> (last accessed: 2018-07-21).
- [19] B. P. Abbott et al. GWTC-1: A Gravitational-Wave Transient Catalog of Compact Binary Mergers Observed by LIGO and Virgo during the First and Second Observing Runs. *Phys. Rev. X*, 9:031040, Sep 2019.
- [20] Gravitational-Wave Candidate Event Database. <https://gracedb.ligo.org/superevents/public/O3/>.
- [21] J. Abadie et al. Predictions for the rates of compact binary coalescences observable by ground-based gravitational-wave detectors. *Classical and Quantum Gravity*, 27(17):173001, 2010.
- [22] B. P. Abbott et al. Prospects for observing and localizing gravitational-wave transients with Advanced LIGO, Advanced Virgo and KAGRA. *Living Reviews in Relativity*, 2018.
- [23] R. Abbott et al. GW190814: Gravitational Waves from the Coalescence of a 23 Solar Mass Black Hole with a 2.6 Solar Mass Compact Object. *The Astrophysical Journal*, 896(2):L44, jun 2020.
- [24] K. S. Hirata, T. Kajita, M. Koshiba, M. Nakahata, Y. Oyama, N. Sato, A. Suzuki, M. Takita, Y. Totsuka, T. Kifune, T. Suda, K. Takahashi, T. Tanimori, K. Miyano, M. Yamada, E. W. Beier, L. R. Feldscher, W. Frati, S. B. Kim, A. K. Mann, F. M. Newcomer, R. Van Berg, W. Zhang, and B. G. Cortez. Observation in the Kamiokande-II detector of the neutrino burst from supernova SN1987A. *Phys. Rev. D*, 38:448–458, Jul 1988.
- [25] Kip S. Thorne. Gravitational-wave research: Current status and future prospects. *Rev. Mod. Phys.*, 52:285–297, Apr 1980.
- [26] Christian D Ott. The gravitational-wave signature of core-collapse supernovae. *Classical and Quantum Gravity*, 26(6):063001, 2009.
- [27] Kei Kotake. Multiple physical elements to determine the gravitational-wave signatures of core-collapse supernovae. *Comptes Rendus Physique*, 14(4):318 – 351, 2013. Gravitational waves / Ondes gravitationnelles.
- [28] S. E. Gossan, P. Sutton, A. Stuver, M. Zanolin, K. Gill, and C. D. Ott. Observing gravitational waves from core-collapse supernovae in the advanced detector era. *Phys. Rev. D*, 93:042002, Feb 2016.
- [29] Mark Zimmermann. Revised estimate of gravitational radiation from Crab and Vela pulsars. *Nature*, 271:524, 1978.
- [30] Peter R Saulson. *Fundamentals of interferometric gravitational wave detectors*. World Scientific, 1994.
- [31] David G Blair, EJ Howell, L Ju, and C Zhao. *Advanced gravitational wave detectors*. Cambridge University Press, 2012.

- [32] J. Aasi et al. Gravitational waves from known pulsars: Results from the initial detector era. *The Astrophysical Journal*, 785(2):119, 2014.
- [33] Bruce Allen. The Stochastic gravity wave background: Sources and detection. In *Relativistic gravitation and gravitational radiation. Proceedings, School of Physics, Les Houches, France, September 26-October 6, 1995*, pages 373–417, 1996.
- [34] B. P. Abbott et al. Constraints on cosmic strings using data from the first Advanced LIGO observing run. *Phys. Rev. D*, 97:102002, May 2018.
- [35] B. P. Abbott et al. GW170817: Implications for the Stochastic Gravitational-Wave Background from Compact Binary Coalescences. *Phys. Rev. Lett.*, 120:091101, Feb 2018.
- [36] B. P. Abbott et al. Upper Limits on the Stochastic Gravitational-Wave Background from Advanced LIGO’s First Observing Run. *Phys. Rev. Lett.*, 118:121101, Mar 2017.
- [37] B. P. Abbott et al. GW170817: Implications for the Stochastic Gravitational-Wave Background from Compact Binary Coalescences. *Phys. Rev. Lett.*, 120:091101, Feb 2018.
- [38] B. P. Abbott et al. Astrophysical Implications of the Binary Black-hole Merger GW150914. *The Astrophysical Journal Letters*, 818(2):L22, 2016.
- [39] Ilya Mandel and Alison Farmer. Merging stellar-mass binary black holes. *arXiv*, 2018.
- [40] B. P. Abbott et al. Tests of General Relativity with GW150914. *Phys. Rev. Lett.*, 116:221101, May 2016.
- [41] Michele Maggiore. Gravitational wave experiments and early universe cosmology. *Physics Reports*, 331(6):283 – 367, 2000.
- [42] B. P. Abbott et al. A gravitational-wave standard siren measurement of the Hubble constant. *Nature*, 551:85–88, Nov 2017.
- [43] Walter Del Pozzo. Inference of cosmological parameters from gravitational waves: Applications to second generation interferometers. *Phys. Rev. D*, 86:043011, Aug 2012.
- [44] M. E. Gertsenshtein and V. I. Pustovoit. On the Detection of Low Frequency Gravitational Waves. *Sov. Phys. JETP*, 16:433, 1962.
- [45] J. Weber. Evidence for Discovery of Gravitational Radiation. *Phys. Rev. Lett.*, 22:1320–1324, Jun 1969.
- [46] P. Astone et al. Methods and results of the IGEC search for burst gravitational waves in the years 1997–2000. *Phys. Rev. D*, 68:022001, Jul 2003.
- [47] Viviana Fafone. Developments in resonant-mass detectors. *Classical and Quantum Gravity*, 23(8):S223, 2006.
- [48] G. Hobbs and A. Archibald et al. The International Pulsar Timing Array project: using pulsars as a gravitational wave detector. *Classical and Quantum Gravity*, 27(8):084013, 2010.
- [49] K. Danzmann. LISA – An ESA cornerstone mission for the detection and observation of gravitational waves. *Advances in Space Research*, 32(7):1233 – 1242, 2003. Fundamental Physics in Space.

- [50] Alberto Sesana. Prospects for Multiband Gravitational-Wave Astronomy after GW150914. *Phys. Rev. Lett.*, 116:231102, Jun 2016.
- [51] P. Amaro-Seoane et al. Laser Interferometer Space Antenna. *ArXiv e-prints 1702.00786*, February 2017.
- [52] M. Armano et al. Sub-Femto- g Free Fall for Space-Based Gravitational Wave Observatories: LISA Pathfinder Results. *Phys. Rev. Lett.*, 116:231101, Jun 2016.
- [53] W. Chaibi, R. Geiger, B. Canuel, A. Bertoldi, A. Landragin, and P. Bouyer. Low frequency gravitational wave detection with ground-based atom interferometer arrays. *Phys. Rev. D*, 93:021101, Jan 2016.
- [54] Savas Dimopoulos, Peter W. Graham, Jason M. Hogan, Mark A. Kasevich, and Surjeet Rajendran. Gravitational wave detection with atom interferometry. *Physics Letters B*, 678(1):37 – 40, 2009.
- [55] C J Moore, R H Cole, and C P L Berry. Gravitational-wave sensitivity curves. *Classical and Quantum Gravity*, 32(1):015014, 2015.
- [56] LIGO Timeline. <https://www.ligo.caltech.edu/page/timeline> (last accessed: 2018-08-06).
- [57] Virgo Timeline. <http://www.virgo-gw.eu/docs/GW170814/timelines.pdf> (last accessed: 2018-08-06).
- [58] F. Acernese et al. Advanced Virgo: a second-generation interferometric gravitational wave detector. *Classical and Quantum Gravity*, 32(2):024001, 2015.
- [59] F. Acernese et al. Measurements of Superattenuator seismic isolation by Virgo interferometer. *Astroparticle Physics*, 33(3):182 – 189, 2010.
- [60] Carlton M. Caves. Quantum-mechanical radiation-pressure fluctuations in an interferometer. *Phys. Rev. Lett.*, 45:75–79, Jul 1980.
- [61] Michele Punturo. The VIRGO sensitivity curve. Technical Report VIR-NOT-PER-1390-51, 2004.
- [62] Ian Harry and Tanja Hinderer. Observing and measuring the neutron-star equation-of-state in spinning binary neutron star systems. *Classical and Quantum Gravity*, 35(14):145010, 2018.
- [63] Stefan Hild. 3rd Generation GW detectors. Lecture at Les Houches School on Gravitational waves, July 2018.
- [64] Gregory M Harry, Andri M Gretarsson, Peter R Saulson, Scott E Kittelberger, Steven D Penn, William J Startin, Sheila Rowan, Martin M Fejer, D R M Crooks, Gianpietro Cagnoli, Jim Hough, and Norio Nakagawa. Thermal noise in interferometric gravitational wave detectors due to dielectric optical coatings. *Classical and Quantum Gravity*, 19(5):897, 2002.
- [65] Garrett D. Cole, Simon Gröblacher, Katharina Gugler, Sylvain Gigan, and Markus Aspelmeyer. Monocrystalline $\text{Al}_x\text{Ga}_{1-x}\text{As}$ heterostructures for high-reflectivity high-Q micromechanical resonators in the megahertz regime. *Applied Physics Letters*, 92(26):261108, 2008.

- [66] Takashi Uchiyama, Shinji Miyoki, Souichi Telada, Kazuhiro Yamamoto, Masatake Ohashi, Kazuhiro Agatsuma, Koji Arai, Masa-Katsu Fujimoto, Tomiyoshi Haruyama, Seiji Kawamura, Osamu Miyakawa, Naoko Ohishi, Takanori Saito, Takakazu Shintomi, Toshikazu Suzuki, Ryutaro Takahashi, and Daisuke Tatsumi. Reduction of Thermal Fluctuations in a Cryogenic Laser Interferometric Gravitational Wave Detector. *Phys. Rev. Lett.*, 108:141101, Apr 2012.
- [67] T Akutsu et al. Construction of KAGRA: an underground gravitational-wave observatory. *Progress of Theoretical and Experimental Physics*, 2018(1):013F01, 2018.
- [68] M. G. Beker, G. Cella, R. DeSalvo, M. Doets, H. Grote, J. Harms, E. Hennes, V. Mandic, D. S. Rabeling, J. F. J. van den Brand, and C. M. van Leeuwen. Improving the sensitivity of future GW observatories in the 1–10 Hz band: Newtonian and seismic noise. *General Relativity and Gravitation*, 43(2):623–656, Feb 2011.
- [69] M G Beker, J F J van den Brand, E Hennes, and D S Rabeling. Newtonian noise and ambient ground motion for gravitational wave detectors. *Journal of Physics: Conference Series*, 363(1):012004, 2012.
- [70] J. Abadie et al. A gravitational wave observatory operating beyond the quantum shot-noise limit. *Nature Physics*, 7:962, 2011.
- [71] H. J. Kimble, Yuri Levin, Andrey B. Matsko, Kip S. Thorne, and Sergey P. Vyatchanin. Conversion of conventional gravitational-wave interferometers into quantum nondemolition interferometers by modifying their input and/or output optics. *Phys. Rev. D*, 65:022002, Dec 2001.
- [72] Yiqiu Ma, Haixing Miao, Belinda Heyun Pang, Matthew Evans, Chunnong Zhao, Jan Harms, Roman Schnabel, and Yanbei Chen. Proposal for gravitational-wave detection beyond the standard quantum limit through EPR entanglement. *Nature Physics*, 13:776, 2017.
- [73] Yanbei Chen. Sagnac interferometer as a speed-meter-type, quantum-nondemolition gravitational-wave detector. *Phys. Rev. D*, 67:122004, Jun 2003.
- [74] Carlton M. Caves. Quantum-mechanical noise in an interferometer. *Phys. Rev. D*, 23:1693–1708, Apr 1981.
- [75] D. F. Walls and G. J. Milburn. *Quantum Optics*. Springer, 1995.
- [76] Mark Fox. *Quantum Optics, an introduction*. Oxford University Press, 2013.
- [77] James N. Hollenhorst. Quantum limits on resonant-mass gravitational-radiation detectors. *Phys. Rev. D*, 19:1669–1679, Mar 1979.
- [78] Sheon S. Y. Chua. *Quantum Enhancement of a 4km Laser Interferometer Gravitational-Wave Detector*. PhD thesis, Australian National University, 2013.
- [79] Carlton M. Caves and Bonny L. Schumaker. New formalism for two-photon quantum optics. I. Quadrature phases and squeezed states. *Phys. Rev. A*, 31:3068–3092, May 1985.
- [80] Thomas Corbitt, Yanbei Chen, and Nergis Mavalvala. Mathematical framework for simulation of quantum fields in complex interferometers using the two-photon formalism. *Phys. Rev. A*, 72:013818, Jul 2005.
- [81] M. Evans, L. Barsotti, P. Kwee, J. Harms, and H. Miao. Realistic filter cavities for advanced gravitational wave detectors. *Phys. Rev. D*, 88:022002, Jul 2013.

- [82] Bonny L. Schumaker and Carlton M. Caves. New formalism for two-photon quantum optics. II. Mathematical foundation and compact notation. *Phys. Rev. A*, 31:3093–3111, May 1985.
- [83] P. Kwee, J. Miller, T. Isogai, L. Barsotti, and M. Evans. Decoherence and degradation of squeezed states in quantum filter cavities. *Phys. Rev. D*, 90:062006, Sep 2014.
- [84] Michael Steve Stefszky. *Generation and Detection of Low-Frequency Squeezing for Gravitational-Wave Detection*. PhD thesis, Australian National University, 2012.
- [85] Amnon Yariv. *Optical Electronics*. Holt-Saunders, 1985.
- [86] David S. Hum and Martin M. Fejer. Quasi-phaseshifting. *Comptes Rendus Physique*, 8(2):180 – 198, 2007. Recent advances in crystal optics.
- [87] James Lough et al. First demonstration of 6 db quantum noise reduction in a kilometer scale gravitational wave observatory. 5 2020.
- [88] L. McCuller, C. Whittle, D. Ganapathy, K. Komori, M. Tse, A. Fernandez-Galiana, L. Barsotti, P. Fritschel, M. MacInnis, F. Matichard, K. Mason, N. Mavalvala, R. Mittleman, Haocun Yu, M. E. Zucker, and M. Evans. Frequency-Dependent Squeezing for Advanced LIGO. *Phys. Rev. Lett.*, 124:171102, Apr 2020.
- [89] Yuhang Zhao, Naoki Aritomi, Eleonora Capocasa, Matteo Leonardi, Marc Eisenmann, Yuefan Guo, Eleonora Polini, Akihiro Tomura, Koji Arai, Yoichi Aso, Yao-Chin Huang, Ray-Kuang Lee, Harald Lück, Osamu Miyakawa, Pierre Prat, Ayaka Shoda, Matteo Tacca, Ryutaro Takahashi, Henning Vahlbruch, Marco Vardaro, Chien-Ming Wu, Matteo Barsuglia, and Raffaele Flaminio. Frequency-Dependent Squeezed Vacuum Source for Broadband Quantum Noise Reduction in Advanced Gravitational-Wave Detectors. *Phys. Rev. Lett.*, 124:171101, Apr 2020.
- [90] R. E. Slusher, L. W. Hollberg, B. Yurke, J. C. Mertz, and J. F. Valley. Observation of Squeezed States Generated by Four-Wave Mixing in an Optical Cavity. *Phys. Rev. Lett.*, 55:2409–2412, Nov 1985.
- [91] H.J. Kimble. Squeezed states of light: an (incomplete) survey of experimental progress and prospects. *Physics Reports*, 219(3):227 – 234, 1992.
- [92] Kirk McKenzie, Nicolai Grosse, Warwick P. Bowen, Stanley E. Whitcomb, Malcolm B. Gray, David E. McClelland, and Ping Koy Lam. Squeezing in the Audio Gravitational-Wave Detection Band. *Phys. Rev. Lett.*, 93:161105, Oct 2004.
- [93] H Vahlbruch, S Chelkowski, K Danzmann, and R Schnabel. Quantum engineering of squeezed states for quantum communication and metrology. *New Journal of Physics*, 9(10):371, 2007.
- [94] M S Stefszky, C M Mow-Lowry, S S Y Chua, D A Shaddock, B C Buchler, H Vahlbruch, A Khalaidovski, R Schnabel, P K Lam, and D E McClelland. Balanced homodyne detection of optical quantum states at audio-band frequencies and below. *Classical and Quantum Gravity*, 29(14):145015, 2012.
- [95] Henning Vahlbruch, Moritz Mehmet, Karsten Danzmann, and Roman Schnabel. Detection of 15 dB Squeezed States of Light and their Application for the Absolute Calibration of Photoelectric Quantum Efficiency. *Phys. Rev. Lett.*, 117:110801, Sep 2016.
- [96] J. Aasi et al. Enhanced sensitivity of the LIGO gravitational wave detector by using squeezed states of light. *Nature Photonics*, 7:613, 2013.

- [97] M. Tse et al. Quantum-Enhanced Advanced LIGO Detectors in the Era of Gravitational-Wave Astronomy. *Phys. Rev. Lett.*, 123:231107, Dec 2019.
- [98] F. Acernese et al. Increasing the Astrophysical Reach of the Advanced Virgo Detector via the Application of Squeezed Vacuum States of Light. *Phys. Rev. Lett.*, 123:231108, Dec 2019.
- [99] Experimental Squeezing for Optomechanics. ANR, Appel à projet générique 2015 - Défis de tous les savoirs.
- [100] Leonhard Neuhaus, Rémi Metzdorff, Salim Zerkani, Sheon Chua, Thibaut Jacqmin, Samuel Deléglise, Tristan Briant, Antoine Heidmann, and Pierre-François Cohadon. Cooling a macroscopic mechanical oscillator close to its quantum ground state. In *Quantum Information and Measurement (QIM) 2017*, page QF2C.3. Optical Society of America, 2017.
- [101] A. G. Kuhn, J. Teissier, L. Neuhaus, S. Zerkani, E. van Brackel, S. Deléglise, T. Briant, P.-F. Cohadon, A. Heidmann, C. Michel, L. Pinard, V. Dolique, R. Flamini, R. Taïbi, C. Chartier, and O. Le Traon. Free-space cavity optomechanics in a cryogenic environment. *Applied Physics Letters*, 104(4):044102, 2014.
- [102] Eric D. Black. An introduction to Pound–Drever–Hall laser frequency stabilization. *American Journal of Physics*, 69(1):79–87, 2001.
- [103] P. A. Franken, A. E. Hill, C. W. Peters, and G. Weinreich. Generation of Optical Harmonics. *Phys. Rev. Lett.*, 7:118–119, Aug 1961.
- [104] Periodically Poled Lithium Niobate (PPLN) - tutorial. <https://www.thorlabs.com/catalogpages/690.pdf> (last accessed:2019-11-09).
- [105] MgO:PPLN for 1064nm SHG. <https://www.covesion.com/products/magnesium-doped-ppln-mgoppln-crystals/mgo-ppln-for-second-harmonic-generation/1064nm.html> (last accessed:2019-11-09).
- [106] Michael Stefszky, Conor M Mow-Lowry, Kirk McKenzie, Sheon Chua, Ben C Buchler, Thomas Symul, David E McClelland, and Ping Koy Lam. An investigation of doubly-resonant optical parametric oscillators and nonlinear crystals for squeezing. *Journal of Physics B: Atomic, Molecular and Optical Physics*, 44(1):015502, dec 2010.
- [107] H. Kogelnik and T. Li. Laser Beams and Resonators. *Appl. Opt.*, 5(10):1550–1567, Oct 1966.
- [108] A. R. Wade, G. L. Mansell, T. G. McRae, S. S. Y. Chua, M. J. Yap, R. L. Ward, B. J. J. Slagmolen, D. A. Shaddock, and D. E. McClelland. Optomechanical design and construction of a vacuum-compatible optical parametric oscillator for generation of squeezed light. *Review of Scientific Instruments*, 87(6):063104, 2016.
- [109] Alexander Khalaidovski, Henning Vahlbruch, Nico Lastzka, Christian Gräf, Karsten Danzmann, Hartmut Grote, and Roman Schnabel. Long-term stable squeezed vacuum state of light for gravitational wave detectors. *Classical and Quantum Gravity*, 29(7):075001, mar 2012.
- [110] Kirk McKenzie, Eugeny E Mikhailov, Keisuke Goda, Ping Koy Lam, Nicolai Grosse, Malcolm B Gray, Nergis Mavalvala, and David E McClelland. Quantum noise locking. *Journal of Optics B: Quantum and Semiclassical Optics*, 7(10):S421–S428, sep 2005.
- [111] Simon Chelkowski, Henning Vahlbruch, Karsten Danzmann, and Roman Schnabel. Coherent control of broadband vacuum squeezing. *Phys. Rev. A*, 75:043814, Apr 2007.

- [112] Sheon S. Y. Chua, Michael S. Stefszky, Conor M. Mow-Lowry, Ben C. Buchler, Sheila Dwyer, Daniel A. Shaddock, Ping Koy Lam, and David E. McClelland. Backscatter tolerant squeezed light source for advanced gravitational-wave detectors. *Opt. Lett.*, 36(23):4680–4682, Dec 2011.
- [113] Nicolas Straniero, Jérôme Degallaix, Raffaele Flaminio, Laurent Pinard, and Gianpietro Cagnoli. Realistic loss estimation due to the mirror surfaces in a 10 meters-long high finesse Fabry-Perot filter-cavity. *Opt. Express*, 23(16):21455–21476, Aug 2015.
- [114] Frequency domain INterfErometer Simulation SoftwarE. <http://www.gwoptics.org/finesse/> (last accessed: 2020-01-11).
- [115] Nicolas Letendre, Alain Masserot, Benoit Mours, Jean-Marc Nappa, Emmanuel Pacaud, and Loïc Rolland. ADC7674 User Manual V2. Technical Report VIR-0937A-17, 2017.
- [116] A. Dalmas, N. Letendre, A. Masserot, B. Mours, E. Pacaud, S. Petit, and L. Rolland. Daqbox and Mezzanines user manual. Technical Report VIR-0750B-19, 2020.
- [117] Julia Casanueva and ISC team. ISC tools: VPM, Acl and Data Display. Technical Report VIR-0129A-18, 2018.
- [118] R. Bonnand, A. Masserot, B. Mours, L. Rolland, E. Pacaud, M. Was, and D. Passuello. The Algorithms for Control and Locking (Acl)server Documentation. Technical Report VIR-00XX-16, 2019.
- [119] Tcs650 thermistor. Datasheet at <https://www.teamwavelength.com/download/Datasheets/TCS-series-thermistors.pdf> (last accessed:2020-05-02).
- [120] OptoCad: Tracing Gaussian TEM00 beams through an optical set-up. <http://www2.mpg.de/~ros/optocad.html> (last accessed: 2020-05-05).
- [121] L. Neuhaus et al. Pyrpl. <https://github.com/lneuhaus/pyrpl>.
- [122] Red Pitaya. <http://redpitaya.com/>.
- [123] Robert W. Boyd. *Nonlinear Optics*. Academic Press, 1992.
- [124] Peter E. Powers. *Field Guide to Nonlinear Optics*. SPIE, 2013.
- [125] Eric Oelker, Tomoki Isogai, John Miller, Maggie Tse, Lisa Barsotti, Nergis Mavalvala, and Matthew Evans. Audio-Band Frequency-Dependent Squeezing for Gravitational-Wave Detectors. *Phys. Rev. Lett.*, 116:041102, Jan 2016.
- [126] The Virgo Collaboration. Advanced Virgo Plus Phase I Design Report. Technical Report VIR-0596A-19, 2019.

Titre: Dépasser la Limite Quantique Standard pour le détecteur d'ondes gravitationnelles Advanced Virgo

Mots clés: Advanced Virgo, ondes gravitationnelles, squeezing, optique quantique

Résumé: Dans le cadre de l'amélioration du détecteur d'ondes gravitationnelles Advanced Virgo, il est nécessaire de réduire la contribution du bruit quantique au bruit du détecteur afin d'augmenter la sensibilité et donc le volume d'Univers observable. Pour cela une des techniques envisagées afin de dépasser la Limite Quantique Standard est l'utilisation d'états comprimés de la lumière, dit états squeezés, dépendant de la fréquence. L'implémentation de

cette technique est testée sur la plateforme expérimentale CALVA au LAL/IJCLab dans le cadre de l'ANR Exsqueeze en collaboration avec le LKB, le LMA/IP2I et le LAPP. L'objet de cette thèse est la conception de l'expérience ainsi que l'installation et la caractérisation des premiers systèmes optiques utilisés pour générer et mesurer des états squeezés indépendants de la fréquence.

Title: Beating the Standard Quantum Limit for the Advanced Virgo gravitational wave detector

Keywords: Advanced Virgo, gravitational waves, Squeezing, Quantum Optics

Abstract: In the context of the improvement of the Advanced Virgo gravitational wave detector, the quantum noise contribution to the detector noise has to be reduced in order to increase its sensitivity and consequently the observable volume of the Universe. One of the idea to go beyond the Standard Quantum Limit is to use frequency dependent squeezed states of light. The implementation of this technique is

tested on the CALVA experiment at LAL/IJCLab in the framework of the Exsqueeze ANR in collaboration with LKB, LMA/IP2I and LAPP. The aim of this thesis is the design of the experiment followed by the installation and characterization of the first optical systems used to produce and measure frequency independent squeezing.

